Lawrence Berkeley National Laboratory

Recent Work

Title

ELECTRONIC STRUCTURE OF COMPLEX CRYSTALLINE AND AMORPHOUS SEMICONDUCTORS

Permalink

https://escholarship.org/uc/item/55r4k83x

Author

Joannopoulos, John.

Publication Date

1974-05-01

eScholarship.org Powered by the California Digital Library
University of California

RECEIVED
LAWRENCE
RADIATION LABORATORY

JUN 4 1974

LIBRARY AND
DOCUMENTS SECTION

LBL-2724
c.2

ELECTRONIC STRUCTURE OF COMPLEX CRYSTALLINE AND AMORPHOUS SEMICONDUCTORS

John Joannopoulos
(Ph.D. thesis)

May 1974

Prepared for the U. S. Atomic Energy Commission
under Contract W-7405-ENG-48

TWO-WEEK LOAN COPY

This is a Library Circulating Copy which may be borrowed for two weeks. For a personal retention copy, call Tech. Info. Division, Ext. 5545

LAWRENCE BERKELEY LABORATORY
UNIVERSITY OF CALIFORNIA
BERKELEY

LBL-2724
c.2

DISCLAIMER

This document was prepared as an account of work sponsored by the United States Government. While this document is believed to contain correct information, neither the United States Government nor any agency thereof, nor the Regents of the University of California, nor any of their employees, makes any warranty, express or implied, or assumes any legal responsibility for the accuracy, completeness, or usefulness of any information, apparatus, product, or process disclosed, or represents that its use would not infringe privately owned rights. Reference herein to any specific commercial product, process, or service by its trade name, trademark, manufacturer, or otherwise, does not necessarily constitute or imply its endorsement, recommendation, or favoring by the United States Government or any agency thereof, or the Regents of the University of California. The views and opinions of authors expressed herein do not necessarily state or reflect those of the United States Government or any agency thereof or the Regents of the University of California.

ELECTRONIC STRUCTURE OF COMPLEX CRYSTALLINE AND AMORPHOUS SEMICONDUCTORS

Contents

ELECTRONIC STRUCTURE OF COMPLEX CRYSTALLINE AND AMORPHOUS SEMICONDUCTORS

John Joannopoulos

Department of Physics, Inorganic Materials Research Division,
Lawrence Berkeley Laboratory and University of California
Berkeley, California 94720

ABSTRACT

A study of the electronic structure of some complex crystalline[1] and amorphous phases of Group IV, binary and Group VI compounds is present with the emphasis on understanding the effects of long- and short-range order and disorder.

The effects of long-range order are studied by comparisons of calculations of change densities of ZnS in the zinc blende and wurtzite structures using the empirical pseudopotential method (EPM).[2] A scheme for obtaining the charge density from only a few representative $\vec{k}$ vectors is presented.

Effects of short-range order and disorder are studied by an examination of the band structures, electronic densities of states, and optical properties of Ge and Si in the diamond, wurtzite, BC-8,[1] and ST-12[1] crystal structures using the EPM and simple tight binding models. A complete band structure, critical point analysis and group theoretical discussion of the wurtzite, BC-8 and ST-12 structures is presented. Dipole matrix elements P(E) and joint densities of states J(E) are calculated and examined in order to discern information about the effects of disorder on the optical properties. In addition a new method is introduced to obtain the density of states of an infinite system using only information about local topologies.

Effects of disorder on the density of states of binary compounds are studied by taking GaAs as a prototype and constructing various GaAs structures using the atomic positions of the wurtzite, BC-8 and ST-12 structures. The density of states of GaAs in these structures is calculated using the EPM and simple tight binding models. Two density of states models are presented simulating the effects of disorder with and without like-atom bonds. In addition, charge densities are used in order to study the nature of like-atom bonds.

Finally, a comparative study of the electronic densities of states of Se and Te in the trigonal and amorphous phases is presented. New EPM calculations on trigonal Se and Te are performed which are in excellent agreement with recent photoemission results.[41,42] Charge densities are calculated for certain regions of energy which associate peaks in the densities of states with particular bonding characteristics. In addition, a new method for determining bonding charge by extracting short wavelength components from the charge density is introduced. The changes observed in the densities of states of amorphous Se and Te are examined and interpreted.

I. INTRODUCTION

We present a theoretical study of the electronic structure of various crystalline and amorphous semiconductors with emphasis on understanding the influences of long- and short-range order and disorder. We begin in Section II with an examination of the effects of long-range order on the electronic charge densities of ZnS in a zinc blende and an ideal wurtzite structure. A comparison of the charge densities reveals the presence of a net polarization in the ideal wurtzite structure. In addition, two representative $\vec{k}$ points are found whose total change density is in very good agreement with the charge density obtained by summing over many points in the irreducible part of the Brillouin zone.

From here we proceed in the following sections to a study of short-range disorder (SRD) on the electronic and optical properties of some complex crystalline and amorphous semiconductors. In Section III we present calculations of the band structures and electronic densities of states of Ge and Si in the diamond, wurtzite, Si III[1] (BC-8), and Ge III[1] (ST-12) structures. This is a series of crystals which exist in nature and are listed in order of increasing number and positional disorder of atoms in the primitive cells. From the increase complexity of the crystal structures we find that SRD is able to account well for the density of states of amorphous Ge and Si. These calculations also provide a method of explaining various features in the amorphous density of states and show what structural aspects of the amorphous state are responsible for these features. In addition, using a simple Hamiltonian, we introduce a new method to study explicitly the effects of local topology on the density of states of an infinite system. Our results show that the number and type of rings of bonds in the vicinity of and passing through a certain atom are intimately related to the position and number of peaks in the local density of states of this atom. In Section IV we calculate and examine the imaginary part of the dielectric function ε_2 as a function of energy for Ge and Si in the aformentioned crystal structures. In particular we have obtained the symmetries of wave functions along important symmetry directions and identified the major contributions to the optical structure. In addition, a further study is made into the optical properties of amorphous Ge and Si which reveals that the amorphous ε_2 spectrum has the same form as an averaged matrix element as a function of frequency. In Section IV we extend our methods to study the amorphous binary compounds. Specifically, we investigate the effects of two types of disorder on the density of states of III-V semiconductors. For the first type of disorder we consider a stoichiometric system with fourfold coordination, all bonds satisfied, variations in bond lengths and angles, and only <u>unlike-atom bonds</u>. The second type of disorder includes the properties of the first with the addition of <u>like-atom bonds</u>. These two types of disorders are studied explicitly by taking GaAs as a prototype and making various GaAs structures using the atomic positions of the previously mentioned crystal structures. A comparison of the trends observed in the densities of states with the inclusion of different types of disorder reveals valuable information concerning the relationship of the structural nature of an amorphous system to its density of states. From our results we construct two density of states models for amorphous III-V compounds which simulate the effects of these two types of disorder respectively.

Finally, in Section VI we study the electronic structure of chain-like elements, i.e., Se and Te. We have obtained electronic densities of states and charge distributions for the valence electrons in trigonal Se and Te and we have explored the relation between density of states structure and charge density. In particular structures in the photoemission spectra are identified with particular interchain and intrachain bonding states. These results are then used to interpret the changes observed in the experimental photoemission spectra of amorphous Se and Te.

The calculational methods that we have used in all our work include the empirical psendopotential method[2] and various tight binding models. These methods will be discussed in detail in the text and in the Appendices.

II. ELECTRONIC CHARGE DENSITIES FOR ZnS IN THE WURTZITE AND ZINC BLENDE STRUCTURES

In this section, we wish to obtain and compare the electronic distributions of two different crystal structures of the same compound. Specifically, we have calculated the electronic charge density as a function of position in the unit cell for ZnS in the wurtzite and zinc blende structures. These two crystal structures are shown in Fig. 1, with the wurtzite structure aligned so that the c axis is in the direction and the zinc blende structure is aligned with its (111) direction in the z direction. The difference between the two structures occurs first at third nearest neighbors and a detailed discussion of the wurtzite structure is given in Appendix C along with the structural parameters used.

The charge density was obtained individually for each valence and conduction band and for the sum of the valence bands from a band structure calculation using the empirical pseudopotential method[2] (EPM). This method is discussed in Appendix A but briefly it involves solving a secular equation for the pseudopotential Hamiltonian which has the form

$$\mathcal{H} = -(\hbar^2/2m)\, \nabla^2 + V(\vec{r}) \quad . \tag{1}$$

To take advantage of the crystal symmetry, the weak crystalline pseudopotential $V(\vec{r})$ is expanded in the reciprocal lattice $\{\vec{G}\}$

$$V(\vec{r}) = \sum_{\vec{G}} V(|\vec{G}|)\; S(\vec{G})\; e^{i\vec{G}\cdot\vec{r}} \tag{2}$$

where $S(\vec{G})$ is a structure factor and contains information about the position of the atoms in the primitive cell and the $V(|\vec{G}|)$ are called form factors and are the fourier components of the atomic pseudopotentials. Because of $S(\vec{G})$ one only needs a small number of $V(|\vec{G}|)$ in order to specify the crystalline pseudopotential. The EPM is particularly useful in studying different crystal structures of the same compound since if one has a good set of form factors for a given crystal structure one only needs to perform a suitable interpolation to obtain the form factors for any other crystal structure defined by $S(\vec{G})$. This was done first by Bergstresser and Cohen[3] for ZnS in the wurtzite structure and it is these factors that we have used in our study.

In order to obtain good convergence in the wave functions it was necessary to diagonalize a 90×90 matrix for zinc blende and a 135×135 matrix for wurtzite. Eighty additional plane waves were brought in through the use of a perturbation technique developed by Löwdin.[4]

We now have in principle all the information necessary to obtain the charge density. Since the wave functions $\phi_{n,\vec{k}}(\vec{r})$ are known as a function of band index we can postulate a "band" charge density:

$$\rho_n(\vec{r}) = e \sum_{n}^{BZ} \phi^*_{n,\vec{k}}(\vec{r})\ \phi_{n,\vec{k}}(\vec{r}) \tag{3}$$

$$\rho_n(\vec{r}) = e \sum_{\vec{\Gamma}} \sum_{\vec{G}} \sum_{\vec{k}}^{BZ} \alpha^*_n(\vec{G} - \vec{\Gamma},\vec{k})\ \alpha_n(\vec{G},\vec{k})\ e^{i\vec{\Gamma}\cdot\vec{r}} \tag{4}$$

The total charge density is then given by

$$\rho(r) = \sum_n \rho_n(\vec{r}) \tag{5}$$

where the sum in Eq. (5) is over the valence bands.

The expression in Eq. (4) is a general result; however, the procedure involved in evaluating this expression depends on the symmetry properties of the crystal studied. The zinc blende charge density calculation was carried out exactly as in Ref. 5. The wurtzite charge density calculation will now be described briefly.

The Brillouin Zone (BZ) for the hexagonal structure and its irreducible part are well known. Although the energies $E_n(\vec{k})$ are exactly the same at related points in the BZ, the wave functions in general are not. Our procedure was to calculate the $\phi_{n,\vec{k}}$ in 1/34 of the zone at 84 points and obtain the rest of the $\phi_{n,\vec{k}}$ by rotations of $\pi/3$, inversions and mirror reflections in k space. The method used to find how the $\phi_{n,\vec{k}}$ transform is discussed in Appendix B.

A. Results

Since we are dealing with pseudowavefunctions which should not be valid near the core it is important to say something quantitative about the size of the Zn and S cores. The electronic configuration of the Zn and S cores is $1s^2 2s^2 2p^6 3s^2 3p^6 3d^{10}$ and $1s^2 2s^2 2p^6$ respectively. Using the wave functions obtained by Herman and Skillman[6] we found that:

(i) Ninty per cent of all the Zn core electrons are within a radius of 12% of the nearest neighbor distance. In particular this radius contains 86% of the 3d shell, 93% of the 3p and 3s shells and approximately 100% of the rest.

(ii) Ninty per cent of all the S core electrons are within a radius of 0.16 of the nearest neighbor distance. In particular this radius contains approximately 88% of the 2p and 2s shells and approximately 100% of the 1s shell.

We are confident that for such small cores the wave functions are quite adequate.

1. Cubic

In the cubic case, chains of bonds that lie in a plane only occur in a zigzag pattern. If one sights along the direction of any bond one sees the same symmetrical distribution or environment of atoms. Thus the effects of this environment through long range electrostatic interactions will be along the direction of the bonds and the short range tetrahedral symmetry will be preserved.

We found the charge density of ZnS in the zinc blende structure to be very similar to that of ZnSe obtained by Walter and Cohen.[5] Because of this similarity we show in Fig. 2 only a contour plot of the total charge density. There is only one type of plane of interest and that is the $(1\bar{1}0)$ plane or the plane formed by the dotted lines in Fig. 1b. The charge density is evaluated on a grid of over 1500 points. In Fig. 3 we show a contour plot of the total crystalline pseudopotential, obtained from Eq. (6), in the same plane as the charge density. The potential was evaluated on a grid of over 3500 points and the zero of potential was chosen arbitrarily such that the average crystalline potential is zero. The tetrahedral symmetry in Figs. 2 and 3 is evident. The amount of charge around the S atom within a radius of 3/4 the nearest neighbor distance is approximately 7.3 e, and only 2% of this charge is in the core region.

2. Hexagonal

In the wurtzite structure we have four atoms in the unit cell so that we have eight valence bands. We found that the charge density of bands 1 and 2 are almost identical so that in Figs. 4 through 7 we show contour plots of the charge density for bands 1 through 8. In Fig. 7 we also show a plot for the hypothetical situation where the conduction band is full of electrons. The plane in these figures is the (110) plane or plane I in Fig. 1a. The charge densities were evaluated on a grid of more than 4000 points. We notice that bands 1 and 2 are very s-like whereas the rest of the bands have pronounced p-like character. In particular bands 6 and 8 are almost pure p_{xy}-like and p_z-like respectively. We also notice that the character of the conduction band is almost free electron-like although there still is some localization around the S atoms. In Fig. 8 we show a plot of the total charge density in plane I. In this plane, the atoms form square wave-like chains of bonds which cannot be found in zinc blende. The zigzag patterns in the cubic case, however, can be found in the (101) plane or plane II in Fig. 1a. A contour plot of the total charge density in this plane is shown in Fig. 9. In Figs. 10 and 11 we also show contour plots of the total charge density in planes III and IV. These planes help provide a three-dimensional view of the charge density. Comparing Figs. 8 and 9 we notice immediately an asymmetry in the electron distribution. Although the ionic cores are in a perfect tetrahedral arrangement the charge density is not. There seems to be a difference between bonds in the z directions and bonds in the other three corresponding tetrahedral directions. Firstly, the maximum charge density occurs only for bonds in the z direction and secondly, the charge density is pushed slightly out of the bond for those bonds which are not in the z direction. This asymmetry is actually a direct manifestation of the potential. This is clear in Fig. 12 in which we show contour plots of the crystalline pseudopotential in plane I.

Actually these results are not surprising. In the zinc blende structure the environment of each bond is the same for all bonds. In the wurtzite structure, however, this is not the case. If one sights along a bond in the z direction all the atoms which affect it are placed symmetrically, in planes perpendicular to the z direction. The net effect of these atoms is then directed along the bond. If one now sights along any other bond not in the z direction one finds an asymmetrical distribution of atoms. The net effect of this type of environment is not directed along the bond, but actually directed slightly out of the bond. To show this in a simple way consider the following model. We assume we can construct a ZnS crystal out of two types of constituents: (1) positively charged Zn cores with a charge of $2e^-$ and (2) S cores curroounded by a perfect tetrahedral distribution of electrons as in Fig. 2 of the cubic charge density. The net charge on this second part being $-2e^-$. We are thus taking implicitly into account the short range interactions and we shall be interested in the effect of long-range electrostatic interactions on the bond electrons of type (2) constituents. If we now arrange these constituents in a zinc blende structure and calculate the net electric field acting on these electrons we find of course that the field is directed along the bond preserving the tetrahedral symmetry. However, if we construct a wurtzite crystal out of these constituents and calculate the net electric field on the electrons in the diagonal bonds we find that the field is directed primarily along the bond direction appart from a small z component which has the effect of pushing electrons out of the bond in the positive z direction. This is exactly what we find in our charge densities.

This asymmetrical distribution of charge in "ideal" wurtzite will produce a polarization. We can calculate the dipole moment p per primitive cell analytically using the fourier expansion of the charge density. We find:

$$p \sim 10^{-19} \text{ esu cm} \quad . \tag{6}$$

This is only about 50 times smaller than a usual ferroelectric-like $BaTiO_3$. Although we do not expect our value for p to be accurate we do believe that there will be a resultant polarization. This polarization will then change the electronic and core positions so that the crystal reaches a lower energy state and the polarization is minimized. This tempts one to suggest that the non-ideal c/a ratio found in real crystals results from changes in the crystal structure to reduce p.

B. Representative k Vectors for the Total Charge Density

The idea here is to find a few $\vec{k}$ points whose charge density will give a good approximation to the total charge density. Baldereschi[7] first proposed this and obtained one representative $\vec{k}$ point which gave an approximate total charge density for compounds in an fcc lattice. Chadi and Cohen,[8] using wave functions expanded in terms of Wannier functions, obtained three representative $\vec{k}$ points at whose weighted sum of charge densities gives better agreement than the Baldereschi point.

In this section we wish to present a simple method of obtaining the same conditions for the k points without using any wave functions. Let $\hat{\rho}(\vec{r})$ be defined in the following way:

$$\hat{\rho}(\vec{k},\vec{r}) = \sum_{T} \rho(T\vec{k},\vec{r}) \tag{7}$$

where $\rho(\vec{k},\vec{r})$ is the charge density of the point $\vec{k}$ and $\{T\}$ represents the set of point operations for the lattice. Now $\hat{\rho}_{\vec{k}}(\vec{r})$ is a periodic function of $\vec{k}$, so that we can expand it in the following way:

$$\hat{\rho}(\vec{k},\vec{r}) = \sum_{\vec{\ell}} \hat{\hat{\rho}}(\vec{\ell},\vec{r})\, e^{i\vec{k}\cdot\vec{\ell}} \quad . \tag{8}$$

Now since $\hat{\rho}(\vec{k},\vec{r}) = \hat{\rho}(T\vec{k},\vec{r})$, $\hat{\hat{\rho}}(\vec{\ell},\vec{r}) = \hat{\hat{\rho}}(T\vec{\ell},\vec{r})$. Therefore,

$$\hat{\rho}(\vec{k},\vec{r}) = \sum_{\vec{\ell}} \hat{\hat{\rho}}(\vec{\ell},\vec{r}) \sum_{T} e^{i\vec{k}\cdot T\vec{\ell}} \tag{9}$$

$$\hat{\rho}(\vec{k},\vec{r}) = \sum_{\vec{\ell}} \hat{\hat{\rho}}(\vec{\ell},\vec{r})\; \xi(\vec{k},\vec{\ell}) \tag{10}$$

where $\hat{\hat{\rho}}(0,\vec{r})$ is the total charge density in question. Thus, if we could find a $\vec{k}_0$ that makes all the $\xi(\vec{k},\vec{\ell})$ equal to zero for $\vec{\ell} \neq 0$ then $\hat{\hat{\rho}}(\vec{k}_0,\vec{r})$ would be exactly equal to the total charge density. We have found that $\rho(\vec{k},\vec{r})$ is a slowly varying function of $\vec{k}$ so that we expect the $\hat{\rho}(\vec{\ell},\vec{r})$ to decrease in magnitude as $|\vec{\ell}|$ increases. The object then is to find a k_0 which will make as many of the $\xi(\vec{k}_0,\vec{\ell})$ for small $|\vec{\ell}|$ equal to zero as possible. The Baldereschi point gives ξ equal to zero for the first two $|\vec{\ell}|$ shells. In this calculation we obtained two $\vec{k}$ points for an *hcp lattice* which give ξ equal to zero for the first ten shells except for the fifth shell. The total charge density we obtained using the average charge density of these points, agrees very well with this calculation.

The points are given by:

$$k_1 = \left(\frac{\sqrt{3}}{4}, \frac{\sqrt{3}}{8}, \frac{1}{4}\right) \tag{11}$$

$$k_2 = \left(\frac{\sqrt{3}}{8}, \frac{-\sqrt{3}}{8}, \frac{1}{4}\right) \tag{12}$$

and the components are with respect to the primitive reciprocal lattice vectors $\vec{A}$, $\vec{B}$ and $\vec{C}$ hexagonal with $\hat{A} \cdot \hat{B} = 0.5$.

Recently, Chadi and Cohen[9] have developed a systematic way of generating larger and larger sets of special k points. This is very useful since a one or two point scheme is inadequate for calculating the individual $\rho_n(\vec{r})$ although it works very well in obtaining the total charge density. On the other hand, the Chadi and Cohen[9] ten (for zinc blende) or twelve (for wurtzite) point scheme is excellent for the total charge density and works very well for the $\rho_n(\vec{r})$.

III. ELECTRONIC DENSITIES OF STATES OF COMPLEX CRYSTALLINE AND AMORPHOUS PHASES OF Ge and Si

The electronic densities of states of amorphous Ge and Si as obtained from ultraviolet (UPS)[10] and X-ray (XPS)[11] photoemission spectroscopy exhibit some very interesting features when compared with the corresponding ones of their crystalline phases. For example, one finds experimentally the retention of a "gap" in the amorphous phase. This has been shown theoretically for some special models by Weaire and Thorpe[12] and McGill and Klima.[13] However, the conduction band density of states seems to have none of the structure found in the crystalline phase (see Fig. 21a). Furthermore, the form of the valence band density of states in the amorphous phase consists of a smoothed, blue shifted, peak at the top of the valence band and a seemingly large broad peak at the bottom of the valence band[12,13] (see Fig. 23). This is in contrast to the three strong peaks found in the valence bands of the crystalline phase.

Amorphous samples can be prepared in a variety of ways with a range of bulk density from 25% less to approximately the same as the bulk density of the crystalline case. There also exists a lot of speculation as to the structural nature of the amorphous phase. On this point there have been primarily two main schools of thought. First that the amorphous structure is made up of small domains of perfect crystals separated by disordered boundaries, which is called the "microcrystallite model". For example, Rudee and Howie[14] found that their amorphous films gave consistent diffraction ring patterns with a microcrystallite model if their amorphous sample were made up of "wurtzite" microcrystals. Another approach is that the amorphous phase can exist in a completely disordered structure while each atom retains an imperfect tetrahedral arrangement of nearest neighbors. In this case, if all the bonds are satisfied, the model is called a "random network model". Spicer and co-workers[10] seem to be able to prepare their amorphous samples in an "ideal" manner such that they have a negligible presence of microvoids and dangling bonds and have the same nearest neighbor distance and approximately the same bulk density as that of the crystalline case. It is this type of sample that we will have in mind when we discuss and compare our results with the "amorphous phase".

It is clearly a formidable task to perform a realistic calculation on a structure with long range disorder. However, we could ask the following question. How much disorder is necessary to achieve the distinctive features evident in the amorphous data? To explore the possible answers to this question, we have calculated the band structure and density of states for Ge and Si in the diamond, "wurtzite", Si III,[1] and Ge III[1] structures using the EPM[2] and the tight-binding model used recently by Weaire.[12] From the pseudopotential band structure we have also calculated the optical properties of these structures. The diamond structure is face-centered cubic with two atoms per primitive cell (FC-2), wurtzite is hexagonal 2H with four atoms per primitive cell (2H-4), Si III is body-centered cubic with eight atoms per primitive cell (BC-8), and Ge III is simple-tetragonal with twelve atoms per primitive cell (ST-12). The Si III and Ge III structures are complicated, dense, metastable crystalline phases which are recovered from high pressure experiments and persist at normal pressures. When Ge occurs in the Si III structure it is called Ge IV.[15] Because of this rather unfortunate terminology we shall use the notation described above in parentheses for the specification of these various structures.

FC-2, 2H-4, BC-8 and ST-12 provide us with a series of structures that become more and more locally disordered. What we imply by local disorder is that we have a crystal (long range order) and yet the atoms in the primitive cell of our crystal are in a "disordered" tetrahedral-like arrangement. The FC-2, 2H-4 and BC-8 structures are all similar in that they have sixfold rings of bonds and one type of atomic environment. The ST-12 structure, however, is very novel in that it has fivefold rings of bonds and two types of atomic environment. The electronic properties of these structures should then provide us with some interesting tests for the microcrystallite and random network models and should provide us with an idea of how much disorder is necessary to reproduce the important features of the experimental amorphous data.

A detailed discussion of the structure of these polymorphs and their parameters is given in Appendic C. The bulk densities of Ge ST-12 (Si ST-12) and Ge BC-8 (Si BC-8) differ by about 1%. However, they are both about 10% greater than those of Ge FC-2 (Si FC-2) and certain types of amorphous Ge (Si).[10] Therefore, a comparison of the differences between the density of states of Ge FC-2 (Si FC-2) and Ge BC-8 (Si BC-8) can be attributed primarily to structural and symmetry differences. Hence, comparisons of the polymorphs provide a method of filtering out the effects of greater density, which should not be very important as long as the bond lengths do not change appreciably.

It would be appropriate at this time to mention that we were able to build a crystal with the same symmetry and number of atoms in the primitive cell as Ge ST-12 but with the same nearest neighbor distance and bulk density as amorphous Ge. The method consisted of finding three independent bond lengths b_1, b_2 and b_3 which were functions of a, x_1, x_2, x_3 x_4 and V such that $c = V/a^2$. Once the density was fixed through V we minimized the function

$$M(x_1,x_2,x_3,x_4,a) = \sum_{i=1}^{3}(b_i[x_1,x_2,x_3,x_4,a] - \ell_i)^2$$

by a method of steepest decent. Although we obtained the correct bond lengths ℓ_i, bulk density and a good radial distribution function, we obtained some bond angles that were 40% bigger than the ideal tetrahedral angle. These large deviations in our modified crystal produced large deviations in the Hamiltonian matrix elements and we found that we obtained a semimetal. This is in large contrast to the fact that we found quite a sizeable gap for Ge ST-12. This will be of interest later when we discuss what different structural aspects affect the size of the gap.

Since no experimental data are available at this time for the polymorphes we have studied, the form factors we have obtained might have to be adjusted slightly to give better agreement with experiment. In Table I and Table II we list the unnormalized form factors for Ge and Si and the corresponding reciprocal lattice vectors for the 2H-4, BC-8 and ST-12 crystal structures. For the 2H-4 structure we used 50-60 plane waves as a basis set along with another 140 plane waves through a perturbation scheme developed by Löwdin.[4] We calculated $E(\vec{k})$ in 1/24 of the BZ at 275 grid points. For the BC-8 structure we used approximately 60-65 plane waves as a basis with about 160 additional plane waves through perturbation theory. We diagonalized our Hamiltonian in 1/48 of the BZ at 240 grid points. Finally, for ST-12 we used about 70 plane waves as a basis set along with approximately 270 more plane waves through the Löwdin scheme. The eigenvalues were obtained in 1/16 of the BZ at 251 grid points. For all these structures we obtain a convergence of ≤0.1 eV for almost all the states in valence band and for the states in the conduction band in the vicinity of the gap.

In our tight binding calculation we took the model used recently by Weaire and Thorpe.[12] The Bloch wave functions for each band have the form:

$$\psi_{\vec{k},n}(\vec{r}) = \sum_m C^n_m X_{\vec{k},m}(\vec{r}) \tag{13}$$

where the $X_{k,m}(\vec{r})$ form a basis set of order M of tight binding Bloch states given by

$$X_{\vec{k},m}(\vec{r}) = \frac{1}{\sqrt{N}} \sum_{\vec{R}} e^{i\vec{k}\cdot\vec{R}} \phi(\vec{r} - \vec{R} - \vec{\tau}_i - \vec{\rho}_\ell) \tag{14}$$

where $m \equiv i, \ell$; N is the number of primitive cells and the ϕ_m are localized orthonormal states which can be taken as (sp^3) hybridized directed orbitals (four of each atom). The position of the i^{th} atom in the primitive cell is given by $\vec{\tau}_i$, and $\vec{\rho}_\ell$ designates the direction and center of mass position of the ℓ^{th} directed orbital of the i^{th} atom. Furthermore, for $i \neq i'$, $\ell' = \ell$ will imply $-\vec{\rho}_\ell = \vec{\rho}_{\ell'}$ and that $|\vec{\tau}_i - \vec{\tau}_{i'}|$

is equal to a bond length. Thus states $\phi_{i',\ell}$ and $\phi_{i,\ell}$ are orbitals from different atoms which lie in the same bond and $\phi_{i,\ell}$ and $\phi_{i,\ell'}$ represent different orbitals defined with respect to the same atom.

In this model there are only two important nonzero matrix elements given by:

$$\langle i,\ell|H|i,\ell'\rangle = V_1 \quad \text{and} \quad \langle i,\ell|H|i',\ell\rangle = V_2 \quad . \tag{15}$$

The parameters V_1 and V_2 for the FC-2 structure were obtained by fitting them to the valence band density of states of Ge FC-2 using the EPM. The values obtained were $V_1 = -2.22$ and $V_2 = -6.20$ and were taken to be the same for the BC-8 and ST-12 structures. The Weaire model of course assumes all the bond lengths are equal and a perfect tetrahedral arrangement for the atoms. The most prominent features of this model are a flat band at the top of the valence band containing two states per atom, a rather inadequate conduction band due to the limited number of basis functions and an energy gap which is the same for all structures with even membered rings of bonds. An extension of this model to include all interactions between nearest neighbors works very well and is discussed in Appendix D.

Once the band structure is known the density of states can be obtained using the following expression:

$$N(E) = \frac{1}{NN_a} \sum_{\vec{k}} \sum_{n} \delta(E - E_n(\vec{k})) \tag{16}$$

where N_a is the number of atoms in the primitive cell, N is the number of primitive cells and N(E) is normalized to the number of states per atom. The method used to evaluate the integral in Eq. (16) is due to Gilat and Raubenheimer.[16] The energy derivatives required by this method were obtained using $\vec{k}\cdot\vec{p}$ perturbation theory.

A. Results

The band structures of Ge and Si in the 2H-4, BC-8 and ST-12 structures are shown in Figs. 14 through 19. In Fig. 13 we show the Brillouin zones for these structures and the symmetry and notation used by Leuhrman.[17]

Certain symmetry directions in the 2H-4 structure can be compared with analogous ones in the FC-2 structure through an alignment of the Brillouin zones.[18] One finds the ΓL direction (FC-2) maps into the ΓAΓ direction (2H-4) so that the indirect gap at L for Ge FC-2 becomes a direct gap at Γ in Ge 2H-4 and is equal to 0.55 eV. Although the ΓX direction (FC-2) is not associated with any symmetry direction in 2H-4, the X point is found to lie 2/3 along the U axis from M to L (2H-4). Si, however, which has an indirect gap at X in the FC-2 structure has an indirect gap at M in the 2H-4 structure equal to 0.85 eV.

In the BC-8 structure we find direct gaps for Si and Ge and they both occur at H. For Ge we obtain a zero gap whereas for Si we obtain 0.43 eV. It is interesting that in the Weaire tight binding BC-8 band structure we find the bottom of the conduction band also occurs at H.

In the ST-12 structure we find a direct gap for Ge 0.7 of the way from Γ to M_z. The magnitude of the gap is 1.47 eV. For Si we obtain an indirect gap with the top of the valence band 0.4 of the way from Γ to M_z and the bottom of the conduction band about 0.75 of the way between Γ and Z_x. The Si gap is equal to 1.6 eV. It should be mentioned, however, that since the valence band is rather flat along many symmetry directions and the conduction band has many dips at very nearly the same energy, the actual experimental gap could be direct or indirect and could lie in a variety of places. It is interesting, nevertheless that we find using the Weaire tight binding model that the ST-12 gap lies at M_z.

What is striking in this calculation is that the Ge and Si ST-12 gaps are about 50% larger than those of all the other structures. This is probably due to the influence of the large numbers of five and sevenfold rings in the ST-12 structure which would prevent the presence of low-lying, antibonding s-like states in the conduction band. Weaire et al.[12] have suggested this might happen in structures with odd-numbered rings, but the degree wo which it happens is shown in Fig. 20. Here we show the results of our calculation on an "ideal" ST-12 and BC-8 structure using the Weaire model. At the top of the valence band we have the p-like delta function peak containing two states per atom, while the rest of the valence band is s-like and also contains two states per atom. We notice in Fig. 20(b) that we now have a "valence gap" and a "conduction gap". The "conduction gap" for ST-12 is considerably larger than that of BC-8 and FC-2 (dotted line). In fact, we find a 200% increase in the gap if we include an ad hoc 2.0 eV broadening of the delta function peak at the top of the valence band. In this model the "valence" and "conduction" gaps are intimately related. This is because the conduction and valence band eigenvalues (except for the pure p-like states) are associated through the same analytic transformation (aside from a sign) to the eigenvalues of a one-state Hamiltonian.[19] The coefficient of a one-state wave function is then equal to the sum of the coefficients of the corresponding four states in the old Hamiltonian which is just the s coefficient of these four states. Thus, the omission of antibonding states in the one-state Hamiltonian will reflect itself in the omission of s-like states from the top of the valence band and bottom of the conduction band.

In the EPM case we do not expect such large effects since we obtain a much more realistic band structure. Nevertheless, the low energy conduction band states are rather localized and so we still expect the influence of odd-membered rings to be important. In fact, we can even observe a "valence gap" in Figs. 18 and 19 for Ge ST-12 and Si ST-12. In Ge ST-12 the s-like and p-like states area almost separated while in Si ST-12 there is just a little mixing around -4.4 eV.

In Figs. 21a, b and c and we show plots of the density of states for Ge in the FC-2, 2H-4, BC-8 and ST-12 structures. Similar results for Si are shown in Fig. 22. Superimposed on the Ge (Si) FC-2 density of states is a sketch of the amorphous density of states obtained by Donovan and Spicer[10] (Pierce and Spicer). The sharp peaks are primarily due to Bragg gaps[20] and would be smoothed out in a structure with no periodicity. Keeping this in mind we can make some interesting comparisons among these structures and we can examine the trends in going from FC-2 to 2H-4, to BC-8, to ST-12, to amorphous.

First we notice that the conduction band becomes more and more smoothed out as we go from FC-2 to ST-12. These lack of large structure also seems to be evident in the amorphous phase. Next we notice that the two large peaks at the bottom of the valence band in FC-2 seem to gain more structure as we go to 2H-4 and BC-8. Nevertheless, these peaks still retain most of their individual identity. In the ST-12 structure, however, there is a thorough mixing of the two peaks. This is similar to the suggestion by Thorpe et al.[21] for the amorphous case. Experimentally Wiech and Zöpf[22] did find a seemingly large broad peak at the bottom of the valence band for amorphous Si using a soft X-ray spectroscopy. Recently, this has been confirmed by Ley et al.[11] for amorphous Si and Ge using X-ray photoelectronic spectroscopy. These results are shown in Fig. 23. The fact that states are introduced in the valley between the two lower valence band peaks in Figs. 21a and 22a for the amorphous and ST-12 phases, in such a way as to obtain a large hump where the valley used to be, can be primarily attributed to the presence of odd numbered rings of bonds. This is suggested by the following simple argument. The FC-2 structure can be considered to be made up of six membered rings in the "chair" configuration. That is, we can pick a set of rings which can be brought together to make an FC-2 structure and we will assume for the moment that they do not loose their identity. Let us now isolate one of these rings and place one localized orbital at each of the atomic sites. We are thinking in terms of the one-state Hamiltonian mentioned earlier. The symmetry of this ring is D_{3d} and if we assume that these localized states transform into one another under D_{3d}, they then form a basis for the six dimensional representation $\Gamma_6 = A_1 + E_1 + E_2 + B_1$. Thus, we have six states consisting of two single states of symmetry A_1 and B_1, and two doubly degenerate states of symmetry E_1 and E_2. If we now assume only nearest neighbor interactions $\mathcal{H}_I$ we obtain $E(A_1) = -2|\mathcal{H}_I|$, $E(E_1) = -|\mathcal{H}_I|$, $E(E_2) = |\mathcal{H}_I|$ and $E(B_1) = 2|\mathcal{H}_1|$. Let us now isolate N rings at infinity. The density of states for this system is just an N-fold degenerate single ring density of states. As we bring these rings closer together, to make an FC-2 or 2H-4 structure, the rings will interact and the states are going to spread. Since we are considering only nearest neighbor interactions we so not expect any drastic or significant differences when the inter-ring interaction becomes equal to the intra-ring interaction. For example, we can bring two rings together in such a way as to make a total of five rings. However, the energy spectrum for this system consists of just a splitting of each energy level of the two single ring system by about $|\mathcal{H}_I|$. This is what we expected and thus the N-ring system should have a density of states which consists of two big humps and some type of valley in between. This density of states is then analogous to the two peaks at the bottom of the valence band in Figs. 21a and 22a.

Consider now the same analysis with a five membered ring which we may take to have symmetry D_5. Assuming again that the localized states transform into each other under D_5, they span a five dimensional representation $\Gamma_5 = A_1 + E_1 + E_2$. Thus we have five states consisting of a single state of symmetry A_1 and two double degenerate states of symmetry E_1 and E_2. We then obtain $E(A_1) = -2|\mathcal{H}_I|$, $E(E_1) = -2 \cos \frac{2\pi}{5} |\mathcal{H}_I|$ and $E(E_2) = -2 \cos \frac{4\pi}{5} |\mathcal{H}_I|$. The states of symmetry E_1 and E_2 lie intermediate in energy to those of the sixfold rings with symmetry E_1, E_2 and B_1. Thus fivefold rings will introduce states in the valley between the two density of states peaks at the bottom of the valence band. In fact the eigenvalues of any ring of order N are given by:

$$E_n = -2|\mathcal{H}_I| \cos \frac{2n\pi}{N} , \quad n = 0, 1, \ldots , N - 1 . \tag{17}$$

Therefore, sevenfold rings will also introduce states in the valley. Thus five and sevenfold rings will help to produce a one hump type of structure with a peak where the valley used to be. These results are consistent with those obtained by Weaire and Thorpe[19] for "Husumi cacti" made up of five and sixfold rings. In Section III-B we will use a different approach which will lead us to the same conclusions.

The valence band density of states edges of Ge and Si in the FC-2, 2H-4 and BC-8 structures (Figs. 21 and 22) are all similar in that they gradual slopes. On the other hand, Ge and Si in the ST-12 and amorphous phases have very sharp edges. Along with this is the fact that there is a very noticeable shift of the hump at the top of the valence band to higher energies in the amorphous and ST-12 structures. We believe that the reason for this is an increase in the coulomb repulsion energy and kinetic energy because of variations in the bond angle in the amorphous and ST-12 phases. This can be shown by the following argument. Consider a system with a perfect tetrahedral arrangement of atoms like Ge FC-2 for example. The states in the large hump at the top of the valence band localize the electrons primarily in the bond whereas the states in the two large peaks at the bottom of the valence band localize the electrons primarily on the atoms. It is the electrons in the bonds which are more sensitive to changes in bond angle. Now the states at the high energy side in the hump have a larger kinetic energy than the states at the lower energy side in this hump. This reflects itself in the fact that the former states are very localized in the bonds whereas the latter states are more spread out in the bonds. Let us now consider an amorphous system and let us naively assume that we have just as many larger bond angles as smaller bond angles. Since the interaction between the bonds is not linear we will have an increase in the energy of each electronic state. However, the states at the lower energy side in the large hump will have a larger overlap and a larger increase in energy than the states near the gap. This will produce an increase in the number of states near the gap and a steepening of the band edge. A simple calculation shows that the increase in the energy involved is of the same order as that observed in the amorphous case (Fig. 21a). In the pseudopotential calculation for ST-12 coulomb effects are not taken explicitly into account and the shifting of the peak is mainly due to an increase in the kinetic energy. We may argue in the same manner as above since variations in bond angles will produce a larger decrease in the effective volume occupied by the electrons at the lower energy side of the hump than the electrons in states near the gap which are more localized in the bonds. This will result in an increase in the kinetic energy and we should obtain the same effect as in the amorphous case. This is evident in Fig. 21d. Although the BC-8 structure has much smaller deviations in bond angles than ST-12 we can still notice an introduction of states near the gap when we compare BC-8 with 2H-4.

Finally, we would like to make some comparisons between our results for the BC-8 and ST-12 structures using the EPM and the Weaire model. If we compare ST-12 (Weaire) with Ge ST-12 (EPM) we notice a very good matching of gross structure. The delta function at -2 eV represents the large hump at the top of the valence band. The two strong peaks near -4 eV and -6 eV are obtained in both cases and reveal a characteristic property of the structure. In Si ST-12 the peak at -4 eV has merged with the forward hump. In the BC-8 structure the comparisons are not as good. However, we still get a characteristic dip near -8 eV for both cases. The peak near -6 eV seems also to be well reproduced.

In summary, we have shown that long range disorder is not necessary to reproduce the essential features of the amorphous data. By studying a series of structures that became more and more locally disordered we were able to draw some interesting conclusions as to what properties of the amorphous structure are important. We have found that deviations in bond angles will produce an enhancement of the states near the gap and what seems like a shift of the hump in the density of states at the top of the valence band to higher energies. The presence of local disorder also seems to smear out the strong structure in the region near the bottom of the conduction band. The presence of five and seven membered rings will enhance the number of states in the valley between the two low energy density of states peaks at the bottom of the valence band. The odd-numbered rings also have an effect in producing a "valence gap" and perhaps it is this feature that helps to retain the dip in the amorphous density of states shown in Fig. 23. Finally, the odd-membered rings seem to have an effect on the size of the intrinsic energy gap. We found this to be a very large influence on the gap in the Weaire model. Now one may argue that this is of no realistic consequence since the conduction band in the Weaire model is inadequate and insufficient. Nevertheless, in the EPM calculation we find that the states near the gap at the bottom of the conduction band are s-like and are rather localized. In this sense the predictions of the Weaire model may still be valid for these states. However, we are not implying that the presence of fivefold rings will produce an increase in the energy gap. As we found in our modified crystal the gap depends very critically on the Hamiltonian matrix elements. Furthermore, the amorphous phase is less dense and, hence, has probably fewer five-membered rings than the ST-12 case. Therefore, this fact along with variations in the Hamiltonian matrix elements could produce a gap in the amorphous phase which is very nearly the same as that of FC-2.

We also believe that a microcrystallite model with 2H-4 microcrystallites is not substantiated by our calculations. This is clearly the case in the optical properties even if we average the $\varepsilon_2(\omega)$ function since the peak lies higher in energy than the amorphous hump. This is also the case in the density of states for 2H-4 since an averaging does not reproduce in any way the amorphous features. One might suggest an amorphous structure made up of ST-12 microcrystallites and argue that small regions of microvoid structure could make up for bulk density differences. However, the radial distribution function for these structures would be quite different. The next nearest neighbors in the Ge ST-12 structure at 3.45Å and 3.64Å would be hard to lose.

The random network model seems like a reasonable model for the amorphous state. It's major problem is, of course, that of non-uniqueness. It is clearly obvious that one could make a random network model and obtain a zero gap. Thus, effects of stability must be very important in determining the particular types of random network structure that can exist in a metastable state. The fact that amorphous samples are always prepared with very nearly the same gap clearly reflects this.

B. Method to Study Densities of States Using Local Configurations

In this part we shall be mainly concerned with effects of topology and in particular the effects of topology on the "s-like" states of Ge and Si. As we have seen the four-state Weaire Hamiltonian provides a good description of these states and has eigenvalues which are related by an analytic transformation to the eigenvalues ε of a much simpler one-state Hamiltonian with only nearest neighbor interactions V. Using this one-state Hamiltonian for simplicity, we have developed a new, simple method of calculating the local density of states of an atom in terms of the local environment of that atom. The system of atoms we consider consists of an infinite connected network of atoms with tetrahedral like coordination. The proceedure used to calculate the local density of states is as follows. We pick a particular atom as a reference point and a small cluster of atoms surrounding and including this atom is removed from the system. The cluster is chosen such that every atom in the cluster belongs to a ring passing through the reference or central atom. The Bethe lattice is now introduced as a boundary condition to assure that all bonds are satisfied and simulates the effect of the rest of the system. The local Green function for the central atom of this cluster-Bethe system can now be obtained exactly.

The Bethe lattice was chosen as a boundary condition since it provides a soluble method of treating an infinite system of atoms without being restricted to periodicity. In addition, it provides a total density of states which is smooth and featureless. Consequently any structure obtained in the local density of states is very closely related to the local configuration of atom. In the diamond structure we choose a cluster of (1 + 28) atoms which contains 12 sixfold rings passing through the central atom; each of the 28 non-central atoms is in at least one of the 12 rings. There are five inequivalent classes of atoms: the central atom, 4 nearest-neighbors and an infinite number outside the cluster in the Bethe lattice. The diagonal element $\langle o|g|o\rangle$ of the Green function is in this model given by

$$\langle o|g|o\rangle = \{\varepsilon - 4\, V^2\, [\varepsilon - 3\, V^2(\varepsilon - V\alpha)^{-1}\, \Sigma^{-1}]^{-1}\}^{-1} \quad , \qquad (18)$$

where

$$\Sigma = 1 - 4\, V^2(\varepsilon - 2\, V\alpha)^{-1}\, (\varepsilon - V\alpha)^{-1} \quad , \qquad (19)$$

and

$$\alpha = [\varepsilon - (\varepsilon^2 - 12\, V^2)^{1/2}]/6V \quad . \qquad (20)$$

These equations are obtained by solving a set of (4×4) linear equations in the unknown $\langle i|g|o\rangle$; α given by Eq. (20) is the contribution from the Bethe lattice.

The local density of states obtained from Eq. (18) is given in Fig. 24a. Superimposed we show the density of states of the Bethe lattice and the diamond structure. In Fig. 24b we show similar results obtained by suing the four-state Hamiltonian. It is easily seen from these figures that the local environment of the atoms gives the main contribution to the density of states. In particular the association of structure in the local density of states with the ring statistics of the cluster is shown in Figs. 24c through e. Here we have constructed five clusters which are made up of six rings of <u>only one type</u> (i.e., fivefold, sixfold, sevenfold and eightfold rings respectively. Each pair of bonds of the central atom is part of a ring. In Fig. 24c we have plotted the local density of states for these ring-cluster-Bethe systems corresponding to the Hamiltonian (Eq. (1)). In Fig. 24d we show the equivalent calculations for the four-state sp^3 Hamiltonian. The structure in these densities of states can be easily identified with the eigenvalues of isolated rings as shown in Fig. 24e. The agreement is excellent and indicates that the ring-like nature of the local environment is paramount in determining the type of structure found in the density states. A close examination of Fig. 24c shows that the strength of peaks is larger the smaller the ring. This indicates the importance of the small rings in a cluster.

We have also applied our method to examine the total density of states of the BC-8 and ST-12 structures which have proven to be very important in the study of the structural aspects of amorphous Ge and Si. In the BC-8 structure we only have one type of atom and consequently, as in diamond, the local and total densities of states are equivalent. We have chosen a cluster in the same manner as described previously: it contains 26 atoms. The results for the BC-8-Bethe system are shown in Figs. 25a and b along with the crystalline BC-8 spectrum. Again, the agreement between the BC-8 and BC-8-Bethe spectra is good, indicating the importance of a local configuration. A comparison of Figs. 25a and b with Figs. 24c and d reveals the sixfold ring character of the BC-8 structure, which is caused by the nine sixfold rings passing through each atom.

The ST-12 structure is quite interesting since it provides us with a system which exhibits five, six, seven and eightfold ring character. There are two types of atoms in the primitive cell with four atoms of type I and eight atoms of type II. Consequently, we have two types of clusters and the local density of states for these ST-12-Bethe systems are shown in Figs. 25c and d. In the cluster with a type I central atom we have four fivefold, two sixfold, six sevenfold and three eightfold rings of bonds with a total of 27 atoms. Comparing this spectrum with that of Figs. 24c and d we find that the peak at 1.5 in Fig. 25c is mainly caused by a sixfold ring peak and the overlap of a five and sevenfold ring peak. The shoulder around 0.3 seems to be caused principally by an overlap of a five and eightfold ring peak. Finally, the peak at (-2.6) is due to a fivefold ring peak and the overlap of a seven and eightfold ring peak. Similarly, in the cluster with a type II central atom, we have 31 atoms with three fivefold, two sixfold, five sevenfold and eight eightfold rings of bonds. Again a comparison of this spectrum with Figs. 24c and d reveals that the peak at 2.1 is mainly caused by a sevenfold ring peak and the overlap of a six and eightfold peak. The hump near 0 is due primarily to an eightfold ring peak and the overlap of a five and sevenfold ring peak. Finally, the little bump at (-1.4) is caused mostly by a sixfold ring peak and the peak at (-2.7) is mostly due to a fivefold ring peak and the overlap of a seven and eightfold ring peak.

In Figs. 25e and f we show the total density of states of the ST-12-Bethe system as obtained from a weighted average over the local density of states spectra. We also show the crystalline ST-12 spectrum which is considerably more complicated than the BC-8 and diamond spectra.

Nevertheless, we are still able to say that the total density of states is mainly due to the local configuration. We have found that for all these structures the local densities of states are nearly independent of how the rings are arranged in the clusters and depend mainly on the number and type of rings.

In conclusion we believe that our method provides a powerful way of studying the total density of states of an infinite system of atoms in terms of the local environment of each atom. In particular, this enabled us to calculate the total density of states of any system given the percentage of atoms with the same ring statistics. Conversely, given a total density of states it may be possible to distinguish between possible ring statistics. This method could even be extended to deal with problems of impurities and surface effects.

IV. OPTICAL PROPERTIES OF COMPLEX CRYSTALLINE AND AMORPHOUS PHASES OF Ge and Si

In this section we are concerned with the spectra of the imaginary part of the dielectric function ε_2 for Ge and Si in the FC-2, 2H-4, BC-8 and ST-12 structures as obtained from the EPM. From a band structure point of view we present a detailed analysis of the structure in ε_2 for Ge and Si in the 2H-4, BC-8 and ST-12 cases along with their band structures containing the symmetries of wave functions along important directions. This is of interest since the BC-8 and ST-12 structures may have a variety of applications, e.g., exciton droplets and when doped, superconductivity. From the point of view of understanding the amorphous phase the trends observed in ε_2 as the structures become more and more complex may give some insight into the amount of disorder necessary to produce the distinctive features of the amorphous ε_2. We shall show that our short range disorder model is the only theoretical model until now that can account for <u>both</u> the amorphour density of states and the amorphous ε_2.[10] In particular we shall show that when one measures the amorphous ε_2 spectrum one is essentially just measuring an averaged energy dependent matrix element.

The parameters and potentials used in these calculations are the same as those in Section III. The reader who is only interested in the amorphous phase may proceed to part C with no loss in continuity.

A. Symmetry Considerations

We find that the 2H-4 structure has a symmetry classification of D_{6h}^4 and is therefore associated with a non-symmorphic space group. The BC-8 and ST-12 structures have symmetry classifications T_h^7 and D_4^4

respectively and are thus also associated with space groups which are non-symmorphic. The Brillouin zones (BZ) for these structures are shown in Fig. 13 with the notation used by Leurhmann.[17] In order to label the symmetries of our wave functions, shown in Figs. 26, 38, 30, 32, 33 and 35, we have used the notation for point group elements and the character tables found in Zak.[23] In our case, of course, these point operations must be followed by the appropriate translations. However, several remarks must be made relating to the additional symmetry, in some cases, demanded by time reversal invariance, and to the symmetry notation for points located in the interior of the zone.

In the 2H-4 (D_{6h}^4) structure time reversal invariance adds additional symmetry to R. Thus R_1 and R_2 in our notation are obtained from $R_1 + R_4$ and $R_2 + R_3$, respectively, using Zak's character table. In the case of M (D_{2h}) our notation is identified by replacing U^x and σ^x with U^1 and σ^1 in the character table for D_{2h} in Zak. For $\Sigma(C_{2v})$ we obtain our character table by replacing C_2, σ_v and σ_v with U^1, σ, and σ^z respectively in the character table for C_{2v} in Zak. Similarly for $\Gamma(D_{6h})$ and $\Delta(C_{6v})$ our notation is identified by replacing σ_h, $3\sigma_v$ with σ^z, $\sigma^{(x)}$ and $3\sigma_v$, $3\sigma_d$ with $3\sigma^{(x)}$, $3\sigma^{(1)}$ respectively in the appropriate character tables found in Zak.

In the BC-8 (T_h^7) structure time reversal invariance adds additional symmetry to Λ, P, D, Γ and H. Thus for $\Lambda(C_3)$, Λ_1 and Λ_2 in our notation is obtained from 1 and 2 + 3, respectively, using Zak's character table. Similarly for P, time reversal invariance requires P_1 remain P_1 and $P_2 + P_3$ becomes P_2. For $D(C_2)$, $D_1 + D_2$ becomes D_1 and for $\Gamma(T_h)$, 1 becomes Γ_1, 2 + 3 become Γ_2, 4 becomes Γ_3, 5 becomes Γ_4, 6 + 7 becomes Γ_5 and 8 becomes Γ_6. The character table for H is the same as for T_h; it can be treated the same way as Γ. In the case of $\Delta(C_{2v})$ our notation is identified by replacing C_2, σ_v, and σ_v with C_2^x, σ^y and σ^z respectively in the character table for C_{2v} in Zak.

In the ST-12 (D_4^4) structure our notation regarding labeling of symmetry points and directions is that of Leuhrman, as mentioned before, and for this case it differs from Zak's notation. Aside from this, time reversal invariance requires that U^y, M^z, S, R, T, M and U^z have additional symmetry. Thus $Y_1 + Y_2$ using Zak's notation becomes U_1^y using our notation. Similarly for M^z, we have M_1 becomes M_1^z, $M_2 + M_3$ becomes M_2^z, and $M_4 + M_5$ becomes M_3^z, and for S we have $S_1 + S_2$ become S. For R we have $A_1 + A_2$ becomes R_1 and for T, $T_1 + T_2$ become T_1. Finally, for M we obtain M_1 from $R_1 + R_2$ and M_2 from $R_3 + R_4$ and for U_z we obtain U_1^z from $W_1 + W_2$. In the case of $\Gamma(D_4)$, $\Delta(C_2)$, $\Sigma(C_2)$ and $\Delta^z(C_4)$, which are internal symmetry points, our notation is identified using the character tables for D_4, C_2, and C_4 respectively found in Zak.

B. Results

The band structures of Ge and Si in the 2H-4, BC-8 and ST-12 structures, shown in Figs. 26, 28, 30, 32, 33 and 35 were obtained from EPM calculations and the form factors used were given in Section III. In Figs. 27, 29, 31, 34 and 36 we show the ε_2 spectra calculated from these band structures using

$$\varepsilon_2(E) = \frac{1}{3}\cdot\frac{e^2\hbar^4}{\pi m^2 E^2}\sum_{c,v}\int_{BZ}\delta(E_c(\vec{\underset{\sim}{k}}) - E_v(\vec{\underset{\sim}{k}}) - E)\left|\langle\vec{\underset{\sim}{k}},c|\vec{\nabla}|\vec{\underset{\sim}{k}},v\rangle\right|^2 d^3\vec{\underset{\sim}{k}} \qquad (21)$$

where $|\vec{k},v\rangle$ is a Bloch state in the valence band and the integral is over the entire BZ.

For the 2H-4 and ST-12 structures we can distinguish between the polarization of the electric vector and the c axis taken to be in the z-direction. In this case the factor of 1/3 in Eq. (21) is removed and we have parallel polarization if we use d/dz in the matrix element and perpendicular polarization if we use d/dx or d/dy. The integration was performed using the Gilat-Raubenheimer scheme.[16] Tables III through VIII summarize the major contributions to the various peaks in the ε_2 spectra for the six compounds. The first column identifies the energy of a particular peak and the second column contains the major contributions to this peak identified by interband transitions which are listed in order of decreasing strength. In particular, we list the bands which contribute more strongly once we are away from symmetry points and lines. The third column assigns the interband transitions to various regions of the BZ. Finally, in columns four and five we list the symmetries of the critical points and their associated energies respectively. In some cases, the symmetries were obtained from a preliminary analysis and warrant further investigation. These are designed in the tables by a tilde.

The complexity of the BC-8 and the ST-12 structures introduces the possibility that we may have critical points which are also inflection points along certain directions. Although it is rather difficult to determine this, it is conceivable that some of the critical points whose symmetries are uncertain may be of this type.

For completeness we present an analysis for all six compounds and although experimental optical data are not available at the present, the contributions and identification of strong interband transitions to the optical properties will not vary appreciably with small changes in the form factors.

1. Ge 2H-4

The threshold in $\varepsilon_2^{\perp}$ (Figs. 26 and 27) at 1.46 eV is caused by $\Gamma_5 - \Gamma_8$ transitions and the threshold in $\varepsilon_2^{\parallel}$ at 1.77 eV is caused by $\Gamma_1 - \Gamma_8$ transitions. The rise in $\varepsilon_2^{\perp}$ around 2.25 eV is caused by $\Gamma_6 - \Gamma_{10}$ transitions which are associated with an M_0 critical point (cp) and a region along $\Delta(\Delta_6 - \Delta_3)$ with small energy derivatives and large matrix elements. The shoulder at 2.25 eV is caused by an M_1 cp and associated transitions $A_3 - A_1$ at 2.26 eV. The small shoulder near 2.50 eV in $\varepsilon_2^{\parallel}$ seems to be caused by an M_0 cp near the center of the ΓALM face from bands 7-9. However, the shoulder near 2.50 eV in $\varepsilon_2^{\perp}$ is caused by $\Delta_5 - \Delta_1$ transitions and an M_1 cp approximately 3/5 of the way from Γ to A. The small peak at 2.68 eV in $\varepsilon_2^{\perp}$ is caused by $U_4 - U_2$ transitions and what seems like an M_1 cp at about 7/10 of the way from M to L. Although regions off symmetry directions around this critical point also contribute to $\varepsilon_2^{\parallel}$ near 2.68 eV, this effect is overshadowed by $U_2 - U_2$ transitions and an M_1 cp near (0.5,0,0.4) at about 2.78 eV. These transitions are responsible for the peak observed around 2.75 eV in $\varepsilon_2^{\parallel}$. The shoulder near 3.15 eV in $\varepsilon_2^{\parallel}$ is caused by 7-10 transitions from a region near the T symmetry direction from an M_0 critical point at about (0.08,0.08,0.2) with energy 3.03 eV. In addition 7-9 transitions contribute to this shoulder from a probable M_2 cp at 3.14 eV and near (0.11,0.11,0.2). The shoulder in

$\varepsilon_2^{\perp}$ at 3.35 eV is caused by transitions from bands 6-9 in a large region mainly in the ΓALM plane around an M_1 cp approximately at (0.2,0,0.25). A similar shoulder in $\varepsilon_2^{\parallel}$ at 3.57 eV is caused by a region with large matrix elements around what appears to be an M_1 cp near (0.2,0.2,0.35) at about 3.57 eV. The strongest peak in $\varepsilon_2^{\perp}$ occurs at 3.60 eV and is caused mainly by 6-9 transitions in a large region with strong matrix elements around $M_7 - M_1$ particularly along $U_3 - U_1$ and $\Sigma_4 - \Sigma_1$. However, additional strength is obtained by 8-10 transitions in a region around $R_2 - R_1$ about 1/2 of the way from A to L and from an M_2 cp near (0.2,0,0.4) at 3.80 eV. The matrix elements are large from $\hbar\omega < 3.80$ eV and very small for $\hbar\omega > 3.80$ eV. The largest peak in $\varepsilon_2^{\parallel}$ occurs at 3.72 eV caused mainly by an M_1 cp near H at the same energy. The peak in $\varepsilon_2^{\perp}$ at 4.52 eV is caused by small contributions from three different interband transitions. The main contribution is from 8-11 transitions in a region (U_4-U_2) around $L_2 - L_1$, tentatively designated an M_0 cp at 4.40 eV. A slightly weaker contribution is from bands 8-9 caused by a region around the T symmetry direction with what seems like an M_0 cp near (0.23,0.23,0) at 4.45 eV. The final contribution to the peak at 4.52 eV for $\varepsilon_2^{\perp}$ is probably caused by an M_1 cp near the center of the ΓALM face at 4.53 eV. This critical point privides the strongest contribution to the peak at 4.52 eV for $\varepsilon_2^{\parallel}$ because of large matrix elements. The other main contribution to this peak is caused by 8-9 transitions with an M_2 cp at K and a region along T'. The shoulder around 4.70 eV in $\varepsilon_2^{\perp}$ is mainly caused by 7-9 transitions with a probable M_2 cp at K and a small region extending along T'. Additional contributions to this shoulder are from 8-9 transitions in a small region around (0.4,0.15,0.15) with an M_3 cp at

4.72. The final contribution to this shoulder is from a region around A particularly along S with a probable M_2 cp near (0.03,0.03,0.45) at 4.71 eV. The shoulder in $\varepsilon_2^{\parallel}$ around 4.70 eV is caused by an M_0 cp near M about 0.1 of the way along T' and from 7-9 transitions in a region near K along P with a probable M_3 cp at about 4.9 eV near (0.33,0.33,0.15). The last descernible peak in $\varepsilon_2^{\perp}$ occurs at 5.23 eV and is caused mainly by $\Gamma_5 - \Gamma_{12}$ transitions which are associated with an M_2 cp at 5.23 eV. Additional contributions to this peak are from 8-11 transitions in a small region around (0.08,0.08,0.35) which has an M_3 cp at 5.30 eV. The last discernible shoulder in $\varepsilon_2^{\parallel}$ around 5.29 eV is caused by $M_5 - M_4$ and $\Sigma_3 - \Sigma_4$ transitions at 5.33 eV and 5.31 respectively. We have not determined the symmetry of these critical points. Other contributions to this shoulder are from 8-11 transitions in a small region around (0.3,0.1,0.15) at 5.29 eV.

2. Si 2H-4

The threshold in $\varepsilon_2^{\perp}$ (Figs. 28 and 29) at 2.60 eV is caused by $\Sigma_1 - \Sigma_1$ transitions and a probable M_0 cp near (0.3,0,0) while the region around this cp off symmetry directions contributes to the threshold in $\varepsilon_2^{\parallel}$ at nearly the same energy. The first shoulder in $\varepsilon_2^{\parallel}$ at 3.10 eV is caused by an M_0 cp near the center of the ΓALM face from bands 7-9. The next shoulder in $\varepsilon_2^{\parallel}$ occurs around 3.35 eV and is caused by $U_2 - U_2$ transitions with an M_1 cp near (0.5,0,0.35) at about 3.34 eV. The rise in $\varepsilon_2^{\perp}$ around 3.35 eV is caused by $\Gamma_6 - \Gamma_{10}$ transitions which are associated with an M_0 cp and a region along $\Delta(\Delta_6 - \Delta_3)$. The shoulder at 3.35 eV is caused by an M_1 cp and associated transitions $A_3 - A_1$. The next shoulder in $\varepsilon_2^{\perp}$ at 3.60 eV is a result of $\Delta_5 - \Delta_1$ transitions and an M_1

cp approximately 1/2 of the way from Γ to A. The lartest peak in $\varepsilon_2^{\perp}$ at 4.10 eV is caused mainly by 6-9 transitions in a large region with strong matrix elements around $M_7 - M_1$ particularly along $U_3 - U_1$ and $\Sigma_4 - \Sigma_1$. To a much lesser extent additional strength to this peak is obtained from a region around $R_2 - R_1$, specifically 1/2 of the way from A to L. Here we find an M_2 cp near (0.15,0,0.5) at about 4.13 eV. The first large peak in $\varepsilon_2^{\parallel}$ occurs around 4.25 eV and is caused by a region with large matrix elements around what appears to be an M_1 cp near (0.2,0.2,0.35) at about 4.21 eV. In addition, a region near H along S' which also has large matrix elements contributes around 4.26 eV. The shoulder at $\varepsilon_2^{\perp}$ near 4.38 eV is a result of an M_2 cp around (0.2,0,0.4) at 4.38 eV and transitions in a region around $R_2 - R_1$ near (0.2,0,0.5). The second large peak in $\varepsilon_2^{\parallel}$ occurs around 4.68 eV and is the result of several contributions. First, we have 8-10 transitions in a region near M about 0.2 of the way along T' where we have a probable M_2 cp at 4.64 eV. Next, there are 8-9 transitions in a small region around (0.3,0.1,0) with an M_1 cp at 4.68 eV and 7-11 transitions with an M_0 cp at 4.61 near (0.4,0,0.35). Finally, we have contributions from the shoulder of a non-discernible peak around 4.75 eV caused by 7-9 transitions along T with what is probably an M_2 cp at 4.74. The peak in $\varepsilon_2^{\perp}$ at 4.69 eV is caused mainly by 8-9 transitions along the T symmetry direction with an M_0 cp at 4.57 eV and to a lesser extent from $\Delta_6 - \Delta_5$ transitions with what seems like an M_1 cp at 4.69 eV near (0,0,0.3). The peak in $\varepsilon_2^{\perp}$ at 4.89 eV is a result of what appears to be an M_2 cp at K around 4.87 eV and a probable M_2 cp near (0.3,0.25,0.25) around 4.89 eV. The shoulder in $\varepsilon_2^{\parallel}$ at 4.91 eV is caused by a probable M_2 cp for 7-10 and 8-10 transitions at 4.91 eV and 4.93 eV near (0.2,0.08,0) and (0.2,0.1,0) respectively. The shoulder in $\varepsilon_2^{\perp}$ at 4.96 eV is caused mainly by 8-11 transitions slightly off the Σ direction at a probable M_2 cp near (0.35,0.05,0.05) at 4.96 eV, while the shoulder at 5.50 eV is a result of $\Gamma_5 - \Gamma_{12}$ transitions with an associated M_1 cp at 5.47. Finally, the shoulder around 5.55 eV in $\varepsilon_2^{\parallel}$ is caused by $M_5 - M_4$ and $\Sigma_3 - \Sigma_4$ transitions at 5.61 and 5.54 eV respectively.

3. Ge BC-8

The first peak in ε_2 (Figs. 30 and 31) at 2.03 eV is caused by $\Sigma_1 - \Sigma_2$ transitions with an M_1 cp about 4/5 of the way from Γ to N. The shoulder at 2.46 is caused by a small region around $\Sigma_2 - \Sigma_2$ with a probable cp near (0.4,0.4,0) at 2.46 eV whose symmetry we have not determined. Additional contributions to this shoulder are from $\Delta_4 - \Delta_4$ transitions and an M_0 cp about 1/2 the way along Δ at 2.41 eV. The main contribution to the peak at 2.70 eV is from 13-17 transitions in a small region around an M_0 cp near (0.2,0.8,0.15) at 2.67 eV. A smaller contribution is from $G_2 - G_1$ transitions with what appears to be on M_0 cp near (0.15,0.85,0) at 2.65 eV. The large peak at 3.21 eV is a result of many contributions. First, we have 16-19 transitions in a region of large matrix elements around an M_0 cp near (0.25,0.35,0.25) at 3.19 eV. Next, we have $G_1 - G_2$ transitions with an M_2 cp near (0.4,0.6,0) at 3.24 eV and a region of large matrix elements around (0.3,0.4,0.15) at about 3.23 eV. Thirdly, there are 14-17 transitions in a region around (0.2,0.4,0.15) with what appears to be an M_2 cp at 3.21 eV. Finally, we have 13-18 transitions near (0.3,0.45,0) with an M_1 cp at 3.21 and $G_1 - G_1$ transitions with a probable cp at (0.22,0.78,0) whose symmetry we have not determined. The shoulder around 3.76 eV is also the result of several contributions. The first is from 15-19 transitions in a region near N with $G_2 - G_1$ transitions and an M_3 cp near (0.4,0.55,0) at 3.78 eV. Next we have 12-18 transitions near N with $G_2 - G_1$ transitions and an M_1 cp near (0.35,0.65,0) at 3.76 eV. Finally, we have contributions from a small region around Γ with $\Gamma_2 - \Gamma_6$ transitions and an M_3 cp at 3.74 eV. The shoulder at 3.98 eV is caused by 14-19 transitions in a large region around (0.25,0.65,0.15) at 4.0 eV. The last discernible peak occurs at 4.50 eV and is caused by 12-19 transitions in a region around (0.26,0.63,0.15) and 14-20 transitions in a large region around (0.1,0.5,0.1) both with strong matrix elements. In addition, we have contributions from 16-21 transitions in a region around (0.15,0.2,0.1) with an M_2 cp near 4.48 eV and $\Delta_1 - \Delta_4$ transitions with an M_0 cp near (0.25,0,0) at 4.42 eV.

4. Si BC-8

The threshold in ε_2 (Figs. 31 and 32) at 0.43 eV is caused by $H_3 - H_4$ transitions. The small bump around 1.70 eV is a result of $\Delta_1 - \Delta_4$ transitions with an M_0 cp near (0.55,0,0) at 1.65 eV. The next small bump at 2.04 eV is caused by what appears to be an M_2 cp near (0.3,0.55,0). The shoulder at 2.60 eV is primarily caused by $\Sigma_1 - \Sigma_2$ transitions with an M_2 cp near (0.4,0.4,0) at 2.62 eV. Additional structure is obtained by 15-17 transitions in a region around an M_0 cp near (0.3,0.5,0) at 2.54 eV. The shoulder at 3.0 eV is caused by 13-17 transitions in a small region around an M_0 cp near (0.2,0.7,0.15) at 2.96 eV. The large peak at 3.45 eV is the result of many contributions. The first is from 13-17 transitions in a region of every large matrix elements around (0.1,0.5,0.1) at about 3.46 eV. Next we have 14-17 transitions in a region around what appears to be an M_2 cp near (0.2,0.4,0.15) at 3.45 eV with strong matrix elements. Also, there are 16-19 transitions in a small region with very large matrix elements and an M_1 cp near (0.3,0.4,0.2) at 3.43 eV. Finally, there is a region around $\Gamma_1 - \Gamma_6$ transitions with an associated M_0 cp at 3.38 eV.

The shoulder at 3.7 eV is caused by a small region around $G_1 - G_2$ transitions with an M_2 cp at 3.7 eV near (0.45,0.55,0) and by a small region around $D_1 - D_1$ transitions with large matrix elements and an M_1 cp at 3.68 eV around (0.5,0.5,0.15). The shoulder at 4.05 eV is the result of several types of transitions. First, we have 16-21 transitions in a small region around (0.2,0.6,0.15) with large matrix elements and $\Delta_1 - \Delta_2$ transitions with an M_2 cp near (0.5,0,0) at 4.04 eV. Next we have 15-21 transitions in a small region around (0.2,0.6,0.1) with an associated M_0 cp at 4.02 eV and $G_1 - G_1$ (13-18) transitions with a probable cp near (0.2,0.8,0) whose symmetry we have not yet determined. Finally, we have 14-19 transitions in a region around what appears to be an M_1 cp near (0.25,0.65,0.1) at 4.07 eV. The large peak at 4.20 eV is mainly caused by 16-22 transitions in a region of very large matrix elements around what appears to be an M_2 cp near (0.2,0.5,0) at 4.20 eV. In addition we have contributions from 12-18 and 15-22 transitions in a small around an M_2 cp near (0.15,0.7,0.15) at 4.22 eV and an M_0 cp near (0.15,0.7,0) at 4.14 eV respectively. Finally, the shoulder at 5.05 eV can be attributed to 14-21 transitions in a small region around an M_2 cp near (0.2,0.6,0.1) at 5.05 eV and $D_1 - D_1$ transitions with a probable cp near (0.5,0.5,0.1) at 5.0 eV whose symmetry we have not determined.

5. Ge ST-12

In this section and the section on Si ST-12 we shall treat the perpendicular component of $\varepsilon_2^{\perp}$ first and discuss the parallel component in the last paragraph.

The threshold in $\varepsilon_2^{\perp}$ (Figs. 33 and 34) occurs at 1.46 eV and is caused by $\Sigma_1 - \Sigma_1$ transitions. The shoulder at 2.10 eV is caused by equal contributions from 24-25 and 23-25 transitions in small regions (tubular along the z direction) around an M_0 cp near (0.4,0.1,0.3) at 2.08 eV and an M_1 cp near (0.4,0,0.3) at 2.18 eV respectively. The shoulder around 2.55 eV is caused mainly by 24-26 transitions in a region around an M_1 cp near (0.5,0.1,0.3) at 2.48 eV along with much weaker contributions from $T_1 - T_1$ (0.5,0.5,0.4) and $U_1^z - U_1^z$ (0.5,0,0.3) transitions at 2.52 eV and 2.50 eV respectively whose critical point symmetries have not been determined. Next we have 23-26 transitions in a region of relatively large matrix elements around (0.4,0.15,0.25) contributing at 2.62 eV. Other contributions to this shoulder are from 22-25 and 21-25 transitions, with a probable M_2 cp near (0.4,0,0.25) at 2.62 eV and an M_1 cp near (0.4,0.15,0.25) at 2.60 eV respectively, along with transitions at M in a much weaker sense at 2.60 eV. Finally, we have 24-25 transitions with an M_0 cp near (0.1,0.1,0.4) at 2.54 eV.

The peak around 2.80 eV is the result of several types of transitions whose contributions are all of comparable weight. First, we have 23, 24-26 transitions in a region (mostly along z direction) around $S_1 - S_1$ with an M_2 cp near (0.4,0.4,0.5) at 2.87 eV. Next there are 21-25 transitions in a region around an M_1 cp near (0.4,0.15,0.25) at 2.60 eV which contributes to 2.75 eV because of matrix elements and in a weaker sense $\Delta_1 - \Delta_1$ (0.4,0,0) transitions with a cp of undetermined symmetry at 2.80 eV. Next we have 24-25 transitions near the U^x symmetry direction with an M_1 cp near (0.2,0,0.4) at 2.70 eV. Finally, we have 24-27 transitions in a small region (tubular along z-direction) around an M_1 cp near (0.5,0.1,0.3) at 2.76 eV along with some weaker $\Gamma_3 - \Gamma_5$ transitions with an M_0 cp at 2.75 eV. The shoulder around 3.0 eV is caused mainly by 20-25 transitions in a region (tubular along z-direction) around an M_0 cp near (0.4,0.15,0.25) at 2.93 eV and 22-25 transitions in a region around $Z_2 - Z_2$ with an associated M_0 cp at 2.98 eV along with much weaker $T_1 - T_1$ (0.5,0.5,0.3) transitions at 3.0 eV. Additional contributions to this shoulder are from 24-27 transitions in a small region near R along T_z with an M_1 cp near (0.5,0.5,0.45) at 3.11 eV and 19-25 transitions in a region of relatively large matrix elements around (0.35,0.18,0) at 2.97 eV along with weaker $M_2^z - M_1^z$ transitions with what appears to be an M_2 cp at 3.0 eV. Finally, we have 22-27 transitions with an M_0 cp near (0.5,0.15,0.3) at 3.04 eV.

The next shoulder around 3.20 eV is caused mainly by $Z_1 - Z_1$ transitions with an associated M_0 cp at 3.18 eV along with much weaker transitions $Z_1^x - Z_1^x$ with an M_3 cp at 3.20 eV. Other contributions to this peak are from 21-25 transitions in a small region around U^x with an M_2 cp near (0.2,0,0.5) at 3.21 eV and 23-28 transitions in a region (tubular along z-direction) near R mostly along T^z with a probable M_1 cp at 3.20 eV. Finally, we also have contributions from 19-25 transitions with an M_2 cp near (0.5,0.15,0.3) at 3.21 eV along with weaker $\Delta_1 - \Delta_1$ transitions near (0.38,0,0) at 3.20 eV. The peak at 3.50 eV is caused mainly by 19-25,26 transitions and a region (along z-direction) around

$R_1 - R_1$ with an M_0 cp at 3.46 eV and 18-25 transitions in a small region around $T_1 - T_1$ near (0.5,0.22,0.5) with a probable M_0 cp at 3.49 eV. Additional contributions are from $S_1 - S_1$ (20-25) transitions with an M_0 cp near (0.06,0.06,0.5) at 3.45 eV and what appears to be an M_1 cp near (0.45,0.45,0.5) also at 3.45 eV. Other contributions are from 17-25 transitions in a small region along T^z near (0.5,0.5,0.3) with a probable M_1 cp at 3.53 eV and 24-27 transitions with a probable M_2 cp near (0,0.1,0.25) at 3.47 eV and to a lesser extent $T_1 - T_1$ transitions near (0.5,0.3,0.5) at about 3.50 eV. Finally, we have $T_1 - T_1$ (20-26) transitions with an M_2 cp at 3.47 eV and 22-27 transitions with an M_2 cp near 3.54 eV and to a lesser extent $\Delta_1 - \Delta_1$ transitions near (0.45,0,0) contributing at 3.50 eV.

The shoulder at 3.65 eV is caused by 17-25 transitions in a region (tubular along z-direction) around an M_2 cp at 3.67 eV near (0.5,0.25,0.3) and in a weaker sense by $Z_1 - Z_2$ transitions with an M_0 cp at 3.65 eV. Other contributions to this shoulder are from 23-27 transitions in a relatively large region around (0.1,0,0.25) which contributes around 3.65 eV, 24-29 transitions in a region around U^x with an M_0 cp near (0.22,0,0.5) at 3.60 eV, and 24-30 transitions at R with an M_1 cp at 3.60 eV. The peak at 4.20 eV is caused by 24-30 transitions in a region (mostly in z-direction) near U^x around (0.3,0,0.4) which contributes at about 4.18 eV along with weaker transitions in a region around M at 4.20 eV. In addition we have 21-27 transitions with an M_2 cp near (0.15,0.15,0.2) at 4.22 eV and 23-28 transitions in a region around $\Delta_2 - \Delta_1$ with most of the contributions near (0.1,0,0.05) at 4.20 eV.

Other transitions contributing to this peak are 21-28 transitions in a small region near U^x around (0.15,0,0.4) at 4.20 eV and 20-25 transitions around $\Sigma_2 - \Sigma_1$ with an M_1 cp near (0.7,0.7,0) at 4.21 eV. Finally, we also have some weak structure from $S_1 - S_1$ (23-32) transitions with a cp of undetermined symmetry near (0.22,0.22,0.5) at 4.20 eV.

The last peak that we shall consider in $\varepsilon_2^{\perp}$ occurs at 4.50 eV and is the result of many different contributions. First, we have 23-31 transitions in a region around $U_1^z - U_1^z$ with a probable M_3 cp near (0.5,0,0.2) at 4.57 eV and $\Sigma_2 - \Sigma_1$ (21-23) transitions with a cp of undetermined symmetry near (0.4,0.4,0) at 4.48 eV. Next we have 22-30 transitions in a small region near U^y with an M_1 cp around (0.45,0.1,0.05) at 4.36 eV and an M_1 cp near (0.3,0.15,0.4) at 4.52 eV. In addition we have 20-26 transitions with an M_3 cp near (0.15,0,0.1) at 4.54 eV and 20-28 transitions with an M_0 cp near (0.15,0.15,0.25) at 4.47 eV. Finally, for completeness we also list in Table V a set of much weaker transitions along symmetry directions at critical points of undetermined symmetry, starting with $M_3^z - M_1^z$ transitions and ending with $U_1^y - U_1^y$ transitions. Taken as a whole they are of comparable weight to the others discussed above.

The threshold in $\varepsilon_2^{\parallel}$ occurs around 1.60 eV with minute matrix elements from $\Sigma_2 - \Sigma_1$ transitions at 1.46 eV and very small matrix elements near 1.6 and appreciable contributions only from $\Delta_2 - \Delta_1$ transitions with a probable M_1 cp near (0.4,0,0) at 1.7 eV. The shoulder around 2.15 eV is caused mainly by $\Sigma_2 - \Sigma_1$ transitions with an M_0 cp near (0.37,0.37,0) at 2.07 eV. In addition we have contributions from 24-25 and 23-25 transitions in small regions around what appears to be an M_0 cp near

(0.4,0.1,0.3) at 2.08 eV and an M_1 cp near (0.4,0,0.3) at 2.18 respectively. The shoulder around 2.65 eV is caused mainly by 21-15 transitions in a region around an M_1 cp near (0.4,0.15,0.25) and 2.60 eV and a region (particularly along U^y) around $Z_1^x - Z_1^x$ with a probable M_2 cp at 2.65 eV and $U_1^y - U_1^y$ transitions contributing at 2.63 eV. Additional contributions are from 22-26 transitions with an M_1 cp near (0.5,0.2,0.25) at 2.74 eV and 22-25 transitions in a region around $M_3^z - M_1^z$ with a probable M_2 cp at 2.70 eV. Finally, to a much lesser extent, we have contributions from $\Gamma_3 - \Gamma_4$ transitions with an M_0 cp at 2.64 eV.

The peak at 3.20 eV is a result of several interband contributions of approximately the same weight. First we have 24-27 transitions in a region around $Z_1 - Z_1$ with an M_0 cp at 3.18 eV along with weaker $Z_1^x - Z_1^x$ transitions with an M_3 cp at 3.20 eV and $\Delta_2 - \Delta_1$ transitions with a probable M_2 cp near (0.45,0,0) at 3.18 eV. Next we have 21-25 transitions in a small region (mostly along z-direction) around U^x with an M_2 cp near (0.2,0,0.5) at 3.21 eV and a region of large matrix elements near (0.2,0.2,0.3) contributing to 3.20 eV. In addition we have 24-26 transitions in a region around $S_1 - S_1$ with an M_3 cp near (0.26,0.26,0.5) at 3.26 eV and in a weaker sense $R_1 - R_1$ (23-28) transitions at 3.20 eV and $\Sigma_2 - \Sigma_1$ (24-28) transitions with a probable M_1 cp near (0.25,0.25,0) at 3.20 eV. The next peak in 3.50 eV is a result, in part, of 20-25 transitions in a region around $Z_2 - Z_2$ with a cp of undetermined symmetry at 3.48 eV and $S_1 - S_1$ transitions with an M_0 cp near (0.06,0.06,0.5) at 3.45 eV. In addition, there are contributions from 22-27 transitions in a small region around an M_2 cp near (0.3,0.1,0.3) at 3.54 eV, $\Gamma_5 - \Gamma_5$ transitions with an associated

M_0 cp at 3.44 eV and 20-26 transitions in a region (tubular along z-direction) of relatively large matrix elements around (0.3,0.1,0.3) at 3.53 eV. Finally, there are weaker contributions from $\Sigma_2 - \Sigma_1$ (24-29) and $\Delta_1 - \Delta_2$ (24-26) transitions with critical points of undetermined symmetry near (0.35,0.35,0) at 3.45 eV and near (0.3,0,0) at 3.48 eV respectively.

The shoulder at 3.70 eV is caused by 24-28 transitions in a small region around $\Delta_1 - \Delta_2$ with a cp of undetermined symmetry near (0.26,0,0) at 3.70 eV and $S_1 - S_1$ transitions with a probable M_2 cp near (0.2,0,0) also at 3.70 eV. Other contributions to this shoulder are from 21-27 transitions around $Z_1^x - Z_1^x$ with an M_1 cp at 3.69 eV and $U_1^z - U_1^z$ transitions with a cp of undetermined symmetry near (0.5,0,0.2) at 3.71 eV. The peak at 3.90 eV is caused in part by 19-25 transitions in a small region (mostly in z-direction) around an M_3 cp near (0.2,0.15,0.3) at 3.92 eV and 24-29 transitions around $\Delta_2^z - \Delta_2^z$ with an M_2 cp near (0,0,0.18) at 3.94 eV. Additional contributions are from 23-29 transitions around $\Delta_1 - \Delta_2$ with what appears to be an M_2 cp at 3.9 eV, $S_1 - S_1$ transitions with a cp of undetermined symmetry at 3.9 eV, and $\Delta_2 - \Delta_1$ (21-26) transitions with a probable M_1 cp near (0.15,0,0) at 3.88 eV. The peak at 4.20 eV is caused in part by 24-29 transitions in a region of very large matrix elements around $\Gamma_3 - \Gamma_4$ with an M_3 cp at 4.22 eV and 20-25 transitions in a region around $\Gamma_3 - \Gamma_4$ with an M_0 cp at 4.16 eV along with an M_1 cp near (0.07,0.07,0) at 4.21 eV from $\Sigma_2 - \Sigma_1$ transitions. Other contributions to this peak are from 21-28 transitions in a region around $\Gamma_2 - \Gamma_1$ with an M_0 cp at 4.22 eV including in particular $\Delta_1^z - \Delta_1^z$ transitions at 4.23 eV, transitions in a small region near U^x around (0.15,0,0.4) at 4.20 eV, and to a lesser extent $S_1 - S_1$ transitions with a cp of undetermined symmetry at 4.20 eV. Still other contributions are from 22-29 transitions with an M_0 cp near (0.15,0.15,0.2) at 4.21 eV and weaker $Z_1^x - Z_1^x$ transitions with an M_2 cp at 4.24 eV. Finally, we have 24-30 transitions with an M_1 cp near (0.1,0.1,0.3) at 4.26 eV and 22-30 transitions in a region around (0.3,0.25,0.25) contributing at 4.21 eV.

The last peak that we shall consider in $\varepsilon_2^{\parallel}$ occurs at 4.40 eV and is the result of many different contributions. First we have 20-26 transitions in a region (tubular along z-direction) around an M_2 cp near (0.17,0.17,0.1) at 4.42 eV and 18-27 transitions in a region around $Z_1 - Z_1$ with an M_0 cp at 4.26 eV. Next we have 23-28 $(\Sigma_1 - \Sigma_2)$ transitions and 22-27 $(\Sigma_1 - \Sigma_2)$ transitions with a critical points of undetermined symmetry near (0.14,0.14,0) at 4.40 and 4.37 eV respectively along with $\Delta_1 - \Delta_2$ transitions with a cp near (0.25,0,0) at 4.40 eV. Other contributions are from 23-24 transitions around $M_2^z - M_1^z$, with a probable M_2 cp at 4.40 eV and $\Sigma_1 - \Sigma_2$ transitions with a cp of undetermined symmetry near (0.35,0.35,0) at 4.40 eV. In addition, we have weaker contributions from 16-26 transitions in a small region around $Z_2 - Z_2$, particularly along $\Delta_2^z - \Delta_3^z$ at 4.40 eV, with a probable M_1 cp at 4.37 eV. Finally, we have 23-30 transitions with an M_3 cp near (0.35,0.15,0.3) at 4.42 eV, $\Delta_1 - \Delta_2$ transitions with a cp of undetermined symmetry near (0.37,0,0) at 4.40 eV, and 22-31 transitions around $U_1^y - U_1^y$ with a cp near (0.5,0.3,0) at 4.40 eV.

6. Si ST-12

The threshold in $\varepsilon_2^\perp$ (Figs. 35 and 36) occurs at 1.76 eV and is the result of 24-25 transitions around an M_0 cp near (0.4,0.2,0). The shoulder at 2.33 eV is caused by 23-25 transitions and 24-25 transitions in a region (tubular along z-direction) around an M_0 cp near (0.4,0,0.3) at 2.31 eV and around an M_1 cp near (0.4,0,0.45) at 2.33 eV respectively. The shoulder at 2.50 eV is caused by 23-26 and mainly 24-26 transitions in a region around M with a probable M_1 cp at 2.50 eV. In particular, we have contributions from $T_1 - T_1$ transitions with an M_1 cp near (0.5,0.15,0.5) at 2.52 eV and $U_1^z - U_1^z$ transitions at 2.51 eV. Finally, we have weaker transitions from a region near Z^x along $U_1^y - U_1^y$ contributing to 2.45 eV.

The peak at 2.80 eV is a result in part of 23,24-26 transitions in a region around $S_1 - S_1$ (0.4,0.4,0.5) at 2.76 eV with particularly strong contributions off the symmetry axis with an M_1 cp near (0.4,0.4,0.4) at 2.80 eV. Other contributions are from 21-25 transitions with an M_0 cp near (0.45,0.15,0.3) at 2.73 eV, $\Delta_2 - \Delta_1$ transitions with a cp of undetermined symmetry near (0.45,0,0) at 2.80 eV, and $U_1^y - U_1^y$ transitions with an M_1 cp near (0.5,0.2,0) at 2.79 eV along with 22-26 transitions in a large region (along z-direction) around (0.5,0.3,0.15) contributing at 2.82 eV. Finally, we have contributions from $Z_1 - Z_1$ (23-28) transitions with an M_0 cp at 2.78 eV and 22-25 transitions with an M_2 cp near (0.4,0,0.25) at 2.74 eV. The shoulder at 3.20 eV is caused mostly by 20-25 transitions in a region of relatively large matrix elements around $\Delta_1 - \Delta_1$, with an M_0 cp near (0.39,0,0) at 3.17 eV and a region around

$\Sigma_1 - \Sigma_1$ with an M_2 cp near (0.37,0.37,0) at 3.21 eV, along with 19-25 transitions in a region (along z-direction) around $\Sigma_1 - \Sigma_2$ with a probable M_1 cp near (0.4,0.4,0) at 3.18 eV. Additional contributions are from 22-25 transitions in a region around $Z_2 - Z_2$ with an M_0 cp at 3.18 eV and an M_1 cp near (0.2,0.2,0.25) at 3.16 eV and 20-26 transitions in a region around U^y with an M_1 cp near (0.5,0.35,0.05) at 3.17 eV and a cp of undetermined symmetry near (0.4,0.4,0) from $\Sigma_1 - \Sigma_1$ transitions at 3.20 eV. Other contributions are from 22-28 transitions, from a cp of undetermined symmetry around $U_1^y - U_1^y$ near (0.5,0.4,0) at 3.20 eV and $R_1 - R_1$ transitions at 3.20 eV, and 21-26 transitions in a region around T^z with an M_2 cp near (0.5,0.5,0.4) at 3.23 eV.

The largest peak in $\varepsilon_2^{\perp}$ occurs at 3.38 eV and is the result of many types of transitions. First, we have 20-25 transitions in a region near R along T^z with an M_1 cp near (0.5,0.5,0.45) at 3.39 eV and 19-25 transitions in a similar region around T^z with a probable M_3 cp near (0.48,0.48,0.4) at 3.45 eV, along with $\Sigma_2 - \Sigma_1$ transitions near (0.35,0.35,0) with a cp of undetermined symmetry at 3.35 eV. Next, we have 22-26 transitions, with a large region (along z-direction) around an M_2 cp near (0.25,0.25,0.3) at 3.36 eV. Additional contributions are from 18-25 transitions, with an M_0 cp near (0.4,0.2,0) at 3.35 eV and $U_1^y - U_1^y$ transitions near (0.5,0.38,0) with a cp at 3.4 eV, and 24-27 transitions with an M_1 cp near (0.15,0,0.3) at 3.38 eV and $U_1^z - U_1^z$ transitions near (0.5,0,0.15) with a cp around 3.38 eV. Finally, we have 22-28 transitions, with an M_0 cp at 3.37 eV from $Z_2 - Z_1$ transitions and an M_1 cp near (0.45,0.4,0.3) at 3.35 eV, and 23-27 transitions with contributions from various regions of the zone contributing at around 3.35 eV. The shoulder at 3.60 eV is caused in part by 20-25 transitions in a region near Z around U^x with an M_0 cp near (0.1,0,0.5) at 3.60 eV and 21-26 transitions with a probable M_1 cp near (0.3,0.2,0.25) also at 3.60 eV. Other contributions are from 22-27 transitions in a region around $\Sigma_2 - \Sigma_1$ with an M_0 cp near (0.3,0.3,0) at 3.50 eV, 21-29 transitions in a region around $R_1 - R_1$ with an M_0 cp at 3.59 eV and 23-27 transitions with an M_0 cp near (0.1,0.1,0.25) at 3.54 eV. Finally, we have 23-28 transitions with an M_1 cp near (0.5,0.15,0.3) at 3.58 eV, 22-26 transitions in a region around $\Delta_2^z - \Delta_4^z$ with a cp of undetermined symmetry near (0,0,0.3) at 3.60 eV and 22-28 transitions in a region around $\Sigma_2 - \Sigma_1$ with a cp near (0.32,0.32,0) at 3.60 eV.

The peak around 3.85 eV is the result of many types of transitions contributing approximately equally to $\varepsilon_2^{\perp}$. First, we have 24-29 transitions in a region around $Z_1^x - Z_1^x$ with an M_2 cp at 3.92 eV and 23-28 transitions in a region (tubular along z-direction) around $\Gamma_5 - \Gamma_1$ with an M_0 cp at 3.71 eV along with $\Delta_4^z - \Delta_1^z$ transitions with an M_2 cp near (0,0,0.24) at 3.85 eV. Next we have 23-29 transitions in various regions of the zone with strongest contributions from a large tubular region in the z-direction around (0.35,0.15,0.25) contributing at 3.85 eV and 17-25 transitions in a large region around $U_1^z - U_1^z$ (0.5,0,0.33) parallel to the T direction contributing at 3.85 eV. Other contributions are from 22-27 transitions, with a probable M_1 cp near (0.15,0.15,0.2) at 3.81 eV, 21-29 transitions, with contributions from a small region around $\Sigma_1 - \Sigma_2$ and an M_1 cp near (0.42,0.42,0) at 3.88 eV, and 20-26 transitions with what appears to be an M_1 cp near (0.15,0.1,0.4) at 3.89 eV. Finally, we have 16-25 transitions in a region around $M_3^z - M_2^z$ with an M_1 cp at

3.86 eV and 23-20 transitions with a probable M_1 cp near (0.35,0.35,0.25) at 3.81 eV.

The last structure we shall consider in the $\varepsilon_2^{\perp}$ spectrum occurs at 4.45 eV. This shoulder is caused in part by 20-26 transitions in a region (along z-direction) around what appears to be an M_2 cp near (0.1,0,0.1) at 4.48 eV, $\Sigma_1 - \Sigma_1$ transitions with a cp of undetermined symmetry near (0.12,0.12,0) at 4.44 eV and 23-25 transitions with a cp at $M_2^z - M_3^z$ at 4.46 eV. Other contributions are from 15-27 transitions in a region around $M_3^z - M_1^z$ with a probable M_1 cp at 4.45 eV and 15-26 transitions near M^z with a cp from $\Sigma_2 - \Sigma_1$ transitions near (0.44,0.44,0) at 4.42 eV along with $U_1^z - U_1^z$ transitions with a cp near (0.5,0,0.34) at 4.45 eV. Next we have 14-26 transitions, with a cp at $M_3^z - M_2^z$ at 4.41 eV and a cp from $T_1 - T_1$ transitions near (0.5,0.28,0.5) at 4.45 eV, and 21-27 transitions with a probable M_1 cp near (0.2,0,0.2) at 4.40 eV and a cp from $\Delta_3^z - \Delta_2^z$ transitions near (0,0,0.27) at 4.45 eV. Finally, we have contributions from $\Sigma_2 - \Sigma_1$ (22-33) transitions with a cp near (0.44,0.44,0) at 4.45 eV, $\Sigma_1 - \Sigma_1$ (22-33) transitions with a cp near (0.4,0.4,0) at 4.45 eV, 19-27 transtions with an M_2 cp near (0.35,0.15,0.3) at 4.48 eV and a series of weaker transitions listed for completeness in Table V.

The threshold in $\varepsilon_2^{\parallel}$ occurs at 1.76 eV and is the result of 24-25 transitions around an M_0 cp near (0.4,0.2,0) which are weaker than in the $\varepsilon_2^{\perp}$ case. The shoulder starting at 2.32 eV is caused in part by 23-25 transitions and 24-25 transitions in a region (mostly along z-direction) around an M_0 cp near (0.4,0,0.3) at 2.31 eV and around an M_1 cp near (0.4,0,0.45) at 2.33 eV respectively. Other contributions are from 24-26 transitions in a region around U_1^z - U_1^z with an M_0 cp near (0.5,0,0.4) at 2.46 eV and 22-25 transitions in a region around Σ_2 - Σ_1 with an M_0 cp near (0.35,0.35,0) at 2.32 eV. The shoulder around 2.80 eV is caused to a large extent by 24-26 transitions in a small region around an M_0 cp near (0.1,0.1,0.4) at 2.81 eV and an M_0 cp near (0.2,0.2,0.5) at 2.79 eV. Other strong contributions are from 21-25 transitions with an M_0 cp near (0.45,0.15,0.3) at 2.73 eV, U_1^y - U_1^y transitions with an M_1 cp near (0.5,0.2,0) at 2.78 eV and 22-26 transitions in a region (along z-direction) around 0.5,0.3,0.15) at 2.82 eV and an M_0 cp at M at about 2.65 eV. Weaker contributions are from Z_1 - Z_1 (24-27) transitions with an M_0 cp at 2.79 eV and 24-25 transitions with an M_2 cp near (0.2,0.05,0.4) at 2.81 eV.

The peak at 3.30 eV is caused in part by 21-25 transitions in a region (tubular along z-direction) around U^x with an M_2 cp near (0.2,0,0.5) at 3.33 eV and 23-27 transitions with an M_1 cp near (0.35,0.15,0.3) at 3.31 eV. Additional contributions to this peak are from 22-26 transitions in a region around what appears to be an M_2 cp near (0.25,0.25,0.3) at 3.36 eV and 23-26 transitions in a region near Γ with particularly strong contributions from Δ_4^z - Δ_4^z transitions at about 3.3 eV. Finally, we have contributions from 24-26 transitions with an M_2 cp near (0.12,0.12,0.25) at 3.25 eV and 21-28 transitions in a region around Σ_2 - Σ_1 with a cp of undetermined symmetry near (0.14,0.4,0) at 3.3 eV. The peak at 3.65 eV is the result of three main types of contributions. First, we have 22-27 transitions in a region near Z off the S direction with a probable M_1 cp near (0.15,0.1,0.45) at 3.64 eV along with an M_1 cp near (0.2,0,0.4) at 3.69 eV, and 21, 22-27 transitions in a region of relatively large matrix elements near M off the U^x direction with a probable M_0 cp near (0.37,0.1,0.4) at 3.62 eV and an M_0 cp near (0.3,0.3,0.25) at 3.60 eV. Secondly, we have 19-25 transitions, in a region near Z around $S_1 - S_1$, with an M_0 cp near (0.1,0.1,0.5) at 3.65 eV, and 20-25 transitions also near Z but around U^x with an M_0 cp near (0.1,0,0.5) at 3.60 eV and what appears to be an M_0 cp near (0.2,0.1,0.3) at 3.62 eV. Thirdly, we have 24-28 transitions, with a cp of undetermined symmetry near $S_1 - S_1$ (0.25,0.25,0.5) at 3.65 eV and a region around $T_1 - T_1$ with an M_3 cp near (0.5,0.21,0.5) at 3.74 eV and 23-28 transitions with an M_1 cp near T at about (0.5,0.15,0.4) at 3.60 eV along with weaker $\Delta_1 - \Delta_2$ (24-27) transitions with a cp near (0.35,0,0) at 3.65 eV.

The large peak at 3.90 eV is caused in part by 24-30 transitions in a region around an M_1 cp near (0.5,0.22,0.25) at 3.92 eV and 24-29, 30 transitions in a region around $Z_1^x - Z_1^x$ with an M_0 cp at 3.93 eV and particularly strong contributions along $U_1^y - U_1^y$ at 3.95 eV. Other important contributions are from $\Gamma_3 - \Gamma_4$ with an M_2 cp at 3.98 eV and 23-29 transitions with an M_0 cp near (0.2,0,0.3) at 3.91 eV. Next, we have 18-25 transitions in a region around (0.3,0,0.4) contributing at 3.90 eV, $\Delta_2 - \Delta_1$ transitions with a cp near (0.35,0,0) also at 3.90 eV, and 21-26 transitions in a region around $\Sigma_2 - \Sigma_1$ with an M_1 cp near (0.16,0.16,0) at 3.92 eV. Finally, we have 22-30 transitions with an M_0 cp near (0.35,0.35,0.1) at 3.81 eV and 23-28 transitions with a cp near (0,0,0.22) at 3.88 eV.

The shoulder around 4.26 eV is caused in part by 20-25 transitions in a region (along z-direction) of large matrix elements around $\Gamma_3 - \Gamma_4$ with an M_0 cp at 4.07 eV, 22-29 transitions in a region (along z-direction) around M with a probable M_1 cp at 4.28 eV, and 22-32 transitions in a region around $M_3^z - M_3^z$ with a cp at 4.30 eV and in a region around $U_1^y - U_1^y$ with a cp near (0.5,0.3,0) at 4.26 eV. Additional contributions to this shoulder are from 20-28 transitions in a region around 0.4,0.2,0.25) at 4.30 eV, 18-27 transitions in a region around $Z_1 - Z_1$ with an M_1 cp at 4.25 eV and 19-25, 26 transitions in a region around (0.25,0.25,0.3) at 4.28 eV. Finally, we have 24-30 transitions with critical points of undetermined symmetries near $U_1^z - U_1^z$ (0.5,0,0.15) at 4.26 eV, $S_1 - S_1$ (0.3,0.3,0.5) at 4.27 eV, $\Delta_1 - \Delta_2$ (0.36,0,0) at 4.26 eV and an M_3 cp near (0.3,0.1,0.2) at 4.41 eV. The last structure we shall consider in the $\varepsilon_2^{\parallel}$ spectrum occurs at 4.96 eV. This shoulder is caused in part by 20-38, 29 transitions in a region (mostly along z-direction) around (0.3,0,0.25) at 4.95 eV. Other contributions to this shoulder from critical points of undetermined symmetry are listed in Table VIII.

C. Discussion of Amorphous Phases

The experimental amorphous dielectric function $\varepsilon_2(E)$[10] (Figs. 37 and 38) consists of a seemingly featureless spectrum with one broad peak positioned near the Λ peak in the FC-2 ε_2. This spectrum is quite different from any known crystalline ε_2 (except for ST-12) and cannot be obtained by simply averaging the peaks in the FC-2 spectrum.

The theoretical attempts[24-29] to explain the amorphous ε_2 have all assumed that long range disorder is of primary importance. They have taken the FC-2 band structure as a starting point and have applied various modifications to study the effect of long range disorder. In some cases[24,28] complete k non-conservation was considered in the sense of a non-direct transition (NDT) model and in other cases[25-27,29] partial $\vec{k}$ non-conservation was proposed which enabled the introduction of some type of short range order parameter. In all cases, however, the results are similar, in good agreement with experimental ε_2 data, and the authors agree that strong $\vec{k}$ non-conservation (long range disorder) is a requisite in explaining the amorphous ε_2. None of these theories, however, predicts even a correct trend to the density of states of the amorphous phase. The single broad peak[11] at the bottom of the valence band density of states for the amorphous case is very striking and cannot be accounted for by a simple broadening of the two s-like peaks in the FC-2 structure. This problem was discussed in Section III where we suggested that the experimental results could be explained by a short range disorder which would make the presence of five and sevenfold rings of bonds appreciable. It is precisely the lack of this short range disorder in these theories that produces this inconsistency with the experimental data. To see this let us examine one of the most interesting and sophisticated of the aforementioned theories, which is that of a complex band structure (CBS).[27,28] It was instigated by the work of Maschke and Thomas[26] and developed by Kramer. A one electron Green function is expanded in a Born series and a configurational averaging is applied by introducing in each term containing n scattering centers an n-particle correlation function which is integrated over all n sites. It is then assumed that the n-particle correlation functions can be approximated by products of two particle correlation functions which are taken to be sums of

Gaussian-like functions centered on lattice sites, with half-widths which increase with increasing distance from a given lattice point and are proportional to a small parameter α which describes the amount of disorder. This type of approximation treats correctly multiple scattering at one atom only while higher multiple scattering terms are treated approximately correctly if one has $\alpha << 1$. The two body correlation functions can be related to experimental amorphous radial distribution functions (RDF), however, we notice that in Ge for example it would be difficult to reproduce the second and third hump in the RDF[30] curves by simply placing Gaussian-like functions at FC-2 lattice points.

Nevertheless, the averaged Green function series, which is written in terms of pseudopotentials $v(q)$,[31] can be reduced if one assumes slowly varying potential functions and small enough α so as to take $v(q)$ constant in the $\vec{k}$-integration which in turn permits decoupling of terms and a resummation of the series. The poles of this averaged Green function are now obtained from a generalized pseudopotential secular equation which is now no longer Hermitian. Kramer then finds that he obtains complex energies whose real parts are approximately the energies of the crystal and whose imaginary parts can be interpreted as average reciprocal lifetimes or equivalently average energy widths. The average ε_2 spectrum is obtained by using the Kubo formula and performing a similar configurational averaging on a product of two one electron Green functions. With some approximations the forms for the averaged ε_2 and density of states are similar in that they are written as a sum over partial spectra belonging to different regions of the BZ where the reciprocal lifetimes can be taken constant. The partial spectra are then given by a convolution of the crystalline spectrum (shifted in energy when appropriate as shown below) with a Lorentzian which depends on an average reciprocal lifetime. The parameter α was chosen to fit the ε_2 spectrum of amorphous Ge and Si.

Kramer's results show the valence band being affected very slightly while the conduction band is broadened considerably. In particular, for Ge the $\Gamma_{25} - \Gamma_2$ and $L_1 - L_3$ gaps become smaller while the $X_4 - X_1$ gap becomes larger. Furthermore, Γ_2 is very slightly broadened, L_2 is slightly broadened, and X_1 is largely broadened. This is not surprising nor difficult to understand. In principle, we would expect the electrons in the conduction band to be affected more by long range disorder than the very well localized valence electrons. In fact, if we look at the charge density at symmetry points in the conduction band, we find that X_1 is largely spread out while L_3 is somewhat localized and Γ_2 shows difinite signs of localization. This is exactly the same trend observed in the reciprocal lifetimes mentioned above. The effect of this on ε_2 is then to average out most of the X peak while preserving the Λ peak and shifting it to slightly lower energies. The agreement with the experimental amorphous ε_2 is good. The effect of Kramer's disorder on the density of states, however, is a strong averaging of the conduction band and a very small averaging of the valence band peaks of FC-2. This is certainly not in agreement with experiment.[11] The problem is that one is dealing here with a system that has the short range order of diamond. In fact, the parameter α, used to fit ε_2, is very small and corresponds, for example, to all first, second and half the third nearest neighbors being within a deviation of only 0.04a of the crystalline FC-2 positions. It could be suggested that the density of states might agree better with experiment if α was taken to be larger. But now the ε_2 would be shifted to lower energies and agreement with experiment here would be considerably marred. Besides, the approximations involved in obtaining Kramer's final expressions may not be valid for large α.

Thus, we believe that the conclusions drawn by applying the CBS theory to the FC-2 structure are not valid for the amorphous case. The suggestion[32] that the peak in the amorphous ε_2 is due to Λ transitions because of the preservation of the bonding direction is highly questionable and is only a conjecture supported by analyzing a hypothetical "amorphous" system that is too close to the FC-2 structure.

The results from these theories lead us to suspect that the ε_2 spectrum may not be a good judge of the microscopic structural aspects of the amorphous state and that one needs a theory that will be able to account for <u>both</u> the density of states and ε_2 in the amorphous phase. In Section III we applied the concept of short range disorder to the density of states and obtained good agreement with experiment. We show how to do the same for the ε_2 spectrum.

There are two features of the amorphous ε_2 spectrum which are of primary importance. These are, of course, the one hump form of the spectrum and the position in energy of this hump. We shall attempt to account for these features in the following analysis.

The crystalline $\varepsilon_2(E)$ may be written as:

$$\varepsilon_2(E) = CJ(E)\sum_{\vec{k}}\sum_{c,v}\delta(E_c(\vec{k}) - E_v(\vec{k}) - E)\left|\langle\psi_c(\vec{k})|\vec{r}|\psi_v(\vec{k})\rangle\right|^2/j(E) \quad (22)$$

where C is a constant and J(E) is the joint density of states given by:

$$J(E) = \sum_{\vec{k}} \sum_{c,v} \delta(E_c(\vec{k}) - E_v(\vec{k}) - E) \quad . \tag{23}$$

Equation (22) is just an expression for an average matrix element P(E) mulitplied by the joint density of states J(E). If we now incorporate the constant C into J(E) we can write.

$$\varepsilon_2(E) = J(E)\, P(E) \quad . \tag{24}$$

This is a physically reasonable expression and could be used to study the amorphous phase since it is essentially the number of states accessible for transitions at an energy E, multiplied by an average probability for those transitions. When one does band structure calculations, however, it is easier to calculate an associated average matrix element M(E) obtained by a weighted averaging of $|\langle \psi_c(\vec{k})|\vec{\nabla}|\psi_v(\vec{k})\rangle|^2$. Then Eq. (23) can be written as[33]

$$\varepsilon_2(E) = J(E)\cdot\frac{M(E)}{E^2} \quad . \tag{25}$$

Equation (23) or (24) can now be used to qualitatively account for the amorphous ε_2 spectrum in a simple way. In the amorphous case we would expect J(E) to be a monotonically <u>increasing</u> function of energy without any sharp structure from specific localized regions in the BZ. Similarly, we would expect the average dipole matrix element P(E) to be a smooth monotonically decreasing function of energy. The product of these two functions would then give a one hump structure which would explain the shape of the amorphous ε_2. To examine this in more detail we have calculated ε_2, J/E^2 and M, and J and M/E^2 as a function of energy for

Ge and Si in the FC-2, 2H-4, BC-8 and ST-12 structures using the Gilat-Raubenheimer[16] integration scheme. The results are shown in Figs. 37 and 38. For each row the product of the two curves in the second and third columns gives the ε_2 spectrum in the first column. In the cases of 2H-4 and ST-12 structures we show the weighted average of the parallel and perpendicular components of ε_2. We are interested in observing the trends as we go from FC-2 down the columns to more and locally disordered and complicated crystal structures. For the moment let us concentrate on the third column in each figure. We notice that with the increasing complexity of the crystal structures, J gradually loses the sharp structure prominent in the FC-2 case which was caused by the simplicity and symmetry of this band structure. When we reach ST-12, J is almost a smooth and featureless spectrum which would compare well with what we expected in the amorphous case. In addition the average dipole matrix element M/E^2 for ST-12 is for the most part a smooth decreasing function of energy. This is particularly the case for Ge ST-12 in a large energy region while in ST-12 this is true for $E>3$ eV which, however, contains the peak of ε_2. If we now examine the ε_2 spectra we notice that it is precisely the ST-12 structure that has the qualities of the superimposed amorphous ε_2 spectrum obtained by Donovan and Spicer[10] for Ge and by Pierce and Spicer[10] for Si. The agreement between the ST-12 spectra and the amorphous spectra is quite encouraging and shows that the kind of short range disorder which accounted for the amorphous density of states also accounts for the important features of the amorphous ε_2 spectrum. The discrepancy in magnitude of the ε_2 curves is irrelevant in this discussion and is caused in part by the differences in bulk density of the ST-12 and amorphous structures.

An interesting feature that comes out of this analysis is that J/E^2 should look something like a step function in the amorphous case since J is such a smooth polynomial-like increasing function of energy. This would then suggest that the average gradient matrix element M must contain most of the information about ε_2. This is shown in Figs. 37 and 38 as we go down the second column where we have plotted J/E^2 and M. In the FC-2 case the ε_2 spectrum looks mostly like J/E^2 while M simply modulates the J/E^2 spectrum. In the 2H-4 structure we find that the form of the ε_2 spectrum is now shared between J/E^2 and M where M contributes most of the first peak and J/E^2 contributes the second peak. When we examine the BC-8 case we find that the ε_2 spectrum now looks mostly like M while J/E^2 just modulates the M spectrum. Finally, in the ST-12 structure we find that J/E^2 is a relatively featureless step-like function of energy and again ε_2 looks like M.

Therefore, we can safely conclude from this that the average gradient matrix element M determines the position in energy of the hump in the amorphous ε_2, and most important, when one measures the amorphous ε_2 spectrum, one is essentially just measuring the average matrix element M.

In summary our aim in this work has been twofold. First to make a complete band structure analysis of Ge and Si in a series of novel, interesting and complicated crystal structures. This included calculating energy eigenvalues, densities of states, optical functions, determining the symmetry of wave functions and identifying optical structure. Secondly, to use the increasing complexity of the crystal structures to study the trends observed in the density of states and the impainary part of the dielectric function as we approach the amorphous phase. To this end we have made particular use of the ST-12 structure which has deviations in bond lengths and angles and has odd-numbered rings of bonds. We have not used the ST-12 structure as a replica of amorphous Ge and Si, but rather as a tool to probe the important microscopic structural aspects of the amorphous phase.

We have found that if one is to make a reliable model of the amorphous phase, one cannot start with a long-range disorder model applied to the FC-2 structure. On the other hand, a short-range disorder model, defined as a system with deviations in bond angles, bond lengths, with all bonds, satisfied and with odd-numbered rings of bonds, could account for both the amorphous density of states and imaginary part of the dielectric function. In particular we found that the amorphous ε_2 is just the spectrum of an average matrix element.

If we now include long-range disorder to our short-range disorder, we would expect to have a much better model for the amorphous phase. Our point is, however, that the effects of long-range disorder are of secondary importance.

V. EFFECTS OF DISORDER ON THE ELECTRONIC DENSITY OF STATES OF BINARY COMPOUNDS

In this paper we would like to investigate in some detail the effects of disorder on the electronic density of states of amorphous III-V semiconductors. We shall restrict our disorder to topologically disordered stoichiometric structures with atoms in fourfold coordination and no dangling bonds. We will divide this disorder into two main types which we shall call disorder (U) and disorder (L). Disorder (U) describes a disorder connected network of atoms with deviations from the ideal tetrahedral bond lengths and angles but with the restriction of having only <u>unlike</u>-atom bonds (i.e., only III-V atom bonds). On the other hand, disorder (L) can also have <u>like</u>-atom bonds (i.e., III-III and V-V bonds). As we shall see this division of disorder into these two types is useful since the effects of like-atom bonds on the density of states are very strong and for the most part overshadow effects from disorder (U). Structures with disorder (L) will always have equal numbers of III-III and V-V bonds since we are assuming stoichiometric systems. In general, if we let $N_{III-III}$, N_{V-V}, N_{III} and N_V be the total number of type III-III bonds, type V-V bonds, type III atoms and type V atoms respectively, then we have:

$$\frac{N_{III-III}}{2} + \frac{N_{III-V}}{4} = N_{III} \tag{26}$$

$$\frac{N_{V-V}}{2} + \frac{N_{III-V}}{4} = N_V \tag{27}$$

so that the difference in percentage of type III-III and type V-V bonds is equal to the difference in percentage of type III and type V atoms.

We wish to examine the effects and differences of disorder (U) and disorder (L) on the electronic density of states. The purpose of this would be to examine an experimental amorphous density of states spectrum and to determine the type of disorder present.

To our knowledge, there have been as yet no published experimental XPS or UPS spectra on amorphous III-V compounds.

To understand the influences of disorder (U) and disorder (L) on the density of states we shall be interested primarily in effects due to:

(i) topological arrangement of atoms
(ii) bond angle and bond length distortions
(iii) percentage of like-atom bonds
(iv) different clustering configurations of like-atoms
(v) topological variations of clusters of like-atoms

These effects can be studied in the context of short range disorder as we have done previously in our work on amorphous Ge and Si. We can take a series of crystals whose primitive cells are becoming gradually larger. This permits, and in fact we have an increase in the positional disorder of the atoms. Thus, a study of the trends observed in the density of states for these crystals can give us specific information about the effects of particular types of disorder.

As we have shown in our work on complex structures of Ge and Si, the effects of long range disorder (i.e., the fact that we do not have crystals) are of secondary importance.

In this paper we shall again take the 2H-4, 4H-8, BC-8, ST-12 and SC-16 (BC-8 taken as a simple cubic lattice) structures as a basis for our studies. In the case of disorder (U) we shall use the 2H-4, 4H-8 and SC-16 structures while in the case of disorder (L) we shall examine the 2H-4, 4H-8, BC-8 and ST-12 structures. The reasons for these choices will be given later.

To study these crystal structures we shall use simple three-parameter tight binding models and the EPM. The right binding scheme will be used to easily discern structural features in the density of states and the EPM will provide a more realistic examination of the density of states. We also present charge density calculations in order to examine the nature of like-atom bonds.

In all our calculations we shall take GaAs as a prototype of the III-V compounds and we assume that our results on these effects of disorder will be applicable to all III-V compounds. However, we are not able at the present to predict with any certainty what III-V compounds could exist with disorder (U) or disorder (L).

In Appendix C we examine the topological properties of the 2H-4, 4H-8, BC-8, ST-12 and SC-16 structures in detail. If we place <u>equal numbers of Ga and AS atoms</u> at the atomic positions defining the basis for each of these five basic crystal structures we find that we can make $N!/((N/2)!)^2$ different substructures respectively assuming each atomic position to be distinct, where N is the total number of atoms in the primitive cell. Some of these substructures are of course identical and many of them are quite similar. In what follows we shall break up each group of substructures into smaller groups defined by the percentage of like-atom bonds present. We shall then break up each of the smaller groups into sub-groups depending upon the number of like-atom bonds for each atom. This is of interest since it characterizes each substructure by the immediate environment of each of its atoms. Now the substructures in the subgroups can be divided further into classes depending upon the particular clustering configurations of like atoms. However, from stability considerations we restrict ourselves to substructures that have atoms with only two or less like atom nearest neighbors. The method used to investigate the total energy per atom of these structures is described in Appendix E.

With this restriction we are effectively left with substructures that have like-atoms which can cluster into chain-like configurations which may be open or closed. A chain is defined by a series of <u>nearest</u> neighbor like-atoms. These substructures can be very conveniently characterized or identified by using the following notation:

$$\left(N^1_{Ga},\ N^2_{Ga},\ \ldots\ N^M_{Ga}/N^1_{As},\ N^2_{As},\ \ldots\ N^L_{As}\right) \tag{28}$$

where M(L) is the total number of chains of Ga (As) atoms in the primitive cell and N^i_{Ga} (N^i_{As}) is the number of Ga (As) atoms in the i^{th} chain. The fraction of like-atom bonds in a particular structure is given by

$$\frac{\sum_{i=1}^{M} (N^i_{Ga} - 1)}{2\sum_{i=1}^{M} N^i_{Ga}} = \frac{N_T - 2M}{2N_T} \tag{29}$$

where N_T is the total number of atoms in the primitive cell. Since we are dealing with stoichiometric structures an equivalent expression to Eq. (29) could be obtained by replacing N^i_{Ga} by N^i_{As}. In Eq. (29) we are assuming finite chains of like-atom bonds. In the case of rings or infinite chains we can use Eq. (29) but we must replace $N^i_{Ga}-1$ by N^i_{Ga}, where N^i_{Ga} would represent the number of like-atoms of the i^{th} ring or infinite chain in the primitive cell. We could also make this explicit in the notation Eq. (28) by placing an R (ring) or I (infinite chain) after the number N^i. The number of atoms in the structure that have zero like-atom neighbors is just given by the total number of one-link chains (i.e., $N^i = 1$). The number of atoms that have one like-atom neighbor is given by twice the total number of finite chains of order greater than one. Finally, the number of atoms in the structure with two like-atom neighbors is given by the total number of atoms in finite chains of order greater than two minus twice the number of finite chains of order greater than two plus the total number of atoms in rings or infinite chains.

As an example, let us find what information we can obtain about two substructures of the ST-12 structure if they are designated by (5,1/4,2) and (3,3/4I,1,1) respectively. In the first structure we have two Ga atom chains of order five and order one and two As atom chains of order four and order two. In the second structure we have two Ga atom chains of order three, an infinite As atom chain with four atoms in a primitive cell and two one As atom chains. The fraction of like-atom bonds in both structures is 1/3. In the first (second) structure there is one (two) atom(s) with zero like-atom nearest neighbors, six (four) atoms with one like-atom nearest neighbor and five (six) atoms with two like-atom nearest neighbors.

We may now proceed to analyze the 2H-4, 4H-8, BC-8, ST-12 and SC-16 structures using the aforementioned notation as an aid to our characterization and discussion. We shall not study all the possible distinct substructures that can be made but rather we select and describe in Appendix C those which are most useful for our purposes. Furthermore, in many cases the notation $\left(N^1_{Ga} \ldots N^M_{Ga}/N^1_{As} \ldots N^L_{As}\right)$ does not uniquely define a particular substructure. For instance, we may have many substructures forming a set in which they are all of type (I,J/K,L). In this case we shall, arbitrarily, use stability (see Appendix E) requirements as a discerning factor in choosing one substructure to study out of this set. It should be noted, however, that the densities of states of all the substructures of a given type are very similar so that the method used in choosing one substructure is relatively unimportant.

In our calculations we have interpolated the form factors obtained by Cohen and Bergstresser[31] for GaAs since in this reference V^S was constrained to be the Ge potential. For other form factors[34] the qualitative features in the density of states are the same and we only get small shifts in the energies of the peaks.

For good convergence in the 2H-4 structure we used 50-60 plane waves as a basis set along with another 140 plane waves through a perturbation scheme developed by Löwdin.[4] We calculated $E(\vec{k})$ in 1/24 of the BZ at 144 grid points. For the 4H-8 structure we used approximately 70 plane waves as a basis set with about 200 additional plane waves through perturbation theory. We diagonalized our Hamiltonian in 1/24 of the BZ at 144 grid points for the (2,1,1/2,1,1) structure and at 62 grid points for the (1,1,1,1/1,1,1,1) structure. In the case of BC-8 we used 60 plane waves as a basis and an additional 140 plane waves through the Lowdin scheme. We used 1/8 of the BZ with a grid of 154 points. For the ST-12 structure we used about 70 plane waves as a basis set and another 270 plane waves through perturbation theory. The Hamiltonian was diagonalized in 1/2 of the BZ at 192 grid points. Finally, for SC-16 we used about 85 plane waves as a basis set along with approximately 235 more plane waves through the Löwdin scheme. The eigenvalues were obtained in 1/2 of the BZ at 256 grid points.

In our tight binding calculations we have taken the following modification of the Weaire Hamiltonian

$$\mathcal{H} = \pm V_o \sum_{i,\ell} |\phi_{i\ell}\rangle\langle\phi_{i\ell}| + V_1 \sum_{i,\ell\neq\ell'} |\phi_{i,\ell}\rangle\langle\phi_{i,\ell'}| + V_2 \sum_{i\neq i',\ell} |\phi_{i,\ell}\rangle\langle\phi_{i',\ell}| . \qquad (30)$$

where the $|\phi_{i\ell}\rangle$ represent localized orthonormal basis functions which can be taken as (SP^3) hybridized directed orbitals (four to each atom). The subscripts i and ℓ label a particular atom and the orbitals of that atom respectively. The first term in this Hamiltonian is a diagonal term which is taken to be $+V_o$ or $-V_o$ depending on whether the states are associated with group V atoms or group III atoms. The second term represents an interaction V_1 between different basis functions on the same atom and the last term is an interaction V_2 between basis functions along the same bond. We have thus ignored the differences in the interactions of basis functions on different atoms and along the different types of bonds and we have assumed equal bond lengths and an ideal tetrahedral arrangement of atoms. We used $V_o = 3.2$ eV, $V_1 = -2.7$ eV and $V_2 = -6.1$ eV which are the same values as those used by Weaire and Thorpe for their calculation of GaAs in the zinc blende structure.[19]

The most prominent features of this tight binding model are an inadequate conduction band because of the limited number of basis functions, a relatively good description of the s-like states, and for the case of structures with all or no bonds that are like-atom bonds, a delta function peak in the density of states at the top of the valence band. This peak contains pure p-like bonding states with a degeneracy of one state per atom. This is interesting because it says that to first order with nearest neighbor interactions which are independent of the dihedral angle the p-like states are not disturbed by topological differences. This is a fact that is supported to some degree by experiment.[11] However, if we introduce the possibility of having like and unlike-atom bonds in our structures it is no longer true that the delta function will contain one state per atom. It would, therefore, be of interest to obtain an expression for the degeneracy of the delta function depending upon the type of like and unlike-atom bond configurations that exist in a particular structure. One thing this will give us is an idea of how much of the density of states of zinc blende is preserved under disorder (L).

Consider first the case where we have only one type of bond in the structure, then there are three p-like functions that can be formed on each atom from the four hybrids. Therefore, there are 3N pure p-like functions that can be formed in a system of N atoms. However, there is one constraint per bond if we wish to make pure p-like bonding or antibonding states. Thus as Weaire and Thorpe[12] have shown, there are 2N independent contraints and, therefore, 3N - 2N = N degenerate pure p-like bonding (or anti bonding) crystalline states. These states are then responsible for the delta function peak with one state per atom. In the case of a structure with both like-atom and unlike-atom bonds we must be a bit more careful. We must now distinguish the p-like functions among bonds of type III-III, V-V and III-V. That is, we are interested in the p-like functions of a certain type (i.e., III-III, V-V or III-V) which can be made from the hybrids along bonds of that type. The number of such functions that can be made on a certain atom given the configuration of nearest neighbor atoms is shown in Table IX. Therefore, given a structure with a particular distribution or arrangement of atoms, we can use Table IX to find the total number of p-like functions of a particular type. Once this is known the total number of bonding (or antibonding) p-like states of a certain type that can be made is just given by this number minus the total number of constraints for bonds of that type. But the number of constraints of a particular type is just equal to the number of bonds of that type. Therefore, the degeneracy of the delta function D^X representing bonding (or antibonding) p-like states of type X (where X represents the three distinct combinations of III and V) is given by:

$$D^X = 3N_4^X + 2N_3^X + N_2^X - N_B^X \tag{31}$$

Here N_I^X represents the number of atoms with I bonds of type X and N_B^X is the total number of bonds of type X. If we now express N_B^X in terms of the N_I^X we get:

$$D^X = N_4^X + \frac{1}{2} N_3^X - \frac{1}{2} N_1^X \tag{32}$$

This expression is quite useful since it tells us immediately that for the structures we are studying there will be no delta function in the density of states representing like-atom (L) bonding states. This is because we chose our structures to have N_4^L and N_3^L equal to zero due to stability requirements. This suggests, therefore, that in the amorphous case the like-atom bonding state regions in the density of states will be quite sensitive to different types of clustering configurations. On the other hand, Eq. (32) also tells us that in the structures we are studying we will definitely have a delta function peak in the density of states representing unlike-atom (U) bonding states as in the case of zinc blende whose degeneracy will be given by $D^U = N_4^U + \frac{1}{2} N_3^U$. One might thus suggest that there will be a region of the p-like states in the density of states of zinc blende whose character will be relatively unaffected by disorder. In other words, the nature of the unlike-atom bonding states in the amorphous density of states should be very nearly the same as that of the zinc blende p-like states. We shall examine this again in part B.

A. Results for Disorder (U)

In the study of disorder (U) we are interested in investigating effects on the density of states caused by the following features:

(i) Topology

(ii) Bond angle and bond length variations.

As we have already mentioned, these features can be studied with the concept of short range disorder. In this case we take GaAs in the 2H-4, 4H-8 and SC-16 structures. The first two structures have ideal tetrahedral arrangements of atoms and provide a comparison of purely topological properties. In the 2H-4 structure each atom sees a hexagonal neighborhood which is different from the cubic neighborhood of the zinc blende structure. This difference starts at the third nearest neighbor. On the other hand, in the 4H-8 structure each atom sees alternate layers of cubic and hexagonal neighborhoods. The SC-16 structure provides us with distorted tetrahedral units and, therefore, has variations in bond lengths and angles. It also provides for a new topology although it is very similar to the 2H-4 structure in that it has the same type of third nearest neighbor environment.

The tight binding model is not very useful in studying these structures with disorder (U) since we could tell no difference between the 2H-4 and 4H-8 structures and only small differences with the SC-16 structure. In addition, the simplicity of the model would be destroyed by the introduction of many parameters to take into account bond length and bond angle deviations. On the other hand, the EPM is very useful and the results of our calculations using the EPM are shown in Fig. 39a-c where we have plotted the density of states of GaAs in the 2H-4(1,1/1,1), 4H-8(1,1,1,1/1,1,1,1) and SC-16 structures. The filled valence band is shown at negative energies and part of the conduction band is shown at positive energies. These are unsmoothed computer plots and no interest should be paid to the small wiggles along the curves. Before we compare these spectra, however, it would be useful to have some information about the average distribution of electrons in each band. From the charge density calculations of Walter and Cohen[5] we know that the region of the density of states (Fig. 39) from about -10 eV to -12 eV contains electrons which are primarily concentrated on the As atoms. They are essentially the As s-like states and we shall be calling this the "s-like region" of the density of states. The middle peak around -6 eV is actually part of a band that tails all the way to 0 eV. Charge density calculations for this band show that the electrons are now more concentrated on the Ga atoms and in the bond. Part of the bonding nature of this band is probably coming from the tail. Actually, if we just took a simple two potential well model in the tight binding sense, the lower energy state would be s-like bonding primarily around the As atom and the higher energy state would be s-like antibonding primarily around the Ga atom. Although this model is certainly too simple it does give us some feeling for the region around -6 eV which we shall be referring to as the "middle peak" region. Finally, the region in the density of states from -4 eV to 0 eV contains electrons which are almost entirely concentrated in the bonds as in Ge and Si. We shall be referring to this region in the density of states as the "p-like region".

Let us now compare and examine the trends in the density of states spectra shown in Fig. 39. As we go from the 2H-4 structure to the 4H-8 structure the spectra seem to be almost identical. All the widths are the same for the two cases and the only difference is in the structure in the p-like region between -1.5 eV and -3.5 eV. What we are seeing here are the effects caused by purely topological differences. In particular in the 4H-8 structure we have the effects of averaging over cubic and hexagonal environments. In fact, the only way to have an amorphous structure with purely topological disorder is to stack randomly two dimensional hexagonal layers of atoms such that the bonds form eigher eclipsed or staggered configurations. From our results we would expect that the effects of such an amorphous structure would be to smooth out the peaks in the p-like region and leave everything else essential intact.

If we now compare the 2H-4 and 4H-8 density of states with that of SC-16 we notice some small but interesting differences. First, we notice a slight broadening of the s-like states. This is caused by variations in the second nearest neighbor distances due to bond angle and bond length distortions. These variations cause variations in the overlap integrals of the As s-like states and consequently a broadening of this band. This broadening corresponds to about a 0.2 eV increase in the width. For the p-like states we first notice a steeping of the band edge by the introduction of states at the top of the valence band around 0.5 eV. This is caused most likely by the deviations of the bond angles from the ideal tetrahedral angle which produce the same effects as in Ge. Secondly, we notice that the p-like region also gets broadened. This is caused by the rather large distribution of first nearest neighbor distances in the SC-16 structure as we discussed in Appendix C. The presence of smaller bond lengths than the ideal bond length would tend to broaden the p-like region as is the case with the SC-16 structure while structures with only larger bond lengths would get a narrowing of the p-like region as is the case with Ge ST-12. These effects, however, are clearly very small. In the middle peak region the most prominent difference is a slight shift of the main peak to higher energies by about 0.5 eV. Perhaps this is also due to the bonding character of the states in this region although it is not really clear what is happening here.

We can get some idea of the distribution of bond lengths and angles in the amorphous case from the radial distribution functions (RDF) of Shevchik and Paul.[35] The RDF's of their amorphous III-V samples were very similar to that of amorphous Ge. In fact, the RDF of amorphous GaAs is almost identical to that of amorphous Ge. Unfortunately, an RDF is not a sufficient condition for a particular structure nor can one prove the existence of fivefold rings of bonds with an RDF. Therefore, if we were to hypothesize a random network structure which gives the same RDF as amorphous GaAs but with disorder (U), we would expect to get the density of states shown by a dotted line in Fig. 39a. First we would expect the p-like behavior to be very similar to that of amorphous Ge since the distribution of bond angles and bond lengths of amorphous Ge and GaAs are very nearly the same. Secondly, we would probably get slight shift of the main peak in the middle-peak region to higher energies as in the case of SC-16. And finally, we would expect to get a smaller broadening of the s-like region in the amorphous GaAs case than in the SC-16 structure since the distribution of second nearest neighbor distances is centered at slightly larger distances in the amorphous phase[35] than in the SC-16 case.

As we shall see in the next section, however, the effects of disorder (U) are rather small and mostly insignificant when compared with the effects of disorder (L).

B. Results for Disorder (L)

In a recent communication[36] we described the gross effects of disorder (L) on the density of states based on a very simple charge density model. We suggested that the entire spectrum would be broadened because of an increase in the overlap integral between like-atoms and the different types of bonding states that are now premissible. We estimated at least a 1.0 eV broadening of the s-like region and we suggested that one may be able to distinguish As-As (Ga-Ga) bonding states at the low (high) energy side of the p-like region.

In this section we shall examine these ideas more carefully and analyze them on a more firm theoretical basis. In particular we would like to study explicitly the effects on the density of states produced by the following features:

(i) topological arrangement of atoms
(ii) bond angle and bond length variations
(iii) percentage of like-atom bonds
(iv) different clustering configurations of like-atoms
(v) topological variations in clustering configurations

The first two features were discussed in Section IV and are overshadowed for the most part by features (iii) to (v). In what follows, we shall concentrate primarily on the effects of (iii) to (v) which can also be studied in the context of short range disorder. Thus we will use the tight binding model and EPM to examine the various substructures of the 2H-4, 4H-8, BC-8 and ST-12 structures mentioned in Section II.

In Fig. 40a-f we show the densities of states for the 2H-4 (1,1/1,1), 2H-4 (2/2), BC-8 (2,2/2,2), BC-8 (4/4), ST-12 (3,3/3,3) and ST-12 (5,1/5,1) structures using the tight binding model. The valence band is mostly at negative energies with the delta function set at 0 eV and E_c designates the bottom of the conduction band. Each spectrum is normalized to 24 for ease in comparisons and the small numbers of top of the peaks give the relative weight for each peak. The solid line at 0 eV represents a delta function of pure GaAs p-like bonding states whose degeneracy is obtained from Eq. (32) and the discussion in Section II. For example, for ST-12 (3,3/3,3) we have $N_4^U = 0$, $N_3^U = 8$ and $N_1^U = 0$ so that the degeneracy of the delta function is $D^U = 4$. The fraction of like-atom bonds for each structure is given by Eq. (29). So that for 2H-4 (1,1/1,1) 2H-4 (2/2), BC-8 (2,2/2,2), BC-8 (4/4), ST-12 (3,3/3,3) and ST-12 (5,1/5,1) we have 0, 25%, 25%, 37-1/2%, 33-1/3% and 33-1/3% of like-atom bonds respectively.

When we examine the trends in the density of states as we go from 2H-4 (1,1/1,1) to 2H-4 (2/2) we notice that the peaks in both the s-like region and the middle peak region have now split into two. In addition in the p-like region there is one peak at higher and lower energies with respect to the position in energy of the delta function. We get the same qualitative results when we examine the density of states for BC-8 (2,2/2,2).

The 2H-4 (2/2) and BC-8 (2,2/2,2) substructures have different topological properties, however, they do have the same type of like-atom clustering configurations. This suggests, therefore, that the splitting of the peak in the s-like region is due to the clustering of As atoms into chains of order two which produces essentially a bonding-antibonding splitting. In a similar way the splitting in the middle peak region is essentially due to the clustering of Ga atoms into chains of order two, although we must again be careful here, as with disorder (U) since the states in this region are not purely Ga s-like states. As for the p-like region the single peaks at high and low energies respectively are probably due to the different binding energies of the like-atom bonds which cluster into chains of order one. Since the As atomic valence states lie lower in energy than the Ga atomic valence states we would expect that the lower energy peak contains mostly As-As bonding states while the higher energy peak contains Ga-Ga bonding states. We shall return to discuss this point with some evidence later. These ideas are further corroborated by an examination of the density of states of BC-8 (4/4), ST-12(3,3/3,3) and ST-12 (5,1/5,1). In the first case we have the effects of like-atoms in chains of order four and like-atom bonds in chains of order three. We notice that the s-like region has now split into four peaks which is exactly what would happen in a system consisting of localized states in a chain of order four with only nearest neighbor interactions. In fact the eigenvalues of any such chain of order N are just the roots of an N^{th} order Chebyshev polynomial of the second kind. We can also distinguish four peaks in the middle peak region presumably caused by the Ga-atom chains. In the p-like region we now have three lower energy peaks and three higher energy peaks. This lends support to the idea that these peaks represent like-atom bonding states and are caused by the like-atom bonds clustering in chains of order three.

The density of states for ST-12 (3,3/3,3) and ST-12 (5,1/5,1) show the same behavior of the s-like and p-like regions when analyzed in terms of chains of atoms and bonds respectively even though they have quite different topological properties from the BC-8 and 2H-4 substructures. For ST-12 (5,1/5,1) we notice the superposition of states in the s-like region due to chains of atoms of order five and order one. For the p-like states we can almost distinguish four lower and higher energy peaks caused by the like-atom bonds that are only forming chains of order four. The middle peak regions for these two ST-12 substructures, however, do not follow very closely the characteristics of chain-like behavior. Nevertheless, they are sensitive to the Ga atom clustering configurations as can be seen by an examination of the wave functions in this region. Furthermore, an examination of the wave functions in the p-like region can give us the nature of the bonding states in the low and high energy regions with respect to the delta function. However, the fact that the lower and higher energy peaks in the p-like regions are actually mostly As-As and Ga-Ga bonding states respectively is very easily observed in Fig. 41a-c. Here we have plotted the density of states of ST-12 (5,1/3,3), ST-12 (4,2/5,1) and ST-12 (3,3/4I,1,1). These substructures all have 33-1/3% like-atom bonds but they are of particular interest since each structure has its Ga and As atoms in different types of clustering configurations. In the density of states for ST-12 (5,1/3,3) we notice three peaks in the s-like region which is consistent with the As atoms forming chains of order three. If we were now to make bonding states that were almost exclusively of As-As bonding character we would expect two peaks in the p-like region. This is exactly what is observed in the lower energy region of the p-like states. On the other hand, at the high energy side of the delta function we can distinguish four peaks and this is consistent with Ga like-atom bonding states caused by the Ga-Ga bonds forming chains of order four. For the ST-12 (4,2/5,1) structure we notice that the s-like region has essentially five peaks with a small splitting of the middle peak. This splitting is due to a difference in environment between the As atoms in the chains of order five and order one. In the p-like region we can have the Ga-like atom bonding states giving three or four peaks while the As-like atom bonding states should give four peaks. From Fig. 41b we notice that both the lower and higher energy peaks are four and so it is rather difficult to distinguish visually the difference between the chains of bonds. Finally, in the density of states for ST-12 (3,3/4I,1,1) we see the effects of an infinite (or four that matter, a very long) chain of As atoms. The s-like region has one slightly split peak near the middle which is caused by two chains of As atoms of order one. Superimposed on this is essentially the familiar one dimensional type of density of states which can be obtained by taking only nearest neighbor interactions in an infinite linear chain of atoms. The width of this s-like region is the largest broadening that we would expect to get from any of the other substructures. The effects of an infinite chain of As-As bonds is shown in the lower energy region of the p-like states. We notice that its width is large enough to mix in with the states in the middle peak region.

By using the tight binding model we have observed some very large effects in the density of states caused by disorder (L) which could be understood quite easily. In particular we found that the s-like and p-like regions in this model follow some very simple tight binding rules which are intimately related to the clustering configurations of the like-atoms and like-atom bonds. We must ask, however, how realistic in fact are these large effects? Use of the EPM provides the answer and as we shall show below many of these large effects actually carry through in a more complicated calculation. Thus the tight binding model serves the valuable prupose of providing a simplicity that aids in the understanding of the effects of disorder (L) using a more realistic model. In Fig. 42a-d we have plotted the density of states using the EPM for the ST-12 (4,2/5,1), BC-8 (2,2/2,2), 2H-4 (2/2) and 4H-8 (2,1,1/2,1,1) substructures which have 33-1/3%, 25%, 25% and 12-1/2% like-atom bonds respectively. Like the tight binding case, these densities of states are normalized to 24 for each substructure and the numbers on top of the peaks represent the approximate strength of those peaks. In addition, there is an overlap between conduction and valence band states near 1 eV. We notice immediately that the effects of disorder (L) using the EPM are just as spectacular as with the simple tight bidding model. Let us first examine the s-like region of the density of states. For the ST-12 (4,2/5,1) substructure we find six peaks which correspond to the six peaks also found in the tight binding case (Fig. 41b). However, a comparison of the s-like region in Fig. 41b with that of Fig. 42a shows that the latter peaks using the EPM are not symmetrically situated around the s-like peak of As atoms in chains of order one. This is caused to a major extent by the increase in the potential between the atoms in chains of order greater than one which causes a shift of these states to lower energies. This is similar to shift of the one electron s-like energies in the hydrogen molecule-ion. In the latter case this shift is always greater or nearly equal to half the splitting or width of the bonding-antibonding states. Similarly in the case of all the substructures we have studied with the EPM this shift is approximately equal to half the broadening of the s-like states. So as a general rule the highest energy peaks of an s-like chain will overlap with the s-like peak of chains of order one. Therefore, one of the two highest energy peaks in the s-like region of ST-12 (4,2/5,1) is a band representing the As atoms in chains of order one. In the s-like region for the 2H-4 (2/2) and BC-8 (2,2/2,2) substructures we only get two peaks. This is due to the As atoms clustering into chains of order two as we saw in the tight binding case. The similarities between shape and energy splitting of these two peaks for the 2H-4 (2/2) and BC-8 (2,2/2,2) substructures shows that the s-like region is relatively insensitive to the topological variations of the atomic chain-like configurations. We also notice that the higher energy s-like peak for both substructures lies very closely in energy to the s-like peak for the As atoms in chains of order one (Fig. 39). Finally, in the 4H-8 (2,1,1/2,1,1) substructure which contains both As atom chains of order one and order two we can again see, directly, the overlap between the antibonding like state (weight one) of the As-atom chain of order two and the band (weight two) of As atoms in chains of order one. Furthermore, the splitting between bonding like and antibonding like states for the As atoms in chains of order two is very nearly the same as that for the 2H-4 (2/2) and BC-8 (2,2/2,2) substructures. Therefore, the size of this splitting, which also happens to be the smallest possible broadening of the s-like region under disorder (L), is also unaffected by the percentage of like-atom bonds present in the substructure. Using the charge density model[36] we estimated a minimum width of about 3 eV in the amorphous case. This is not too far from the results of the present calculations.

If we were now to assume that the amorphous phase with disorder (L) would tend to favor like-atoms clustering in chains or order no larger than two, then we could estimate the percentage of like-atom bonds in principle by measuring the strength of the two s-like peaks. The fraction of like-atom bonds would then be given by $1/[2(1 + H/L)]$ where H/L is the fraction of strength of the higher and lower energy peaks in the s-like region. Generally speaking, however, the effects of disorder (U) are a broadening of the s-like region and a shift of the center of mass of this region to lower energies. In addition, the width of this region depends primarily on the types of chain present and not on the percentage of like-atom bonds or the particular topological configuration of these chains.

Let us now examine the p-like regions for these substructures. The p-like regions are bounded from below approximately by the dashed lines at about -5 eV. These regions are further approximately subdivided into Sections I, II and III representing particular types of bonding characteristics. A comparison of the p-like region for ST-12 (4,2/5,1) using the EPM and the tight binding model suggests that the lower energy region of the p-like states (region I) should presumably represent As-As bonding states while the high energy region (III) should characterize Ga-Ga bonding states. The middle p-like region (II) represents the delta function peak whose nature remains unaffected to first order by effects of disorder (L). This middle p-like region then retains the character of the p-like region without disorder and represents the Ga-As bonding states. Similar classifications can be made with the p-like regions of the other three substructures in this figure. A comparison of the middle p-like regions for the BC-8 (2,2/2,2) and 2H-4 (2/2) substructures reveals that the shape of this region is rather sensitive to the topological properties of the structure. The difference in strength of the two peaks in the middle p-like region for the 2H-4 (2/2) case is most likely caused by the fact that the lower energy p-like region for 2H-4 (1,1/1,1) contains states that mostly describe diagonal unlike-atom bonds while the higher energy region represents mostly vertical (along $\hat{z}$ direction) unlike-atom bonds. Therefore, since the 2H-4 (2/2) structure has only diagonal unlike-atom bonds this anisotropy in the strength of these two peaks is understandable. In an amorphous structure, however, we would not expect this type of anisotropy so that the middle p-like region should look more like the one in the BC-8 (2,2/2,2) substructure. The effects on the p-like region obtained by reducing the percentage of like-atom bonds while retaining similar types of like-atom clustering configurations can be seen from Fig. 42d. The p-like region for the 4H-8 (2,1,1/2,1,1) substructure is just slightly broader than the BC-8 (2,2/2,2) and 2H-4 (2/2) substructures. In addition, the most important change seems to be just a reduction in strength of the As-As and Ga-Ga bonding state regions.

Finally, all that we can say about the middle peak regions for these four substructures is that we obtain an overall broadening in each case as compared with the middle peak region for 2H-4 (1,1/1,1). As for the conduction bands we notice that we get a shift to lower energies when compared to the bottom of the conduction bands for the corresponding substructures without like-atom bonds. In fact, the states at the bottom of the conduction band under disorder (L) are most probably As-As antibonding like states in addition to being plane wave like. This is due to the fact that the low lying conduction states should be orthogonal to the top of the valence band and s-like. At the same time the deeper As-As potential would be a stronger influence on these states and would try to bring them down to a lower energy. However, the effects of shifting of the conduction band and broadening of the p-like region due to like-atom bonds as some very serious consequences.

We have found that all our EPM calculations related to disorder (L) yield semimetals. Experimentally,[37] a large decrease in the gap has been found for amorphous III-V compounds and our results are consistent with Connell's[37] suggestion that this decrease might be caused by like-atom bonds. Before we go into this in any more detail, however, let us first look at some charge density calculations. This way we can explore further some of the speculations that we have seen making regarding the character of various regions of the density of states and we can get some idea of the nature of the like-atom bond. The methods used to obtain the charge densities are discussed in Section II-B and Appendix B. As a simple and typical example, we shall take the 2H-4 (2/2) substructure. Some information about the distribution of electrons in various regions of the density of states can be obtained from band charge densities $\rho_n(\vec{r})$. Charge density contours for $\rho_n(\vec{r})$ for bands 1 to 10 in the (110) plane of the 2H-4 structure are shown in Figs. 43 to 47. In Fig. 43 we show the s-like region where the bonding and antibonding nature of the As s-like states is clearly evident. In Fig. 44 we have what is essentially the middle peak region. The electrons here are mostly spread out around the Ga and As atoms with electrons in the Ga-Ga, Ga-As and As-As bonds. In particular, band 3 has more electrons in the As-As bond and around the Ga atoms than band 4, while band 4 has more electrons in the Ga-As bond. In addition, there seems to be slightly more charge around the Ga atoms than the As atoms. In Fig. 45 we have the charge density for band 5 which should represent approximately the lower energy region of the p-like states. As we see, the electrons are concentrated primarily on the As-As bonds with a small concentration in the Ga-As bonds and negligible distribution in the Ga-Ga bonds. In this same figure we show band 6 which is effectively the first half of the middle p-like region. Now the electrons are primarily concentrated in the Ga-As bonds with a small concentration in the As-As bonding region. Similarly, band 7 in Fig. 46 which is essentially the other half of the middle p-like region has its electrons almost completely occupying the Ga-As bond. The contours to the left of the Ga atoms and to the right of the As atoms represent cross-sectional slices of the other diagonal bonds which are not shown in this plane. In this same figure we show band 8 which approximately represents the states in the high energy region of the p-like states. As we see, the electrons are now primarily concentrated around the Ga-Ga bond with negligible distributions around the As atoms. Finally, in Fig. 47 we show the distribution of electrons in the hypothetical situation where the first two conduction bands are completely filled. The electrons are now very plane-wave like but at the same time are primarily concentrated on the As atoms in an antibonding like configuration.

These charge densities confirm our earlier speculations about the distribution of electrons in certain regions of the density of states. Furthermore, similar results can be obtained by examining an integrated "energy" charge density $\rho_{E_f,E_i}(\vec{r})$ for various intervals $[E_i,E_f]$ as discussed in Appendix B. In Figs. 48-50 we show our calculations of $\rho_{E_f,E_i}(\vec{r})$ for the 2H-4 (2/2) substructure for the intervals (in eV) [-7.2,-6.1], [-6.1,-5.0], [-5.0,-3.7], [-3.7,-1.3], [-1.3,0.6] and [0.6,2.2]. These intervals are labeled with arrows and shown in Fig. 42c. The middle peak region can be also approximated by the intervals [-7.2,-6.1) and [-6.1,-5.0]. The charge density for these cases is shown in Fig. 10. We notice immediately that although the general appearance of the electronic distributions are the same as bands 3 and 4 there are some interesting differences. Unlike bands 3 and 4 the charge density in these two energy intervals are almost identical. In going from the low energy interval to the higher energy interval we observe a very slight increase in charge around the Ga-Ga and Ga-As bonds with a corresponding reduction in charge around the As-As bonds. Furthermore, although the electronic distribution in band 3 is very similar to that of the low energy interval, the charge density of band 4 is quite different in that it lacks As-As bonding character.

This suggests that band 4 has a rather large overlap with the higher bands presumably in the Ga-As bonding region. As we have already mentioned it is rather difficult to characterize the middle peak egion but generally speaking the electrons are spread out around both types of atoms and in all three types of bonds. In Fig. 49 we show the charge density for the interval [-5.0,-3.7] which is essentially the low energy p-like region. This electronic distribution represents the As-As bonding states and agrees well with the charge density of band 5. In this figure, we also show $\rho_{E_f,E_i}(\vec{r})$ for the interval [-3.7,-1.3] which represents approximately the middle p-like region. We notice that the charge is mainly concentrated in the Ga-As bonds and looks mostly like the charge density for band 7. This region then represents the Ga-As bonding states. In Fig. 50, we show the electronic distribution in the interval [-1.3,0.6] and [0.6,2.2]. In the former case we have essentially the Ga-Ga bonding states and this agrees very closely with the results for band 8. In the latter case we have the hypothetical case of a filled conduction band energy interval. We notice that again we obtain plane wave like behavior but at the same time a distinct antibonding s-like distribution around the As atoms. Finally, in Fig. 51 we show the charge density obtained by suming over all the filled bands. We notice that we obtain definite bonding character for all the bonds. The strengths of the Ga-As bonds are very close to their strengths in the zinc blende case. The As-As bonds have a lot of bonding charge which is also quite localized. On the other hand, the Ga-Ga bonds are rather weak and less localized.

Let us now return to the question of the gap in the density of states. What we must ask is whether we shall always get a semimetal under disorder (L). From the charge density calculations we have definite proof that the top of the valence band represents Ga-Ga bonding like states. In addition the bottom of the conduction band has some antibonding As s-like character. Therefore, we would expect a shift in energy of these regions depending on the nearest neighbor distances of the Ga-Ga and As-As bonds. In our calculations of the 2H-4 and 4H-8 substructures we have always taken the ideal situation where the Ga-Ga nearest neighbor distance is equal to that of the As-As nearest neighbor distance which is in turn equal to the ideal Ga-As nearest neighbor distance. Since the top of the valence band has much more charge around the Ga atoms than the conduction band has around the As atoms we would expect a larger sensitivity of the gap to changes in Ga-Ga bonding distances. Hopefully, by increasing the gap we would also be making the Ga-Ga bonding states more bonding like in character and more concentrated in the bonds rather than what we obtain in Figs. 46 and 50. We find that in the 2H-4 (2/2) substructure the gap increases by about 0.08 eV for every 1% reduction in the Ga-Ga bonding distance. Furthermore, this gap increases by only 0.01 eV for every 1% increase in As-As bonding distance. In Fig. 52a we show our results for the density of states of 2H-4 (2/2) with a 10% decrease in the Ga-Ga nearest neighbor distance and a 3% increase in the As-As bonding distance. In this structure we obtain a 0.1 eV gap and at the same time we have the same bulk density as before and only very small changes in the bonds angles and Ga-As bonding distances. This result on the gap is very encouraging and we would expect to get similar effects by changing the Ga-Ga and As-As distances in the other structures. The important point to remember is that given a particular configuration of like-atom bonds the Ga-Ga and As-As nearest neighbor distances would be critical in determining whether a gap could exist or not. In this structure we also obtain a small shift in the s-like region due to the decrease in As-As bonding distances. This shift corresponds to about a 0.1 eV change for a 1% change in As-As nearest neighbor distance.

At this point we have enough knowledge about how disorder (L) affects various regions of the density of states that we could make some definite statements as to what would be observed in a random network model with like-atom bonds. We begin by assuming a 10% presence of like-atom bonds which as Shevchik and Paul[35] have shown would contribute very slightly to the heat of crystallization of the amorphous phase. From stability considerations we would expect that clustering configurations of like-atoms to be in the form of chains or rings. However, we must also assume the presence of only low order (one, two or three) chains[38] of like-atoms since these will affect the possibility of obtaining a nonzero energy gap as is observed experimentally.[37] As we have already seen in Fig. 42a, fourfold chains of atoms would make a rather large overlap between the Ga-Ga bonding-like states and the conduction band. Thus, without a restriction for low order chains we would need rather large unrealistic changes in the Ga-Ga bonding distances in order to get a nonzero gap. In this model, with only low order chains, we simply assume a 10% decrease in Ga-Ga nearest neighbor distances and a 3% increase in As-As nearest neighbor distances. This way we would expect to get a nonzero gap as in 2H-4 (2/2) Fig. 52a. We should notice also that these changes in nearest neighbor distances for 5% anion-anion and 5% cation-cation bonds are compatible with some of the RDF's of Shevchik and Paul[35] (e.g., GaP) just in case these RDF's represent systems with disorder (L).

Therefore based on all these considerations our model for the density of states of an amorphous phototype GaAs compound with disorder (L) would have the form shown in Fig. 52b. For comparison we also show the density of states of GaAs in the zinc blende structure as the solid curve. Let us first concentrate on the s-like region. As we mentioned earlier, there should be a shift in the center of mass of the s-like states to a lower energy. Along with this is the fact that the highest energy states of a particular chain tend to overlap with the states of chains of order one. This suggests that we may divide the s-like region into two main peaks. The first peak is what we may call the lower energy s-like peak and would contain all the states except the highest energy states of all the As like-atom chains of order greater than one. The second peak which we may call the higher energy s-like peak would contain only the highest energy states of all the As like-atom chains and would be located around the energy of the states for As chains of order one. By making these simplifications the fraction of like-atom bonds is again given by $1/[2(1 + H/L)]$ where H and L are the strengths of the higher and lower s-like peaks respectively. In addition, as we have already seen, the splitting between the higher and lower energy peaks will be around 3 eV. Thus for 10% like-atom bonds H/L $\sim$ 4 and we get an s-like region as shown in Fig. 52b. In principle, therefore, an unfolding of the s-like region into two peaks should give us some idea of the fraction of like-atom bonds which are present in an amorphous sample.

In the middle peak region our calculations can only suggest a general overall broadening. In particular our results imply an increase in broadening in the amorphous case by about 0.6 eV. In the p-like region we should have a shoulder in the lower energy region representing the As-As bonding states. This should look something like the one in the BC-8 (2,2/2,2) substructure but with less strength. In addition we should have a middle p-like region which represents Ga-As bonding like states and is, therefore, the only part of the density of states whose character is retained under disorder. Its shape is, however, sensitive to topological disorder so it should look mostly like the middle p-like regions in the BC-8 (2,2/2,2) or ST-12 (4,2/5,1) substructures. Finally, the higher energy p-like region representing the Ga-Ga bonding-like states will tend to overlap with the middle p-like region in order to obtain a nonzero gap as in Fig. 52a. From these considerations we propose a p-like region as shown in Fig. 52b which should be about 5 eV wide. For the bottom of the conduction band we should have a small shift to lower energies as we have observed in all the substructures with like-atom bonds. For our choice of like-atom nearest neighbor distances in this model, we should have band edges at energies which are similar to those for 2H-4 (2/2) in Fig. 52a. As we have already seen in Section IV the effects of disorder (U) on the size of the gap seem to be rather small. In addition, the similarity in the overlap of the conduction and valence bands for the 2H-4 (2/2) and BC-8 (2,2/2,2) structures suggests that the most important influence on the gap is just the presence of like-atom bonds with or without disorder. Unfortunately, however, although the size of the gap is very sensitive to the Ga-Ga bonding distances it cannot be used alone as a measure of this bonding distance. This is because the contributions from the As-As bonds, even though they are weaker are not negligible. Nevertheless, a measure of the energy between the s-like high and low energy peaks, together with the size of the gap may be able to provide some information about both the Ga-Ga and As-As nearest neighbor distances.

In summary we have been primarily interested in the structural nature of the amorphous III-V phase. From an experimental point of view the information obtained from optical properties[39] and RDF's[35] is not very sensitive to the microscopic structural aspects of the amorphous phase. Neither of these experiments, for example, is able to give precise information as to what type of disorder is present in any given III-V sample. In the former case one would need a theoretical model that would have to agree very closely with the experimental optical data in order to get any believable information about the disorder present. And in the latter case the RDF is unfortunately not a sufficient condition for any structure. For example, random network models (RNM) have been able to fit experimental RDF's rather well. In all these

RNM's however we find five and sevenfold rings of bonds. It is quite conceivable, nevertheless, and indeed probable that one could make an RNM with only even num-ered rings of bonds, that would also fit the experimental RDF's. This would then have important consequences related to the type of disorder that would be present in the amorphous phase.

All this suggests that the aforementioned experimental data would in some cases still be consistent with two distinct types of disorder which could exist in an amorphous III-V compound. The first type of disorder, which can be called disorder (U), describes the stoichiometric disordered system of atoms in fourfold coordination with only unlike-atom bonds. In addition, we have variations in the bond lengths and angles while keeping all bonds satisfied. The second type of disorder is referred to as disorder (L) and encompasses all the properties of disorder (U) along with the presence of like-atom bonds.

In order to be able to distinguish between these two types of disorder we chose to study their effects on the electronic density of states which would be quite sensitive to the microscopic structural nature of the amorphous phase. In order to study these effects we have used the concept of a short range disorder model and we have been particularly interested in the effects caused by the following structural features

(i) topological variations of atoms
(ii) variations in bond lengths and angles
(iii) percentage of like-atom bonds
(iv) clustering configurations of like-atoms
(v) topological variations of clustering configurations

Our results for disorder (U) and disorder (L) are shown in Figs. 39a and 52b. For disorder (U) we find that the s-like region of the density of states is rather insensitive to the topological arrangement of the atoms. This, however, is not true for the p-like region whose shape is quite sensitive to the local environment of each atom. Furthermore, the s-like region is influenced by the second nearest neighbor distances which are affected by variations in the bond lengths and bond angles. The p-like states are also affected by deviations in the bond angles which cause a steepening of the band edge as in the case of amorphous Ge. The middle peak region of the density of states seems also to shift slightly to higher energies with the inclusion of disorder. This is perhaps due to the relatively delocalized nature of these states. This region, however, is not at the present clearly understood. Finally, the energy gap does not seem to be very sensitive to the topological properties of the system and is affected only slightly by nearest neighbor distances. All in all, the effects of disorder (U) on the density of states are rather small.

With disorder (L), however, we obtain some very interesting effects. Our results show that the s-like region of the density of states is very sensitive to the types of clustering configurations the like-atoms can form. From energy considerations we have preferred clustering configurations in which any given atom does not have more than two like-atom nearest neighbors. This implies that the like-atoms can cluster into various configurations of chains. We find that we obtain N peaks in the s-like region from each group of chains of order N. In addition the position in energy of these peaks is not very sensitive to the different topological arrangements of these chains. The center of mass of each set of N peaks is shifted to lower energies by an amount approximately equal to the interaction between atoms in a chain. This is similar to the shift observed in the electronic energy of a hydrogen molecule-ion. The effect of this shift is to make the highest energy peaks of each cluster of chains of order N to overlap and form one large peak around the energy of the peak for chains of order one. Similarly (particularly true in the case of low order chains) the rest of the peaks will also tend to overlap into one peak at about 3 eV lower than the first one. The splitting of these two main peaks is found to be insensitive to the percentage of like-atom bonds present. However, we have found that the fraction (f) of like-atom bonds can be correlated in a simple and approximate way to the strength (L) and (H) of these low energy and high energy s-like peaks respectively by the expression $f = 1/[2(1 + H/L)]$. In Fig. 14b we have assumed the presence of 10% like-atom bonds and so $H/L \sim 4$.

The p-like region of the density of states is also very sensitive to the clustering configurations of the like-atoms and broadens into three main regions (I, II and III) which we call the low, middle and high energy p-like regions. The low and high p-like regions represent As-As and Ga-Ga bonding states respectively. On the other hand, the middle p-like region represents Ga-As bonding states and is, therefore, the only region of the density of states that retains its character under disorder (L). In addition, the shape of this region is quite sensitive to the topological arrangement of the atoms. The main effect of the percentage of like-atom bonds on the p-like region seems to be just a variation in the strengths of the peaks in these three regions. The width of the p-like region is however sensitive to the order of the like-atom chains and to the Ga-Ga and As-As bonding distances. We have found that in order to get a finite energy gap we would need a structure with only low order chains to atoms ($\leqslant 4$) and Ga-Ga and As-As bonding distances which are smaller and larger respectively than the ideal Ga-As bonding distance.

Finally, we should mention that although we used GaAs to study disorder (U) and disorder (L) we would have obtained similar results from any other III-V compound. This is not to say, however, that all the III-V compounds are equally likely to exist in the amorphous phase with disorder (U) or disorder (L). In particular in the case of disorder (L) we would expect to find only the compounds with the strongest bonding character. Now presumably the bonding charge calculated by Walter and Cohen[5] can be considered a measure of this bonding character. In that case, their results would indicate, for example, that InSb and InP are more likely to be found with disorder (L) than GaAs. In any case, if amorphous samples are to be found with disorder (L), it would seem preferable to prepare them at low enough temperatures so that the diffusivity of the atoms is very small.

VI. ELECTRONIC PROPERTIES OF TRIGONAL AND AMORPHOUS Se AND Te

The electronic structure of trigonal Se and Te has been the subject of many experimental and theoretical studies.[40] Recently, the advent of new ultraviolet (UPS)[41] and X-ray (XPS)[41,42] photoemission measurements has provided important information about the complete valence band and has revealed some inadequacies of present theoretical calculations.[43-45] In one of these calculations[43] a complete merging of s- and p-like bands was proposed which disagrees qualitatively with the recent photoemission data. Other calculations[44,45] show a separation of s- and p-like bands which is in qualitative agreement with these experiments, however, band widths and important structure in the p-like bonding states are not obtained correctly. The experimentally observed characteristic two-peak structure in the p-like bonding states is, as we shall show, intimately related to two types of states so that precise calculations are necessary before a detailed understanding of the electronic structure and bonding nature of Se and Te can be obtained. Finally, the information gained by a careful examination of the crystalline forms of Se and Te is a considerable aid in understanding the amorphous phases of Se and Te[42,46] as well.

A. Discussion of Trigonal Phases

In this part we present new calculations of the electronic densities of states of trigonal Se and Te using the EPM[2] which for the first time agree quantitatively with all the observed structure in the experimental photoemission spectra. In Fig. 53 we show the results of our calculations for trigonal Se and Te, with the filled valence bands at negative energies. The lowest band represents essentially the atomic s-like states of Se and Te respectively. The next band contains p-like bonding states which lie between -6.0 eV and about -2.2 eV for Se and for Te. Finally, the top most valence states are predominantly non-bonding p-like in nature. In order to facilitate comparisons with experiment we have convoluted these spectra with an energy dependent broadening function and the results are shown in Fig. 54. Superimposed, we show the recent photoemission results of Schevchik, et al.[41] for Se and Joannopoulos, et al.[42] for Te. The experiments on Se were obtained by using UPS and XPS measurements on a sputtered and subsequently annealed films, while those on Te were obtained using XPS on a single crystal. All observed structures in the experimental spectra are reproduced with widths, positions and number of peaks now in good quantitative agreement with experiments.

In order to understand the origin of the characteristic two-peak structure found in the p-like bonding states of both Se and Te we have calculated electronic charge distributions of states in each peak. This entails summing over states whose energies (in eV) fall within [-6.0,-3.6] and [-3.6,-2.25] for Se and [-6.0,-3.5] and [-3.5,-2.2] for Te. The results are shown in Fig. 55. The atoms which lie in the same chain are connected by a straight solid line. We notice that the lower bonding p-like states are primarily concentrated in the region between atoms in the same chain whereas the upper bonding p-like states lie mostly in the interstitial region between the chains. We can, however, go one step further and isolate short wavelength Fourier components from the long wavelength Fourier components in these charge densities. This introduces a new method of defining bonding charges and a way to separate out effects of metallicity. The cutoff or boundary wavelength λ_o between short and long wavelength components was found to lie naturally at $\lambda_o = d$ where d is the nearest neighbor separation in Se and Te. The results obtained for Se by retaining only Fourier components with $\lambda \leqslant \lambda_o$ are shown in Fig. 56a and b for the energy intervals [-6.0,-3.6] and [-3.6,-2.25] respectively. The results for Te are similar and are shown in Fig. 57. We notice immediately that the lower energy peak in the p-like bonding states represents states involved in <u>intra-chain bonding</u>. The charge is well localized in the bonds between atoms belonging to the same chain. In the upper or higher energy peak of the p-like bonding states we find states which arise in part because of the hybridization of P_x and P_y states and may also perhaps be considered as contributing to the <u>inter-chain bonding</u> of the crystal. Now the charge is displaced out of the bonds and is concentrated in the region between neighboring chains.

Some measure of intra-chain vs inter-chain bonding strengths is given by the magnitude of the respective bonding charges. For Se we have found 0.07 e^- for the intra-chain bond and 0.04 e^- for the inter-chain bond. It is instructive to compare these values with 0.05 e^- and 0.04 e^- for the intra- and inter-chain bonds of Te respectively. The difference in bonding charge between the intra-chain and inter-chain bonds decreases in going from Se to Te and thus reflects the more three dimensional or more isotropic character of Te. Furthermore, we believe that the smaller amount of total bonding charge in Te is indicative of its more metallic character. However, it should be emphasized that the values of the bonding charges we have obtained should be considered mostly in a relative sense rather than individually.

The more one-dimensional nature of Se vs the more three-dimensional nature of Te is also reflected in the s-like states shown in Fig. 53 a and b. In Se we find two sharp peaks at the edges of the band with a broad valley in between. This is very characteristic of the density of states of an infinite chain of s-like states with nearest neighbor interactions shown in Fig. 58 as a dashed line. For Te, however, we find in addition a peak near the middle of the valley. This new peak is very characteristic of the density of states of a simple cubic lattice of s-like states shown in Fig. 58 as a solid line. In Te this new peak is a result of an increase of the inter-chain vs intra-chain interaction of the s-like states as compared to Se. Furthermore, these results are consistent with the fact that Te becomes simple cubic under uniaxial pressure.

B. Discussion of Amorphous Phases

The recent photoemission measurements on amorphous Se and Te show mainly two very interesting differences when compared with their crystalline counterparts. One of these differences occurs in the s-like states and the other in the p-like bonding states. This is seen in Fig. 59 where we have superimposed the photoemission results of trigonal (solid line) and amorphous (dashed line) Se[41] and Te[42] respectively. In amorphous Se the lower peak of p-like bonding states has now become weaker, whereas the upper peak has become stronger. In amorphous

Te we find the exact opposite effect. From our previous discussion in part 1 we would interpret these differences as a decrease of the intra-chain interaction in amorphous Se and an increase in the intra-chain interaction in amorphous Te.

In the s-like states we find a bigger dip in amorphous Se as compared to trigonal Se whereas the dip in the s-like states of trigonal Te fills up in the amorphous case. This increase of the dip in amrophous Se suggests some very interesting structural properties. For example, it could not be caused by just a breaking of the infinite chains. This would only tend to fill up the dip unless the chains were of order two which seems highly unlikely. The only other reasonable alternative would be the formation of some type of rings. In particular the dip would get bigger only if the rings were of order three, five, six or seven. Rings of order four, eight or five and seven together, would certainly tend to fill up the dip. Furthermore, since the bond angles in the trigonal phase are around 100° we would suspect that the most likely ring structures would be of type fivefold and sixfold or sixfold and sevenfold. We, therefore, propose that amorphous Se contains a substantial number of atoms in ring-like configurations with the rest of the atoms being members of chains.

In amorphous Te the structural information obtained from the s-like states is a bit more difficult to discern. As we have already mentioned, a filling up of the dip could be obtained in many ways; such as a simple cubic structure, fourfold, eightfold, five and sevenfold rings, and broken chains. The simple cubic structure could, however, be dismissed since it would merge the p-like bonding states with the non-bonding or lone-pair states. What remains, therefore, is to discern between a structure which most likely would contain only broken chains or broken chains and rings.

The differences between amorphous Se and Te may lie in the different techniques applied for this preparation. Amorphous Se samples were prepared by sputtering and forming a thin film whereas the amorphous Te samples were obtained by Argon bombardment on a single crystal. Under these conditions the formation of rings may be more likely in Se rather than in Te.

ACKNOWLEDGEMENTS

I am very grateful to Professor Marvin L. Cohen for his guidence and encouragement throughout all aspects of this work. His adivce, interest and thoughtfulness are deeply appreciated.

I would like to thank Professor Charles Kittel, Professor Leo Falicov, Professor David Shirley and Professor Ching Fong for many helpful and stimulating discussions.

I would like to thank Dr. Lothar Ley, Dr. Michael Schlüter, Dr. Felix Yudenain and Dr. Carmen Varea de Alvarez for their friendship and many helpful discussions both in and out of Physics. In particular I thank Dr. Ley and Professor Shirley's group for their collaborations on the experimental aspects of Se and Te, Dr. Schlüter for his collaboration on the theoretical aspects of Se and Te, and Dr. Yudurian for his collaboration on the cluster calculations.

I would also like to thank Jim Chelikowsky, Steve Louie and the rest of the graduate students of the solid state group for many helpful interactions. In particular I thank my close friend Jim Chadi for providing an atmosphere of friendship and conflict at times when each was necessary.

I would also like to thank Mrs. Madeline More and Mrs. Carol Tung for being such efficient and friendly secretaries and Miss Jean Wolslegel for her very friendly service and her efficient typing of the manuscript.

Finally, and most importantly, I would like to thank my parents for their constant support and wisdom during the earlier stages of my life and my wife, Sandy, for her unending understanding, encouragement and care during my graduate years.

This work was supported by the U. S. Atomic Energy Commission and the National Science Foundation.

APPENDIX A. THE EMPIRICAL PSEUDOPOTENTIAL METHOD

Here we shall give a brief description of the various aspects of the Empirical Pseudopotential Theory which are relevant to our calculation. A much more thorough and extensive treatment can be found in Reference 2.

In the pseudopotential theory and other one electron theories one assumes that the crystal is made up of rigid tightly bound spherical ions and a system of valence or conduction electrons. It is the latter group of electrons which are of interest since they are responsible for the physical and chemical nature of the crystal. One now separates the total one electron crystalline potential into two parts: (1) a set of spherical potentials centered on the atoms which makes up the "cores", and (2) the potential everywhere else in a region outside the spheres called the interstitial region. In region (1) the potentials are strong in the sense that they have bound core and valence wave functions. In region (2) the potential is comparably weak and slowly varying. Thus inside the core, the valence electron wave functions will be atomic-like with many oscillations due to the large kinetic energy caused by the deep potential well, whereas, in the interstitial region the valence electron wave functions can be taken to be plane-wave like.

In the pseudopotential theory one begins by expanding a Bloch valence wave function $\psi_{v,\vec{k}}(\vec{r})$ in terms of orthogonalized plane waves (OPW)'s:

$$\psi_{v,\vec{k}}(\vec{r}) = \sum_{c} \alpha_{\vec{k}-\vec{G}}\, \psi_{OPW,\vec{k}-\vec{G}}(\vec{r}) = \sum_{\vec{G}} \alpha_{\vec{k}-\vec{G}}\, e^{i(\vec{k}-\vec{G})\cdot\vec{r}} - \sum_{c} \langle \psi_{c,\vec{k}}(\vec{r}) | e^{i(\vec{k}-\vec{G})\cdot\vec{r}} \rangle \psi_{c,\vec{k}}(\vec{r}) \quad ; \tag{A-1}$$

$$\psi_{v,\vec{k}}(\vec{r}) = \phi_{v,\vec{k}}(\vec{r}) - \sum_{c} \langle \psi_{c,\vec{k}}(\vec{r}) | \phi_{v,\vec{k}}(\vec{r}) \rangle \psi_{c,\vec{k}}(\vec{r}) \tag{A-2}$$

where $\phi_{\vec{k}}$ is defined from Eq. (A-1) and $\psi_{c,\vec{k}}$ is a tight-binding Bloch core wave function which is a solution of the total Hamiltonian with energy ε_c. If one now operates on Eq. (A-2) with this Hamiltonian one obtains a Schrödinger equation for $\phi_{\vec{k}}$ in terms of an effective potential V_{eff} which has two contributions: (1) a local attractive potential due to the atoms and (2) a nonlocal repulsive potential which projects $\phi_{\vec{k}}$ on to the core states. In most cases, it is a good approximation to take repulsive potentials to be local which in turn simplifies matters considerably. This V_{eff} which is now presumably small throughout the crystal and can be considered as an empirical pseudopotential which can be described usually in terms of a small set of parameters called form factors. The pseudopotential is then obtained by fitting the form factors to experimental optical data.^{2} This is called the Empirical Pseudopotential Method (EPM). The $\phi_{\vec{k}}$ is called a pseudowavefunction and, although Eq. (A-2) is now no longer valid, $\phi_{\vec{k}}$ for all practical purposes is taken equal to $\psi_{v,\vec{k}}$ outside the region of the core. Thus, the essence of the pseudopotential method is to remove the strong negative core potential and substitute it with a much weaker potential which will give the correct valence energy eigenvalues of the crystal. At the same time it acts so as to remove the atomic like wiggles of the valence wave functions inside the core leaving the correct valence wave functions outside the core. Since the core is usually very small, approximately 0.2 of the nearest neighbor distance, the pseudowavefunctions should be capable of providing relevant information about bonding character, symmetry, and long range interactions.

Let us now set up the secular equation for the pseudopotential Hamiltonian. The Schrödinger equation is taken as:

$$\mathcal{H}\phi_{n,\vec{k}}(\vec{r}) = -\frac{\hbar^2}{2m}\vec{\nabla}^2\phi_{n,\vec{k}}(\vec{r}) + V(\vec{r})\phi_{n,\vec{k}}(\vec{r}) \qquad \text{(A-3)}$$

and, using Bloch's Theorem:

$$\phi_{n,\vec{k}}(\vec{r}) = e^{i\vec{k}\cdot\vec{r}} \sum_{\vec{G}} \alpha_n(\vec{G},\vec{k})\ e^{-i\vec{G}\cdot\vec{r}} \qquad \text{(A-4)}$$

where the set $\{\vec{G}\}$ is the set of reciprocal lattice vectors for the particular lattice in question.

Now $V(\vec{r})$ is the total crystalline pseudopotential so that it can be written as a sum of atomic speudopotentials:

$$V(\vec{r}) = \sum_{\vec{R},\vec{\tau}_\lambda} v_\lambda(\vec{r} - \vec{R} - \vec{\tau}_\lambda) \qquad \text{(A-5)}$$

where $\vec{R}$ is a real space lattice vector, $\vec{\tau}_\lambda$ is the position of the λ^{th} atom in the primitive cell and $v_\lambda(\vec{r}) = v_1(\vec{r})$ or $v_2(\vec{r})$, depending on whether λ denotes an atom of type 1 or type 2. Since $V(\vec{r})$ has the periodicity of the lattice we can take:

$$V(\vec{r}) = \sum_{\vec{G}} V(\vec{G})\ e^{i\vec{G}\cdot\vec{r}} \qquad \text{(A-6)}$$

and if we use Eq. (A-5), $V(\vec{G})$ can be expressed as:

$$V(\vec{G}) = S^S(\vec{G})\ V^S(|\vec{G}|) + iS^A(\vec{G})\ V^A(|\vec{G}|) \tag{A-7}$$

where S^S and S^A are the symmetric and antisymmetric structure factors and V^S and V^A are the symmetric and antisymmetric form factors given by:

$$S^S(\vec{G}) = \frac{1}{n} \sum_{\lambda} e^{-i\vec{G}\cdot\vec{\tau}_\lambda} \tag{A-8a}$$

$$S^A(\vec{G}) = -\frac{i}{n} \sum_{\lambda} P_\lambda e^{-i\vec{G}\cdot\vec{\tau}_\lambda} \tag{A-8b}$$

$$V^S(|\vec{G}|) = \frac{n}{\Omega} \int \frac{1}{2} [v_1(\vec{r}) + v_2(\vec{r})]\ e^{-i\vec{G}\cdot\vec{r}}\ d^3\vec{r} \tag{A-9a}$$

$$V^A(|\vec{G}|) = \frac{n}{\Omega} \int \frac{1}{2} [v_1(\vec{r}) - v_2(\vec{r})]\ e^{-i\vec{G}\cdot\vec{r}}\ d^3\vec{r} \tag{A-9b}$$

where n is the number of atoms in the primitive cell of volume Ω and P_λ is +1 or -1 if λ denotes an atom of type 1 or type 2. Here we have assumed that the form factors are independent of energy, and since the atomic potentials are taken to be spherical, the form factors are functions of $|\vec{G}|$ only. If in addition we place the center of our coordinate system in such a way that the atoms of type 1 interchange their positions with atoms of type 2 under spacial inverstion, then S^S and S^A are both real. The secular equation is now easily obtained from Eq. (A-3) using Eqs. (A-4), (A-6) and (A-7) and has the form:

$$|\mathcal{H}_{\vec{G},\vec{G}'}(\vec{k}) - E_n(\vec{k})\ \delta_{\vec{G}\vec{G}'}| = 0 \tag{A-10}$$

where

$$\mathcal{H}_{\vec{G}\vec{G}'}(\vec{k}) = \frac{\hbar^2}{2m} (\vec{k} + \vec{G})^2\ \delta_{\vec{G}\vec{G}'} + V^S(|\vec{G} - \vec{G}'|)\ S^S(\vec{G} - \vec{G}') \tag{A-11}$$

$$+ iV^A(|\vec{G} - \vec{G}')|\ S^A(\vec{G} - \vec{G}') \quad .$$

In the zinc blende structures Cohen and Bergstresser[31] used only three symmetric and three antisymmetric form factors to obtain a good agreement of calculated optical properties with experiment. Once one has a good set of form factors, the atomic potentials can be obtained in principle form Eqs. (A-9a) and (A-9b). If one now assumes that the atomic potentials do not change very much from one type of crystal structure to the next; the form factors can be used for a variety of crystalline structures. In this sense the EPM is extremely useful. The procedure essentially involves obtaining a continuous $V^S(|\vec{q}|)$ and $V^A(|\vec{q}|)$ by a suitable interpolation scheme and reading off the $V^S(|\vec{G}|)$ and $V^A(|\vec{G}|)$ for the set of $\vec{G}$ spanning the reciprocal lattice of the particular structure.

APPENDIX B. CHARGE DENSITY AND WAVE FUNCTION TRANSFORMATIONS

Charge density calculations are particularly useful in studying the nature of the bonding properties of a solid. They can also give us information about the distribution of electrons in various regions of the density of states and, therefore, how disorder might affect these various regions.

We can obtain a charge density $\rho(\vec{r})$ using the wave functions $\phi_{n,\vec{k}}(\vec{r})$ that we get from our EPM calculations. Since the wave functions are known as a function of band index n or energy E, we can postulate a "band" charge density $\rho_n(\vec{r})$ or an average "energy" charge density $\rho_E(\vec{r})$. In the former case we would have

$$\rho_n(\vec{r}) = e \sum_{\vec{k}} \phi^*_{n,\vec{k}}(\vec{r}) \cdot \phi_{n,\vec{k}}(\vec{r}) = \sum_{\vec{k}} \rho_n(\vec{k},\vec{r}) \tag{B-1}$$

and in the latter

$$\rho_E(\vec{r}) = e \sum_n \sum_{\vec{k}} \delta(E_n(\vec{k}) - E) |\phi_{n,\vec{k}}(\vec{r})|^2 = \sum_{\vec{k}} \rho_E(\vec{k},\vec{r}) \tag{B-2}$$

where the $E_n(\vec{k})$ are the one electron valence energies. Therefore, in principle in order to obtain $\rho_n(\vec{r})$ or $\rho_E(\vec{r})$ it is necessary to integrate $\rho_n(\vec{k},\vec{r})$ or $\rho_E(\vec{k},\vec{r})$ over the entire BZ.

For our calculations on ZnS in the wurtzite or 2H-4 structure we used the two k point scheme described in Section II-2 and the following alternate approach. Our procedure was to calculate the $\phi_{n,\vec{k}}$ in 1/24 of the zone at 48 points and obtain the rest of the $\phi_{n,\vec{k}}$ by rotations of $\pi/3$, inversions and mirror reflections in k-space. In order to find how the $\phi_{n,\vec{k}}$ transform one must go back to real space and study the symmetry operations of the crystal. Since the wurtzite crystal has a symmetry classification of $P6_3mc$, any rotations of $\pi/3$ in real space must be accompanied by certain translations. Once the space group elements are found, the procedure to find the transformed wave functions is now simple. Let us assume that R^{-1} is some rotation in the point group in the negative sense. In order to make U a symmetry operator of the wurtzite crystal we must take generally:

$$U = TR^{-1} \tag{B-3}$$

where T is the appropriate translation operator with eigenvalue $\vec{\tau}_R$. Now $\phi_{n,\vec{k}}(\vec{r})$ has the form:

$$\phi_{n,\vec{k}}(\vec{r}) = e^{i\vec{k}\cdot\vec{r}} \sum_{\vec{G}} \alpha_n(\vec{G},\vec{k})\ e^{i\vec{G}\cdot\vec{r}} \quad . \tag{B-4}$$

However

$$\phi_{n,\vec{k}}(U\vec{r}) = e^{i\vec{k}\cdot U\vec{r}} \sum_{\vec{G}} \alpha_n(\vec{G},\vec{k})\ e^{i\vec{G}\cdot U\vec{r}} \tag{B-5}$$

is also a solution to $\mathcal{H}$ with exactly the same eigenvalue as $\phi_{n,\vec{k}}(\vec{r})$. Thus we wish to find $\vec{k}'$ such that:

$$\phi_{n,\vec{k}'}(\vec{r}) = \phi_{n,\vec{k}}(U\vec{r}) \quad . \tag{B-6}$$

From Eqs. (B-3) and (B-5) we have:

$$\phi_{n,\vec{k}}(U\vec{r}) = \left(e^{i\vec{k}\cdot R^{-1}\vec{r}}\right) e^{i\vec{k}\cdot\vec{\tau}_R} \times \sum_{\vec{G}} \alpha_n(\vec{G},\vec{k}) \left(e^{i\vec{G}\cdot R^{-1}\vec{r}}\right) e^{i\vec{G}\cdot\vec{\tau}_R} \tag{B-7}$$

$$\phi_{n,\vec{k}}(U\vec{r}) = e^{iR\vec{k}\cdot\vec{r}}\; e^{i\vec{k}\cdot\vec{\tau}_R} \qquad \text{(B-8)}$$

$$\sum_{\vec{G}} \alpha_n(R^{-1}\vec{G},\vec{k})\; e^{i\vec{G}\cdot\vec{r}}\; e^{iR^{-1}\vec{G}\cdot\vec{\tau}_R}$$

and Eq. (B-8) follows from the fact that the set $\{\vec{G}\}$ is equal to the set $\{R^{-1},\vec{G}\}$. Now since

$$\phi_{n,\vec{k}'}(\vec{r}) = e^{i\vec{k}'\cdot\vec{r}} \sum_{\vec{G}} \alpha_n(\vec{G},\vec{k}')\; e^{i\vec{G}\cdot\vec{r}} \qquad \text{(B-9)}$$

a comparison of Eq. (B-9) with Eq. (B-8) reveals that if we let $\vec{k}' = R\vec{k}$ we obtain:

$$\alpha_n(\vec{G},R\vec{k}) = e^{i\vec{k}\cdot\vec{\tau}_R}\; \alpha_n(R^{-1}\vec{G},\vec{k})\; e^{iR^{-1}\vec{G}\cdot\vec{\tau}_R} \qquad \text{(B-10)}$$

which is the required transformation expression.

To obtain a transformation expression involving the inversion operation we must use the concept of the reversal symmetry. Thus we look at

$$\phi_{n,\vec{k}}(\vec{r}) = e^{i\vec{k}\cdot\vec{r}} \sum_{\vec{G}} \alpha_n^*(\vec{G},\vec{k})\; e^{-i\vec{G}\cdot\vec{r}} \quad . \qquad \text{(B-11)}$$

If we now compare Eq. (B-9) and Eq. (B-12) and take $\vec{k}' = I\vec{k} = -\vec{k}$ we obtain:

$$\alpha_n(\vec{G},-\vec{k}) = \alpha_n^*(-\vec{G},\vec{k}) \qquad \text{(B-12)}$$

which is the desired expression.

Finally, we need to find the transformation expression for the mirror reflection operator. If we choose the mirror plane to be the plane defined by Γ, M and A then we will have all the transformations necessary to span all of k space inside the Brillouin zone. In real space this mirror plane becomes plane I shown in Fig. 1. It is clear that this mirror operator M is by itself a symmetry operator of the crystal. Thus proceeding as before:

$$\phi_{n,\vec{k}}(M\vec{r}) = e^{i\vec{k}\cdot M\vec{r}} \sum_{\vec{G}} \alpha_n(\vec{G},\vec{k})\ e^{i\vec{G}\cdot M\vec{r}} \quad ; \tag{B-13}$$

$$\phi_{n,\vec{k}}(M\vec{r}) = e^{iM\vec{k}\cdot\vec{r}} \sum_{\vec{G}} \alpha_n(M\vec{G},\vec{k})\ e^{i\vec{G}\cdot\vec{r}} \quad . \tag{B-14}$$

From this it follows that:

$$\alpha_n(\vec{G},M\vec{k}) = \alpha_n(M\vec{G},\vec{k}) \tag{B-15}$$

and we now have all the transformations equations needed to obtain the wave functions throughout the Brillouin zone.

In our calculations related to amorphous III-V compounds we have taken GaAs as a prototype and used the 2H-4 (2/2) structure as a simple typical example of a structure with like-atom bonds. In this case we have used the Chadi and Cohen[9] twelve point scheme (see Section II-2) to calculate $\rho_n(\vec{r})$. In addition, we have calculated $\rho_E(\vec{r})$ using the aforementioned transformations in order to obtain $\rho_{E_f,E_i}(\vec{r})$ which is defined by

$$\rho_{E_f,E_i}(\vec{r}) = \int_{E_i}^{E_f} \rho_E(\vec{r})\ dE \tag{B-16}$$

for various intervals $[E_i,E_f]$.

APPENDIX C. STRUCTURES AND STATISTICS

In this section we shall describe and discuss the structure and parameters of the crystals we have used throughout this work. These crystal structures include the 2H-4 (wurtzite), 4H-8 (hexagonal 4H), BC-8 (SiIII), ST-12 (GeIII) and SC-16 (BC-8 taken as a simple cubic lattice) structures. We shall also discuss what GaAs sub-structures we made and the criteria used in their selection for the work on the amorphous binary compounds.

1. 2H-4

The 2H-4 structure is a wurtzite-like 2H structure with four atoms in a primitive cell and is described completely by two lattice constants constants a and c and an internal parameter u. If we make $c/a = 1.633$ and $u = 0.375$ then we have an ideal wurtzite or 2H-4 structure and an ideal tetrahedral arrangement of atoms. For ZnS we took the ideal 2H-4 structure with $a = 3.811$Å and $c = 6.223$Å.

Si has been found experimentally to exist in a 2H-4 structure by Wentorf and Kasper[15] with a 2% increase in density as compared to Si FC-2. The lattice constants they obtained were $a = 3.80$Å and $c = 6.28$Å. In our calculations, we assume in addition an ideal $u = 0.375$. Ge on the other hand has not yet been found, to our knowledge, to exist in a hexagonal structure so that we assumed an ideal Ge 2H-4 with the same density and nearest neighbor distance (2.45Å) as that of Ge in the diamond structure.

For the work on the amorphous binary compounds we took Ga and As atoms and made an ideal 2H-4 structure with lattice constants a and c chosen in such a way as to make the bulk density of GaAs 2H-4 the same as that of GaAs in the zinc blende structure. This assured a nearest neighbor distance which was equal to that of GaAs in zinc blende. Out of the possible substructures that can be made with the 2H-4 structure we shall be interested only in two. These can be designated by (1,1/1,1) and (2/2). In the first case we have the wurtzite structure with zero like-atom bonds and in the second case we have a fraction of 1/4 like-atom bonds with the Ga-Ga and As-As bonds occupying the two vertical bond positions in the unit cell. The first structure can be used as a starting point for the study of disorder (U) while the second can be used to study the effects of like-atom bonds on structure contains the smallest fraction, other than zero, of like-atom bonds that can be made in the 2H-4 structure.

2. 4H-8

The 4H-8 structure is a 4H structure with eight atoms in a primitive cell. The lattice constants and internal parameter that describe it are the same as those of 2H-4 except that we now take the lattice constant $c_{4H-8} = 2c_{2H-4}$. Again we have an ideal tetrahedral arrangement of atoms except that we now have a bit more topological disorder in the z-direction. This is of interest in our study of amorphous binary compounds. In particular the 2H-8 structure presents two useful options. First the (1,1,1,1/1,1,1,1) substructure can be an aid in the study of disorder (U) since it contains some topological variations. Secondly, the (2,1,1/2,1,1) substructure contains only a fraction of 1/8 of like-atom bonds and thus contains the smallest fraction of like-atom bonds other than zero that can be obtained from any of the substructures of all the basic five structures we are studying. The (2,1,1/2,1,1) structure has Ga-Ga and As-As bonds occupying two of the four vertical bond positions in the unit cell.

3. BC-8

The BC-8 or Si III[1] structure is body centered cubic with eight atoms in the primitive cell and it is completely specified by a lattice constant a and an internal parameter x. Si and Ge have both been found to exist in the BC-8 structure after retrieving samples which had been under 120 kbars pressure.[15] The lattice constant for Si is a = 6.636Å and for Ge we have a = 6.92Å. The internal parameter x was taken to be x = 0.1. Each linked pair of Si (Ge) atoms has one bond length 2.30Å (2.40Å) and three bonds of length 2.40Å (2.50Å), with an average bond length approximately equal to 2.37Å (2.48Å). There are also two types of bond angles approximately equal to 118° and 100° for both Ge and Si. All the eight atoms in the primitive cell are of one type in that they exist in the same type of environment with the same relative arrangement of neighboring atoms. For Si (Ge) there is one next nearest neighbor at 3.45Å (3.60Å), six at 3.57Å (3.73Å), six at 3.87Å (4.04Å), etc.

To study the amorphous binary compounds we took GaAs BC-8 with a = 6.896Å and x = 0.1. From a topological point of view an interesting feature of the BC-8 structure is that although it only has even numbered rings of bonds we <u>cannot</u> create any substructures with a total of zero like-atom bonds. In the first group containing the smallest fraction

(1/4) of like-atom bonds there are six substructures and they are all of the type (2,2/2,2). The second group containing the next largest fraction (3/8) of like-atom bonds contains 32 substructures. This group can be divided further into two subgroups containing 24 and substructures respectively. The former contains four atoms with one like-atom nearest neighbor and four atoms with two like-atom nearest neighbors while the latter contains six atoms and two like-atom nearest neighbor and two atoms with zero like-atom nearest neighbors. We used stability considerations to choose one structure out of the first group of six and one structure out of the second group of 32 which is of the type (4/4). These two structures will be studied using the tighting binding model and we shall single out the (2,2/2,2) structure for an EPM calculation using stability again as a discerning factor.

4. SC-16

This structure can be obtained by just considering the BC-8 structure as a simple cubic lattice with a basis of 16 atoms and is very useful in studying disorder in binary compounds. All the BC-8 substructures can, therefore, be obtained from the SC-16 structure. The purpose and usefulness of the SC-16 structures is that it provides us with a substructure that has zero like-atom bonds along with short range disorder. It is, therefore, very useful in studying disorder (U). The substructure that we chose was necessarily of the type (1,1,1,1,1,1,1,1/1,1,1,1,1,1,1,1).

The atoms were then allowed to relax slightly to a state of lower energy by a random processes described in Appendix E. This resulted in a small increase in randomness in the bond lengths and angles. In particular we obtained bond lengths that were up to 3% smaller and 5% larger than the ideal bond lengths and bond angles that varied from 97° to 119°.

Unfortunately, there is no SC-16 substructure that can be found with a fraction of like-atom bonds which is smaller than 1/4 other than zero.

5. ST-12

The ST-12 or Ge III[1] structure is a simple tetragonal unit cell with 12 atoms as a basis. It is completely specified by two lattice constants a and c and four internal parameters x_1, x_2, x_3 and x_4.

Ge has been found to exist in the ST-12 structure whereas Si has not. For Ge (Si) we used a = 5.93Å (5.69Å) and c = 6.98Å (6.70Å). The Si lattice constants were chosen so that the c/a ratio is the same as that of Ge ST-12 and the fractional density change from Si FC-2 to Si ST-12 is the same as Ge FC-2 to Ge ST-12. For Ge and Si the internal parameters were taken to be $x_1 = 0.09$, $x_2 = 0.173$, $x_3 = 0.378$ and x_4 0.25. In this structure the bond lengths are all about the same length and approximately equal to 2.49Å (2.39Å) for Ge (Si). The bond angles, however, are quite dissimilar. They range from 20% less to 25% greater than the ideal tetrahedral angle (109° 28 in.). In this structure the Ge or Si atoms are positioned in two different types of environment. In the primitive cell there are four atoms of type (1) and eight atoms of type (2). The atoms of type (2) form long fourfold spiral chains along the z direction while atoms of type (1) form bonds between atoms in the different spirals. For Ge atoms of type (1) have two next nearest neighbors at 3.45Å, two at 3.64Å, two at 3.81Å, etc. Kasper and Richards[1] neglected to mention the presence of the first two pairs of next nearest neighbors. Atoms of type (2) for Ge ST-12 have one next nearest neighbor at 3.45Å, two at 3.56Å, one at 3.64Å, etc. Finally, the ST-12 structure is quite unusual because of the presence of fivefold rings of bonds.

For our work on amorphous binary compounds we took GaAs ST-12 with a = 5.91Å, c = 6.955Å with all the internal parameters the same as for Ge and Si. Since this structure contains odd-numbered rings of bonds there are necessarily no substructures with a total of zero like-atom bonds. The smallest fraction of like-atom bonds that can be found in these substructures is 1/3. The size of the group of substructures with a fraction of 1/3 like-atom bonds is 216. This can be broken into three subgroups containing the following statistics.

(1) Twenty-four substructure with four atoms having two like-atom nearest neighbors and eight atoms with one like-atom nearest neighbor.

(2) Forty-eight substructures with six atoms having two like-atom nearest neighbors, four atoms with one like-atom nearest neighbors.

(3) One hundred and forty-four substructures with five atoms having two like-atom nearest neighbors, six atoms with one like-atom nearest neighbor and one atom with zero like-atom nearest neighbors.

In the first subgroup the substructures are all of type (3,3/3,3) while in the second subgroup we can find substructures of types (5,1/5,1), (3,3/4I,1,1) and (4I,1,1/3,3). Finally, in the third subgroup we find four types of substructures (3,1/3,3), (3,3/5,1) (4,2/5,1) and (5,1/4,2). We have chosen one distinct substructure from each of these eight types. These will be studied using our tight binding model and we shall again single out one substructure (4,2/5,1) using stability considerations, whose atomic positions we shall relax. This structure will then be studied by the EPM.

Although the fraction 1/3 of like-atom bonds in these structures is rather large from a realistic point of view, nevertheless, the ST-12 structure provides us with a series of substructures which have atoms in a variety of topological configurations and this is useful for studying the effects of these configurations in a simple and realistic way.

APPENDIX D. EXTENSION OF THE WEAIRE TIGHT BINDING MODEL

In this section we extend the model discussed in Section II to include all the interactions between nearest neighbor atoms. This introduces three additional parameters as shown in Fig. 60a. In this figure the lobes (labeled 1 to 8) represent sp^3 like orbitals, four for each atom. The Hamiltonian matrix elements between these orbitals are represented by V_1, V_2, V_3, V_4 and V_5. The parameter V_1 represents the interaction between orbitals on the same atom. V_2 represents the interaction between orbitals on different atoms but along the same bond. These are the same parameters as those used by Weaire and Thorpe.[12] In addition we introduce V_3 which represents the interaction between an orbital along the bond and one of the other three orbitals on a nearest neighbor atom which do not lie along the same bond. V_1, V_2 and V_3 still do not give us any information about the dihedral angle so that we would still get a delta function of pure p-like bonding states at the top of the valence band. To remedy this we introduce V_4 and V_5 which bring in effects of dihedral angle explicitly and saturate the number of interactions between nearest neighbor atoms.

Using this complete model, the Hamiltonian matrix for the diamond structure can be written as

$$\mathcal{H}_r = \begin{pmatrix} \hat{V}_1 & \hat{X} \\ \hat{X}^* & \hat{V}_1 \end{pmatrix} \qquad \text{(D-1)}$$

where

$$\hat{V}_1 = \begin{pmatrix} 0 & V_1 & V_1 & V_1 \\ V_1 & 0 & V_1 & V_1 \\ V_1 & V_1 & 0 & V_1 \\ V_1 & V_1 & V_1 & 0 \end{pmatrix} \tag{D-2}$$

and

$$\hat{X}=\begin{pmatrix} V_2+V_5(\xi_1+\xi_2+\xi_3) & V_3(1+\xi_1)+V_4(\xi_2+\xi_3) & V_3(1+\xi_2)+V_4(\xi_1+\xi_3) & V_3(1+\xi_3)+V_4(\xi_2+\xi_1) \\ V_3(1+\xi_3)+V_4(\xi_1+\xi_2) & V_3(\xi_1+\xi_3)+V_4(1+\xi_2) & V_3(\xi_2+\xi_3)+V_4(1+\xi_1) & V_2\xi_3+V_5(1+\xi_1+\xi_2) \\ V_3(1+\xi_2)+V_4(\xi_1+\xi_3) & V_3(\xi_1+\xi_2)+V_4(1+\xi_3) & V_2\xi_2+V_5(1+\xi_1+\xi_3) & V_3(\xi_2+\xi_3)+V_4(1+\xi_2) \\ V_3(1+\xi_1)+V_4(\xi_2+\xi_3) & V_2\xi_1+V_5(1+\xi_2+\xi_3) & V_3(\xi_1+\xi_2)+V_4(1+\xi_3) & V_3(\xi_1+\xi_3)+V_4(1+\xi_2) \end{pmatrix}$$

where

$$\xi_1 = e^{ik_x a/2} e^{ik_y a/2} \qquad \xi_2 = e^{ik_y a/2} e^{ik_z a/2} \qquad \xi_3 = e^{ik_z a/2} e^{ik_x a/2} \quad . \tag{D-4}$$

The density of states for Ge obtained from this model is shown in Fig. 60b. The agreement with the EPM calculations is surprisingly good. This is especially true for the valence bands, whereas, the conduction bands should not be taken too seriously. The p-like states, however, are not yet completely correct since we have not been able to reproduce the dip between Σ_1^{min} and X_4 which would lie near -4 eV. This could be accomplished, however, by introducing explicit interactions with second nearest neighbors. Nevertheless, the model can be quite useful as it stands. The parameters we used in the above calculations are $V_1 = -2.0$ eV, $V_2 = -4.8$ eV, $V_3 = 0.2$ eV, $V_4 = -0.4$ eV and $V_5 = 0.6$ eV. These parameters can also be related to Slaters parameters for the interactions between nearest neighbor s and p basis functions.[47] If we change from a basis of sp^3 orbitals to s and p functions and if we let s, p_x, p_y, p_z and s', p'_x, p'_y, p'_z denote the new basis functions associated with nearest neighbor atoms respectively, then we obtain the following transformation equations

$$\left.\begin{aligned}
\Delta_{sp} &= 4V_1 \\
\Delta_{ss'} &= V_2 + 6V_3 + 6V_4 + 3V_5 \\
\Delta_{sp'_x} &= V_2 + 2V_3 - 2V_4 - V_5 \\
\Delta_{p_xp'_x} &= V_2 - 2V_3 + 2V_4 - V_5 \\
\Delta_{p_xp'_y} &= V_2 - 2V_3 - 2V_4 + 3V_5
\end{aligned}\right\} \qquad \text{(D-5)}$$

Here, Δ_{sp} represents the difference in energy between an s and p orbital and the rest of the Δ_{ab}'s represent Slater's interaction or overlap intergals[47] for the basis functions a and b. From (D-5) we notice that the p-like delta function will broaden out if $\Delta_{p_xp'_x} \neq \Delta_{p_xp'_y}$. This is equivalent to introducing a V_4 and/or a V_5 as we have already mentioned.

Since this model is in general not in such bad agreement with realistic Hamiltonians it might be interesting to do a calculation of the imaginary part of the dielectric function $\varepsilon_2(\omega)$. This is given

$$\varepsilon_2(\omega) = \frac{1}{3} \cdot \frac{e^2}{\pi m^2 \omega^2} \sum_{c,v} \int \delta(E_c(\vec{k}) - E_v(\vec{k}) - \omega) \, |\langle \vec{k}_c | \vec{p} | \vec{k}_v \rangle|^2 \, d^3\vec{k} \qquad \text{(D-6)}$$

where $|\vec{k}_c\rangle$ and $|\vec{k}_v\rangle$ represent Bloch states for the conduction and valence bands respectively. The only additional function that we would now need to evaluate is the matrix element $|\langle \vec{k}_c|\vec{p}|\vec{k}_v\rangle|^2$. This can be done in the following manner. It is much simpler to make a transformation to the matrix element $\langle \vec{k}_c|\vec{r}|\vec{k}_v\rangle$ which is given by:

$$\langle \vec{k}_c|\vec{p}|\vec{k}_v\rangle = \frac{E_c(\vec{k}) - E_v(\vec{k})}{i\hbar} \; m \, \langle \vec{k}_c|\vec{r}|\vec{k}_v\rangle \tag{D-7}$$

Let us now write k as a sum over tight binding Bloch sp^3 like orbitals $\chi_{\vec{k},\ell,m_\ell}(\vec{r})$ where

$$\chi_{\vec{k},\ell,m_\ell}(\vec{r}) = \frac{1}{\sqrt{N}} \sum_j e^{i\vec{k}\cdot\vec{R}_j} \, \phi(\vec{r} - \vec{R}_j - \vec{\tau}_\ell - \vec{\rho}_{m_\ell}) \tag{D-8}$$

where N is the number of primitive cells, ϕ is an sp^3-like orbital, $\vec{R}_j$ is a lattice vector, $\vec{\tau}_\ell$ is the position of the ℓ'th atom in the primitive cell, and $\vec{\rho}_{m_\ell}$ represents the center of mass of the m'th orbital on the ℓ'th atom. Using Eq. (D-8) $\langle \vec{k}_c|\vec{r}|k_v\rangle$ becomes

$$\langle \vec{k}_c|\vec{r}|\vec{k}_v\rangle = \frac{1}{N} \sum_m \sum_{m'} \sum_\ell \sum_{\ell'} \sum_{\vec{R}_j} \sum_{\vec{R}_{j'}} C^*_{\ell',m'} V_{\ell,m} \, e^{i\vec{k}\cdot(\vec{R}_j - \vec{R}_{j'})} \tag{D-9}$$

$$\int \vec{r}\phi^*(\vec{r} - \vec{R}_{j'} - \vec{\tau}_{\ell'} - \vec{\rho}_{m'}) \, \phi(\vec{r} - \vec{R}_j - \vec{\tau}_\ell - \vec{\rho}_m) \, d^3r$$

where $C_{\ell',m'}$ and $V_{\ell,m}$ represent the coefficients of Eq. (D-8) for a conduction and valence state respectively obtained by solving the secular equation with the Hamiltonian (Eq. (D-1)). Expression (D-9) is exact but can be simplified considerably if we assume that the strongest terms one those that contain $\langle s|\vec{r}|p\rangle$ where $|s\rangle$ and $|p\rangle$ are s and p-like functions on the <u>same</u> atom. This should not be a bad approximation and it implies that we should consider in Eq. (D-9) only terms where ϕ^* and ϕ are also on the same atom. If we do this then there are only two intergals in Eq. (D-9) that we need to consider. The first is of the type

$$\int r\phi^*(\vec{r} - \vec{\rho}_{m_\ell})\ \phi(\vec{r} - \vec{\rho}_{m_\ell})\ d^3r \equiv \rho_o \hat{n}_{m_\ell} \tag{D-10}$$

and the second is

$$\int \vec{r}\phi^*(\vec{r} - \vec{\rho}_{m_\ell})\ \phi(\vec{r} - \vec{\rho}_{m'_\ell})\ d^3r \equiv \rho_1\ \hat{n}_{m_\ell,m'_\ell} \tag{D-11}$$

In Eq. (D-10) ρ_o is just the distance between an atom and the center of mass position of one of its sp^3 orbitals. The unit vector $\hat{n}_{m_\ell}$ points along the m'th orbital of the ℓ'th atom. In Eq. (D-11) $\hat{n}_{m_\ell,m'_\ell}$ is a unit vector pointing along the bisector of the angle formed by the m'th and m''th orbital of the ℓ'th atom and ρ_1 represents the value of the integral. The parameter ρ_1, however, is not independent of ρ_o. This is shown by transforming back to a basis set with s and p functions. We obtain simply

$$\rho_o = \frac{\sqrt{3}}{2} \langle s|x|p_x\rangle \tag{D-12}$$

and

$$\rho_1 = \frac{1}{2} \langle s|x|p_x\rangle \tag{D-13}$$

thus

$$\rho_1 = \frac{1}{\sqrt{3}}\ \rho_o \tag{D-14}$$

Therefore, we have only one parameter ρ_o which can be taken physically to be about 1/3 of the nearest neighbor distance. Equation (D-9) now becomes

$$\langle \vec{k}_c | \vec{r} | \vec{k}_v \rangle = \sum_{\ell} \sum_{m} \vec{\tau}_{\ell,m} V_{\ell,m} \tag{D-15}$$

$$+ \rho_o \sum_{\ell} \sum_{m} \hat{n}_{m_\ell} C^*_{\ell,m} V_{\ell,m} + \frac{1}{\sqrt{3}} \rho_o \sum_{\ell} \sum_{m_\ell, m'_\ell} C^*_{\ell,m'} V_{\ell,m} \hat{n}_{m'_\ell, m_\ell}$$

where the prime on the summation in the third term signifies that $m_\ell \neq m'_\ell$. Expression (D-15) can more be used even if we include more interactions in our Hamiltonian since it is based on the assumption that the most important terms are of the type $\langle s | r | p \rangle$ where s and p refer to the same atom.

APPENDIX E. STABILITY AND RELAXATION

In the process of selecting and studying various distinct substructures from substructures with similar like-atom bond clustering configurations it was useful to use stability as a final criterion. To calculate the energy U of a particular configuration of atoms which has both ionic and covalent character we must have a short range contribution and a coulomb contribution. For the short range energy we take a repulsive term due to the interaction between the ionic cores and an attractive term to take account of the covalent bonding nature of the atoms. With a small extension of the work of Keating[48] and Martin[49] he can get the following approximate but simple expression for U when expressed relative to the cohesive energy of the zinc blende structure

$$U = \frac{1}{2}\sum_{s=1}^{n}\sum_{i=1}^{4} f_{s,i}\Delta r_{s,i} + \frac{3}{16}\sum_{s=1}^{n}\sum_{i=1}^{4}\alpha_{s,i}\frac{[\Delta(\vec{r}_{s,i}\cdot\vec{r}_{s,i})]^2}{(r^{o}_{s,i})^2}$$

$$+\frac{3}{8}\sum_{s=1}^{n}\sum_{\substack{i,j\\ j>i}}\beta_{s,i,j}\frac{[\Delta(\vec{r}_{s,i}\cdot\vec{r}_{s,j})]^2}{(r^{o}_{s,i}r^{o}_{s,j})} + \frac{1}{2}\sum_{s=1}^{n}\frac{(e^{*})^2}{\varepsilon r_{o}}\left(\alpha^{M}_{s} - \alpha^{M}_{ZB}\right) \qquad \text{(E-1)}$$

Here U is the energy per primitive cell. The sum over s is over atoms in the primitive cell, the sums over i and j are over the bonds i and j of a particular atom s, $f_{s,i}$ is a parameter describing the linear term of the repulsive ion core potential, $\alpha_{s,i}$ and $\beta_{s,i,j}$ are essentially bond stretching and bond bending force constants respectively, and $r^{o}_{s,i}$ is one of the three equilibrium nearest neighbor bond lengths (since we can have like and unlike atom bonds). For the coulomb part of the energy we assume rigid point ions with charges $\pm e^{*}$ which are the effective charges on the atoms which interact via a screened coulomb potential with the electronic dielectric constant ϵ, α_s^M is the Madelung constant of a particular atom s; α_{ZB}^M is the Madelung constant of the zinc blende structure and r_o is the equilibrium nearest neighbor distance for atoms in the zinc blende structure. For simplicity we take all the $\alpha_{s,i} = \alpha$ and all the $\beta_{s,k,j} = \beta$ and we also assume that the $f_{s,i} = f$. The condition that the zinc blende structure be in equilibrium requires $f = -\frac{1}{4}\alpha_{ZB}^M(e^*)^2/\epsilon r_o^2$ and we can take e^* to be the dynamic effective charge. Then we have from Martin[49] for GaAs in the zinc blende structure: $\alpha = 41.2\ 10^3$ dyn/cm, $\rho = 8.95\ 10^3$ dyn/cm, $r_o = 2.44$ A and $(e^*)^2/\epsilon = 0.441\ e^2$ which, along with the $r_{s,i}^o$ equal to twice Paulings covalent radii for Ga and As, are the values we assumed for the parameters used in Eq. (E-1) to study our various GaAs structures. We ignore the changes in effective charge when we have like-atom bonds.

Equation (E-1) works fairly well in comparing the differences in cohesive energy of various substructures of the same basic structure. In particular, the most important term in Eq. (E-1) for structures with like-atom bonds is the coulomb term. For example, the Madelung energy per primitive cell of the ST-12 substructures which have 33-1/3% like-atom bonds can vary by more than 10 eV. In addition, the largest Madelung energy of these ST-12 substructures is only 20% smaller than the Madelung energy of GaAs in the zinc blende structure. On the other hand, with our approximations the short range energy term will vary only by about 0.1 eV and if we take the $\beta_{s,i,j}$ and the $\alpha_{i,j}$ not all eaual respectively we would expect a variation by not more than 1 eV.

We selected one substructure to study with the tight binding model from each set of substructures with similar like-atom clustering configurations. The selection of one substructure out of a particular set was carried out in two simple steps. First, we found the particular atom A in the primitive cell with the least binding energy for each substructure in the set. Secondly, we picked the substructure with the largest binding energy for the atom A as our choice for that particular set.

We chose one substructure from each of the five basic structures to study with the EPM. The selection was carried out in a similar fashion as we just described above. In addition, we allowed the energies of these substructures to relax to a local minimum. The procedure was similar to that used by Henderson and Ortenburger[50] and consisted of moving each atom by a small random amount. If the energy was lowered the move was accepted, if not then it was rejected. This process was carried out about 2000 times until a local minimum in the cohesive energy was reached. The consequences of this relaxation were to lower slightly the energy of the substructure and to add a small randomness to the distribution of bond angles and bond lengths.

REFERENCES

1. J. S. Kasper and S. M. Richards, Acta Cryst. 17, 752 (1964).
2. M. L. Cohen and V. Heine, Solid State Physics, H. Ehrenreich, F. Seitz and D. Turnbull (Academic Press, Inc., New York, 1970), Vol. 24, p. 37.
3. T. K. Bergstresser and M. L. Cohen, Phys. Rev. 164, 1069 (1967).
4. P. Löwdin, J. Chem. Phys. 19, 1396 (1951).
5. J. P. Walter and M. L. Cohen, Phys. Rev. B4, 1877 (1971).
6. F. Herman and S. Skillman, Atomic Structure (Prentice-Hall, New Jersey, 1966).
7. A. Baldereschi, Bull. A. S. P. 17, 273 (1972).
8. D. J. Chadi and M. L. Cohen, Phys. Rev. B7, 692 (1973).
9. D. J. Chadi and M. L. Cohen, Phys. Rev. B8, 5747 (1973).
10. T. M. Donovan and W. E. Spicer, Phys. Rev. Lett. 21, 1572 (1968); D. T. Pierce and W. E. Spicer, Phys. Rev. 85, 3017 (1972).
11. L. Ley, S. Kowalczyk, R. Pollak and D. A. Shirley, Phys. Rev. Lett. 29, 1088 (1972).
12. D. Weaire and M. F. Thorpe, Phys. Rev. B4, 2508 (1971).
13. T. C. McGill and J. Klima, Phys. Rev. B5, 1517 (1972).
14. M. L. Rudee and A. Howei, Phil. Mag. 25, 1001 (1972).
15. C. H. Bates, F. Dachille and R. Roy, Science 147, 869 (1965); R. H. Wentorj and J. S. Kasper, Science 139, 338 (1963).
16. G. Gilat and L. J. Rubenheimes, Phys. Rev. 144, 390 (1966).
17. A. W. Luehrmann, Thesis, University of Chicago, 1967.
18. J. L. Birman, Phys. Rev. 115, 1493 (1959).

19. D. Weaire and M. F. Thorpe, Computational Methods for Large Molecules and Localized States in Solids, F. Herman, A. D. McLean and R. K. Nesket, eds. (Plenum Press, N. Y., 1972).

20. W. E. Spicer and T. M. Donovan, Phys. Letters 36A, 459 (1971).

21. M. F. Thorpe and D. Weaire, Phys. Rev. Letters 27, 1581 (1971).

22. G. Wiech and E. Zöpf in the Proceedings of the International Conference on Band Structure Spectroscopy of Metals and Alloys, Glasgow, September 1971 (to be published).

23. J. Zak, A. Casher, M. Glück and Y. Gur, The Irreducible Representation of Space Groups, J. Zak and W. A. Benjamin, eds.

24. F. Herman and J. P. VanDyke, Phys. Rev. Lett. 21, 1575 (1968).

25. D. Brust, Phys. Rev. Lett. 23, 1232 (1969).

26. K. Maschke and P. Thomas, Phys. Stat. Sol. 39, 453 (1970).

27. B. Kramer, Phys. Stat. Sol. 41, 649 (1970).

28. K. Maschke and P. Thomas, Phys. Stat. Sol. 41, 743 (1970).

29. B. Kramer, Phys. Stat. Sol. 47, 501 (1971).

30. D. E. Sayers, E. A. Stern and F. W. Lytle, Phys. Rev. Lett. 27, 1204 (1971).

31. M. L. Cohen and T. K. Bergstresser, Phys. Rev. 141, 789 (1966).

32. J. Stuke, J. Non-Cryst. Solids 4, 1 (1970).

33. A. similar expression has also been used by Maschke and Thomas (Ref. 28).

34. J. P. Walter and M. L. Cohen, Phys. Rev. 183, 763 (1969).

35. N. J. Shevchik and W. Paul, J. Non-Cryst. Solids 13, 1 (1973).

36. J. D. Joannopoulos and M. L. Cohen, Solid Stat Comm. (to be published).

37. G. A. N. Connell, Phys. Stat. Sol. (b) **53**, 213 (1972); G. A. N. Connell and W. Paul, J. Non-Cryst. Solids **8-10**, 215 (1972).

38. This essentially has the effect of excluding rings of like-atom bonds since the smallest ring possible would most likely be five-fold.

39. J. Stuke and G. Simmerer, Phys. Stat. Sol. (b) **49**,

40. J. Stuke, in *The Physics of Se and Te*, W. C. Cooper, ed. (Pergamon Press, Oxford, 1969), p. 3.

41. N. J. Shevchik, J. Tejeda, M. Cardona and D. W. Langer, Solid State Comm. **12**, 1285 (1973).

42. J. D. Joannopoulos, M. Schlüter, M. L. Cohen, L. Ley, S. Kowalczyk, R. McFeeley and D. A. Shirley, to be published.

43. S. Tutihasi, I. Chen, Phys. Rev. 158, 623 (1967); I. Chen, Phys. Rev. **B7**, 3672 (1973).

44. R. Sandrock, Phys. Rev. **169**, 642 (1968).

45. B. Kramer, K. Maschke and L. D. Lande, Phys. Rev. **B8**, 5781 (1973).

46. M. Schluter, J. D. Joannopoulos and M. L. Cohen, to be published.

47. J. C. Slater and G. F. Koster, Phys. Rev. **94**, 1498 (1954).

48. P. N. Keating, Phys. Rev. **145**, 637 (1966).

49. R. M. Martin, Phys. Rev. **B1**, 4005 (1970).

50. D. Henderson and I. B. Ortenburger, J. Phys. Chem. **6**, 631 (1973).

Table I. Reciprocal lattice vectors, their magnitudes and form factors for Ge in the 2H-4, BC-8, and ST-12 structures. The reciprocal lattice vectors are expressed with respect to the primitive translation vectors for each structure and the magnitudes of these vectors are in units of $(2\pi/a_0)^2$ where a_0 is the lattice constant for Ge in the FC-2 structure. The form factors are in Ry and should be multiplied by a factor equal to the ratio of bulk densities of the particular Ge structure to the Ge FC-2 structure. Some of the form factors of Ge 2H-4 are omitted since the structure factors are zero for these $\underset{\sim}{G}$'s

Ge 2H-4			Ge BC-8			Ge ST-12					
$\vec{G}$	G^2	V_f	$\vec{G}$	G^2	V_f	$\vec{G}$	G^2	V_f	G	G^2	V_f
(001)	0.750		(100)	1.338	-0.380	(001)	0.658	-0.470	(310)	9.110	0.040
(100)	2.667	-0.255	(11-1)	2.676	-0.255	(100)	0.911	-0.435	(203)	9.562	0.048
(002)	3.000	-0.230	(110)	4.014	-0.165	(101)	1.569	-0.350	(311)	9.768	0.050
(101)	3.417	-0.200	(200)	5.352	-0.093	(110)	1.822	-0.325	(222)	9.918	0.053
(102)	5.667	-0.075	(21-1)	6.690	-0.035	(111)	2.480	-0.270	(213)	10.473	0.060
(003)	6.750		(111)	8.028	-0.010	(002)	2.630	-0.258	(004)	10.521	0.060
(110)	8.000	0.010	(210)	9.366	0.045	(102)	3.541	-0.193	(302)	10.829	0.060
(111)	8.750		(22-2)	10.704	0.060	(200)	3.644	-0.188	(104)	11.432	0.060
(103)	9.417	0.045	(300)	12.042	0.053	(201)	4.302	-0.148	(312)	11.740	0.055
(200)	10.667	0.060	(31-1)	13.380	0.038	(112)	4.522	-0.140	(320)	11.843	0.055
(112)	11.000	0.060	(211)	14.718	0.018	(210)	4.555	-0.135	(114)	12.343	0.050
(201)	11.417	0.060				(211)	5.213	-0.098	(321)	12.501	0.048
(004)	12.000					(003)	5.918	-0.065	(223)	13.206	0.040
(202)	13.667	0.035				(202)	6.274	-0.050	(303)	14.117	0.025
(104)	14.667					(103)	6.829	-0.030	(204)	14.165	0.025
(113)	14.750					(212)	7.185	-0.018	(322)	14.473	0.023
						(220)	7.288	-0.013	(400)	14.576	0.020
						(113)	7.740	0.003	(313)	15.028	0.013
						(221)	7.946	0.010	(214)	15.076	0.013
						(300)	8.199	0.018	(401)	15.234	0.010
						(301)	8.857	0.035	(410)	15.487	0.008

Table II. Reciprocal lattice vectors, their magnitudes and form factors for Si in the 2H-4, BC-4 and ST-12 structures. The convention is the same as Table I.

Si 2H-4			Si BC-8			Si ST-12					
G	G^2	V_f	G	G^2	V_f	G	G^2	V_f	G	G^2	V_f
(001)	0.748	-0.510	(100)	1.339	-0.420	(001)	0.658	-0.520	(310)	9.110	0.068
(100)	2.723	-0.245	(11-1)	2.678	-0.250	(100)	0.911	-0.480	(203)	9.562	0.073
(002)	2.991	-0.210	(110)	4.017	-0.120	(101)	1.569	-0.380	(311)	9.768	0.075
(101)	3.470	-0.165	(200)	5.356	-0.050	(110)	1.822	-0.350	(222)	9.918	0.078
(102)	5.713	-0.035	(21-1)	6.696	-0.001	(111)	2.480	-0.270	(213)	10.473	0.080
(003)	6.729	0.001	(111)	8.035	0.041	(002)	2.630	-0.255	(004)	10.521	0.080
(110)	8.168	0.045	(210)	9.374	0.070	(102)	3.541	-0.160	(302)	10.829	0.080
(111)	8.915	0.063	(22-2)	10.713	0.080	(200)	3.644	-0.153	(104)	11.432	0.080
(103)	9.451	0.073	(300)	12.052	0.078	(201)	4.302	-0.105	(312)	11.740	0.078
(200)	10.890	0.080	(31-1)	13.391	0.065	(112)	4.522	-0.093	(320)	11.843	0.078
(112)	11.158	0.080	(211)	14.730	0.040	(210)	4.555	-0.090	(114)	12.343	0.075
(201)	11.638	0.079				(211)	5.213	-0.058	(321)	12.501	0.075
(004)	11.962	0.078				(003)	5.918	-0.030	(223)	13.206	0.068
(202)	13.881	0.058				(202)	6.274	-0.015	(303)	14.117	0.055
(104)	14.684	0.040				(103)	6.829	0.005	(204)	14.165	0.054
(113)	14.896	0.035				(212)	7.185	0.015	(322)	14.473	0.047
						(220)	7.288	0.020	(400)	14.576	0.045
						(113)	7.740	0.033	(313)	15.028	0.030
						(221)	7.946	0.040	(214)	15.076	0.030
						(300)	8.199	0.045	(401)	15.234	0.025
						(301)	8.857	0.063	(410)	15.487	0.015

Table III. Theoretical ε_2 structure and identifications, including the location in the BZ, symmetry and energy of critical points for Ge and Si in the 2H-4 structure. Details are given in the text.

Ge 2H-4					Si 2H-4				
ε_2 Peaks (eV)	Bands	Location in Zone	Symmetry	Energy (eV)	ε_2 Peaks (eV)	Bands	Location in Zone	Symmetry	Energy
1.46 ⊥	7,8-10	$\Gamma_5-\Gamma_8$	M_0	1.46	2.60 ⊥	7-9	$\Sigma_1-\Sigma_1$(0.3,0,0)	M_0	2.60
1.77 ∥	6-10	$\Gamma_1-\Gamma_8$	M_0	1.77	2.60 ∥	7-9	$\Sigma_1-\Sigma_1$		2.60
2.25 ⊥	5-9	$\Gamma_6-\Gamma_{10}$	M_0	2.08	3.10 ∥	7-9	(0.25,0,0.25)	M_0	3.02
		$\Delta_6-\Delta_3$		2.23	3.35 ∥	7-9	U_2-U_2(0.5,0,0.35)	M_1	3.34
	6-9	$\Delta_3-\Delta_1$	M_1	2.26	3.35 ⊥	5-9	$\Gamma_6-\Gamma_{10}$	M_0	3.21
2.50 ∥	7-9	(0.25,0,0.25)	M_0	2.48			$\Delta_6-\Delta_3$		3.31
2.50 ⊥	8-10	$\Delta_5-\Delta_1$(0,0,0.3)	M_1	2.51		6-9	A_3-A_1	M_1	3.35
2.68 ⊥	8-9	U_4-U_2(0.5,0,0.35)	$\sim M_1$	2.68	3.60 ⊥	8-10	$\Delta_5-\Delta_1$(0,0,0.25)	M_1	3.59
2.75 ∥	7-9	U_2-U_2(0.5,0,0.4)	M_1	2.78	4.10 ⊥	6-9	M_7-M_1		4.08
3.15 ∥	7-10	(0.08,0.08,0.2)	M_0	3.03			$\Sigma_4-\Sigma_1$		4.09
	7-9	(0.11,0.11,0.2)	$\sim M_2$	3.14			U_3-U_1(0.5,0,0.25)	M_2	4.11
3.35 ⊥	6-9	(0.2,0,0.25)	M_1	3.35		7-9	R_2-R_1(0.15,0,0.5)	M_2	4.13
3.57 ∥	8-9	(0.2,0.2,0.35)	$\sim M_1$	3.57	4.25 ∥	8-9	(0.2,0.2,0.35)	$\sim M_1$	4.21
3.60 ⊥	6-9	M_7-M_1		3.61			H,S^1		4.26
		$\Sigma_4-\Sigma_1$		3.59	4.38 ⊥	8-10	(0.2,0,0.4)	M_2	4.38
		U_3-U_1(0.5,0,0.15)	$\sim M_2$	3.60			R_2-R_1(0.2,0,0.5)		4.30
	8-10	(0.2,0,0.4)	M_2	3.80	4.68 ∥	8-10	M,T^1	$\sim M_2$	4.64
		R_2-R_1(0.25,0,0.5)		3.60		8-9	(0.3,0.1,0)	M_1	4.68
3.72 ∥	8-9	(0.3,0.3,0.45)	M_1	3.72		7-11	(0.4,0,0.35)	M_0	4.61
4.52 ⊥	8-11	L_2-L_1, U_4-U_2	$\sim M_0$	4.40		7-9	T(0.2,0.2,0)	$\sim M_2$	4.74
	8-9	T(0.23,0.23,0)	$\sim M_0$	4.45	4.69 ⊥	8-9	T(0.2,0.2,0)	M_0	4.57
	7-11	(0.25,0,0.25)	$\sim M_1$	4.53		5,6-10	$\Delta_6-\Delta_5$(0,0,0.3)	$\sim M_1$	4.69
4.52 ∥	7-11	(0.25,0,0.25)	$\sim M_1$	4.53	4.89 ⊥	7-9	K	$\sim M_2$	4.87
	8-9	K,T^1	M_2	4.52		8-9	(0.3,0.25,0.25)	$\sim M_2$	4.89
4.70 ⊥	7-9	K,T^1	$\sim M_2$	4.67	4.91 ∥	7-10	Σ(0.2,0.08,0)	$\sim M_2$	4.91
	8-9	(0.4,0.15,0.15)	M_3	4.72		8-10	(0.2,0.1,0)	$\sim M_2$	4.93
	8-12	A_3-A_3, S_1-S_1(0.03,0.03,0.45)	$\sim M_2$	4.71	4.96 ⊥	8-11	Σ(0.35,0.05,0.05)	$\sim M_2$	4.96
4.70 ∥	8-11	M,T^1	M_0	4.67	5.50 ⊥	8-14	$\Gamma_5-\Gamma_{12}$	M_1	5.47
	7-9	K, P(0.33,0.33,0.15)	$\sim M_3$	4.90	5.55 ∥	8-12	M_5-M_4		5.61
5.23 ⊥	8-14	$\Gamma_5-\Gamma_{12}$	M_2	5.23			$\Sigma_3-\Sigma_4$		5.54
	8-11	(0.08,0.08,0.35)	M_3	5.30					
5.29 ∥	8-12	M_5-M_4		5.33					
		$\Sigma_3-\Sigma_4$		5.31					
	8-11	(0.3,0.1,0.15)		5.29					

Table IV. Theoretical ϵ_2 structure and identifications, including the location in the BZ, symmetry and energy of critical points for Ge and Si in the BC-8 structure. Details are given in the text.

Ge BC-8					Si BC-8				
ϵ_2 Peaks (eV)	Bands	Location in Zone	Symmetry	Energy (eV)	ϵ_2 Peaks (eV)	Bands	Location in Zone	Symmetry	Energy
2.03	16-17	$\Sigma_1-\Sigma_2(0.37,0.37,0)$	M_1	2.03	0.43	15,16-17	H_3-H_4	M_0	0.43
2.46	15-17	$\Sigma_2-\Sigma_2(0.4,0.4,0)$		2.46	1.70	16-17	$\Delta_1-\Delta_4(0.55,0,0)$	M_0	1.65
	13-17	$\Delta_4-\Delta_4(0.56,0,0)$	M_0	2.41	2.04	16-17	$(0.3,0.55,0)$	$\sim M_2$	2.04
2.70	13-17	$(0.2,0.8,0.15)$	M_0	2.67	2.60	16-18	$\Sigma_1-\Sigma_1(0.4,0.4,0)$	M_2	2.62
	14-18	$G_2-G_1(0.15,0.85,0)$	$\sim M_0$	2.65		15-17	$(0.3,0.5,0)$	M_0	2.54
3.21	16-19	$(0.25,0.35,0.25)$	M_0	3.19	3.00	13-17	$(0.2,0.7,0.15)$	M_0	2.96
	13-17	$G_1-G_2(0.4,0.6,0)$	M_2	3.24	3.45	13-17	$(0.1,0.5,0.1)$		3.46
		$(0.3,0.4,0.15)$		3.23		14-17	$(0.2,0.4,0.15)$	$\sim M_2$	3.45
	14-17	$(0.2,0.4,0.15)$	$\sim M_2$	3.21		16-19	$(0.3,0.4,0.2)$	M_1	3.43
	13-18	$(0.3,0.45,0)$	M_1	3.21		16-17	$\Gamma_1-\Gamma_6$	M_0	3.38
		$G_1-G_1(0.22,0.78,0)$		3.23	3.70	13-17	$G_1-G_2(0.45,0.55,0)$	M_2	3.70
3.76	15-19	$N,G_2-G_1(0.4,0.55,0)$	M_3	3.78		15-19	$D_1-D_1(0.5,0.5,0.15)$	M_1	3.68
	12-18	$G_2-G_1(0.35,0.65,0)$	M_1	3.76	4.05	16-21	$(0.2,0.6,0.15)$		4.05
	15-17, 18	$\Gamma_2-\Gamma_6$	M_3	3.74			$\Delta_1-\Delta_2(0.5,0,0)$	M_2	4.04
3.98	14-19	$(0.25,0.65,0.15)$		4.00		15-21	$(0.2,0.6,0.1)$	M_0	4.02
4.50	12-19	$(0.26,0.63,0.15)$		4.50		13-18	$G_1-G_1(0.2,0.8,0)$		4.02
	16-21	$(0.15,0.2,0.1)$	M_2	4.48		14-19	$(0.25,0.65,0.1)$	$\sim M_1$	4.07
	14-20	$(0.1,0.5,0.1)$		4.50	4.20	16-22	$(0.2,0.5,0)$	$\sim M_2$	4.20
	15-19	$\Delta_1-\Delta_4(0.25,0,0)$	M_0	4.42		12-18	$(0.15,0.7,0.15)$	M_2	4.22
						15-22	$(0.15,0.7,0)$	M_0	4.14
					5.05	14-21	$(0.2,0.6,0.1)$	M_2	5.05
						13-20	$D_1-D_1(0.5,0.5,0.1)$		5.00

Table V. Theoretical ϵ_2 structure, with perpendicular polarization, and identifications. including the location in the BZ, symmetry and energy of critical points for Ge ST-12. Details are given in the text.

Ge ST-12 $\vec{E} \perp \vec{c}$									
ϵ_2 Peaks (eV)	Bands	Location in Zone	Symmetry	Energy (eV)	ϵ_2 Peaks (eV)	Bands	Location in Zone	Symmetry	Energy
1.46	23,24-25	Σ_1-Σ_1(0.35,0.35,0)	M_0	1.46		20-25	S_1-S_1(0.06,0.06,0.5)	M_o	3.45
2.10	24-25	(0.4,0.1,0.3)	~M_0	2.08			S_1-S_1(0.45,0.45,0.5)	~M_1	3.45
	23-25	(0.4,0,0.3)	M_1	2.18		17-25	T^z(0.5,0.5,0.3)	~M_1	3.53
2.55	24-26	(0.5,0.1,0.3)	M_1	2.48		24-27	(0,0.1,0.25)	~M_2	3.47
		T_1-T_1(0.5,0.5,0.4)		2.52			T_1-T_1(0.5,0.3,0.5)		3.50
		U_1^z-U_1^z(0.5,0,0.3)		2.50		20-26	T_1-T_1(0.5,0.35,0.5)	M_2	3.47
	23-26	(0.4,0.15,0.25)		2.62		22-27	(0.3,0.1,0.3)	M_2	3.54
	22-25	(0.4,0,0.25)	~M_2	2.62			Δ_1-Δ_1(0.45,0,0)		3.50
		M		2.60	3.65	17-25	(0.5,0.25,0.3)	M_2	3.67
	21-25	(0.4,0.15,0.25)	M_1	2.60			Z_1-Z_2	M_0	3.65
	24-25	(0.1,0.1,0.4)	M_0	2.54		23-27	(0.1,0,0.25)		3.65
2.80	23,24-26	S_1-S_1(0.4,0.4,0.5)	M_2	2.87		24-29	U^x(0.22,0,0.5)	M_0	3.60
	21-25	(0.4,0.15,0.25)	M_1	2.60		24-30	R_1-R_1	M_1	3.60
		Δ_1-Δ_1(0.4,0,0)		2.80	4.20	24-30	U^x(0.3,0,0.4)		4.18
	24-25	U^x(0.2,0,0.4)	M_1	2.70			M		4.20
	24-27	(0.5,0.1,0.3)	M_1	2.76		21-27	(0.15,0.15,0.2)	M_2	4.22
		Γ_3-Γ_5	M_0	2.75		23-28	Δ_2-Δ_1(0.1,0,0.05)		4.20
3.00	20-25	(0.4,0.15,0.25)	M_0	2.93		21-28	U^x(0.15,0,0.4)		4.20
	22-25	Z_2-Z_2	M_0	2.98		20-25	Σ_2-Σ_1(0.07,0.07,0)	M_1	4.21
		T_1-T_1(0.25,0.5,0.3)		3.00		23-32	S_1-S_1(0.22,0.22,0.5)		4.20
	24-27	T^z(0.5,0.5,0.45)	M_1	3.11	4.50	23-31	U_1^z-U_1^z(0.5,0,0.2)	~M_3	4.57
	19-25	(0.35,0.18,0)		2.97		21-33	Σ_2-Σ_1(0.4,0.4,0)		4.48
		M_2^z-M_1^z	~M_2	3.00		22-30	U^y(0.5,0.1,0.05)	M_1	4.36
	22-27	(0.5,0.15,0.3)	M_0	3.04			(0.3,0.15,0.4)	M_1	4.52
3.20	24-27	Z_1-Z_1	M_0	3.18		20-26	(0.15,0,0.1)	M_3	4.54
		Z_1^x-Z_1^x	M_3	3.20		20-28	(0.15,0.15,0.25)	M_0	4.47
	21-25	U^x(0.2,0,0.5)	M_2	3.21		14-27	M_3^z-M_1^z	M_0	4.46
	23-28	R, T^z	~M_1	3.20		23-34	Σ_1-Σ_1(0.36,0.36,0)		4.48
	19-25	(0.5,0.15,0.3)	M_2	3.21		23-35	Σ_1-Σ_2(0.5,0.35,0)		4.48
		Δ_1-Δ_1(0.38,0,0)		3.20		21-29	Δ_3^z-Δ_1^z(0,0,0.22)		4.50
3.50	19-25,26	R_1-R_1	M_0	3.46		22-31	Δ_1^z-Δ_4^z(0,0,0.3)		4.50
	18-25	T_1-T_1(0.5,0.22,0.5)	~M_0	3.49		24-33	U_1^y-U_1^y(0.5,0.2,0)		4.52

Table VI. Theoretical ϵ_2 structure, with parallel polarization, and identifications including the location in the BZ, symmetry and energy of critical points for Ge ST-12. Details are given in the text.

Ge ST-12 $\vec{E} \parallel \vec{c}$									
ϵ_2 Peaks (eV)	Bands	Location in Zone	Symmetry	Energy (eV)	ϵ_2 Peaks (eV)	Bands	Location in Zone	Symmetry	Energy
1.60	24-25	$\Sigma_2-\Sigma_1(0.35,0.35,0)$	M_0	1.46			$U_1^z-U_1^z(0.5,0,0.2)$		3.71
		$\Delta_2-\Delta_1(0.4,0,0)$	$\sim M_1$	1.70	3.90	19-25	(0.2,0.15,0.3)	M_3	3.92
2.15	21-25	$\Sigma_2-\Sigma_1(0.37,0.37,0)$	M_0	2.07		24-29	$\Delta_2^z-\Delta_2^z(0,0,0.18)$	M_2	3.94
	24-25	(0.4,0.1,0.3)	$\sim M_0$	2.08		23-29	$\Delta_1-\Delta_2(0.37,0,0)$	$\sim M_2$	3.90
	23-25	(0.4,0,0.3)	M_1	2.18			$S_1-S_1(0.26,0.26,0.5)$		3.90
2.65	21-25	(0.4,0.15,0.25)	M_1	2.60		21-26	$\Delta_2-\Delta_1(0.15,0,0)$	$\sim M_1$	3.88
		$Z_1^x-Z_1^x$	$\sim M_2$	2.65	4.20	24-29	$\Gamma_3-\Gamma_4$	M_3	4.22
		$U_1^y-U_1^y$		2.63		20-25	$\Gamma_3-\Gamma_4$	M_0	4.16
	22-26	(0.5,0.2,0.25)	M_1	2.74			$\Sigma_2-\Sigma_1(0.07,0.07,0)$	M_1	4.21
	22-25	$M_3^z-M_1^z$	$\sim M_2$	2.70		21-28	$\Gamma_2-\Gamma_1$	M_0	4.22
	24-25	$\Gamma_3-\Gamma_4$	M_0	2.64			$\Delta_1^z-\Delta_1^z$		4.23
3.20	24-27	Z_1-Z_1	M_0	3.18			$U_x(0.15,0,0.4)$		4.20
		$Z_1^x-Z_1^x$	M_3	3.20			$S_1-S_1(0.25,0.25,0.5)$		4.20
		$\Delta_2-\Delta_1(0.45,0,0)$	$\sim M_2$	3.18		22-29	(0.15,0.15,0.2)	M_0	4.21
	21-25	$U^x(0.2,0,0.5)$	M_2	3.21			$Z_1^x-Z_1^x$	M_2	4.24
		(0.2,0.2,0.3)		3.20		24-30	(0.1,0.1,0.3)	M_1	4.26
	24-26	$S_1-S_1(0.26,0.26,0.5)$	M_3	3.26		22-30	(0.3,0.25,0.25)		4.21
	23-28	R_1-R_1		3.20	4.40	20-26	(0.17,0.17,0.1)	M_2	4.42
	24-28	$\Sigma_2-\Sigma_1(0.25,0.25,0)$	$\sim M_1$	3.20		18-27	Z_1-Z_1	M_0	4.36
3.50	20-25	Z_2-Z_2		3.48		23-28	$\Sigma_2-\Sigma_1(0.14,0.14,0)$		4.40
		$S_1-S_1(0.06,0.06,0.05)$	M_0	3.45		22-27	$\Sigma_1-\Sigma_2(0.14,0.14,0)$		4.37
	22-27	(0.3,0.1,0.3)	M_2	3.54			$\Delta_1-\Delta_2(0.25,0,0)$		4.40
		$\Gamma_5-\Gamma_5$	M_0	3.44		23-34	$M_2^z-M_1^z$	$\sim M_2$	4.40
	20-26	(0.3,0.1,0.3)		3.53			$\Sigma_1-\Sigma_2(0.35,0.35,0)$		4.40
	24-29	$\Sigma_2-\Sigma_1(0.35,0.35,0)$		3.45		16-26	Z_2-Z_2	$\sim M_1$	4.37
	24-26	$\Delta_1-\Delta_2(0.3,0,0)$		3.48			$\Delta_2^z-\Delta_3^z$		4.40
3.70	24-28	$\Delta_1-\Delta_2(0.26,0,0)$		3.70		23-30	(0.35,0.15,0.3)	M_3	4.42
		$S_1-S_1(0.2,0,0)$	$\sim M_2$	3.70			$\Delta_1-\Delta_2(0.37,0,0)$		4.40
	21-27	$Z_1^x-Z_1^x$	M_1	3.69		22-31	$U_1^y-U_1^y(0.5,0.3,0)$		4.40

Table VII. Theoretical ε_2 structure, with perpendicular polarization, and identifications, including the location in the BZ, symmetry and energy of critical points for Si ST-12. Details are given in the text.

Si ST-12 $\vec{E} \perp \vec{c}$									
ε_2 Peaks (eV)	Bands	Location in Zone	Symmetry	Energy (eV)	ε_2 Peaks (eV)	Bands	Location in Zone	Symmetry	Energy
1.76	24-25	(0.4,0.2,0)	M_0	1.76	3.60	20-25	Z,U^x(0.1,0,0.5)	M_0	3.60
2.33	23-25	(0.4,0,0.3)	M_0	2.31		21-26	(0.3,0.2,0.25)	$\sim M_1$	3.60
	24-25	(0.4,0,0.45)	M_1	2.33		22-27	Σ_2-Σ_1(0.3,0.3,0)	M_0	3.50
2.50	23, 24-26	M	$\sim M_1$	2.50		21-29	R_1-R_1	M_0	3.59
		T_1-T_1(0.5,0.15,0.5)	M_1	2.52		23-27	(0.1,0.1,0.25)	M_0	3.54
		U_1^z-U_1^z		2.51		23-28	(0.5,0.15,0.3)	M_1	3.58
		Z^x,U_1^y-U_1^y		2.45		22-26	Δ_2^z-Δ_4^z(0,0,0.3)		3.60
2.80	23, 24-26	S_1-S_1(0.4,0.4,0.5)		2.76		22-28	Σ_2-Σ_1(0.32,0.32,0)		3.60
		(0.4,0.4,0.4)	M_1	2.80	3.85	24-29	Z_1^x-Z_1^x	M_1	3.92
	21-25	(0.45,0.15,0.3)	M_0	2.73		23-28	Γ_5-Γ_1	M_0	3.71
		Δ_2-Δ_1(0.45,0,0)		2.80			Δ_4^z-Δ_1^z(0,0,0.24)	M_2	3.85
	21-25	U_1^y-U_1^y(0.5,0.2,0)	M_1	2.79		23-29	(0.35,0.15,0.25)		3.85
	22-26	(0.5,0.3,0.15)		2.82		17-25	U_1^z-U_1^z(0.5,0,0.33)		3.85
	23-28	Z_1-Z_1	M_0	2.78		22-27	(0.15,0.15,0.2)	$\sim M_1$	3.81
	22-25	(0.4,0,0.25)	M_2	2.74		21-29	Σ_1-Σ_2(0.42,0.42,0)	M_1	3.88
3.20	20-25	Δ_1-Δ_1(0.39,0,0)	M_0	3.17		20-26	(0.15,0.1,0.4)	$\sim M_1$	3.89
		Σ_1-Σ_1(0.37,0.37,0)	M_2	3.21		16-25	M_3^z-M_2^z	M_1	3.86
	19-25	Σ_2-Σ_2(0.4,0.4,0)	$\sim M_1$	3.18		23-30	(0.35,0.35,0.25)	$\sim M_1$	3.81
	22-25	Z_2-Z_2	M_0	3.18	4.45	20-26	(0.1,0,0.1)	$\sim M_2$	4.48
		(0.2,0.2,0.25)	M_1	3.16			Σ_1-Σ_1(0.12,0.12,0)		4.44
	20-26	U^y(0.5,0.35,0.05)	M_1	3.17		23-35	M_2^z-M_3^z		4.46
		Σ_1-Σ_1(0.4,0.4,0)		3.20		15-27	M_3^z-M_1^z	$\sim M_1$	4.45
	22-28	U_1^y-U_1^y(0.5,0.4,0)		3.20		15-26	Σ_2-Σ_1(0.44,0.44,0)		4.42
		R_1-R_1		3.20			U_1^z-U_1^z(0.5,0,0.34)		4.45
	21-26	T^z(0.5,0.5,0.4)	M_2	3.23		14-26	M_3^z-M_2^z		4.41
3.38	20-25	R,T^z(0.5,0.5,0.45)	M_1	3.39			T_1-T_1(0.5,0.28,0.5)		4.45
	19-25	R,T^z(0.48,0.48,0.4)	$\sim M_3$	3.45		21-27	(0.2,0,0.2)	$\sim M_1$	4.40
		Σ_1-Σ_1(0.35,0.35,0)		3.35			Δ_3^z-Δ_2^z(0,0,0.27)		4.45
	22-26	(0.25,0.25,0.3)	$\sim M_2$	3.36		22-33	Σ_2-Σ_1(0.44,0.44,0)		4.45
	18-25	(0.4,0.2,0)	M_0	3.35			Σ_1-Σ_1(0.4,0.4,0)		4.45
		U_1^y-U_1^y(0.5,0.38,0)		3.40		19-27	(0.35,0.15,0.3)	M_2	4.48
	24-27	(0.15,0,0.3)	M_1	3.38		21-28	Δ_3^z-Δ_1^z(0,0,0.24)		4.43
		U_1^z-U_1^z(0.5,0,0.15)		3.38		22-29	U_1^y-U_1^y(0.5,0.11,0)		4.41
	22-28	Z_2-Z_1	M_0	3.37		19-25	Σ_2-Σ_1(0.15,0.15,0)		4.45
		(0.45,0.4,0.3)	M_1	3.35		17-28	M		4.42

Table VIII. Theoretical ϵ_2 structure, with parallel polarization, and identifications, including the location in the BZ, symmetry and energy of critical points for Si ST-12. Details are given in the text.

Si ST-12 $\vec{E} \parallel \vec{c}$									
ϵ_2 Peaks (eV)	Bands	Location in Zone	Symmetry	Energy (eV)	ϵ_2 Peaks (eV)	Bands	Location in Zone	Symmetry	Energy
1.76	24-25	(0.4,0.2,0)	M_0	1.76	3.90	24-30	(0.5,0.22,0.25)	M_1	3.92
2.32	23-25	(0.4,0,0.3)	M_0	2.31		24-29, 30	$Z_1^z-Z_1^x$	M_0	3.93
	24-25	(0.4,0,0.45)	M_1	2.33			$U_1^y-U_1^y$		3.95
	24-26	$U_1^z-U_1^z$	M_0	2.46		24-29	$\Gamma_3-\Gamma_4$	M_2	3.98
	22-25	$\Sigma_2-\Sigma_1$	M_0	2.32		23-29	(0.2,0,0.3)	M_0	3.91
2.80	24-26	(0.1,0.1,0.4)	M_0	2.81		18-25	(0.3,0,0.4)		3.90
		(0.2,0.2,0.5)	M_0	2.79			$\Delta_2-\Delta_1$(0.35,0,0)		3.90
	21-25	(0.45,0.15,0.3)	M_0	2.73		21-26	$\Sigma_2-\Sigma_1$(0.16,0.16,0)	M_1	3.92
	21-25	$U_1^y-U_1^y$(0.5,0.2,0)	M_1	2.78		22-30	(0.35,0.35,0.1)	M_0	3.81
	22-26	(0.5,0.3,0.15)		2.82		23-28	$\Delta_2^z-\Delta_2^z$(0,0,0.22)		3.88
		M	M_0	2.65	4.26	20-25	$\Gamma_3-\Gamma_4$	M_0	4.07
	24-27	Z_1-Z_1	M_0	2.79		22-29	M	$\sim M_1$	4.28
	24-25	(0.3,0.05,0.4)	M_2	2.81		22-32	$M_3^z-M_3^z$		4.30
3.30	21-25	U^x(0.2,0,0.5)	M_2	3.33			$U_1^y-U_1^y$(0.5,0.3,0)		4.26
	23-27	(0.35,0.15,0.3)	M_1	3.31		20-28	(0.4,0.2,0.25)		4.30
	22-26	(0.25,0.25,0.3)	$\sim M_2$	3.36		18-27	Z_1-Z_1	M_1	4.25
	23-26	$\Gamma,\Delta_4^z-\Delta_4^z$		3.30		24-30	$U_1^z-U_1^z$(0.5,0,0.15)		4.26
	24-26	(0.12,0.12,0.25)	M_2	3.25			S_1-S_1(0.3,0.3,0.5)		4.27
	21-28	$\Sigma_2-\Sigma_1$(0.4,0.4,0)		3.30			$\Delta_1-\Delta_2$(0.36,0,0)		4.26
3.65	22-27	Z,S(0.15,0.1,0.45)	$\sim M_1$	3.64			(0.3,0.1,0.2)	M_3	4.41
		(0.2,0,0.4)	$\sim M_1$	3.69		19-25, 26	(0.25,0.25,0.3)		4.28
	21, 22-27	M,V^x(0.37,0.1,0.4)	$\sim M_0$	3.62	4.96	20-28, 29	(0.3,0,0.25)		4.95
	21-27	(0.3,0.3,0.25)	M_0	3.60		20-28	$U_1^z-U_1^z$(0.5,0,0.2)		4.96
	19-25	Z,S_1-S_1(0.1,0.1,0.5)	M_0	3.65		19-33	$\Sigma_2-\Sigma_1$(0.43,0.43,0)		4.94
	20-25	Z,U^x(0.1,0,0.5)	M_0	3.60		19-26	$\Delta_2-\Delta_1$(0.18,0,0)		4.95
		(0.2,0.1,0.3)	$\sim M_0$	3.62		21-29	S_1-S_1(0.3,0.3,0.5)		4.98
	24-28	S_1-S_1(0.25,0.25,0.3)		3.65			$U_1^z-U_1^z$(0.5,0,0.2)		4.96
		T_1-T_1	M_3	3.74		17-31	$\Sigma_2-\Sigma_1$(0.42,0.42,0)		4.97
	23-28	T(0.5,0.15,0.4)	M_1	3.60		23-33	$U_1^z-U_1^z$(0.5,0,0.25)		4.96
	24-27	$\Delta_1-\Delta_2$(0.35,0,0)		3.65		23-31	$\Sigma_2-\Sigma_1$(0.18,0.18,0)		4.94

Table IX. The number and type of p-like functions that can be made for a certain atom given the configuration of nearest neighbor atoms.

Number of unlike-atom nearest neighbors	Number of p-like functions of type III-V	Number of p-like functions of type III-III or V-V
4	3	0
3	2	0
2	1	1
1	0	2
0	0	3

FIGURE CAPTIONS

Fig. 1. (a) Wurtzite and (b) zinc blende crystal structures. The wurtzite structure is aligned with the c axis along the z direction and zinc blende is oriented with the (111) direction pointing along the z direction.

Fig. 2. Total charge density for ZnS in zinc blende structure, $(1\bar{1}0)$ plane.

Fig. 3. Crystalline pseudopotential for ZnS in zinc blende structure, $(1\bar{1}0)$ plane.

Fig. 4. ZnS wurtzite charge density-bands 1 and 3, (110) plane.

Fig. 5. ZnS wurtzite charge density-bands 4 and 5, (110) plane.

Fig. 6. ZnS wurtzite charge density-bands 6 and 7, (110) plane.

Fig. 7. ZnS wurtzite charge density-bands 8 and 9, (110) plane.

Fig. 8. ZnS wurtzite total charge density in plane I, (110) plane.

Fig. 9. ZnS wurtzite total charge density in plane II, (101) plane.

Fig. 10. ZnS wurtzite total charge density in plane III, (001) plane. Only the S atoms lie in this plane.

Fig. 11. ZnS wurtzite total charge density in plane IV, (100) plane. Only the S and Zn atoms in the center of the figure lie in this plane.

Fig. 12. Crystalline pseudopotential for ZnS in wurtzite structure in plane I, (110) plane.

Fig. 13. Brillouin zones and associated symmetry points and lines for the 2H-4, BC-8 and ST-12 structures.

Fig. 14. Band structure Ge in the 2H-4 or wurtzite structure.

Fig. 15. Band structure of Si in the 2H-4 or wurtzite structure.

Fig. 16. Band structure of Ge in the BC-8 or Si III structure.

Fig. 17. Band structure of Si in the BC-8 or Si III structure.

Fig. 18. Band structure of Ge in the ST-12 or Ge III structure.

Fig. 19. Band structure of Si in the ST-12 or Ge III structure.

Fig. 20. Density of states for the (a) BC-8 and (b) ST-12 structures calculated from the tight binding model used by Weaire. The BC-8 structure is shifted slightly to lower energies with respect to the ST-12 structure so as to agree better with Ge BC-8 (EPM). The dotted line in (b) represents the bottom of the condition band for the FC-2 structure using the Weaire model.

Fig. 21. Density of states of Ge in the (a) FC-2, (b) 2H-4, (c) BC-8 and (d) ST-12 structures using the Empirical Pseudopotential Method. The dotted line in (a) represents a sketch of the amorphous density of states obtained by Donovan et al. (Ref. 10). The dotted line in (d) represents the averaging of Bragg gaps for Ge ST-12 in this calculation.

Fig. 22. Density of states of Si in the (a) FC-2, (b) 2H-4, (c) BC-8 and (d) ST-12 structures using the Empirical Pseudopotential Method. The dotted line in (a) represents a sketch of the amorphous density of states obtained by Pierce and Spicer (Ref. 10). The dotted line in (d) represents the averaging of Bragg gaps for Si ST-12 in this calculation.

Fig. 23. Experimental XPS results which are related to the density of states for Ge and Si in the FC-2 and amorphous phases. Top, experimental curve (dots) for Si and Ge in the FC-2 structure along with a sharp theoretical and a broadened theoretical (EPM) calculation. Bottom, XPS results for Si and Ge in the amorphous phase compared with the calculated density of states for Si and Ge in the ST-12 structure (EPM) from this work. The relative sizes of the humps in the Si experimental curves differ from those in Ge because of the differences in scattering cross-sections of the 3x, 3p and 4s, 4p electrons.

Fig. 24. Density-of-state calculations for the diamond and one-class-ring structures. (a) One-orbital Hamiltonian in the diamond structure: Bethe lattice (dashed line), exact calculation from Ref. 19 (light full line) and our results (heavy full line). (b) Four-Orbital sp^3 Hamiltonian in the diamond structure: Bethe lattice (dashed line), exact calculation from Ref. 19 (light full line) and our results (heavy full line). (c) Structure with 6 n-fold rings around the central atom in the one-orbital Hamiltonian: 1 (full line) $n = 6$; 2 (dashed line) $n = 5$; 3 (dotted line) $n = 7$; 4 (broken line) $n = 8$. (d) Structure with 6 n-fold rings in the four orbital sp^3 Hamiltonian. Notation as in (c). (e) The orbital energies for isolated sixfold rings (full lines), fivefold rings (dashed lines), sevenfold rings (dotted lines) and eightfold rings (broken lines) and eightfold rings (broken lines).

Fig. 25. Density-of-state calculations for the BC-8 [(a) and (b)] and ST-12 [(c) through (f)] structures. (a) Our calculation for BC-8 with the one-orbital Hamiltonian. (b) Our calculation for BC-8 with the four-orbital sp^3 Hamiltonian (full line) and the exact calculation (dashed line). (c) The LDOS for the two different atoms in the one-orbital Hamiltonian for ST-12. (d) The LDOS for ST-12 and the four-orbital sp^3 Hamiltonian. (d) The TDOS for ST-12 in our calculation for the one-orbital Hamiltonian. (f) The TDOS (ST-12 structure, four-orbital sp^3 Hamiltonian) according to our calculation (full line) and to the exact results (dashed line).

Fig. 26. Band structure of Ge in the 2H-4 or wurtzite structure.

Fig. 27. Imaginary part of the dielectric function, ε_2, for Ge 2H-4 with parallel (top) and perpendicular (bottom) polarizations.

Fig. 28. Band structure of Si in the 2H-4 or wurtzite structure.

Fig. 29. Imaginary part of the dielectric function, ε_2, for Si 2H-4 with parallel (top) and perpendicular (bottom polarizations.

Fig. 30. Band structure of Ge in the BC-8 structure.

Fig. 31. Imaginary part of the dielectric function, ε_2, for Ge BC-8 (top) and Si BC-8 (bottom).

Fig. 32. Band structure of Si in the BC-8 structure.

Fig. 33. Band structure of Ge in the ST-12 structure.

Fig. 34. Imaginary part of the dielectric function, ε_2, for Ge ST-12 with parallel (top) and perpendicular (bottom) polarizations.

Fig. 35. Band structure of Si in the ST-12 structure.

Fig. 36. Imaginary part of the dielectric function, ε_2, for Si ST-12 with parallel (top) and perpendicular (bottom) polarizations.

Fig. 37. Imaginary part of the dielectric function, ε_2, average gradient matrix element M, associated joint density of states J/E^2, average dipole matrix element M/E^2, and joint density of states J for Ge in the FC-2, 2H-4, BC-8 and ST-12 structures. For each row the product for the two curves in the second and third columns gives the ε_2 spectrum in the first column. The ε_2 for the 2H-4 and ST-12 structures was obtained by averaging over parallel and perpendicular polarizations. The matrix element M is in units of $\left(\frac{2\pi}{a}\right)^2$ where a is the smallest lattice constant of each crystal and J in the figure is in units of $\left(\frac{a}{2\pi}\right)^2$ $(\mathrm{eV})^2$. The unnormalized J(E) defined in Eq. (23) can be obtained from the values of J in the figure by taking J to be in units of

$$\left(\frac{3\pi m^2}{e^2\hbar^4}\right)\left(\frac{a}{2\pi}\right)^2 \frac{1}{(\mathrm{cm})^3\ \mathrm{eV}} .$$

The amorphous ε_2 is from Donovan and Spicer (Ref. 10).

Fig. 38. Imaginary part of the dielectric function ε_2, associated average matrix element M, associated joint density of states J/E^2, average dipole matrix element M/E^2, and joint density of states J for Si in the FC-2, 2H-4, BC-8 and ST-12 structures. The convention is the same as in Fig. 37. The amorphous ε_2 is from Pierce and Spicer (Ref. 10).

Fig. 39. Density of states of GaAs in the (a) 2H-4, (b) 4H-8 and SC-16 structures using the EPM. The dashed line in (a) represents the consequences of disorder (U) as described in the text.

Fig. 40. Density of states of GaAs in the (a) 2H-4 (1,1/1,1), (b) 2H-4 (2/2), (c) BC-8 (2,2/2,2), (d) BC-8 (4/4), (e) ST-12 (3,3/3,3) and (f) ST-12 (5,1/5,1) structures calculated from the simple tight binding model discussed in the text. The solid line at 0.0 eV represents a delta function peak in the density of states. The bottom of the conduction band is designated by E_c and the numbers on top of the peaks represent the approximate strength of these peaks.

Fig. 41. Density of states of GaAs in the (a) ST-12 (5,1/3,3), (b) ST-12 (4,2/5,1) and (c) ST-12 (3,3/4I,1,1) structures using the simple tight binding model discussed in the text. The convention is the same as in Fig. 2.

Fig. 42. Density of states of GaAs in the (a) ST-12 (4,2/5,1), (b) BC-8 (2,2/2,2), (c) 2H-4 (2/2), and (d) 4H-8 (2,1,1/2,1,1) structures using the EPM. There is an overlap of the valence and conduction bands near 1 eV. Regions I, II and III represent the p-like region of the density of states where Region II is analogous to the delta function peak using the tight binding model. The small numbers on top of the densities of states represent the approximate strength of various regions and peaks in these densities of states.

Fig. 43. GaAs 2H-4 (2/2) charge density in the (110) plane for bands 1 and 2.

Fig. 44. GaAs 2H-4 (2/2) charge density in the (110) plane for bands 3 and 4.

Fig. 45. GaAs 2H-4 (2/2) charge density in the (110) plane for bands 5 and 6.

Fig. 46. GaAs 2H-4 (2/2) charge density in the (110) plane for bands 7 and 8.

Fig. 47. GaAs 2H-4 (2/2) charge density in the (110) plane for bands 9 and 10.

Fig. 48. GaAs 2H-4 (2/2) charge density in the (110) plane for the regions of the density of states in the energy intervals [-7.2 eV, -6.1 eV] and [-6.1 eV, -5.0 eV] designated by arrows in Fig. 42(c).

Fig. 49. GaAs 2H-4 (2/2) charge density in the (110) plane for the regions of the density of states in the energy intervals [-5.0 eV, -3.7 eV] and [-3.7 eV, -1.3 eV] designated by arrows in Fig. 42(c).

Fig. 50. GaAs 2H-4 (2/2) charge density in the (110) plane for the regions of the density of states in the energy intervals [-1.3 eV, 0.6 eV] and [0.6 eV, 2.2 eV] designed by arrows in Fig. 42(c).

Fig. 51. GaAs 2H-4 (2/2) total charge density in the (110) plane.

Fig. 52. Density of states of GaAs in the (a) modified 2H-4 (2/2) and (b) FC-2 structures using the EPM. The modified 2H-4 structure was obtained from the ideal 2H-4 structure by taking a 10%

decrease in Ga-Ga bonding distances and a 3% increase in the As-As bonding distances. This resulted in a merging of Regions II and III and the formation of a nonzero energy gap. The dashed curve in (b) represents the consequences of disorder (L) with 10% like-atom bonds as discussed in the text. The dotted line distinguished between the low and high energy s-like peaks.

Fig. 53. The electronic density of states of trigonal Se (a) and Te (b) as obtained from the EPM. The filled valence band is at negative energies.

Fig. 54. Calculated densities of states (solid lines) for trigonal Se (a) and Te (b), which have been broadened by 1.2 eV for the s-like states and by 0.7 eV for the remaining states. Superimposed are the experimental photoemission spectra (dashed lines).

Fig. 55. Electronic charge densities for trigonal Se in the energy intervals (a) [-6.0 eV, -3.6 eV] and (b) [-3.6 eV, -2.25 eV] and for trigonal Te in the intervals (c) [-6.0 eV, -3.5 eV] and (d) [-3.5 eV, -2.2 eV]. The units are e/Ω.

Fig. 56. Bonding charge of trigonal Se for the (a) lower and (b) upper p-like bonding states, calculated as described in the text. Only positive contours are shown, with values in units of e/Ω.

Fig. 57. Bonding charge of trigonal Te for the (a) lower and (b) upper p-like bonding states, calculated as described in the text. Only positive contours are shown, with values in units of e/Ω.

Fig. 58. Sketch of the density of states of a simple cubic lattice (solid line) and an infinite one-dimensional chain (dashed line) for s-like states with only nearest neighbor interactions. The widths of the bands were chosen arbitrarily to be the same.

Fig. 59. Experimental photoemission measurements for trigonal (solid line) and amorphous (dashed line) Se (Ref. 42) and Te (Ref. 41).

Fig. 60. (a) Schematic representation of the interactions V between sp^3-like orbitals on two neighboring atoms. The orbitals are labeled 1 to 8. We show only one representative pair of orbitals for each interaction. (b) The density of states for Ge obtained using the above model and described the text.

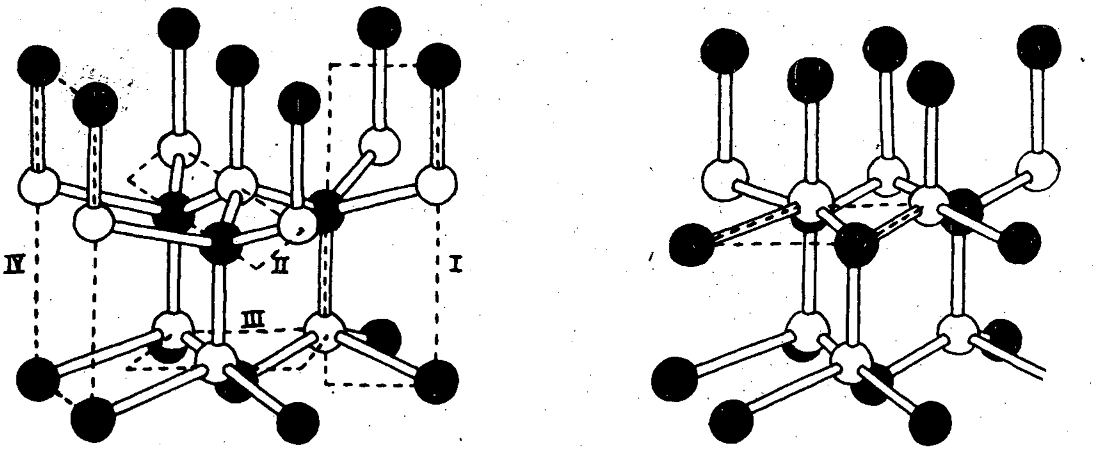

(a) WURZITE

(b) ZINC BLENDE

XBL 744-6069

Fig. 1

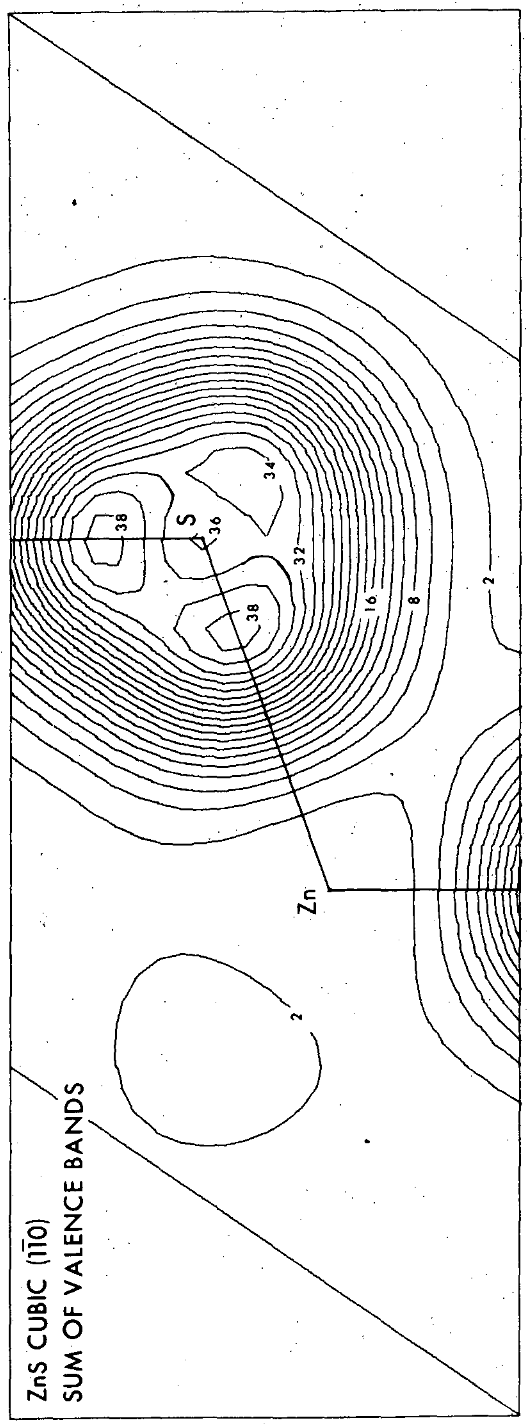

XBL 744-6051

Fig. 2

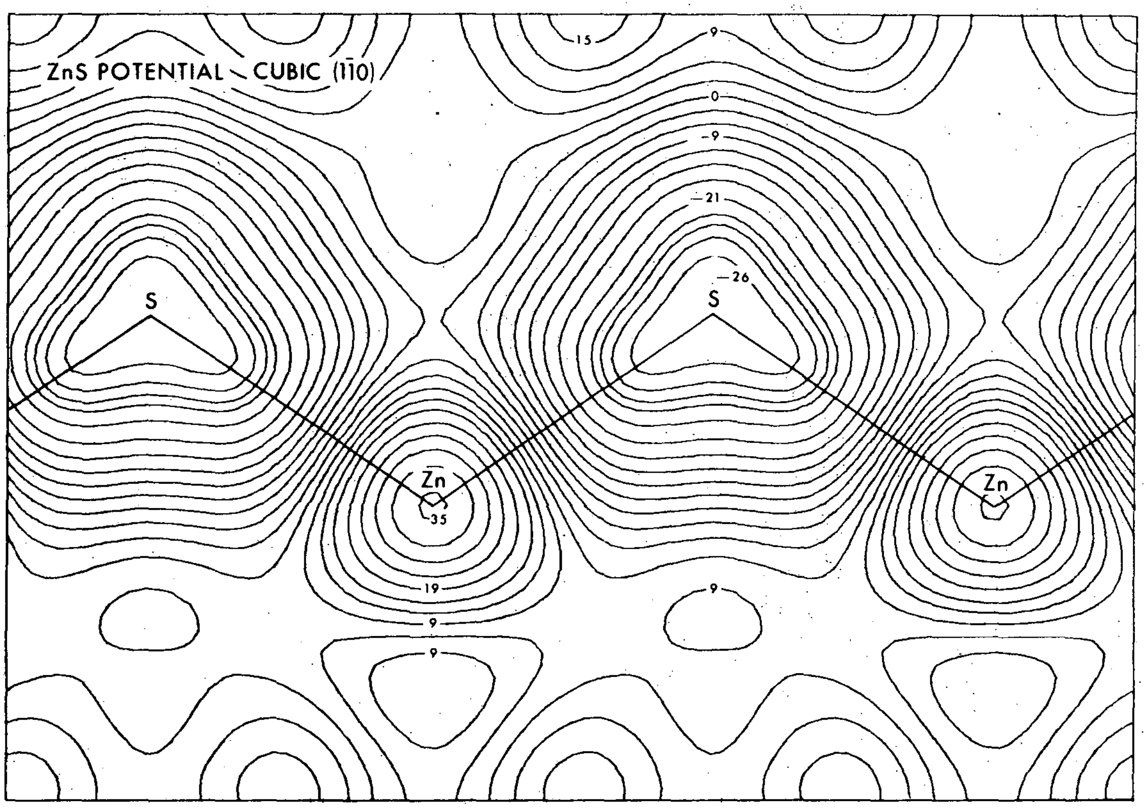

XBL 744-6045

Fig. 3

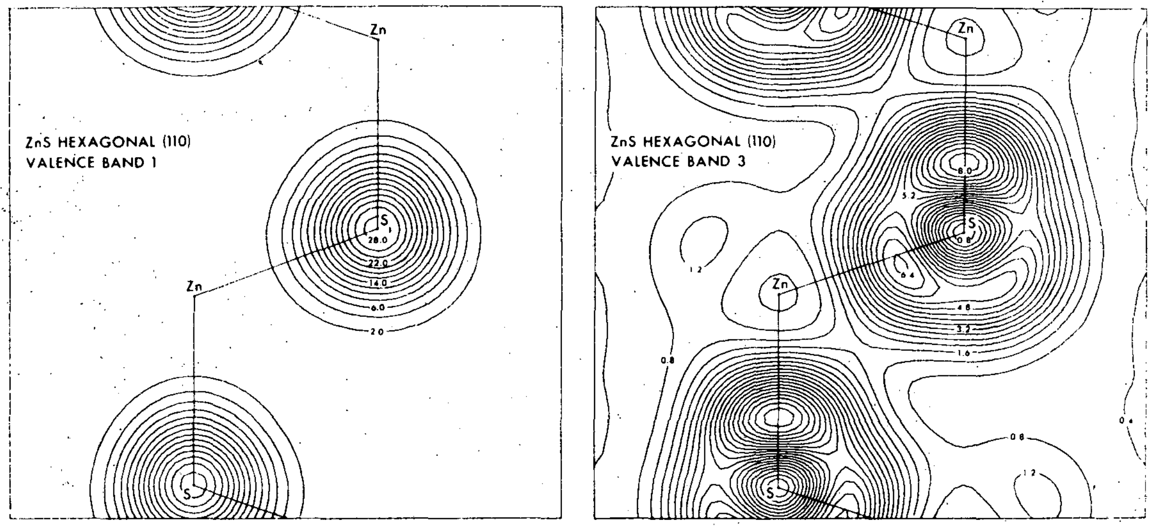

XBL 744-6081

Fig. 4

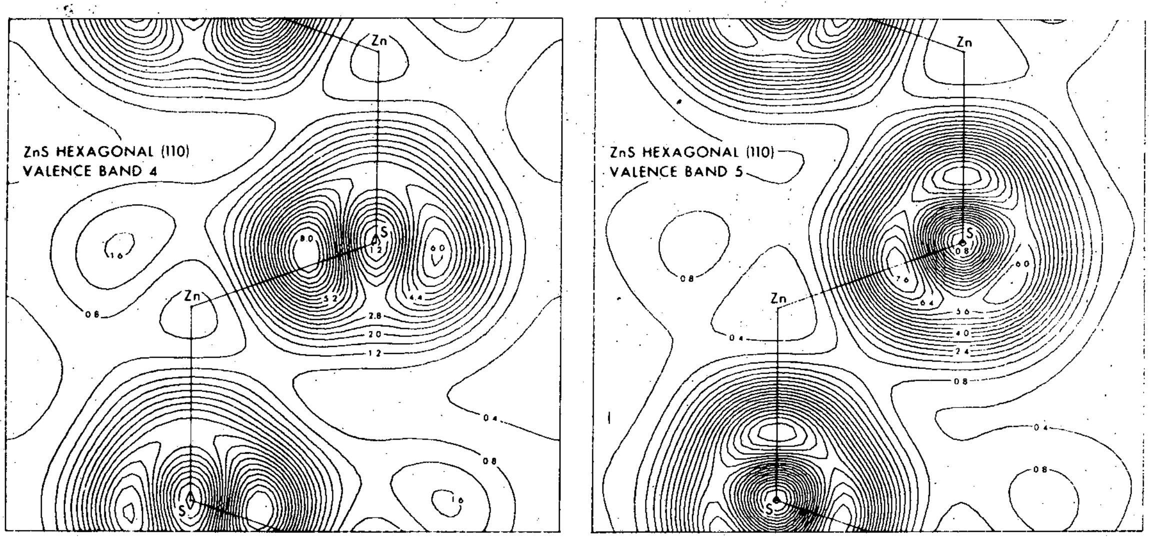

XBL 744-6074

Fig. 5

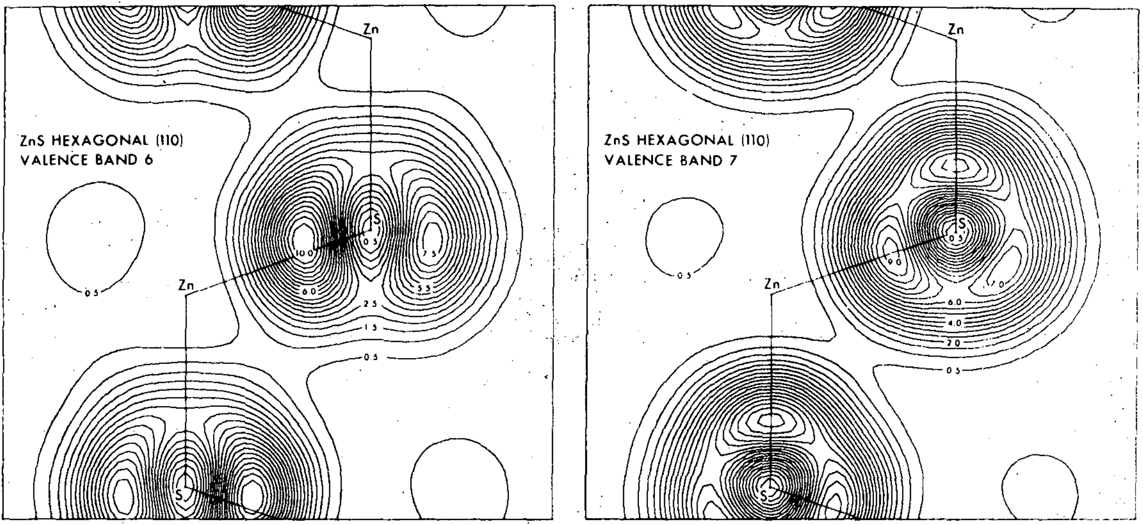

XBL 744-6054

Fig. 6

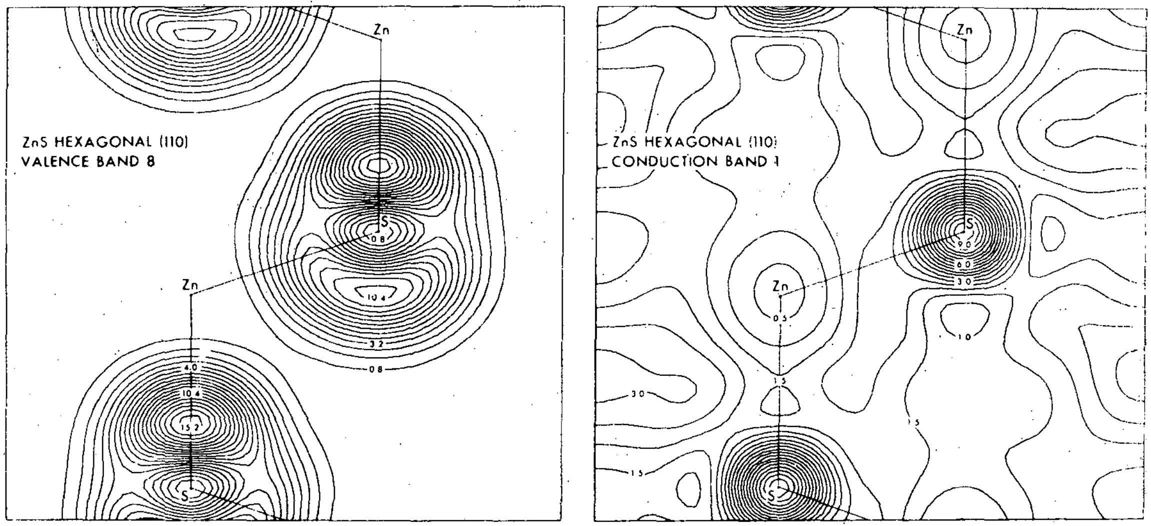

XBL 744-6094

Fig. 7

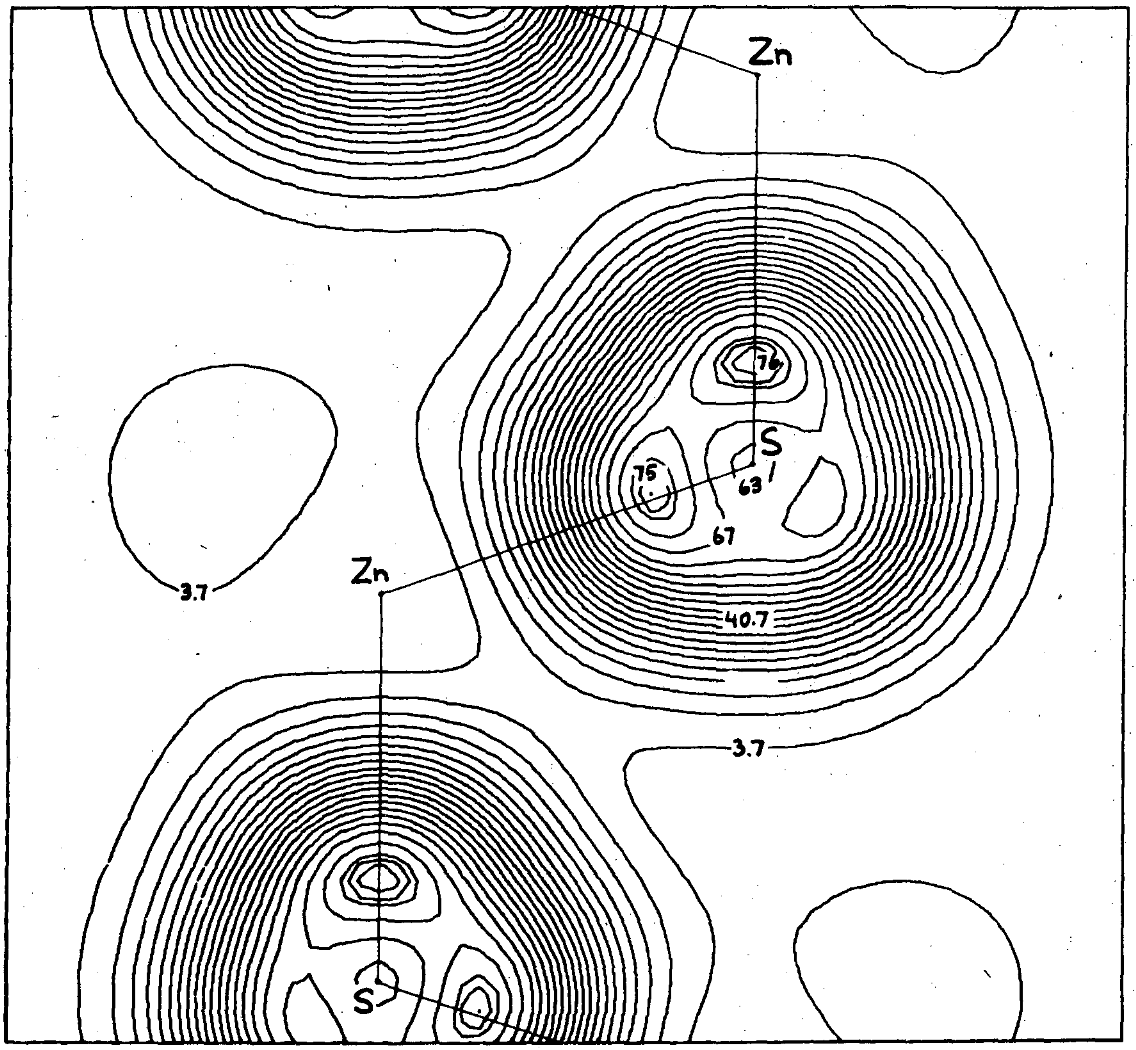

XBL 744-6059

Fig. 8

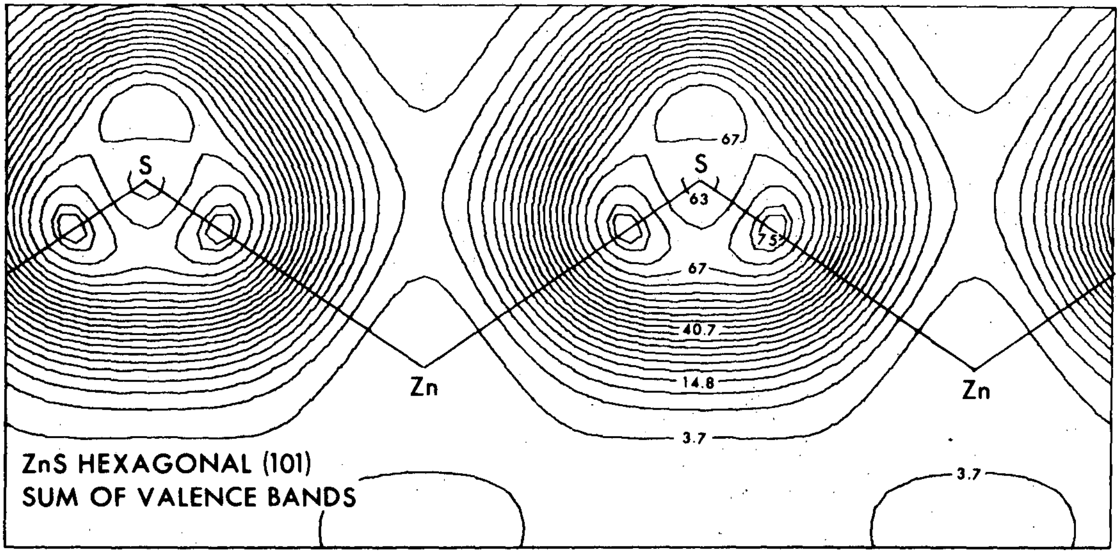

XBL 744-6076

Fig. 9

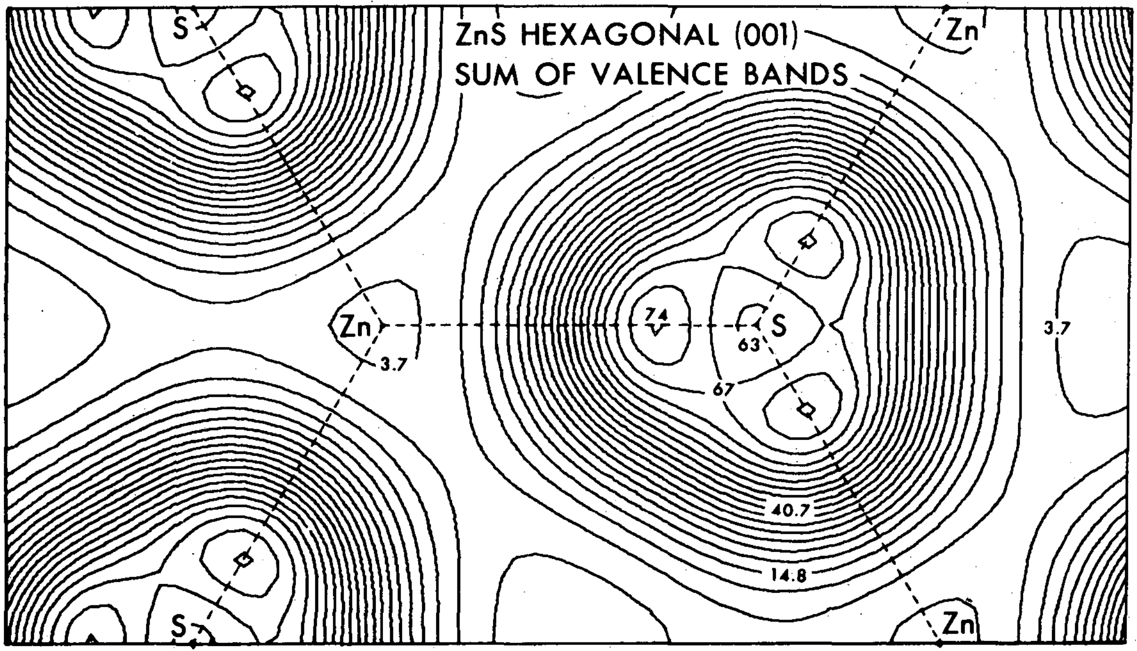

XBL 744-6057

Fig. 10

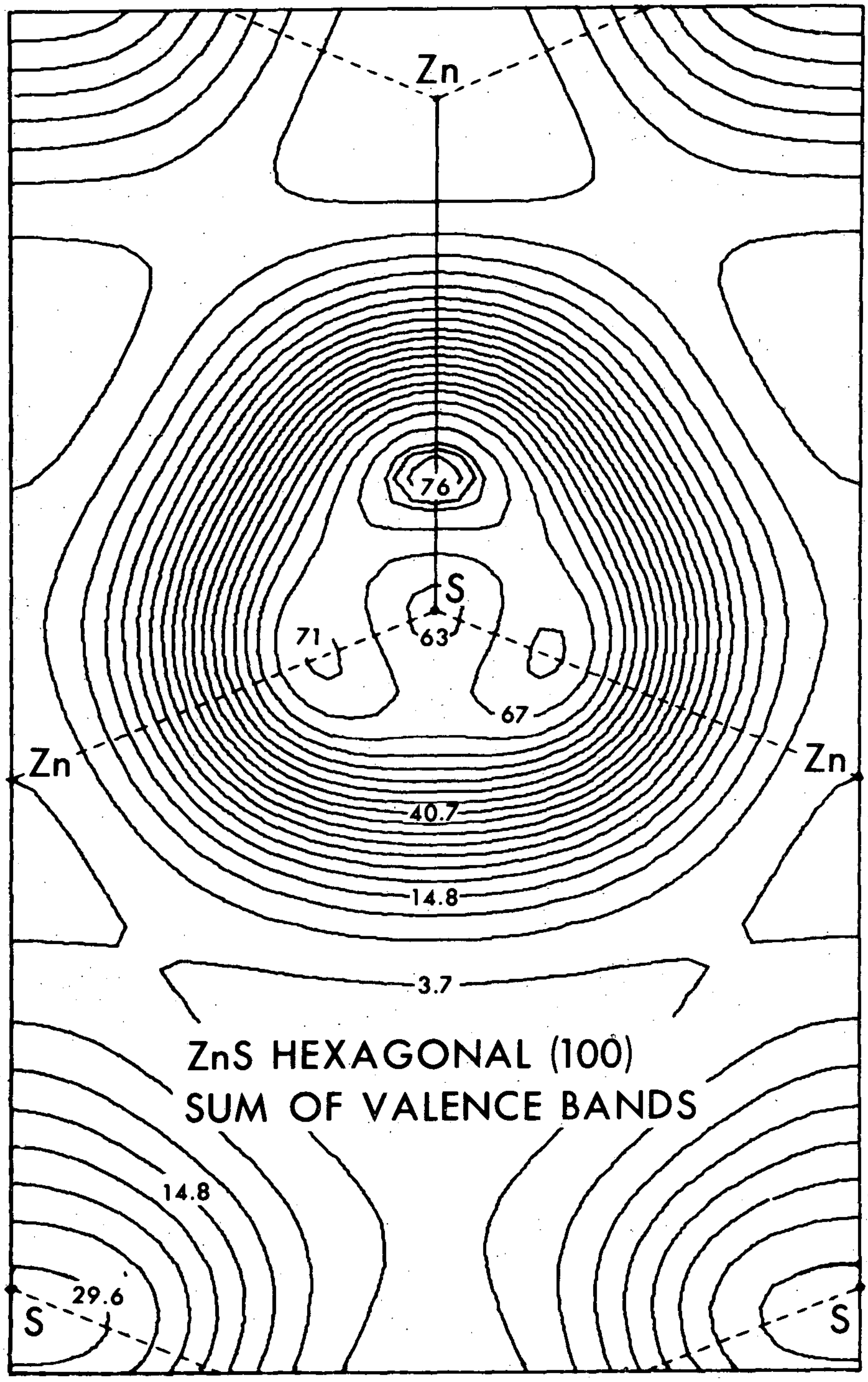

XBL 744-6084

Fig. 11

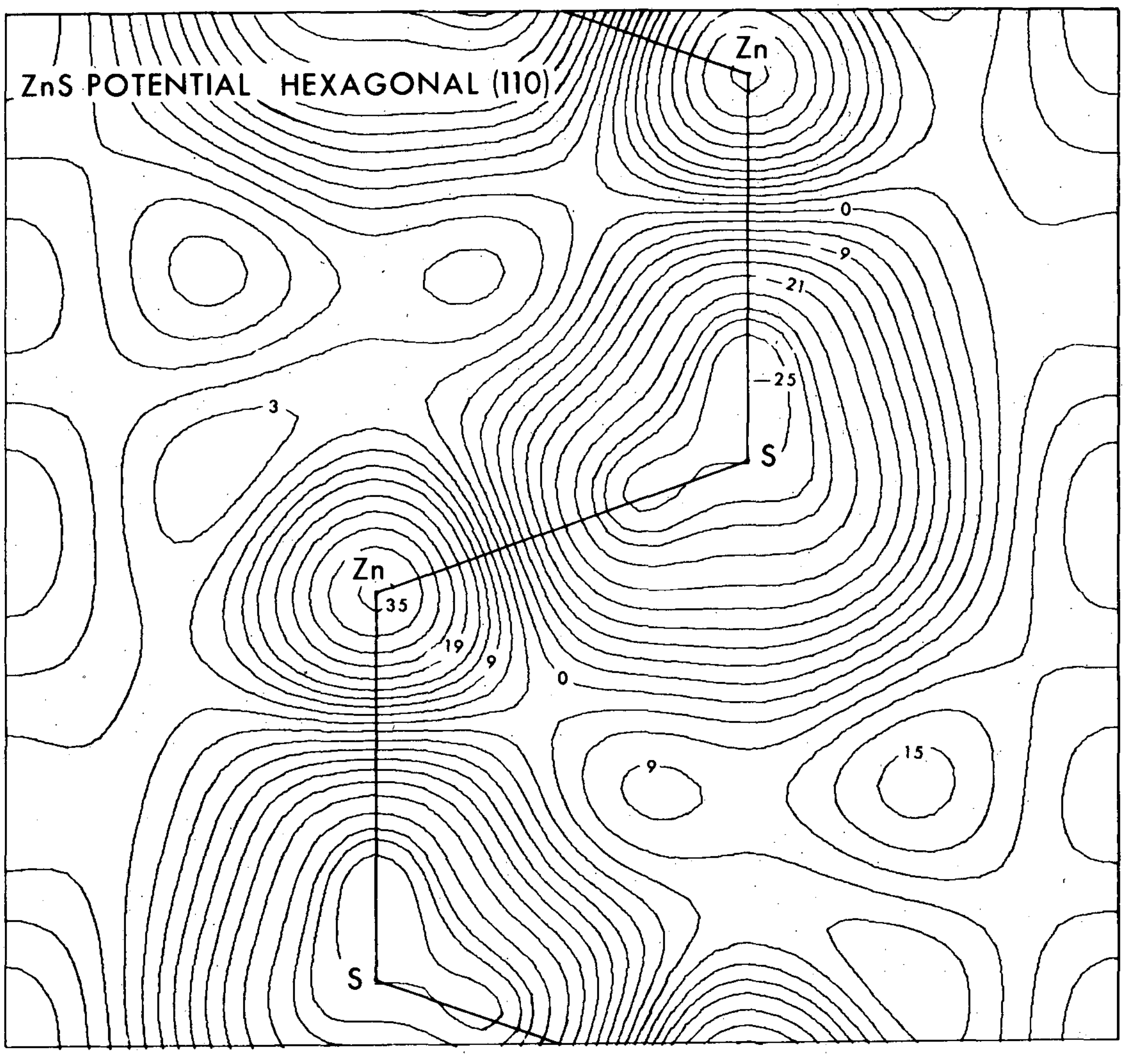

XBL 744-6049

Fig. 12

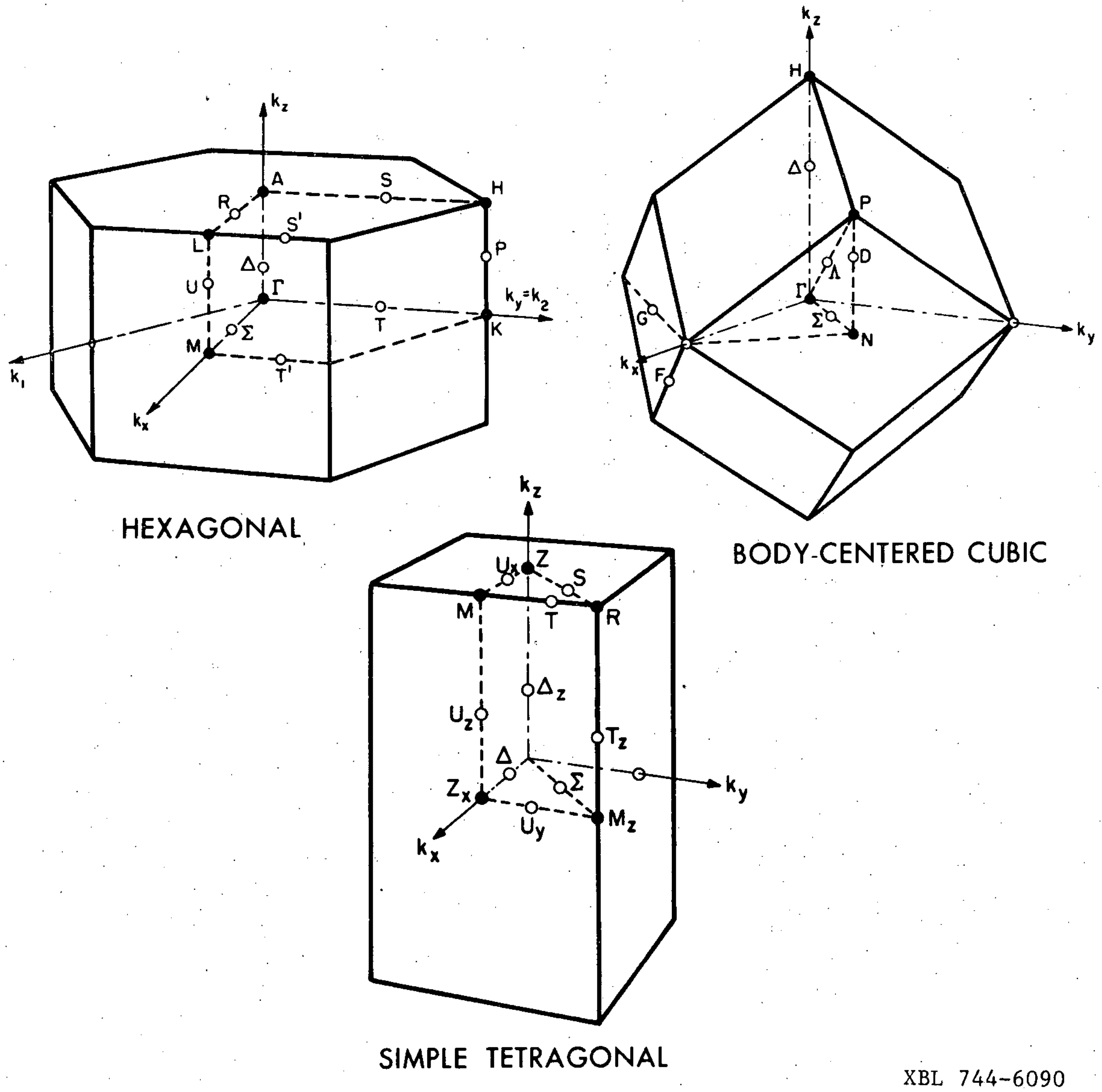

XBL 744-6090

Fig. 13

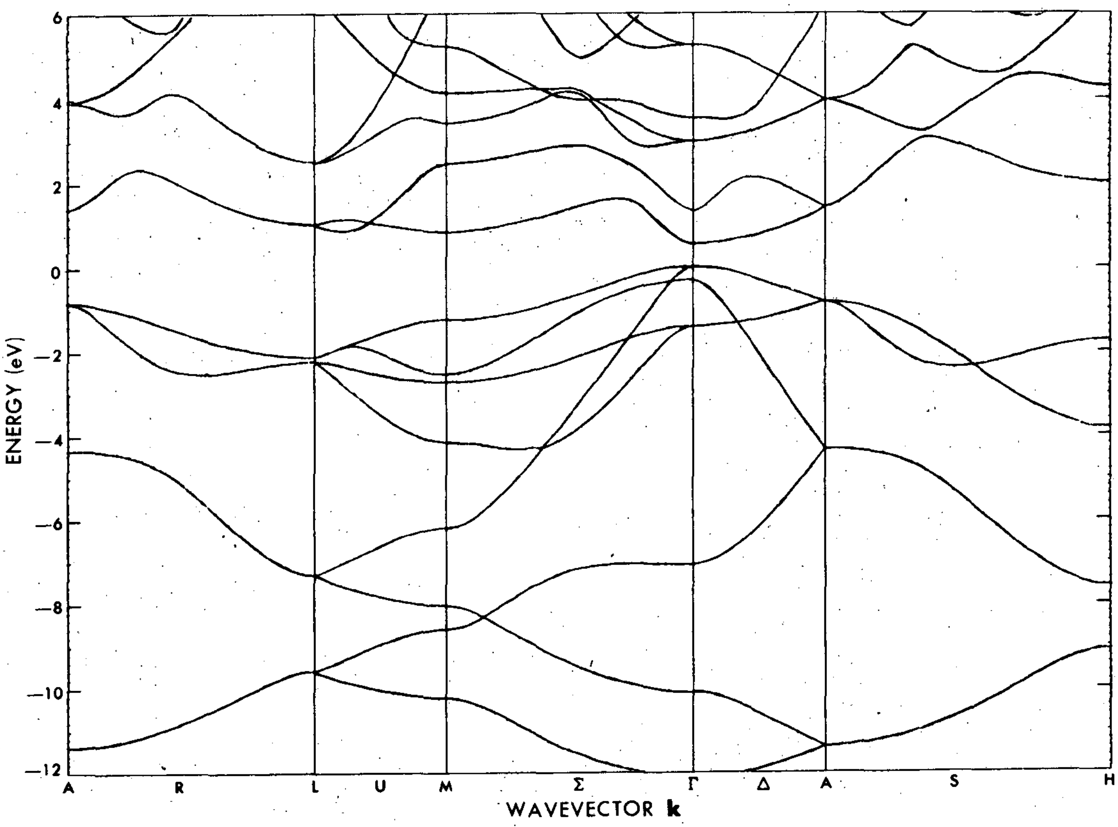

XBL 744-6046

Fig. 14

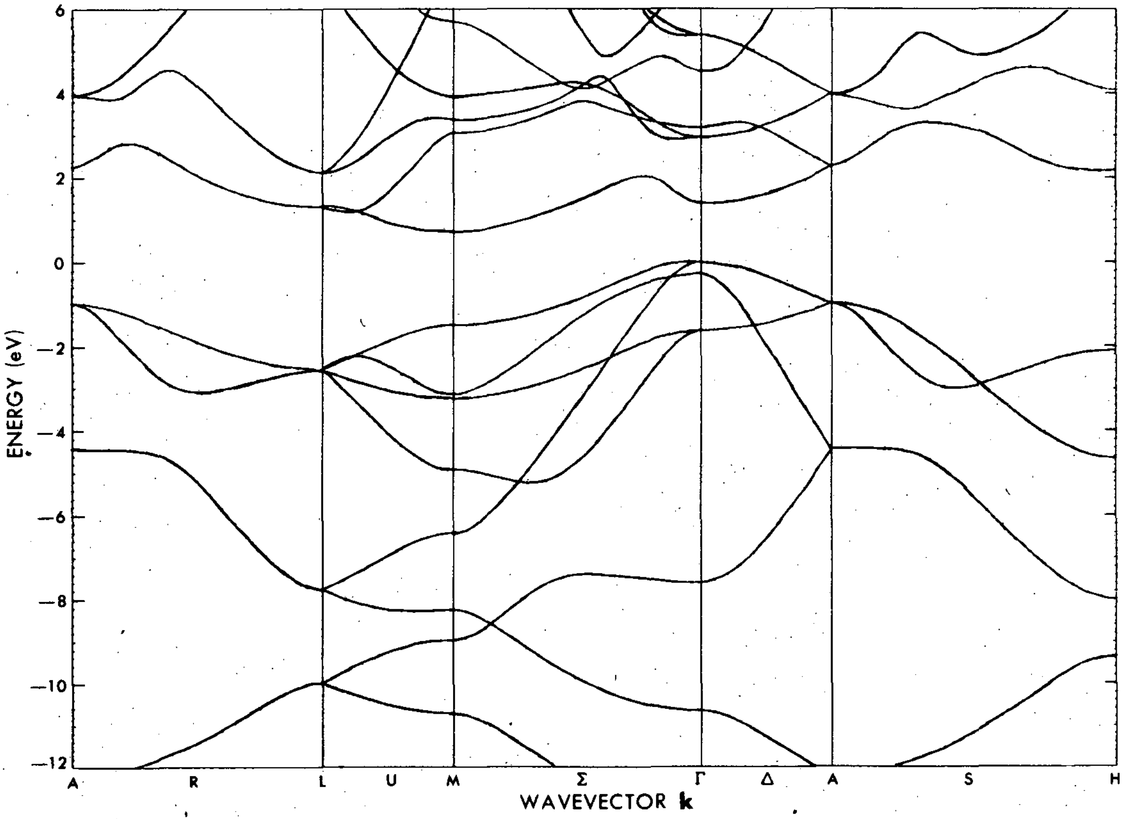

XBL 744-6047

Fig. 15

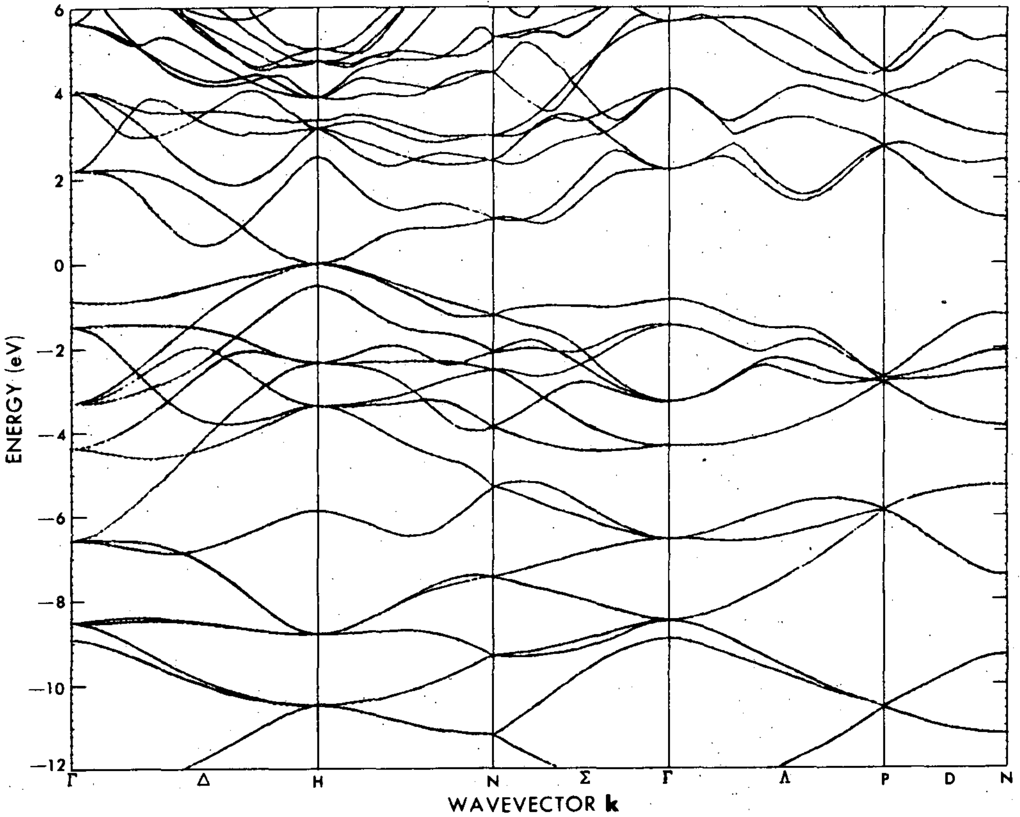

XBL 744-6039

Fig. 16

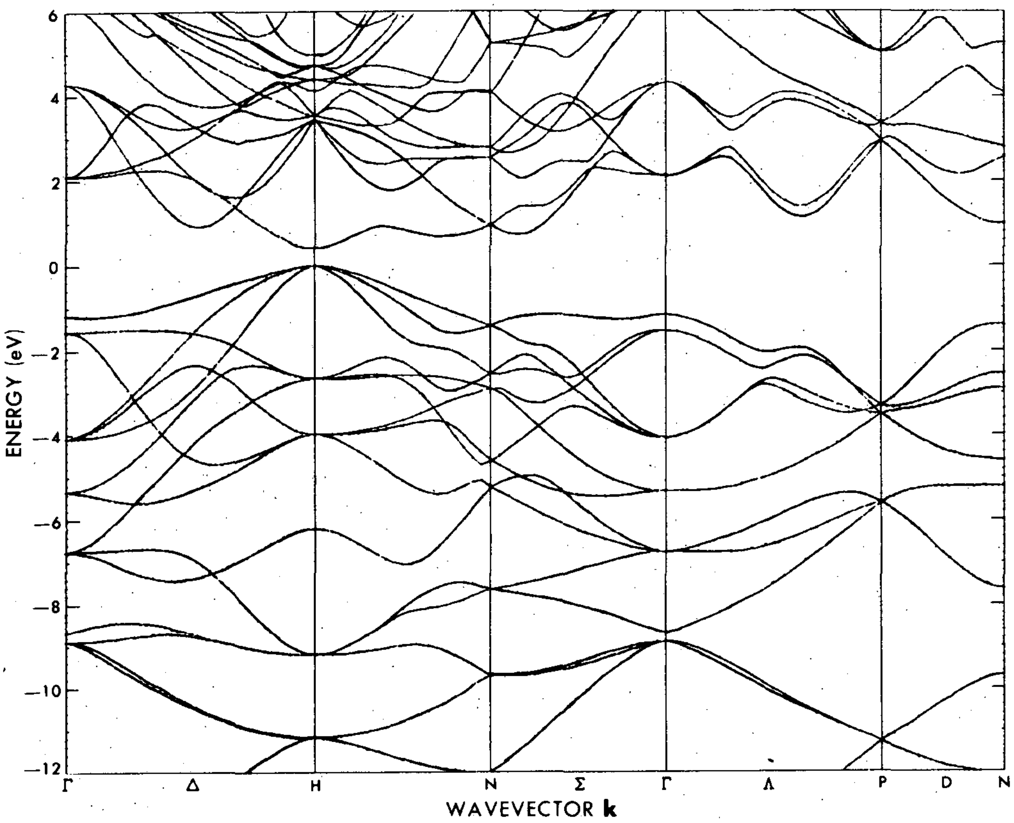

XBL 744-6043

Fig. 17

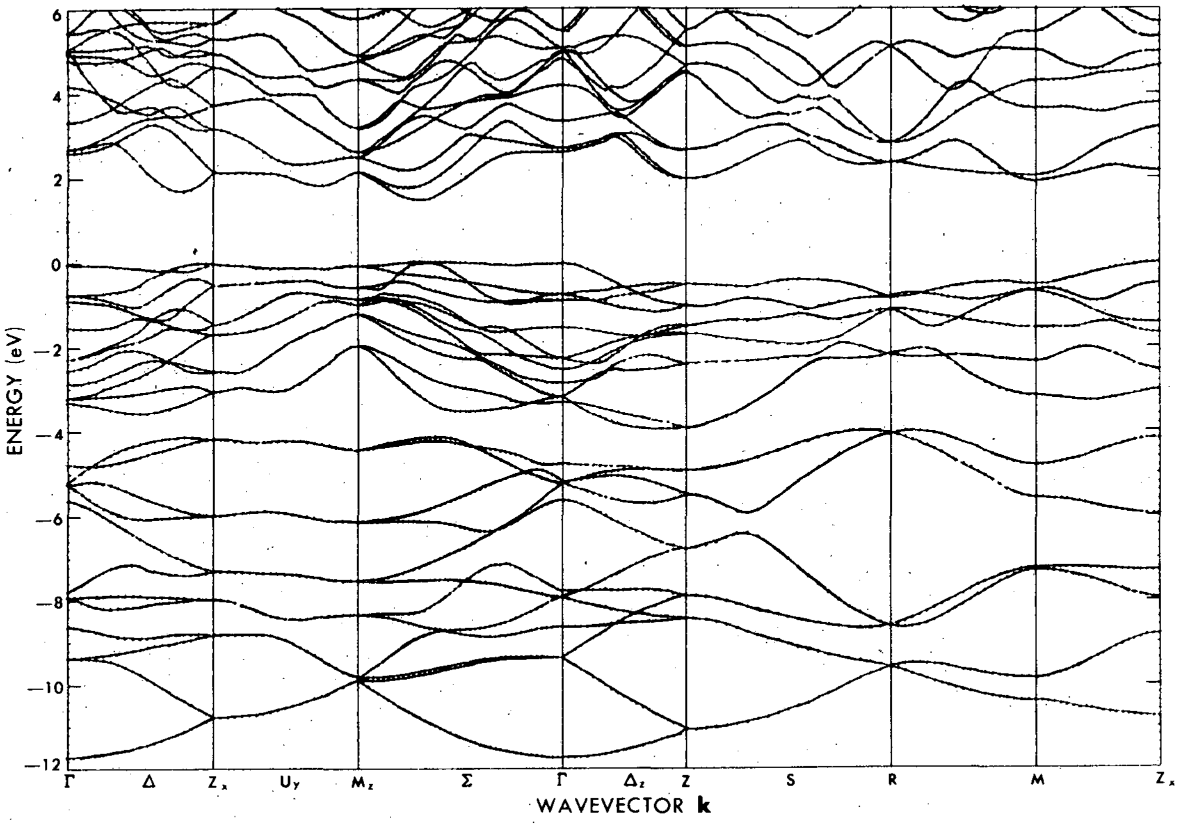

XBL 744-6044

Fig. 18

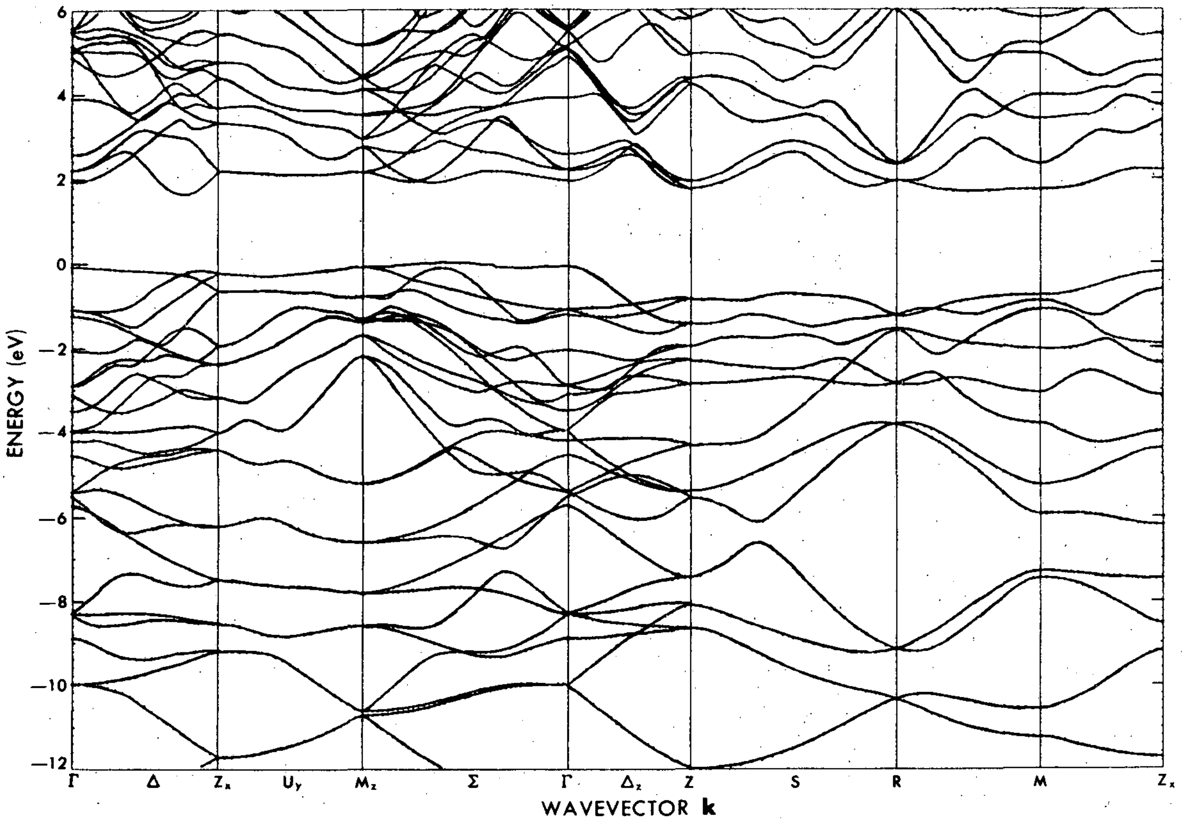

XBL 744-6040

Fig. 19

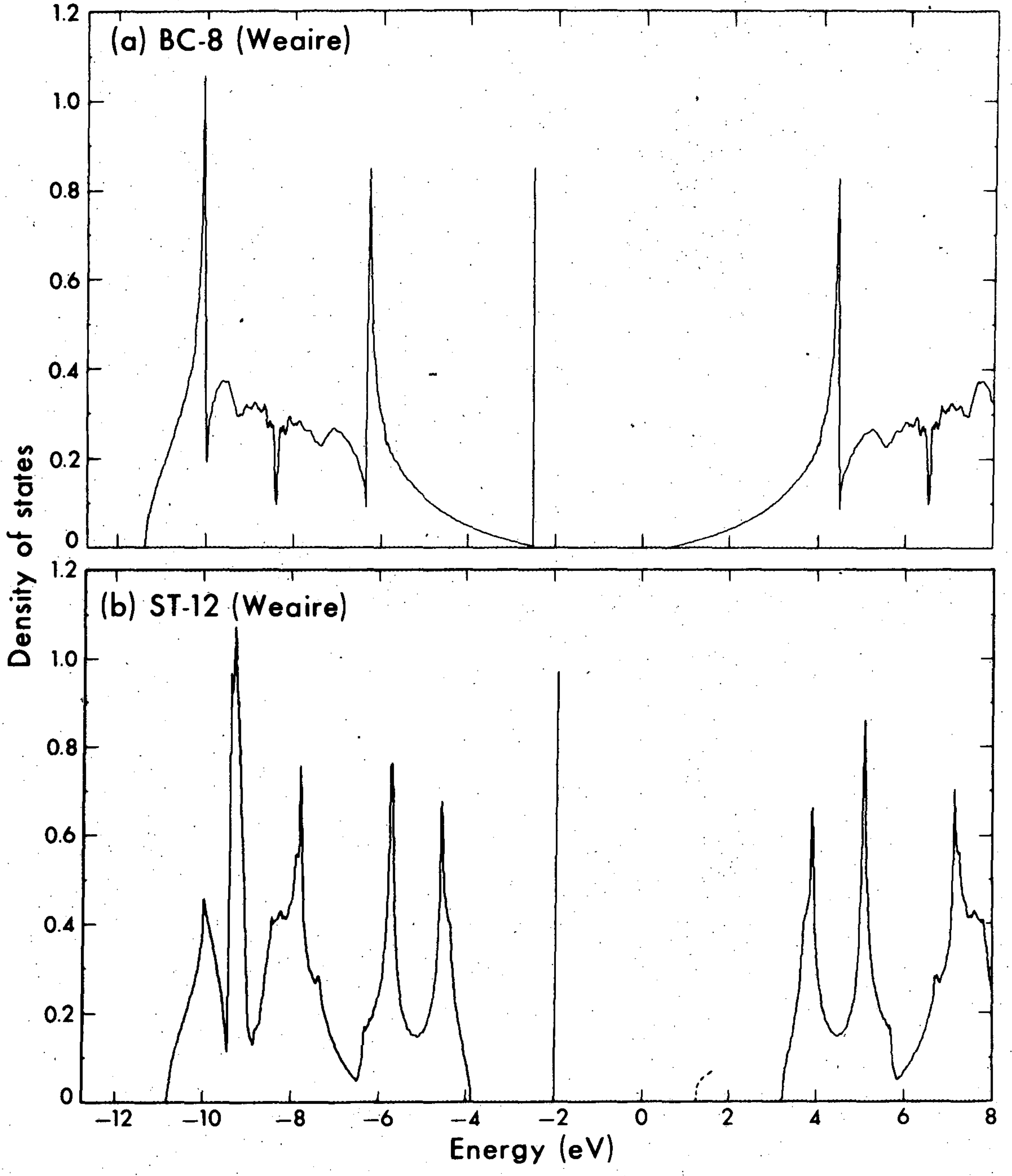

XBL 744-6073

Fig. 20

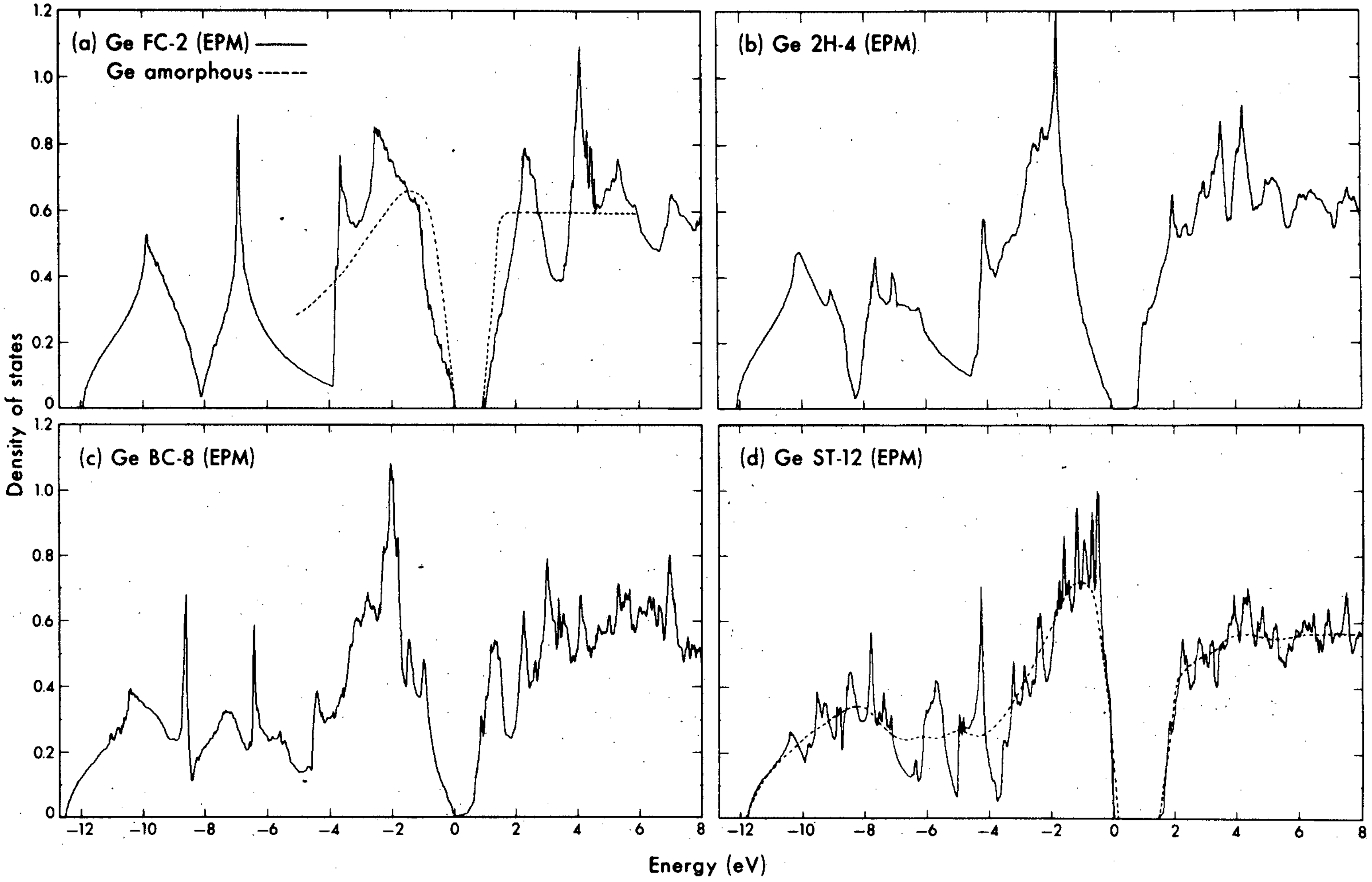

XBL 744-6095

Fig. 21

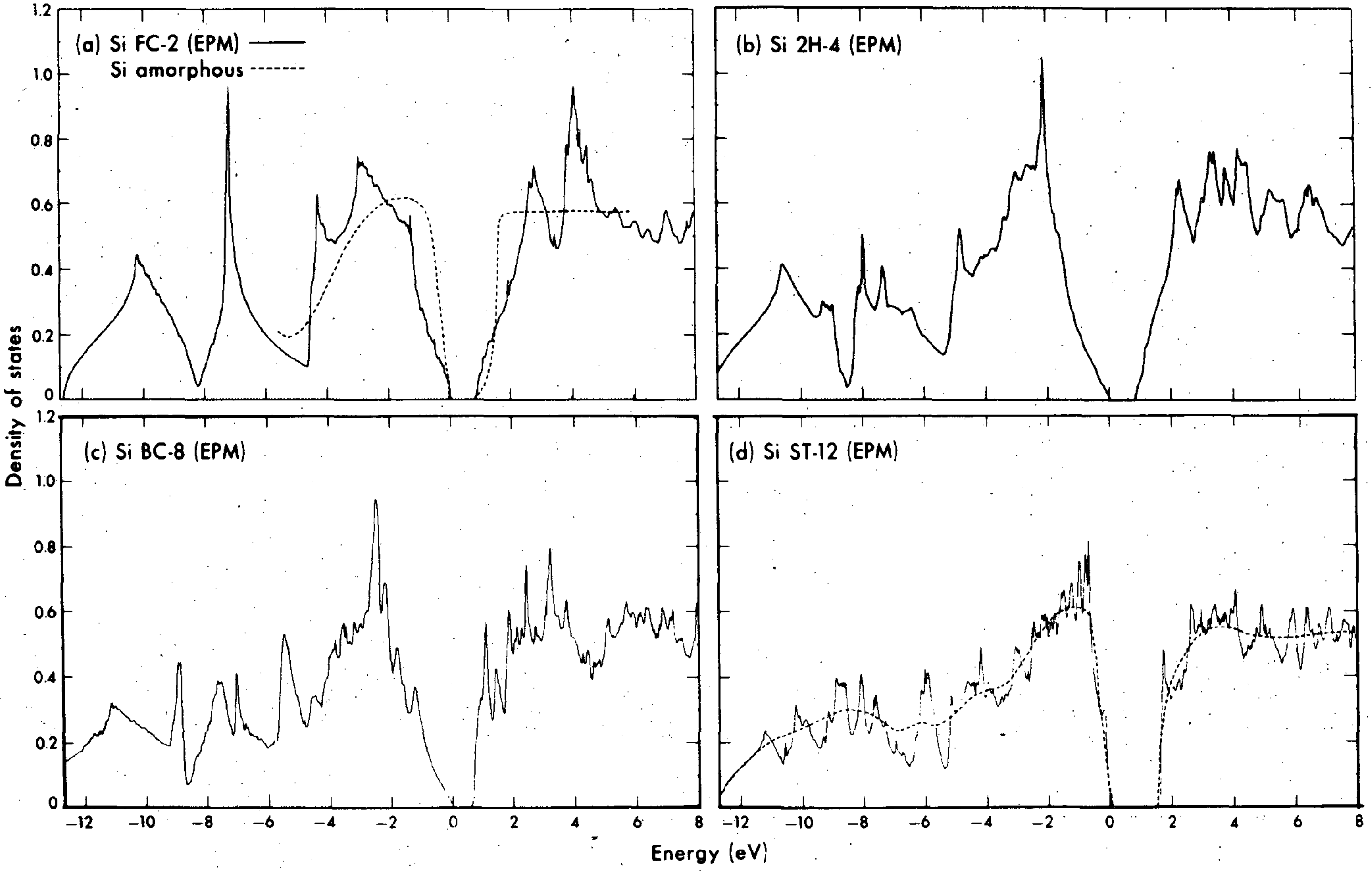

XBL 744-6064

Fig. 22

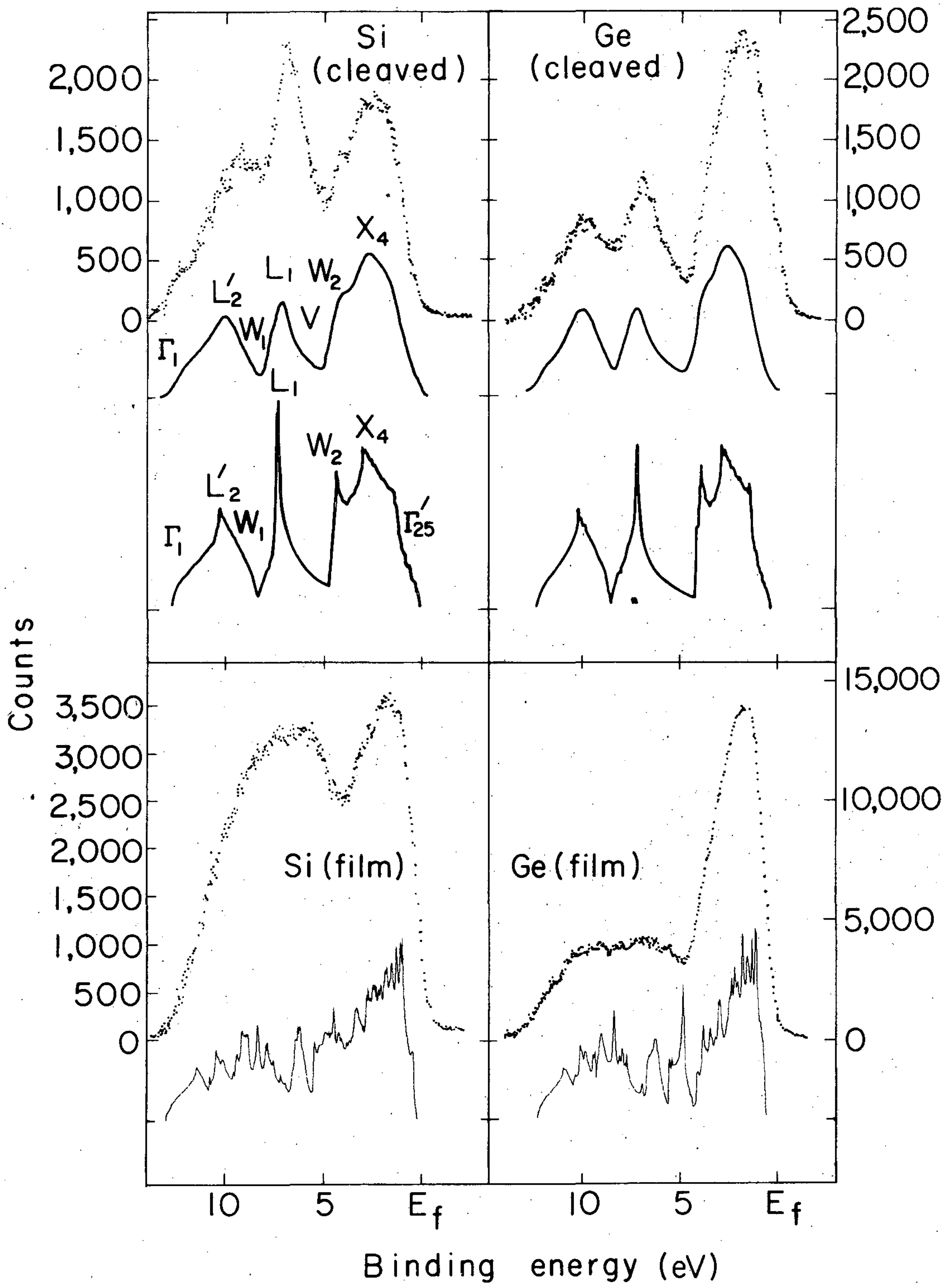
Si
(cleaved)
Ge
(cleaved)
Si (film)
Ge (film)
Counts
Binding energy (eV)
2,000
1,500
1,000
500
0
2,500
2,000
1,500
1,000
500
0
3,500
3,000
2,500
2,000
1,500
1,000
500
0
15,000
10,000
5,000
0
10
5
E_f
10
5
E_f
Γ_1
L'_2
W_1
L_1
W_2
V
X_4
Γ_1
L'_2
W_1
L_1
W_2
X_4
Γ'_{25}
XBL 727-3392A

Fig. 23

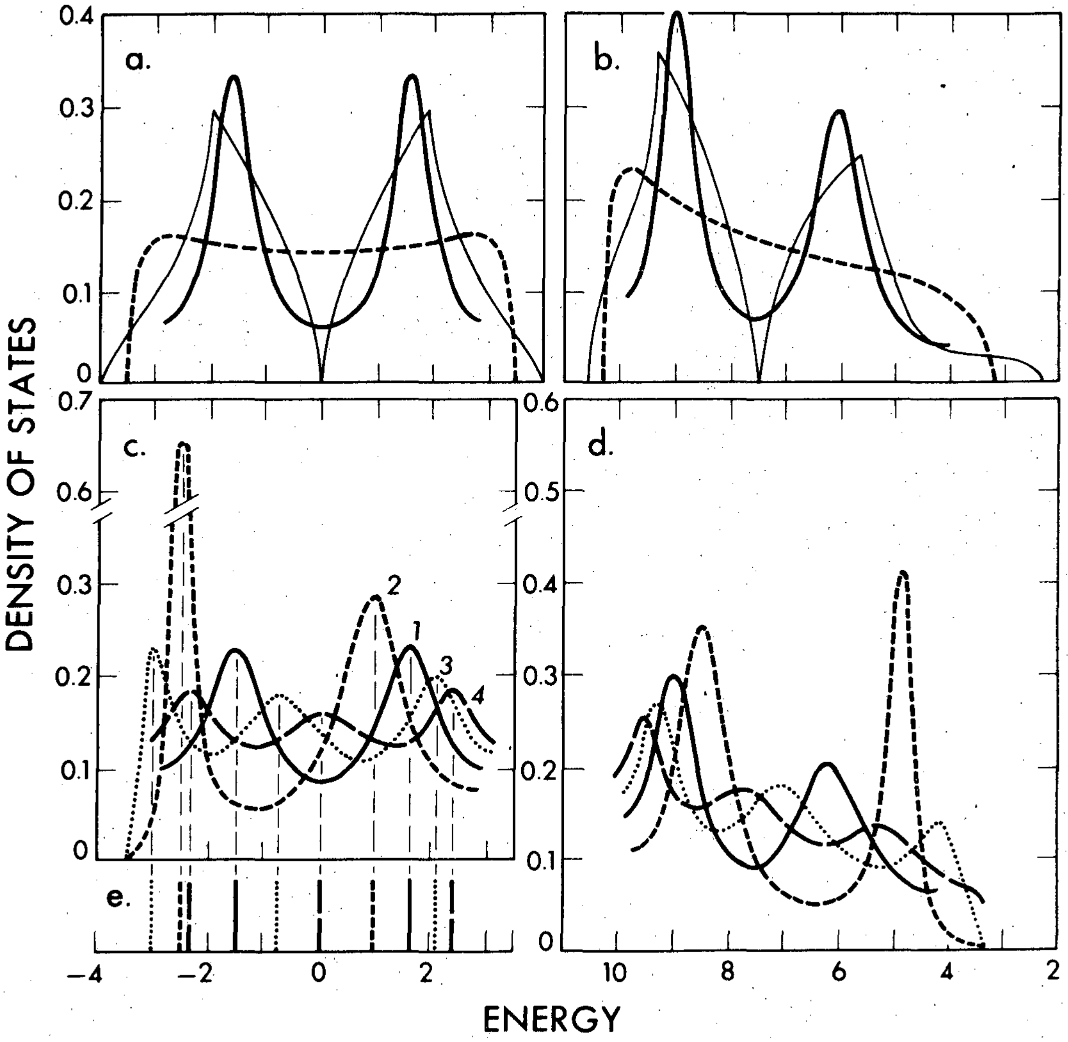

XBL 744-6080

Fig. 24

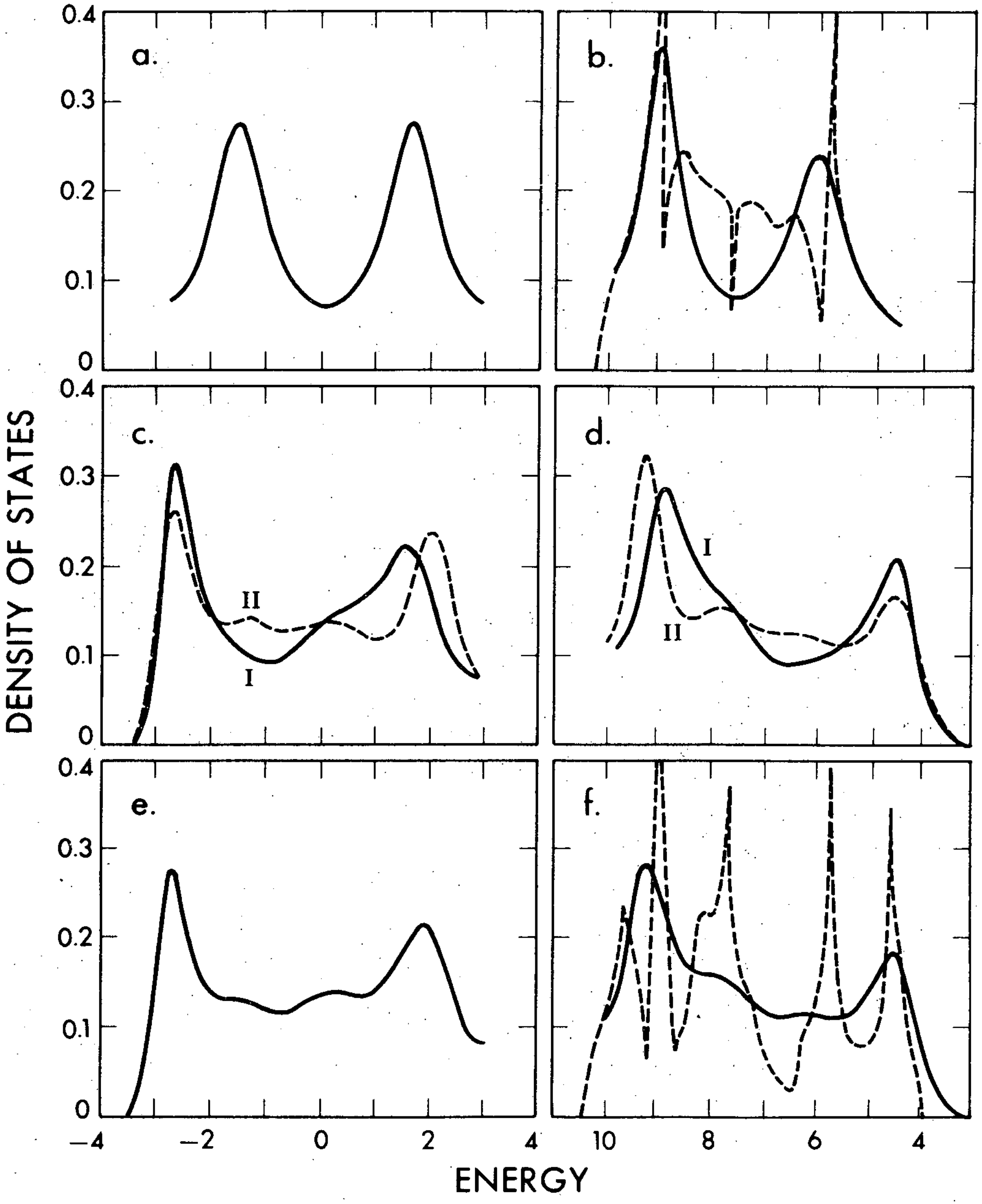

XBL 744-6082

Fig. 25

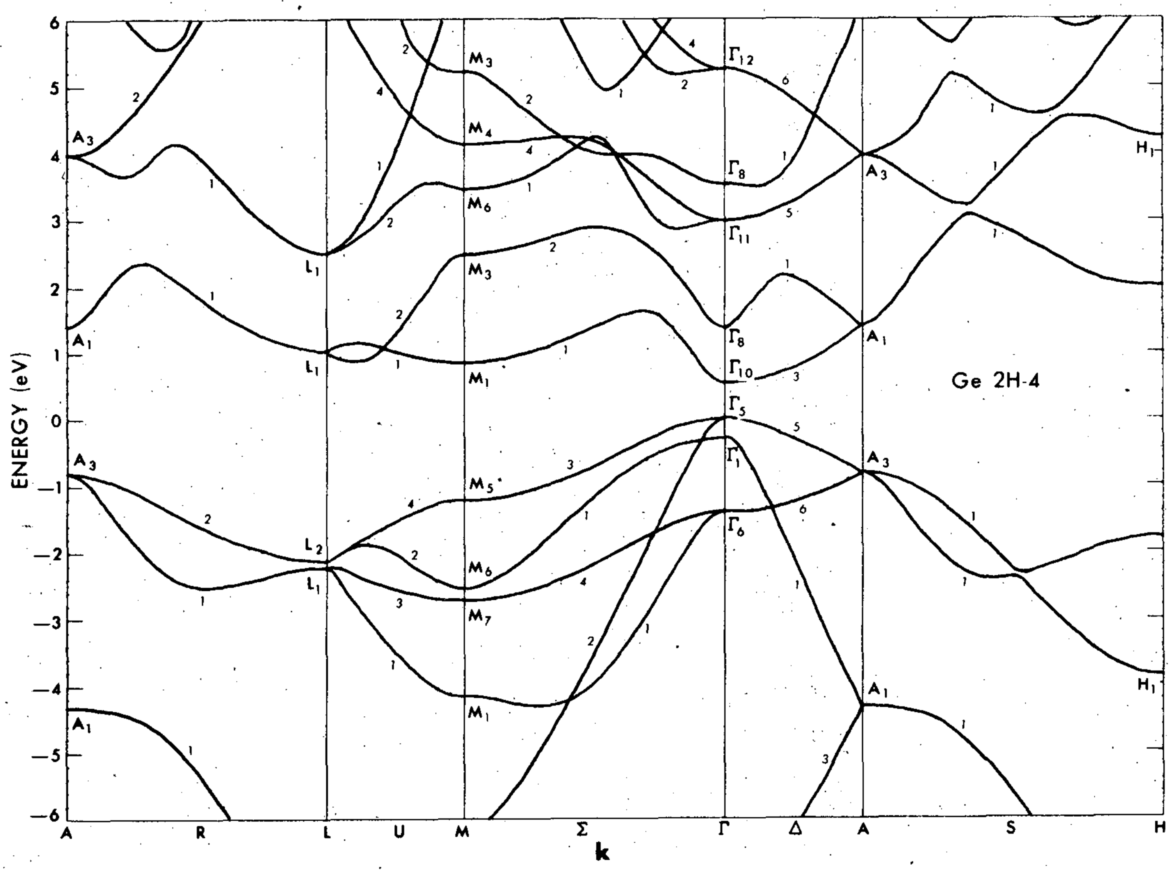

XBL 744-6061

Fig. 26

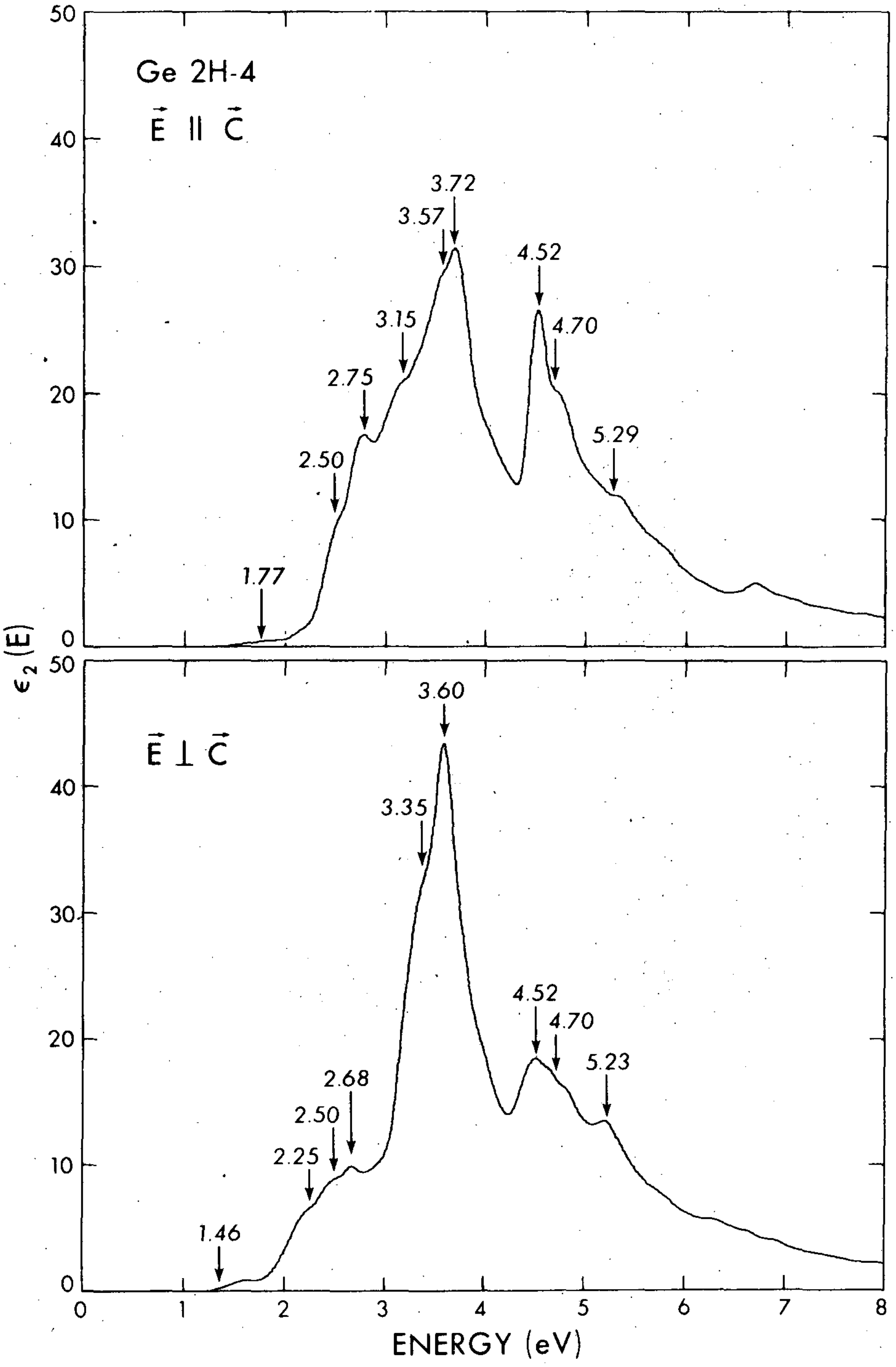

XBL 744-6066

Fig. 27

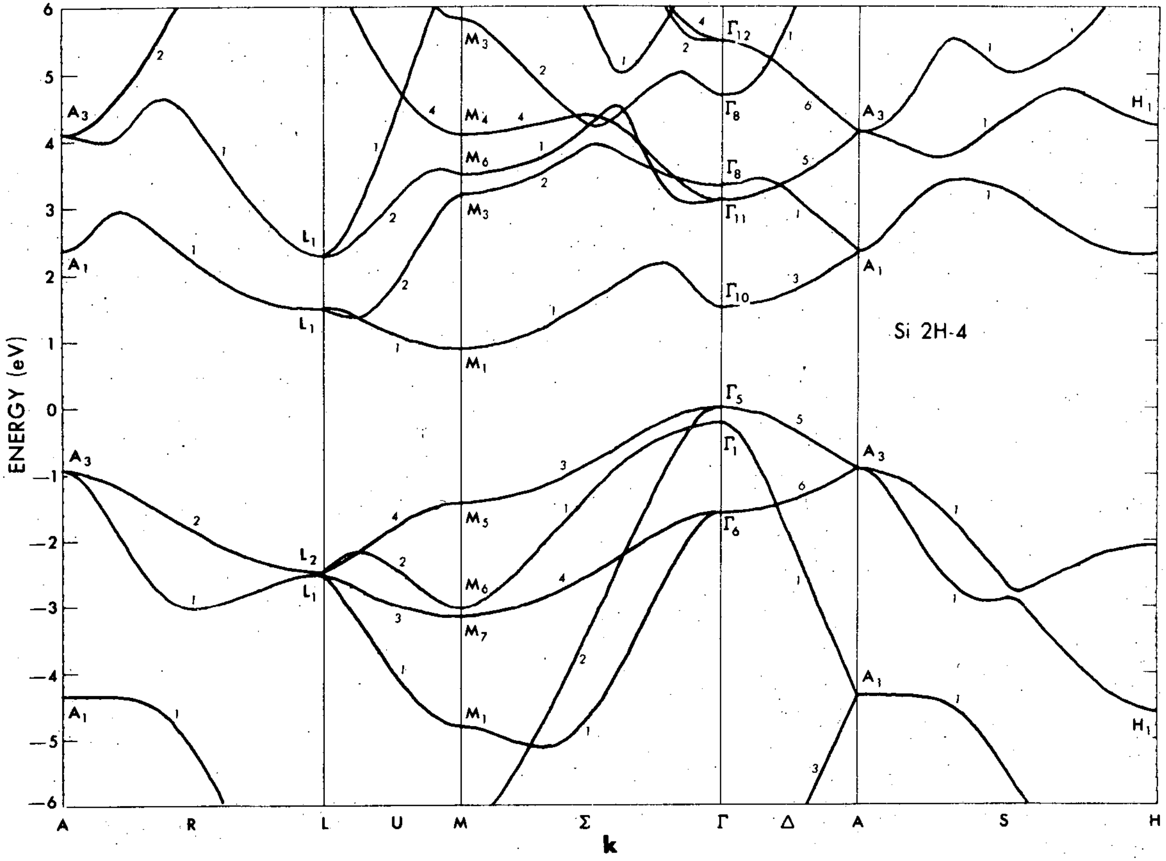

XBL 744-6038

Fig. 28

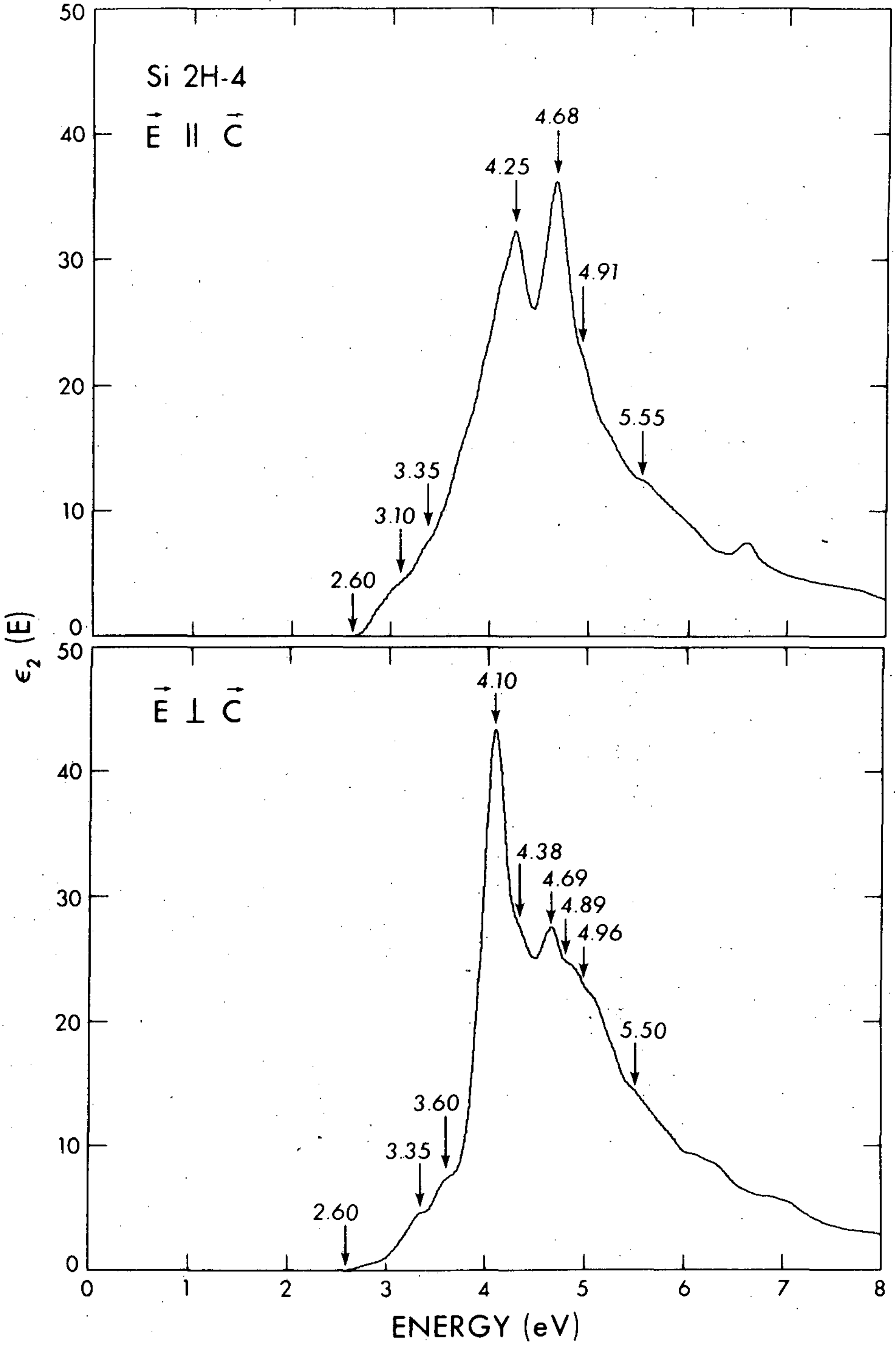

XBL 744-6063

Fig. 29

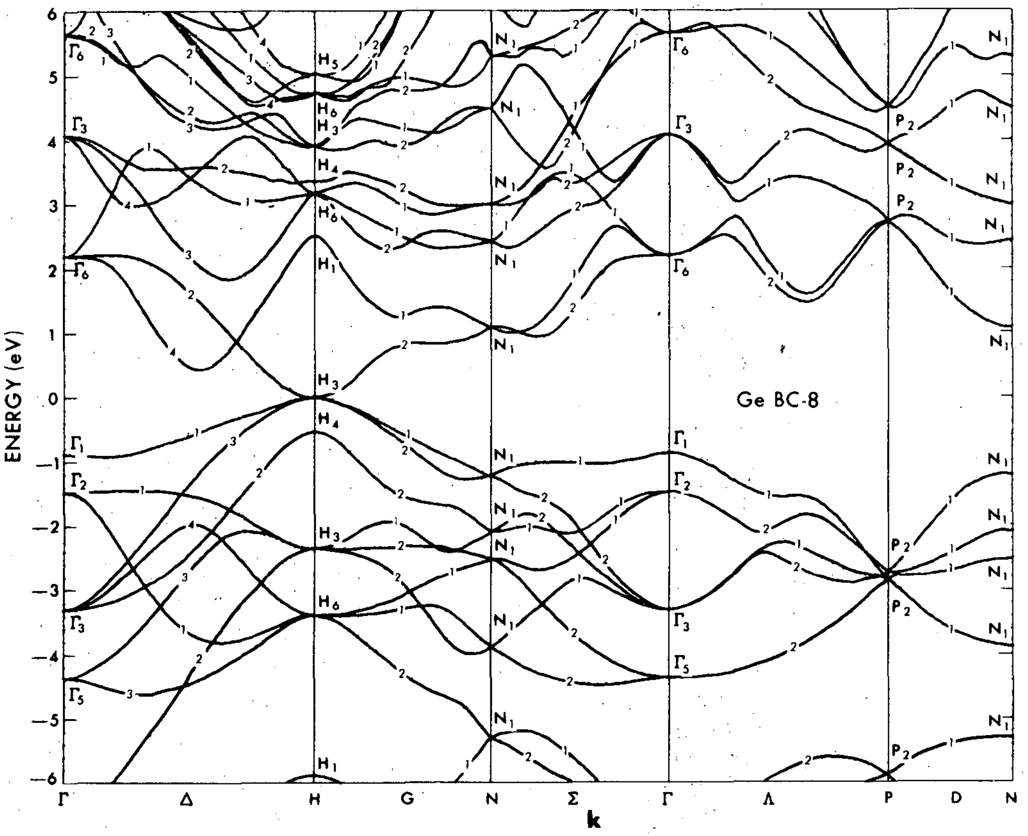

XBL 744-6041

Fig. 30

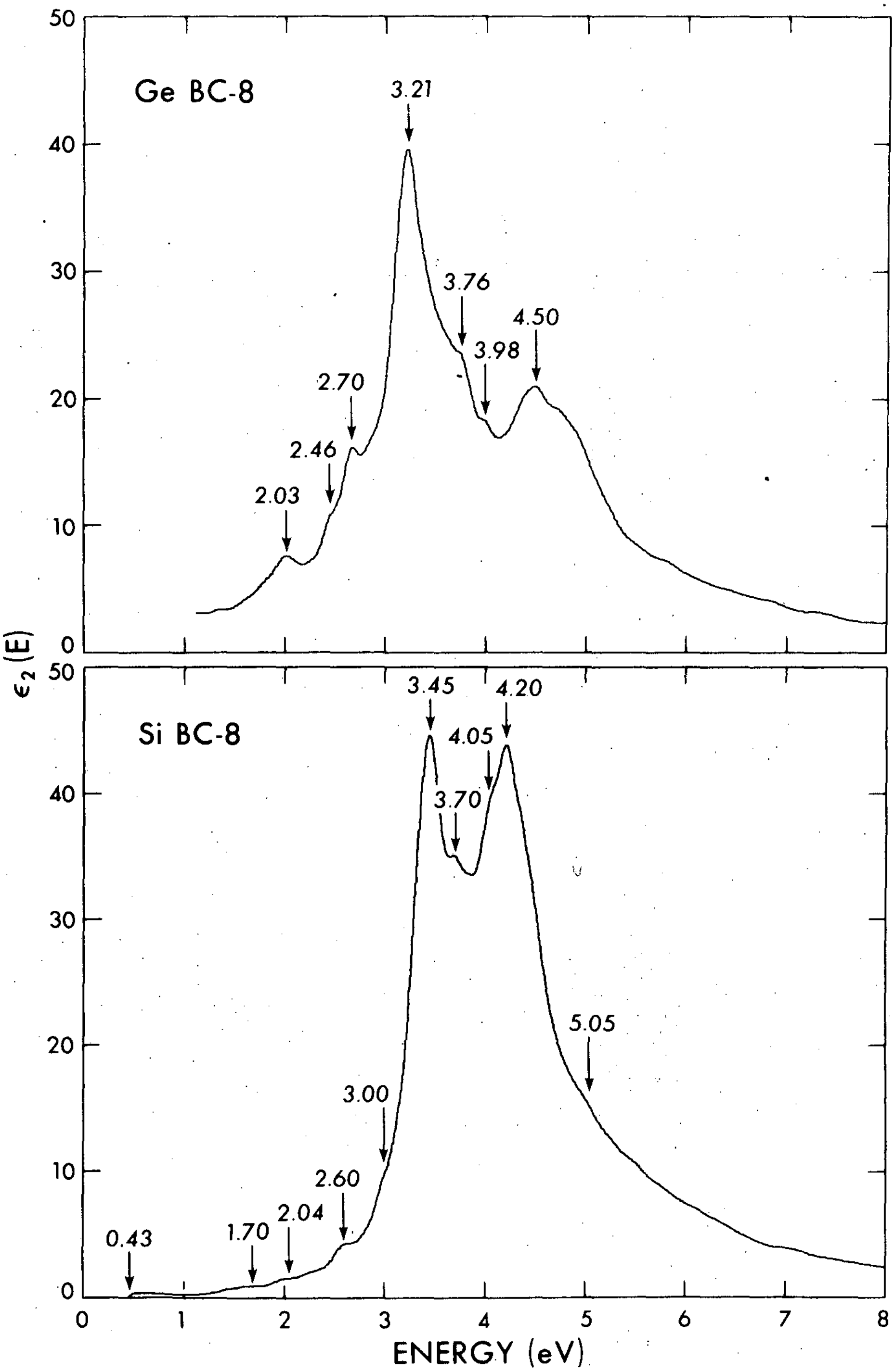

XBL 744-6067

Fig. 31

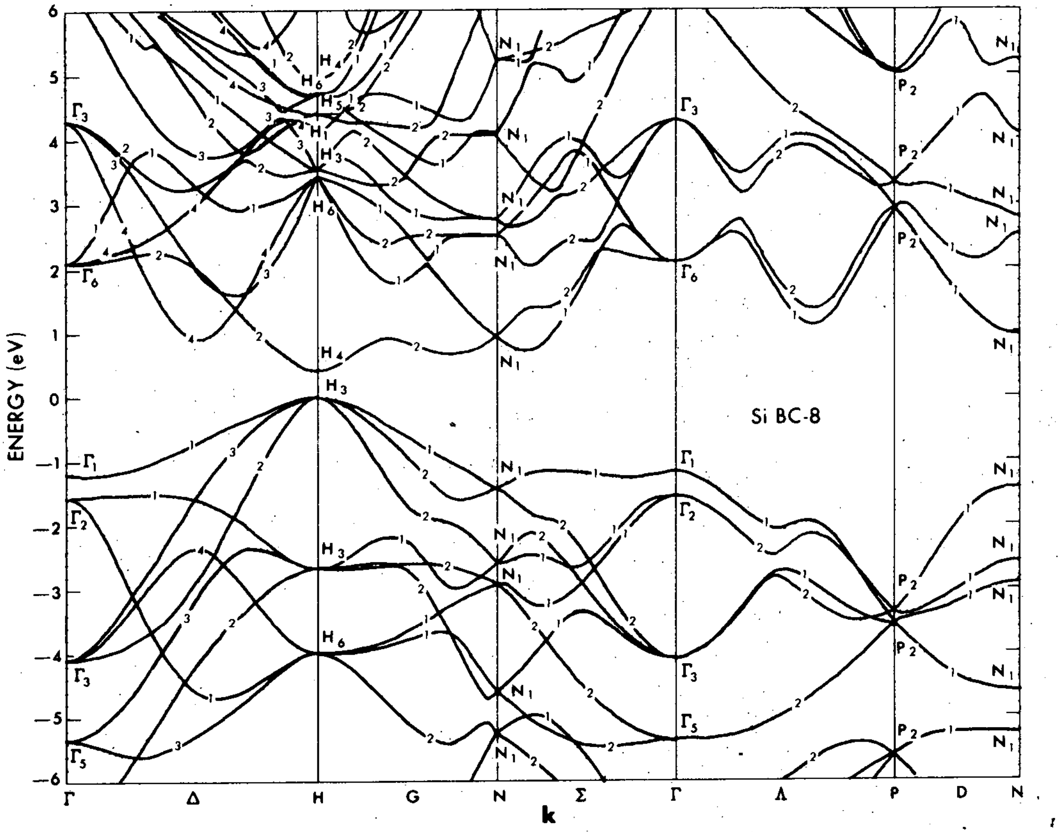

XBL 744-6042

Fig. 32

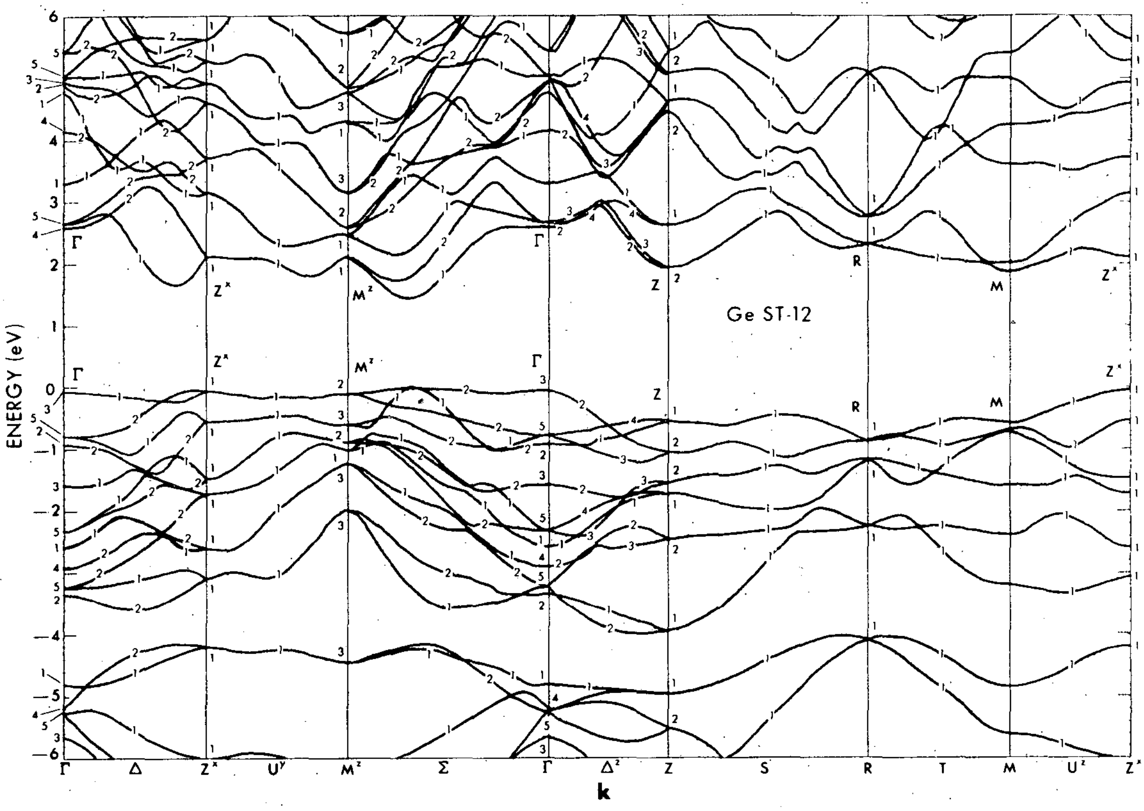

XBL 744-6058

Fig. 33

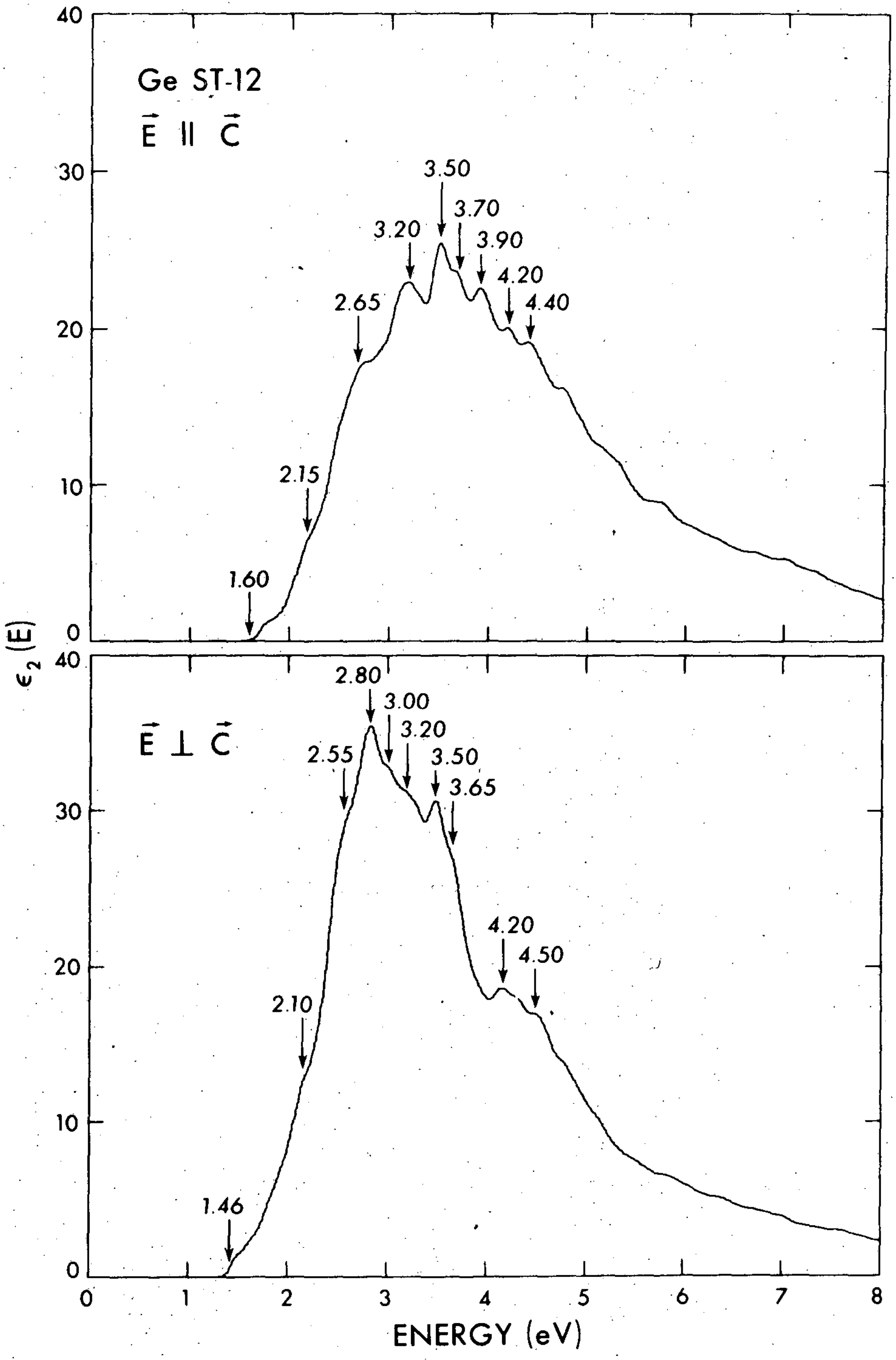

XBL 744-6083

Fig. 34

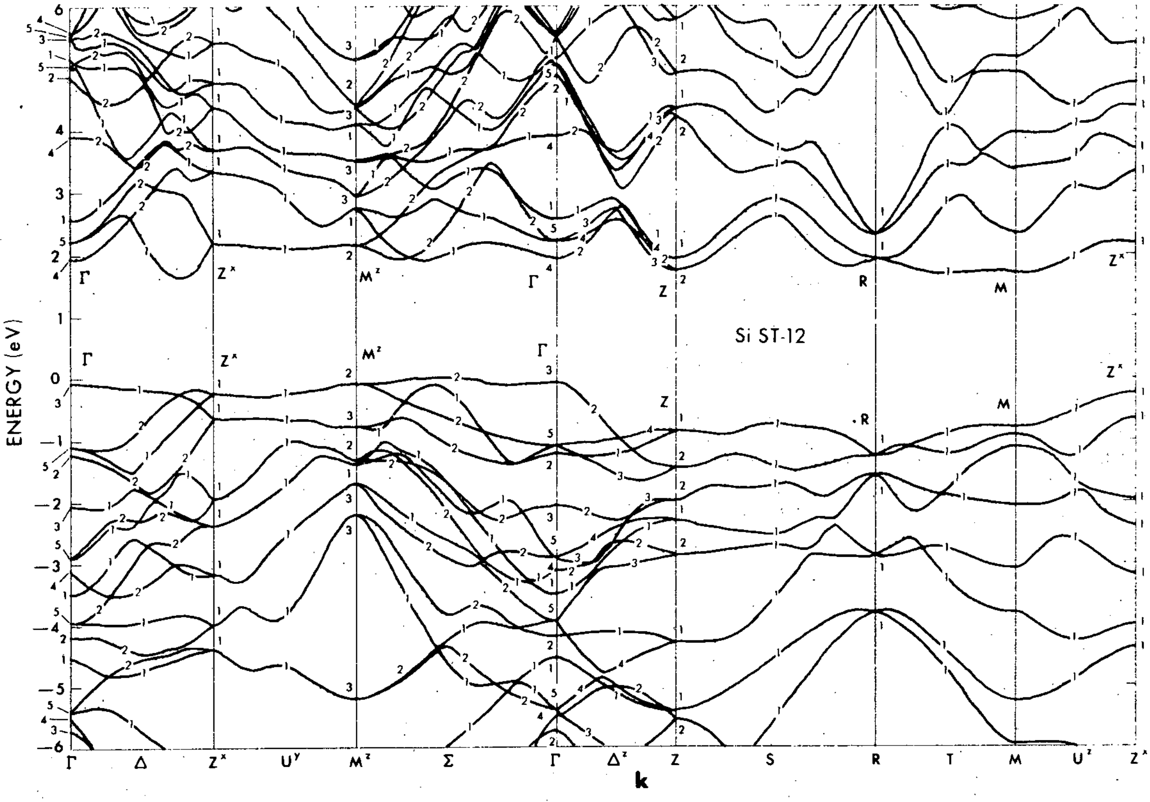

XBL 744-6037

Fig. 35

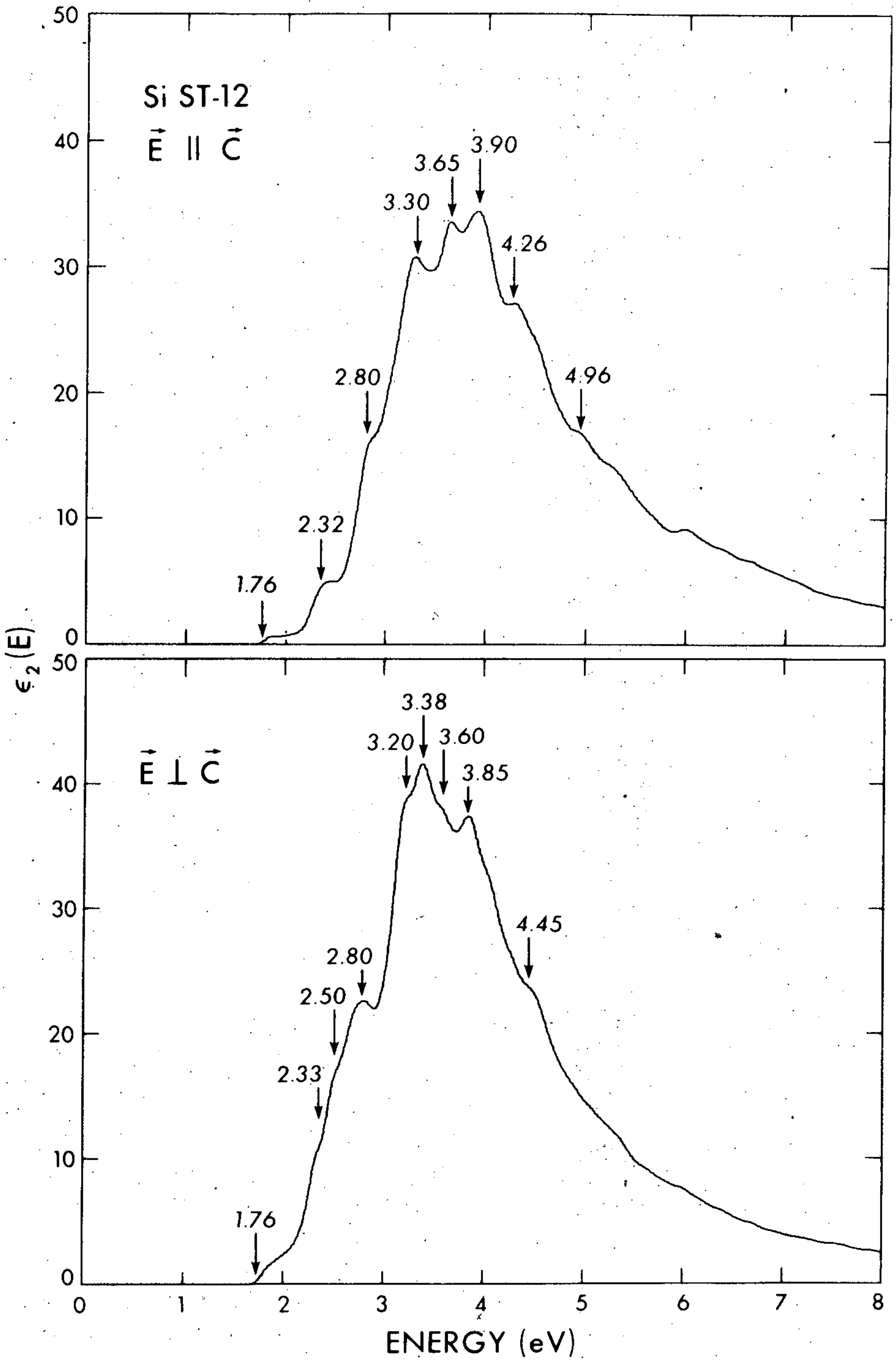

XBL 744-6077

Fig. 36

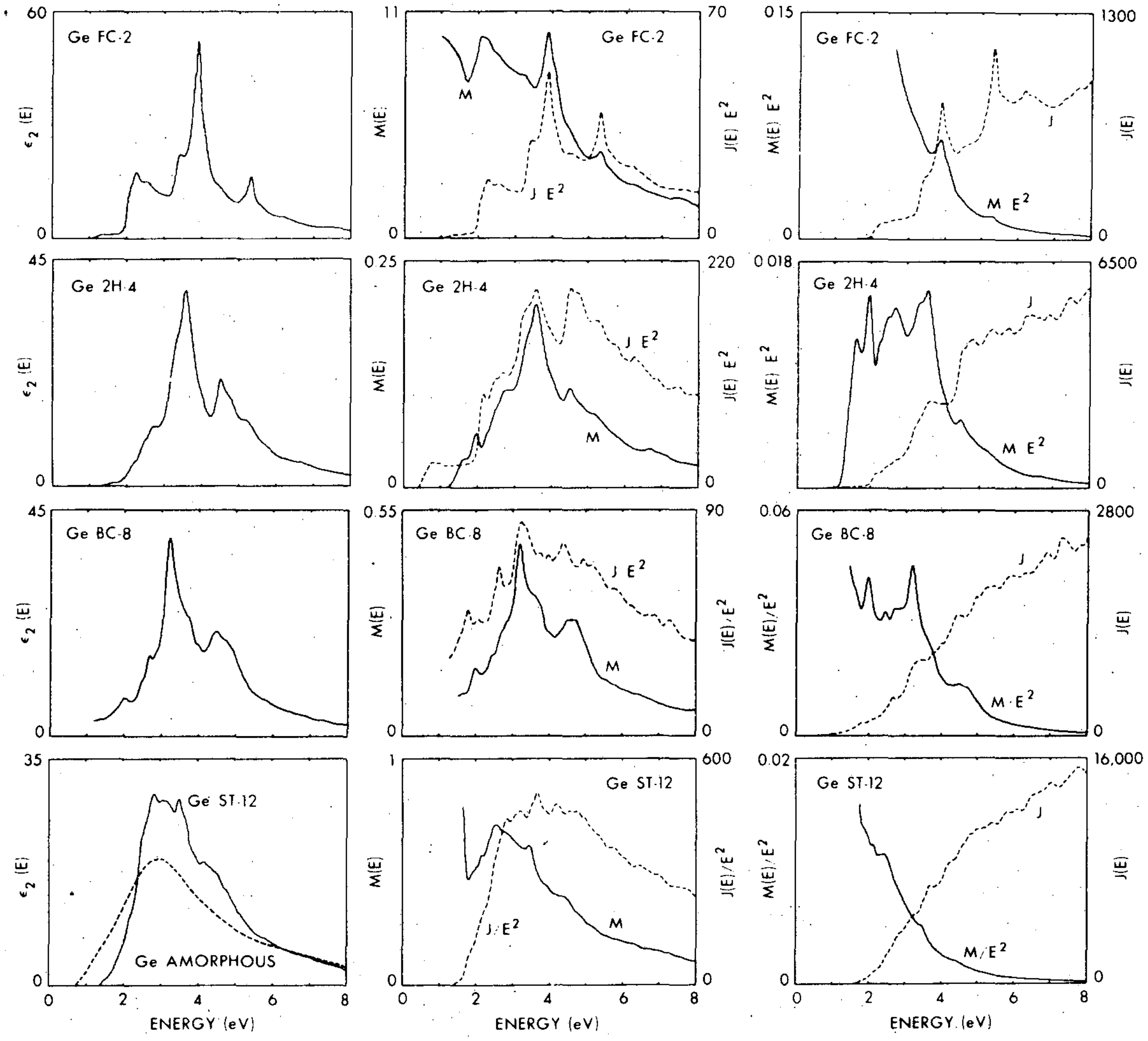

XBL 744-6060

Fig. 37

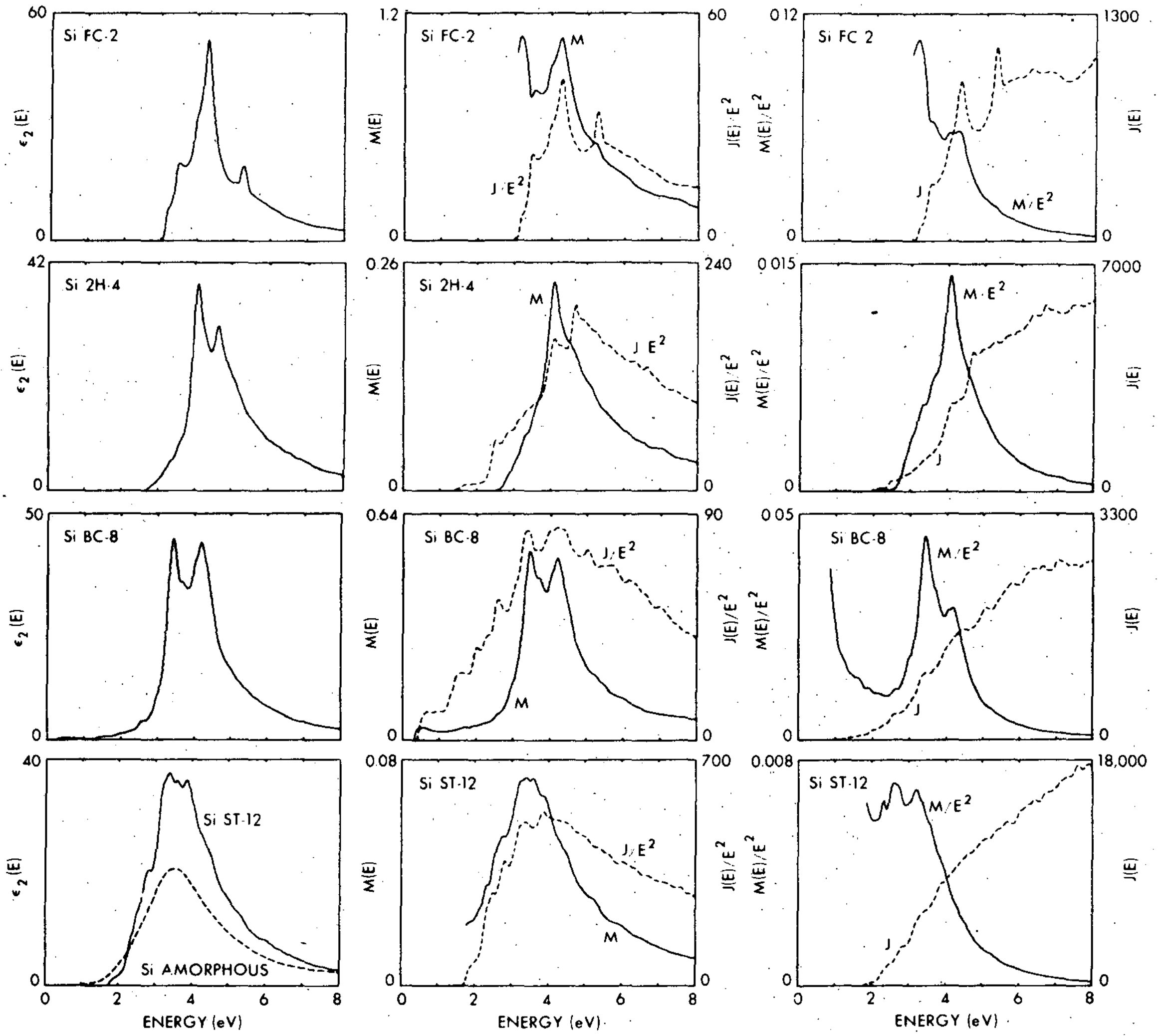

XBL 744-6078

Fig. 38

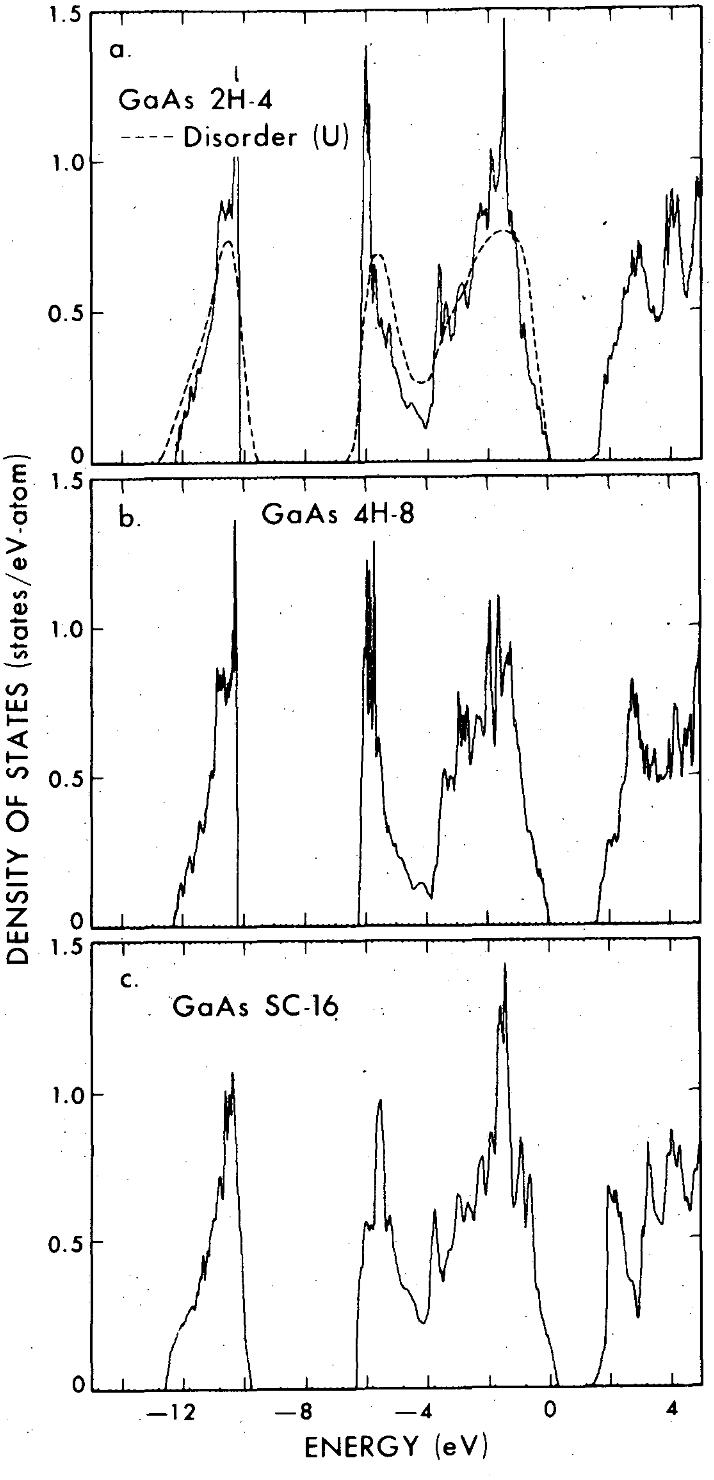

XBL 744-6079

Fig. 39

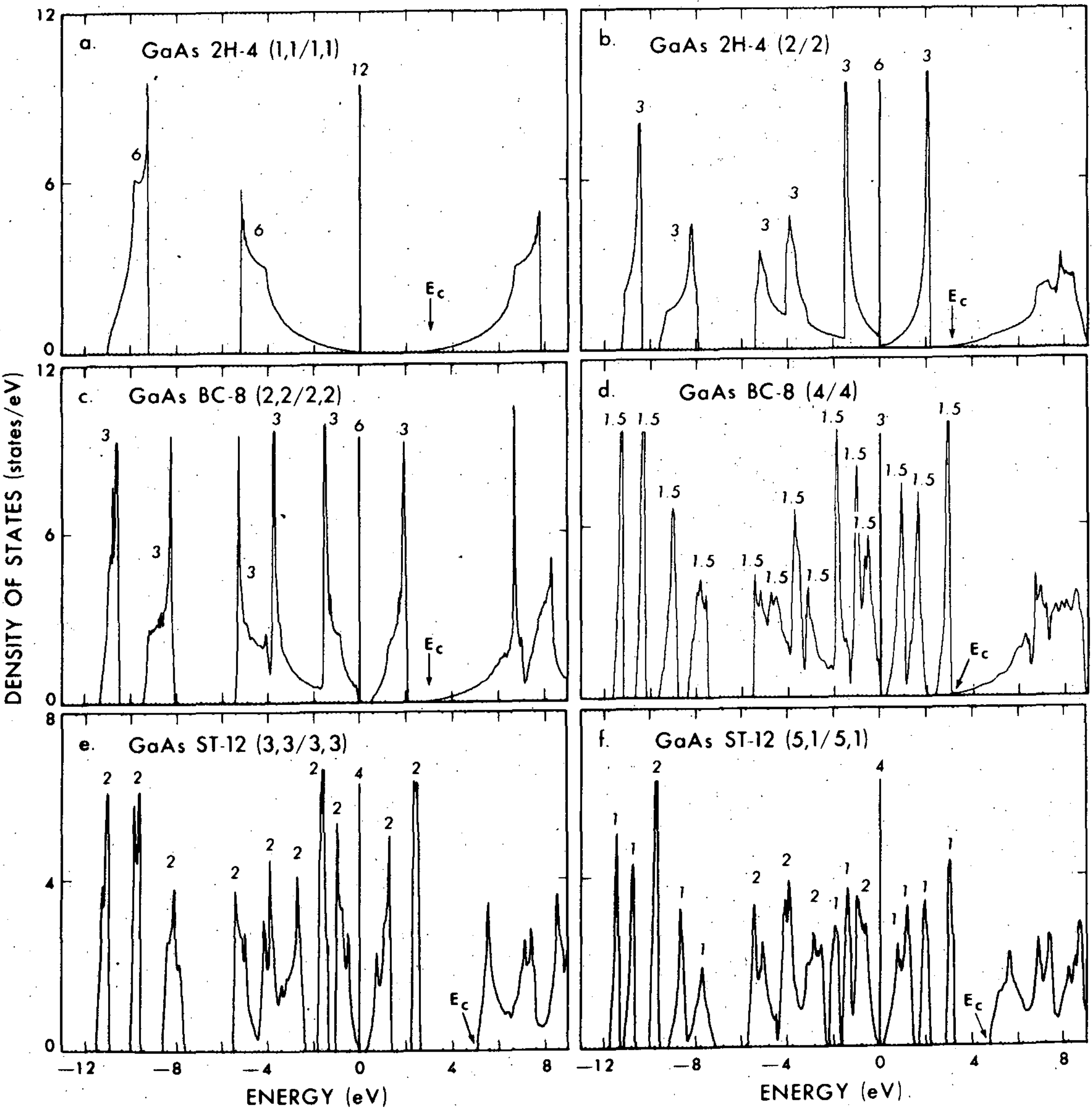

XBL 744-6072

Fig. 40

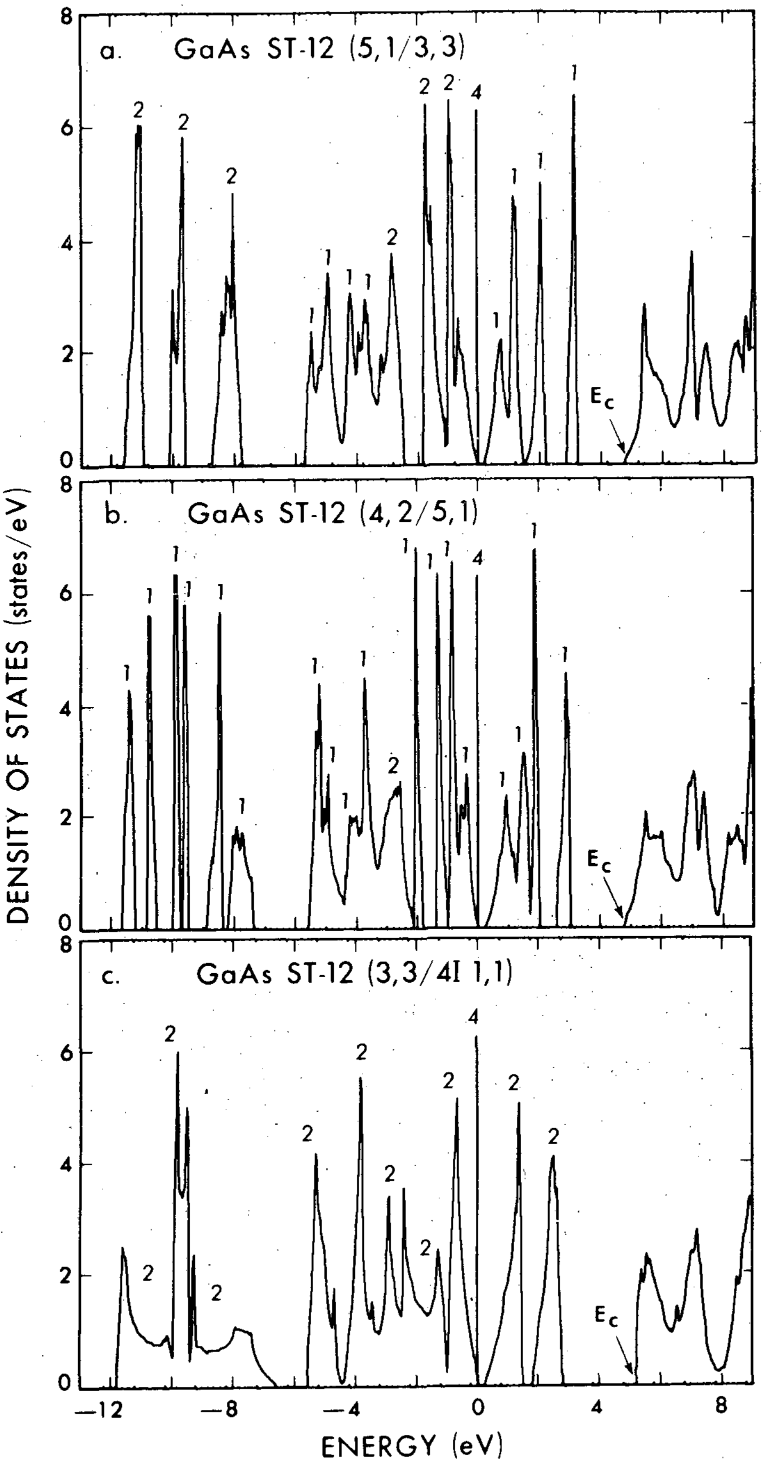

XBL 744-6068

Fig. 41

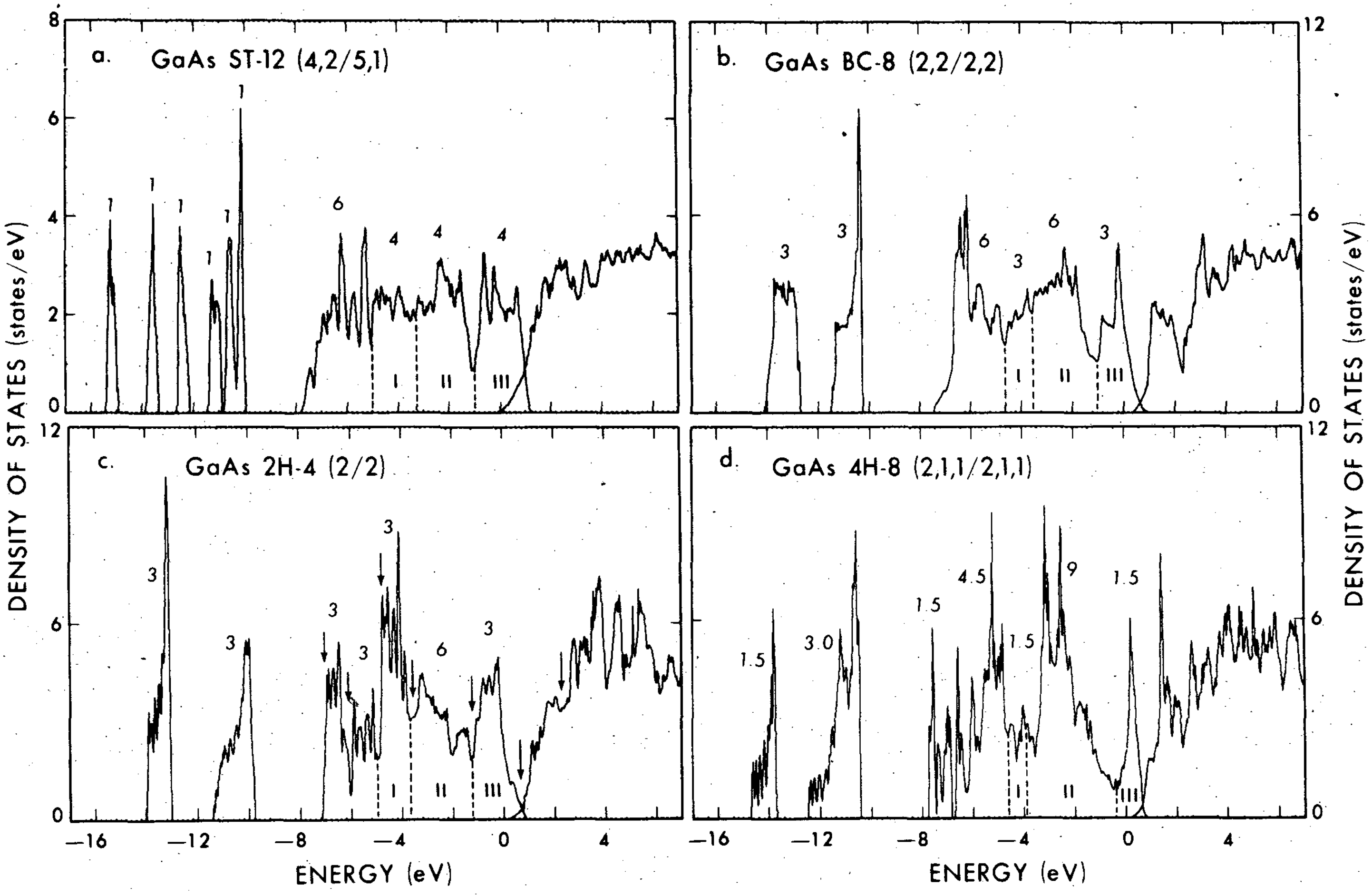

XBL 744-6075

Fig. 42

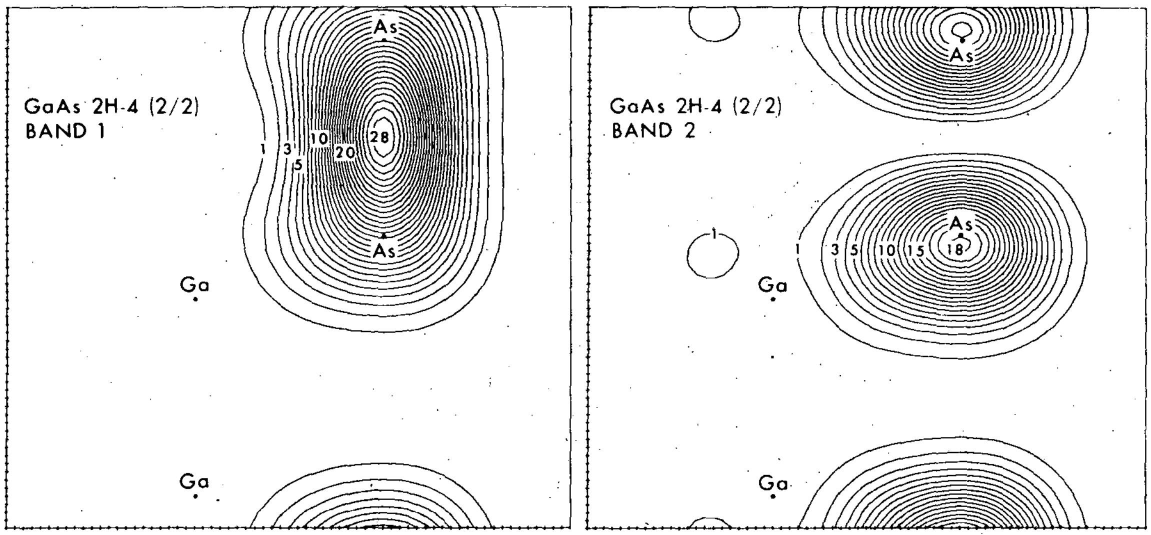

XBL 744-6052

Fig. 43

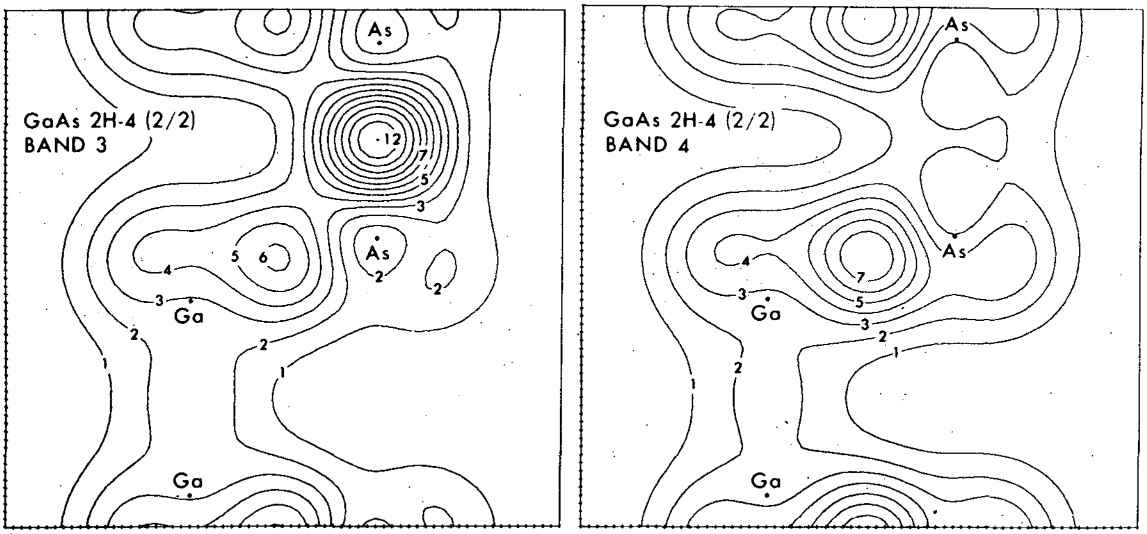

XBL 744-6062

Fig. 44

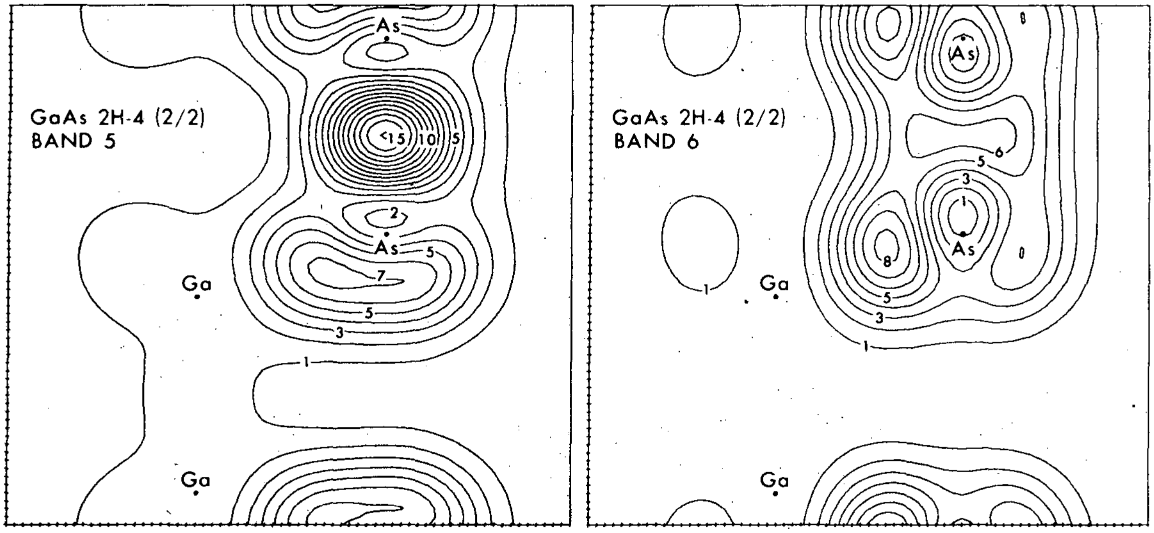

XBL 744-6055

Fig. 45

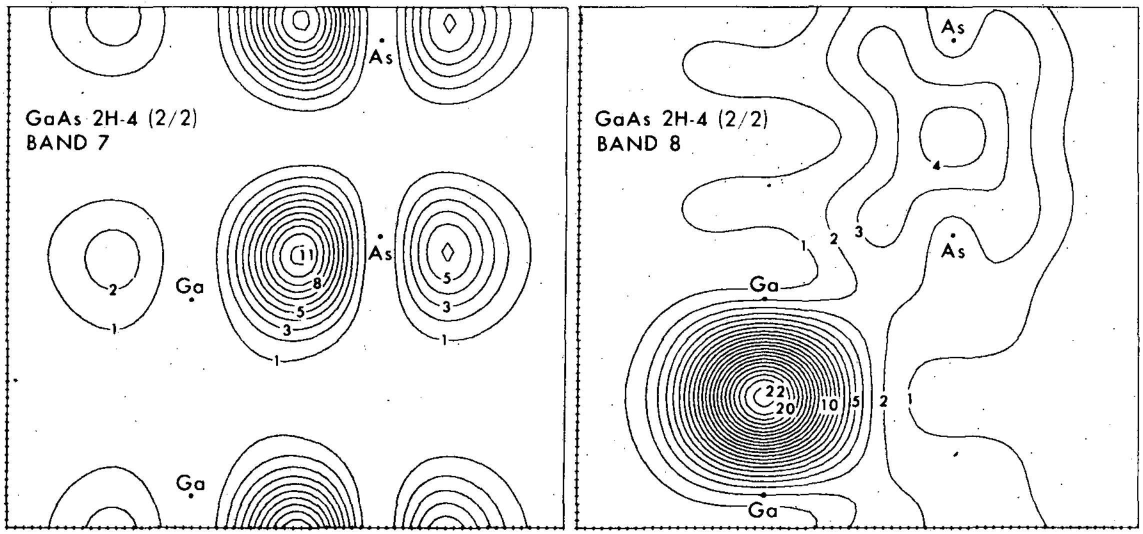

XBL 744-6048

Fig. 46

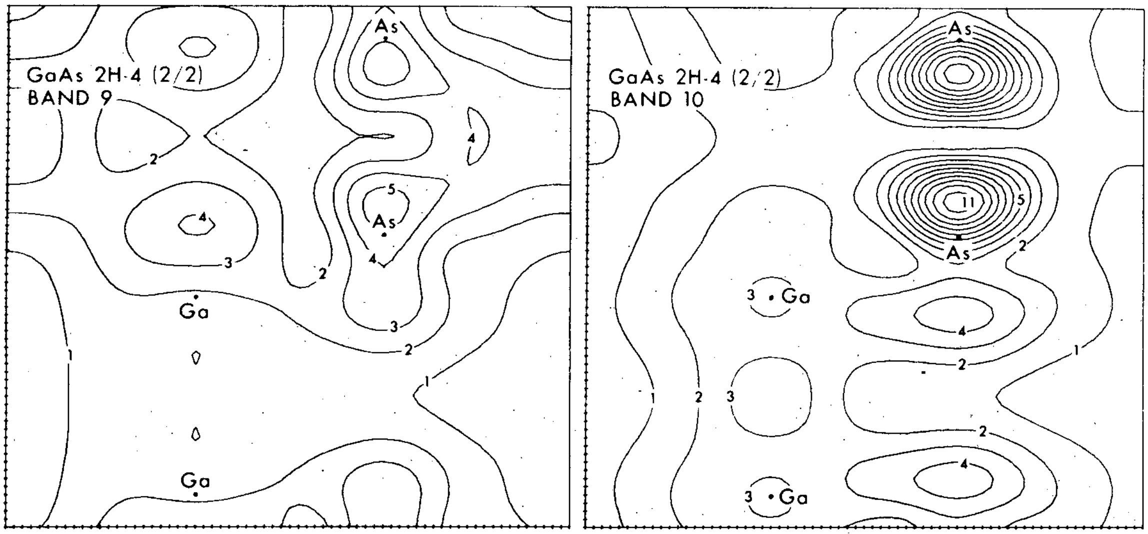

XBL 744-6050

Fig. 47

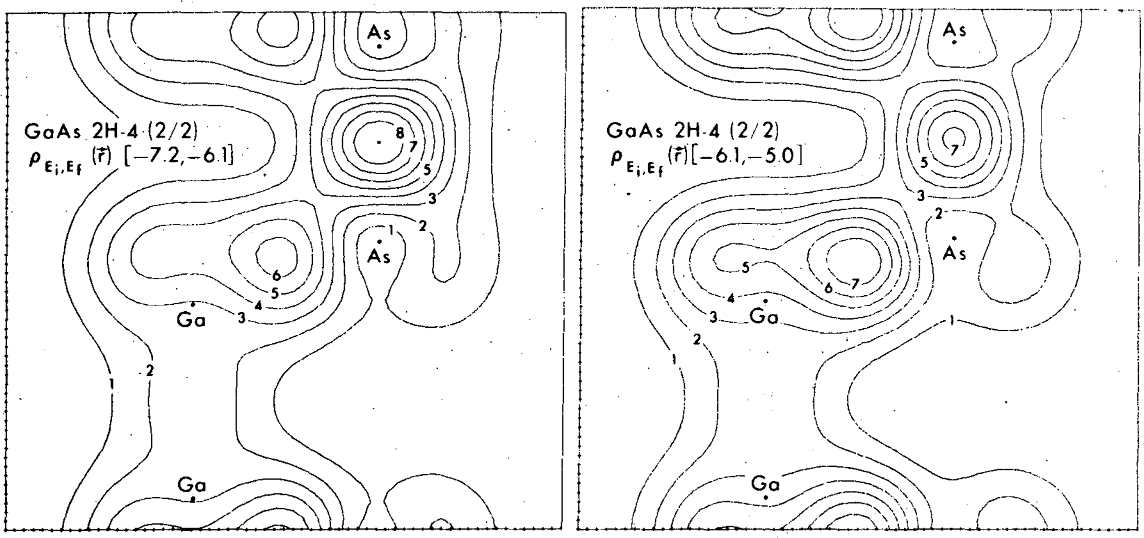

XBL 744-6070

Fig. 48

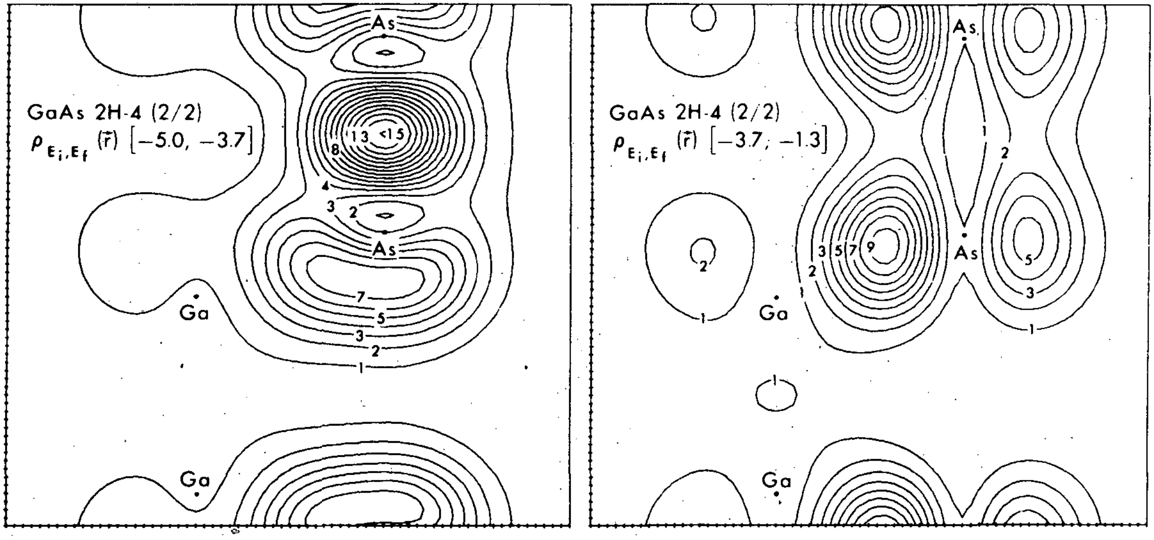

XBL 744-6056

Fig. 49

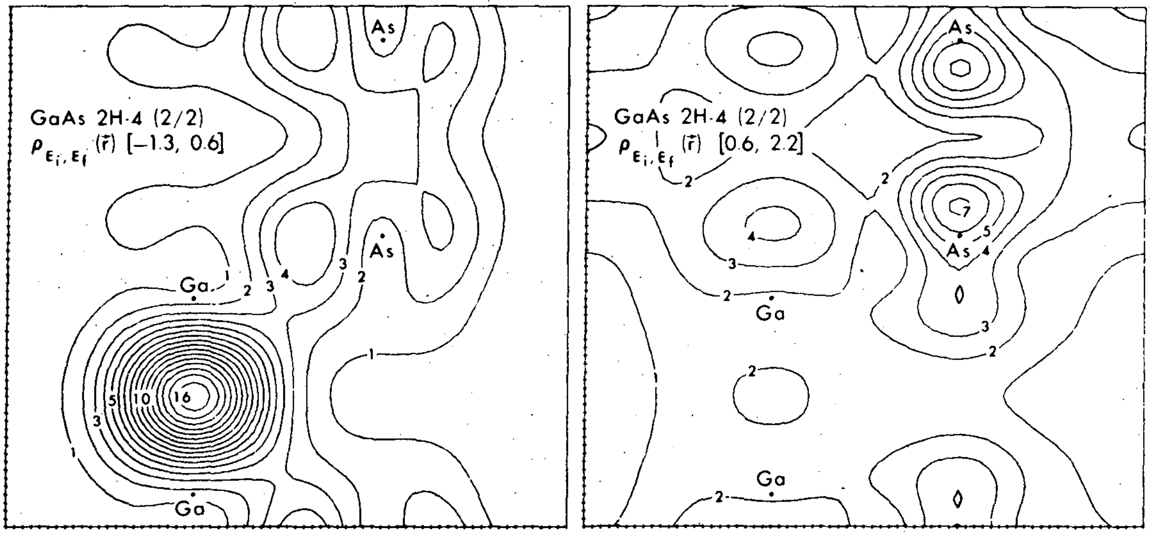

XBL 744-6065

Fig. 50

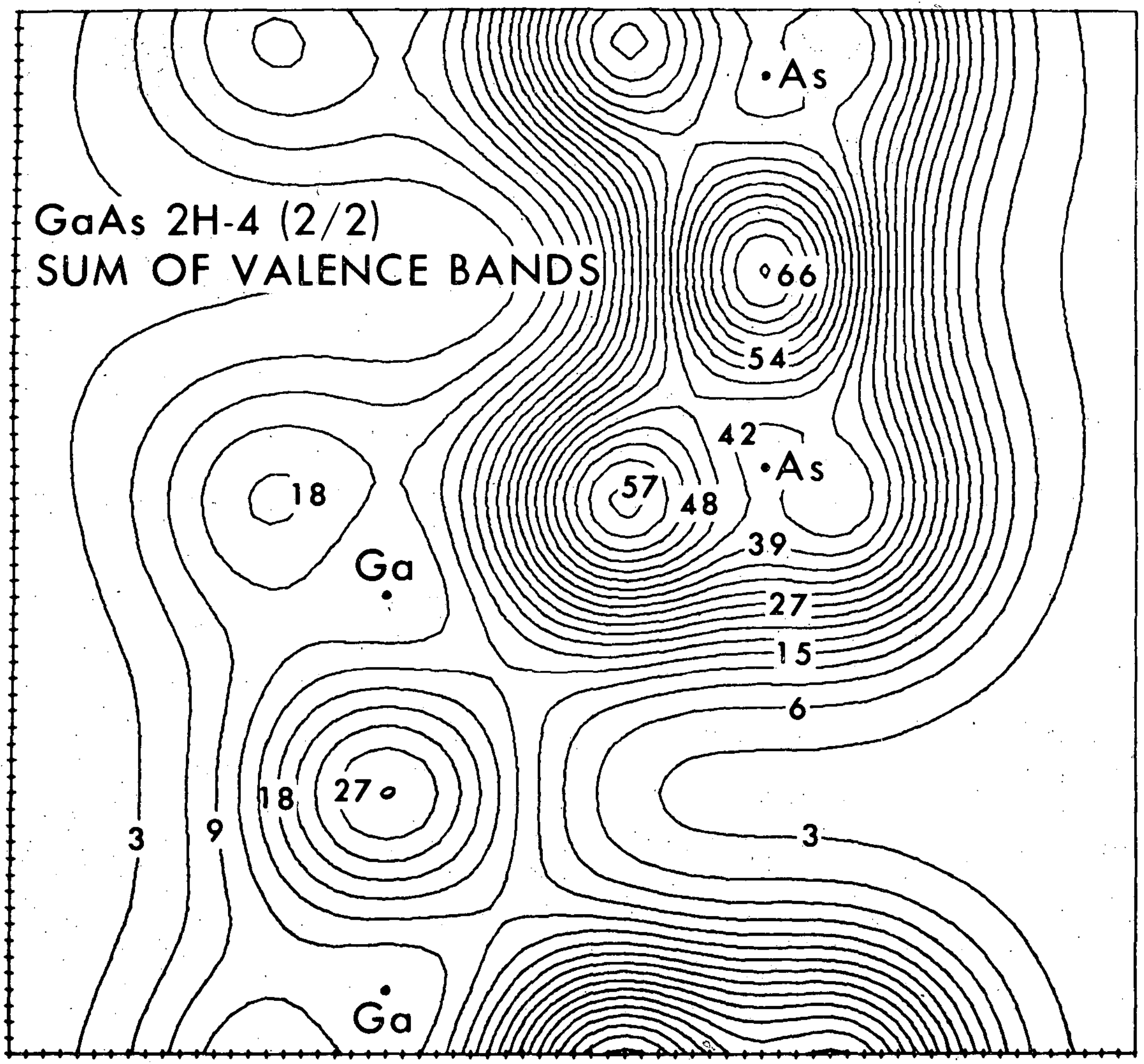

XBL 744-6053

Fig. 51

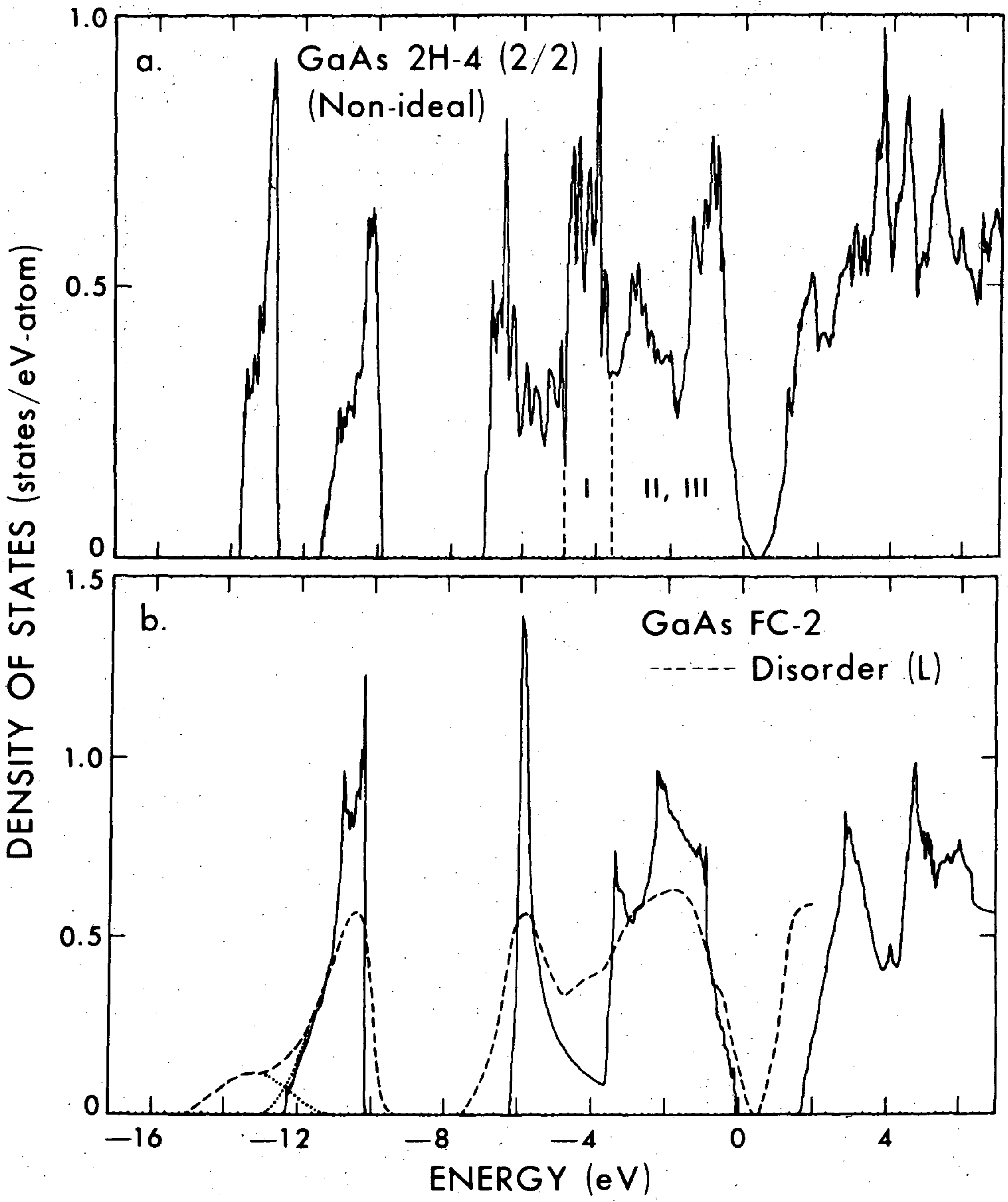

XBL 744-6071

Fig. 52

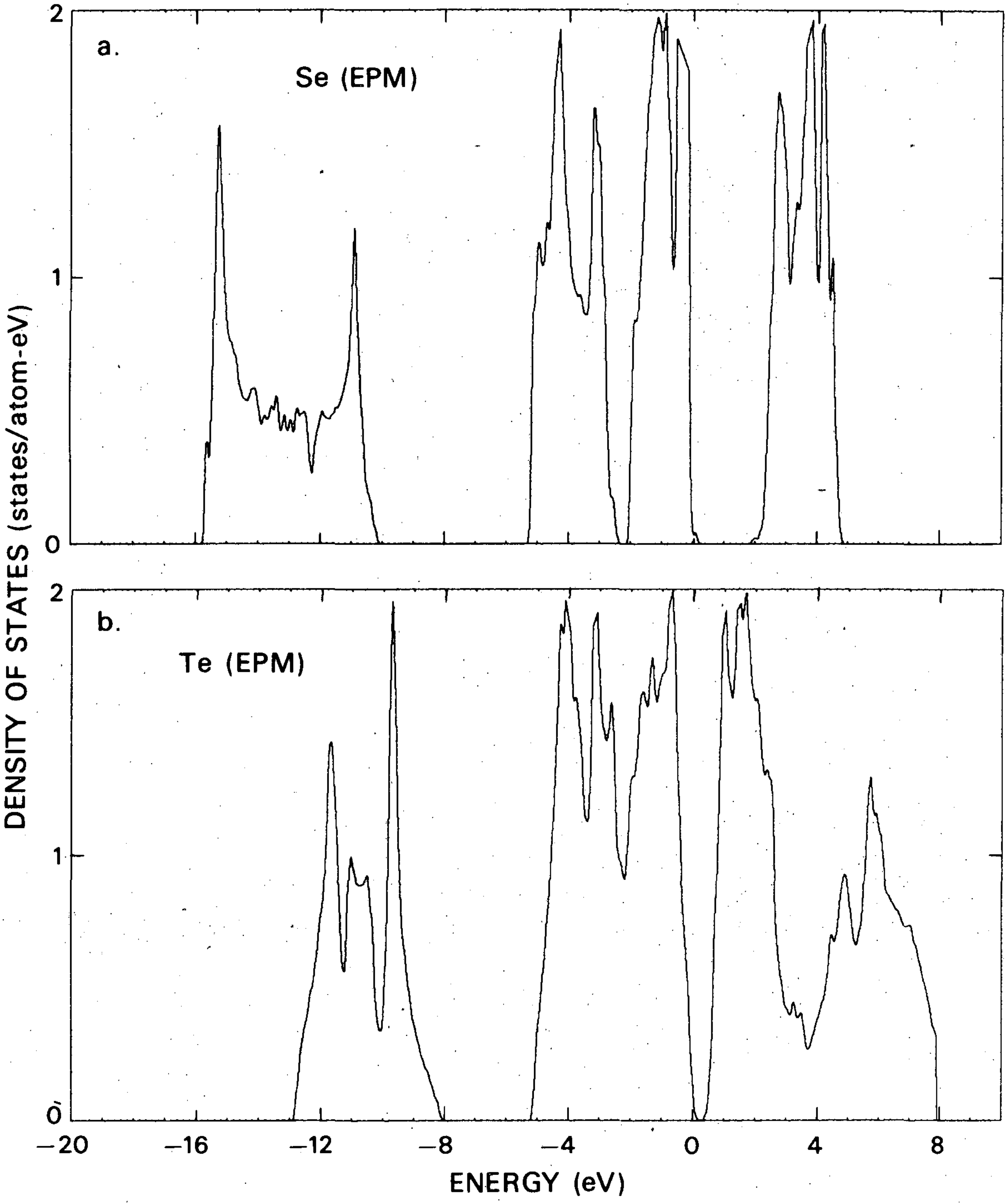

XBL 744-6086

Fig. 53

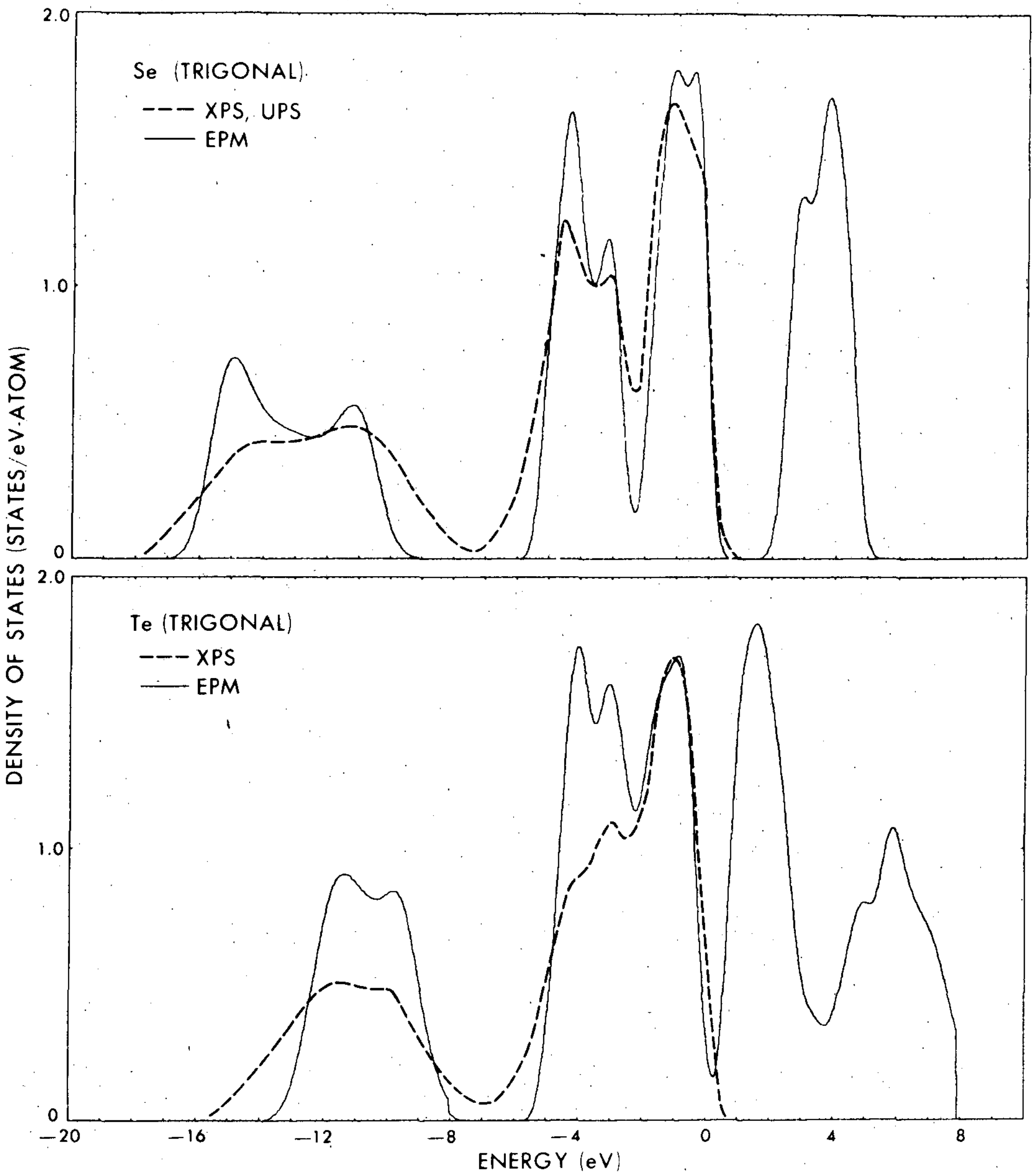

XBL 744-6091

Fig. 54

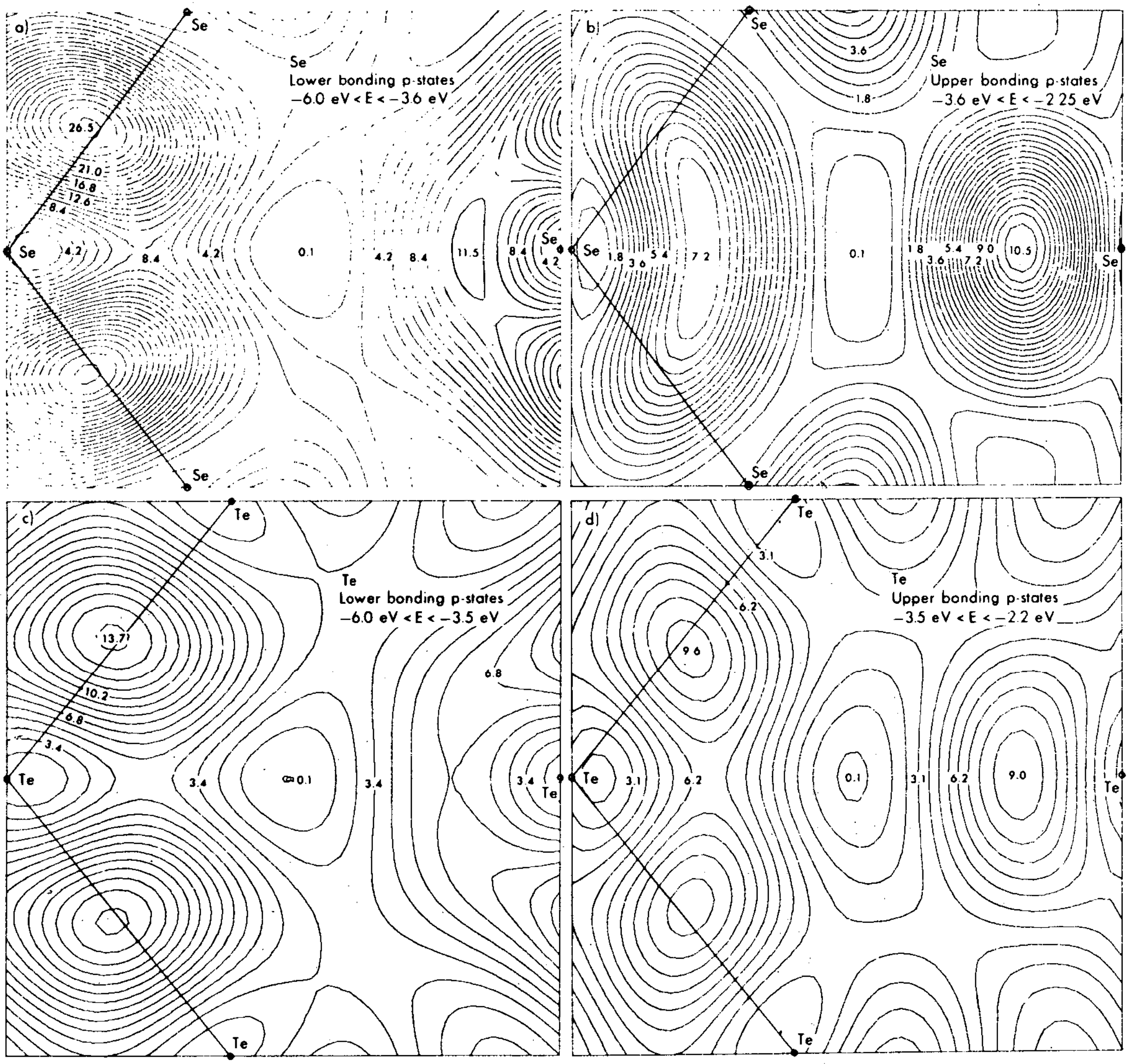

XBL 744-6089

Fig. 55

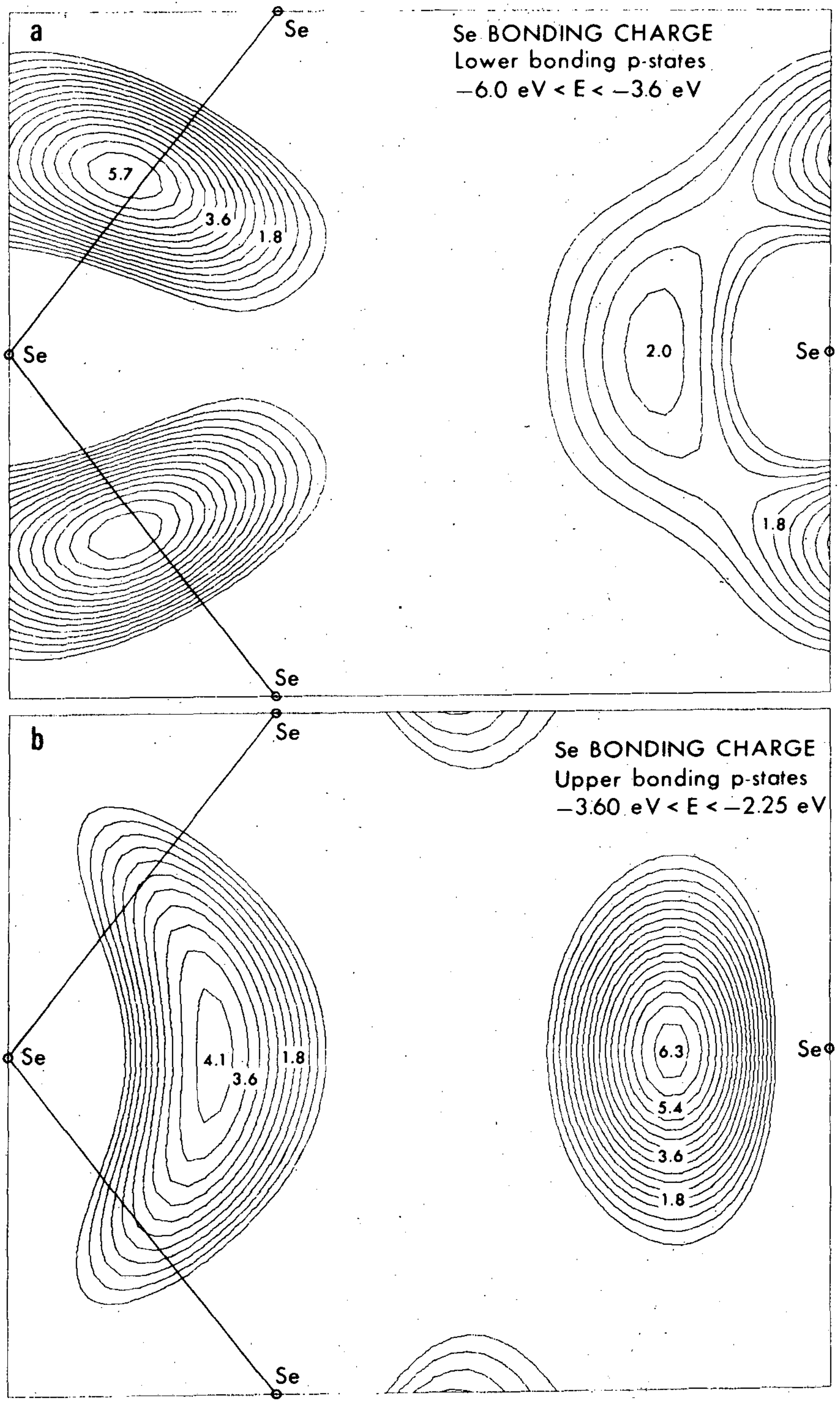

Se BONDING CHARGE
Lower bonding p-states
−6.0 eV < E < −3.6 eV

Se BONDING CHARGE
Upper bonding p-states
−3.60 eV < E < −2.25 eV

XBL 744-6088

Fig. 56

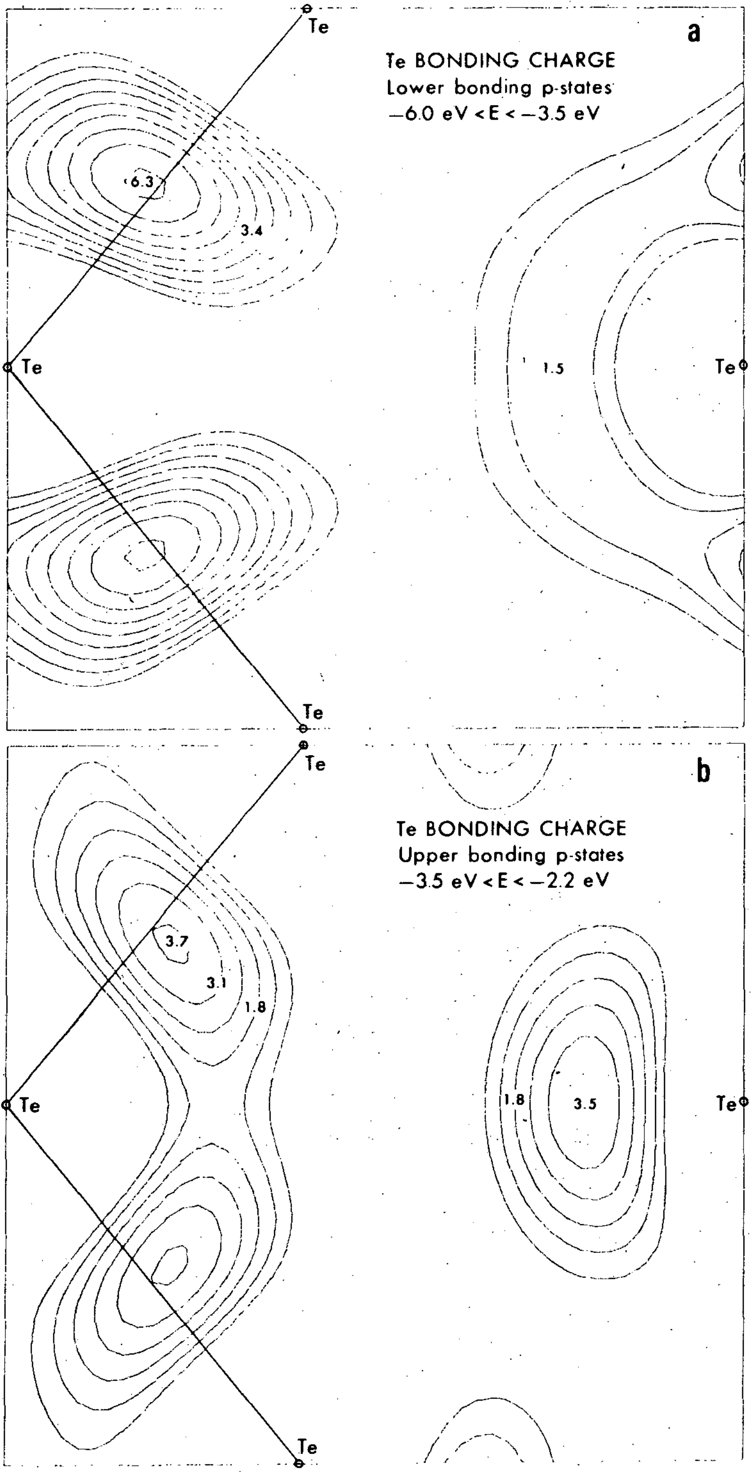

XBL 744-6087

Fig. 57

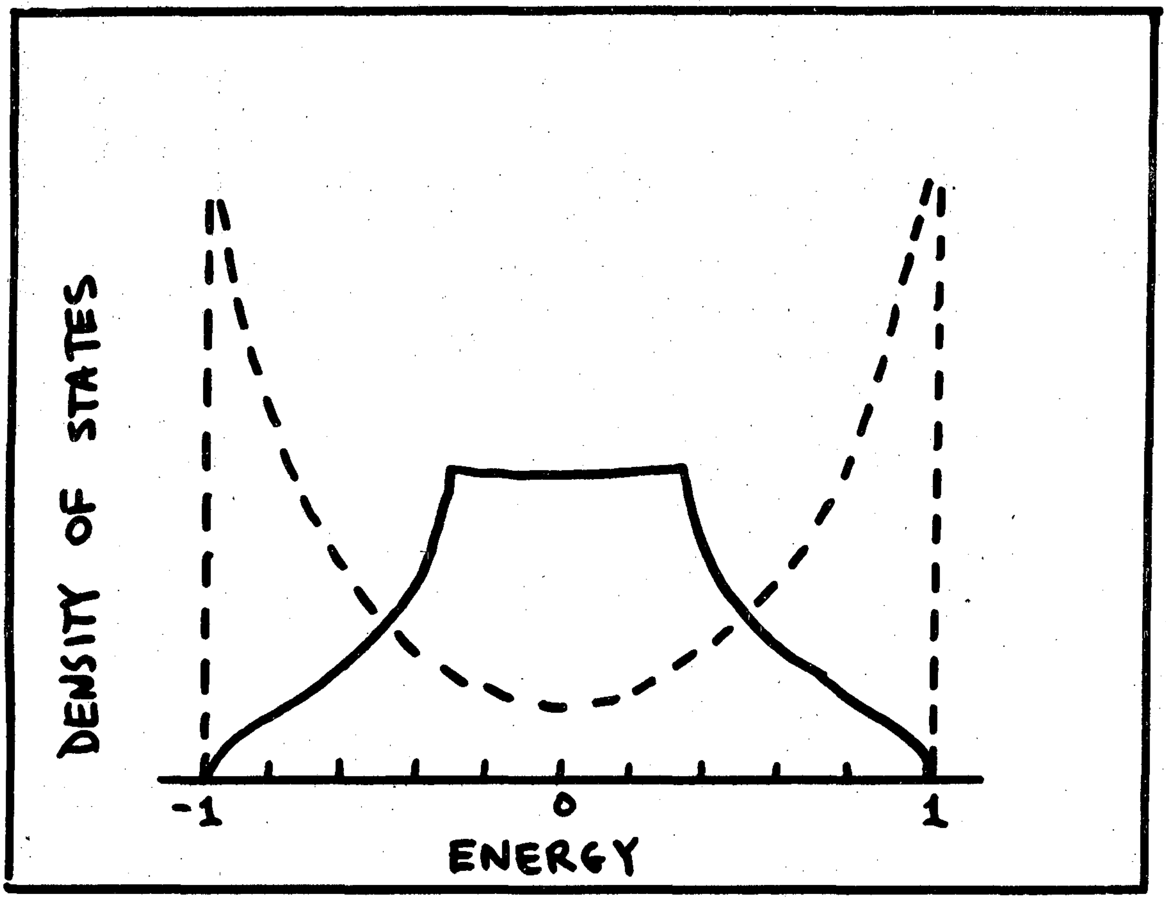

XBL 744-6085

Fig. 58

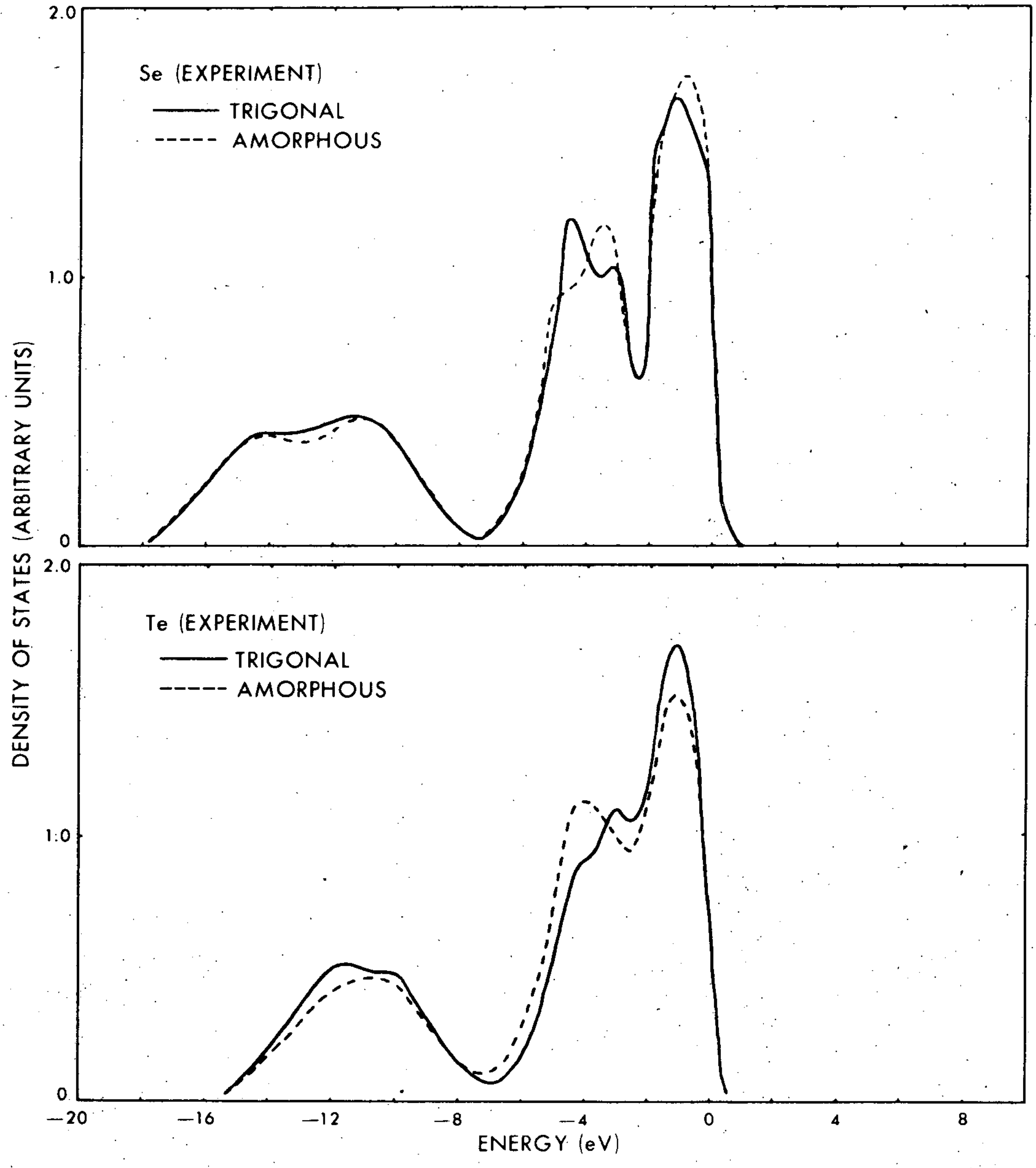

XBL 744-6092

Fig. 59

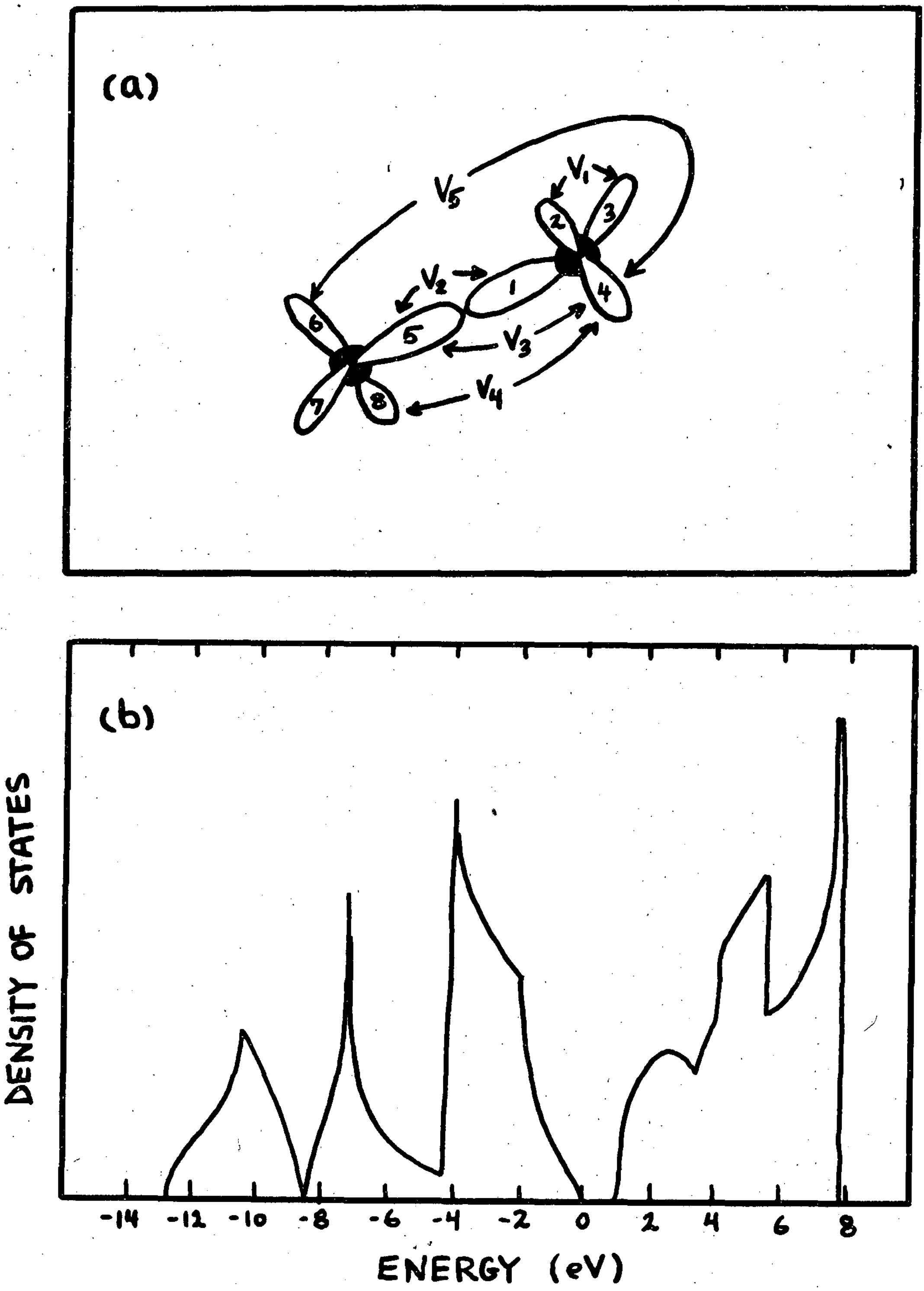

XBL 744-6093

Fig. 60

LEGAL NOTICE

This report was prepared as an account of work sponsored by the United States Government. Neither the United States nor the United States Atomic Energy Commission, nor any of their employees, nor any of their contractors, subcontractors, or their employees, makes any warranty, express or implied, or assumes any legal liability or responsibility for the accuracy, completeness or usefulness of any information, apparatus, product or process disclosed, or represents that its use would not infringe privately owned rights.

TECHNICAL INFORMATION DIVISION
LAWRENCE BERKELEY LABORATORY
UNIVERSITY OF CALIFORNIA
BERKELEY, CALIFORNIA 94720